Charles University in Prague
Faculty of Mathematics and Physics

DOCTORAL THESIS

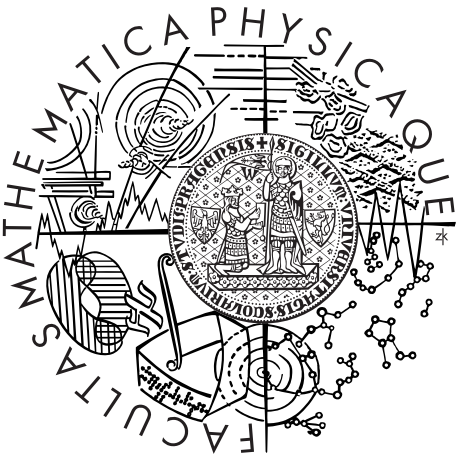

Petra Maierová

Evolution of the Bohemian Massif: Insights from numerical modeling

Department of Geophysics

Supervisor of the doctoral thesis: Doc. RNDr. Ondřej Čadek, CSc.

Study programme: Physics

Specialization: Geophysics

Prague 2012

I am thankful to Doc. Ondřej Čadek for his supervision and particularly for his enthusiasm for geology which led me to where I am now. Many thanks belong to Prof. Karel Schulmann, Dr. Ondrej Lexa and Dr. Stanislav Ulrich for their patience and care when introducing me to the vast field of geological research.

During the years I have spent at the Department of Geophysics, I have enjoyed the friendly and collaborative atmosphere created by the teachers, students, as well as foreign friends of the Department. I particularly appreciate the support by Doc. Ctirad Matyska and Doc. Hana Čížková, and discussions with Prof. Jiří Zahradník, Doc. Oldřich Novotný, Dr. Ondřej Souček, Dr. František Gallovič and Dr. Jakub Velímský about geophysical and numerical issues. I am also grateful to Dr. Gerd Steinle-Neumann and the group of people at the Bayerisches Geoinstitut in Bayreuth where I benefited from the inspiring and challenging atmosphere.

My family and my friend L. deserve warm thanks for their support and understanding throughout my seemingly never-ending studies.

Finite-element computations were performed using the open-source software Elmer developed by the CSC—IT Center for Science. The implementation of my procedures in Elmer was possible only thanks to advice from Dr. Juha Ruokolainen. The Charles University is acknowledged for supporting my studies through projects GAUK-432911 and SVV-2012-265308.

I declare that I carried out this doctoral thesis independently, and only with the cited sources, literature and other professional sources.

I understand that my work relates to the rights and obligations under the Act No. 121/2000 Coll., the Copyright Act, as amended, in particular the fact that the Charles University in Prague has the right to conclude a license agreement on the use of this work as a school work pursuant to Section 60 paragraph 1 of the Copyright Act.

In Prague 10. 10. 2012 Petra Maierová

Název práce: Fyzikální model vývoje Českého masivu

Autor: Petra Maierová

Katedra: Katedra geofyziky

Vedoucí disertační práce: Doc. RNDr. Ondřej Čadek, CSc.

Abstrakt: Český masiv byl konsolidován v důsledku kolize několika kontinentálních mikrodesek v průběhu Variského vrásnění (∼400–300 Ma). Centrální část Českého masivu, Moldanubikum, obsahuje významné množství felsických vysoce metamorfovaných hornin. V této práci představujeme numerický model kontinentální kolize, která vedla k výstupu těchto hornin. Důležitým předpokladem modelu je felsické složení spodní kůry jednoho z kolidujících kontinentálních bloků, a z toho vyplývající její nízká hustota a viskozita a vysoký obsah radioaktivních prvků způsobujících zahřívání materiálu. Zkoumali jsme vliv koncentrace tepelných zdrojů, rychlosti kolize a povrchové eroze na deformaci kůry a na tlakově-teplotní podmínky ve spodněkorovém materiálu. Při časovém vývoji dochází v modelu ke ztluštění kůry, růstu náhorní plošiny a sedimentaci v předpolní pánvi. Pokud je spodní kůra dostatečně změkčená v důsledku radioaktivního zahřívání, je ztluštění kůry doprovázeno gravitačně indukovaným výstupem spodněkorových hornin a následně subhorizontálním tečením ve střední kůře. Naproti tomu v chladnějších a rychlejších modelech je hlavním mechanismem ztluštění kůry vrásnění. Tyto dva typy chování vystihují pozorované rozdíly mezi felsickými vysoce metamorfovanými horninami v moldanubické a v sudetské části Českého masivu.

Klíčová slova: Český masiv, numerický model, felsická spodní kůra, exhumace

Title: Evolution of the Bohemian Massif: Insights from numerical modeling

Author: Petra Maierová

Department: Department of Geophysics

Supervisor: Doc. RNDr. Ondřej Čadek, CSc.

Abstract: The Bohemian Massif was consolidated during the Variscan orogeny (∼400–300 Ma), which involved several oceanic subductions and collisions of continental micro-plates. The central part of the Bohemian Massif, the Moldanubian domain, shows a large accumulation of felsic high-pressure metamorphs. We present a numerical model of exhumation of these rocks due to continental collision and underthrusting. The key feature of the model is a felsic (light, rheologically weak and rich in radioactive elements) material in the lower crust of one of the colliding blocks. We examine the influence of the rate of convergence of the two blocks, radiogenic heating in the felsic lower crust and efficiency of erosion, on the model evolution and pressure–temperature conditions in the lower-crustal material. The models where the material is sufficiently weakened due to radiogenic heating show formation of an orogenic plateau, sedimentation in a foreland basin, and crustal thickening accompanied by gravity-driven exhumation of the lower crust and subsequent sub-horizontal flow in the middle crust. In colder and/or faster models, the thickening is dominated by folding. We correlate the tectonic style of these two types of models with differences between the high-grade rocks in the southern (Moldanubian) and northern (Sudetic) parts of the Bohemian Massif.

Keywords: Bohemian Massif, numerical model, felsic lower crust, exhumation

Contents

Introduction

The tectonics of the Earth's crust and lithosphere are studied by means of geological and geophysical methods. Among the geophysical methods, the studies of seismic-waves propagation are the most powerful tool for determination of material distribution and discontinuities, which can be inferred from the distribution of seismic velocities and seismic reflectors. Besides that, anisotropy and attenuation of seismic waves are studied. The anisotropy corresponds to present or past preferential direction of flow, or it can be related to layered character of the media. The attenuation of waves can be a result of presence of fluids, such as melt or water. These fluids can be also detected due to their high electric conductivity and magnetic susceptibility. Additional information on material distribution comes from measurements of gravity anomalies.

In contrast to the geophysical methods, which reveal the current state of the lithosphere, the geological methods can help to reconstruct its past evolution. The field of geological research is mostly limited to the rocks exposed at the surface, but some of these rocks used to be deeply buried and record the processes that took place in the crust or even in the lithospheric mantle. However, the geological data do not fully constrain the evolution of a studied region. The reconstruction is often complicated due to an overprint of different stages of evolution and associated metamorphism. In the reconstruction, geophysical data can provide important constraints because they allow prolongation of surface features to deeper levels.

Numerical modeling is potentially an ideal tool for further improvement of understanding of tectonic processes and evolution of a particular region, but many challenges arise in numerical implementation of crustal deformation. Unlike the mantle, the crust is very heterogeneous. It consists of materials with distinct rheological properties that are subject to highly varied conditions: low pressure and temperature near the surface of the Earth and relatively high pressure and temperature at a depth of several tens of kilometers. Moreover, the deformation in the upper crust is mostly brittle and the strain is localized into narrow shear zones and thrusts. Another complexity arises from the fact that rock properties change due to phase transitions. Among others, the (partial) melting of rocks largely influences their rheology and plays an important role in the heat transport. A proper numerical treatment of migration of melt and other fluids is a difficult task and its implementation in models of crustal deformation requires a multi-scale modeling approach. In the dynamics of tectonic processes, an interplay between forces from below and from a topography load modified by erosion and sedimentation is of particular importance. For a proper implementation, a model of the surface processes coupled with a climatic model is needed. Also the bottom boundary of the lithosphere is not impermeable, and an interaction with deeper mantle levels is important. Material from the crust and lithosphere can be dragged into the mantle in subduction zones

or it may be detached in a process of delamination. Mantle convection gives rise to hot plumes which may cause thinning and rifting of the lithosphere.

Despite these complexities, the current state of numerical modeling allows to reproduce general characteristics of many types of tectonic processes. Models of oceanic subduction commonly incorporate pressure-temperature-composition dependent rheology including (de)hydration reactions (e.g. Gerya et al., 2008) and several mechanisms of ductile deformation, such as dislocation and diffusion creep (e.g. Čížková et al., 2002). The importance of brittle-ductile character of deformation was examined e.g. in models of continental rifting (e.g. Huismans and Beaumont, 2003), and evolution of fold-and-thrust belts (Ruh et al., 2012). Phase transitions in the solid state were shown to significantly influence exhumation of rocks within continental crust (e.g. Gerya et al., 2004). Melting and solidification at mid-ocean ridges were self-consistently modeled yielding important implications for our understanding of oceanic-crust generation (Katz et al., 2006; Katz, 2008). Three-dimensional models of tectonic deformation coupled with surface processes can reproduce complex topographic structures within mountain belts (Braun and Yamato, 2010).

Although tectonic processes generally operate in three dimensions, a simplified two-dimensional modeling approach is often used. Many characteristics of oceanic subduction and continental collision have been reproduced in two-dimensional models (e.g. Gerya et al., 2008; Beaumont et al., 2001). The sideways motion during continental collision can be modeled in the thin-sheet approach, which approximates the dynamics in a plan view (e.g. Jiménez-Munt and Platt, 2006; Lorinczi and Houseman, 2010). However, some processes, such as deformation at oceanic transform faults, can not be approximated in two dimensions and have to be treated in a fully three-dimensional model (Gerya, 2010).

In the modeling of crustal and lithospheric deformation, most attention is paid to general mechanisms or to explanation of recent processes (active subductions, continental collision), which are mostly described through geophysical observations. However, increasing number of studies deals also with reconstruction of ancient mountain-building processes (e.g. Jamieson et al., 2007), where most of the constraints come from geological studies. An example of an ancient mountain belt comparable in size and heat budget to the modern Himalayas are the Paleozoic Variscides. The Bohemian Massif is the largest well-preserved exposure of the former European Variscan belt. It has been extensively studied by means of geological and geophysical methods, but just a few numerical modeling studies concerning its evolution have been performed so far (Henk, 1997; Gerdes et al., 2000; Arnold et al., 2001; Willner et al., 2002; Duretz et al., 2011; Lexa et al., 2011). A numerical model of a particular episode of the building of the Bohemian Massif is the main focus of this study.

In Chapter 1 we briefly overview the geological and geophysical data available for the Bohemian Massif, and introduce scenarios of its tectonic evolution. We pay special attention to the Variscan evolution (∼400–300 Ma), which can be further divided into several stages. During the last stage, several continental blocks collided, and the collision was accompanied by exhumation of large volumes of rocks from the deep crustal interior. These rocks, now exposed at the surface, bear witness of a complex metamorphic and deformational history. Our aim is to set up a numerical model which would be in agreement with the basic geological data related to this process and which would provide a deeper insight into the dynamics of the

exhumation process. In Chapter 2 we describe the computational tool we developed for this purpose, and we show several simple numerical tests in order to illustrate its accuracy and applicability. Chapters 3 and 4 contain two articles published in international scientific journals. In Chapter 3 we introduce the numerical model of the late Variscan evolution of the Bohemian Massif and discuss its main characteristics. In Chapter 4 we present a parametric study and correlate the differences among the calculated models with the variations observed in the geological record within the Bohemian Massif. The concluding chapter provides a brief summary of the results and outlines a possible continuation of the research.

At the bottom of pages 6–74 a model of crustal deformation presented in Chapter 3 is visualized. The modeling results were plotted using the Generic Mapping Tools (Wessel and Smith, 1998).

Chapter 1

The Bohemian Massif

The Variscan orogeny was a major mountain-building process which operated during the Late Paleozoic (∼400–300 Ma) as a result of convergence between Gondwana and Laurasia. The relics of the European Variscan orogen can be found in a belt spanning the continent from west to east (Fig. 1.1): Iberia, Armorican Massif, Massif Central, Vosges, Rhenish Massif, Harz, Black Forest, Bohemian Massif, and parts incorporated in the Alps and Carpathians. The Bohemian Massif approximately coincides with the Czech Republic, but it extends further to Austria, Germany and Poland. The Bohemian Massif is the largest European Variscan outcrop and it was only marginally affected by later tectonic events. During the Alpine orogeny, its south-eastern part was covered by the Carpathian foreland and pre-existing crustal-scale shear zones were reactivated in conjunction with widespread volcanism during Tertiary.

The topographic relief of the Variscan mountain belt has been reduced by denudation leading to exposure of deep levels of the former crustal root at the surface. Based on the geological (e.g. structural, petrological, geochronological) observations of the exposed rocks, we can constrain the deformation history, pressure and temperature conditions that took place in the interior of the ancient orogen. The geological methods can study the tectonic processes in great detail, but the gathered pieces of information have to be carefully assembled in order to obtain a consistent image of the past evolution of the orogen.

Information on the recent internal architecture of the Bohemian Massif can be inferred from geophysical observations (e.g. seismology, gravity, magnetotelluric data) and it is mostly acquired by inverse modeling methods. The knowledge of limitations of the methods and appropriate error estimates are crucial in evaluating the results. In particular, the inversion of geophysical data in order to obtain a model of the crust and lithosphere (distribution of seismic velocities, density and material structure, presence of fluids) is non-unique and depends on the applied approach. A combination of geological and geophysical methods together with a larger frame of European tectonics thus has to be used in order to constrain the evolution of the Bohemian Massif.

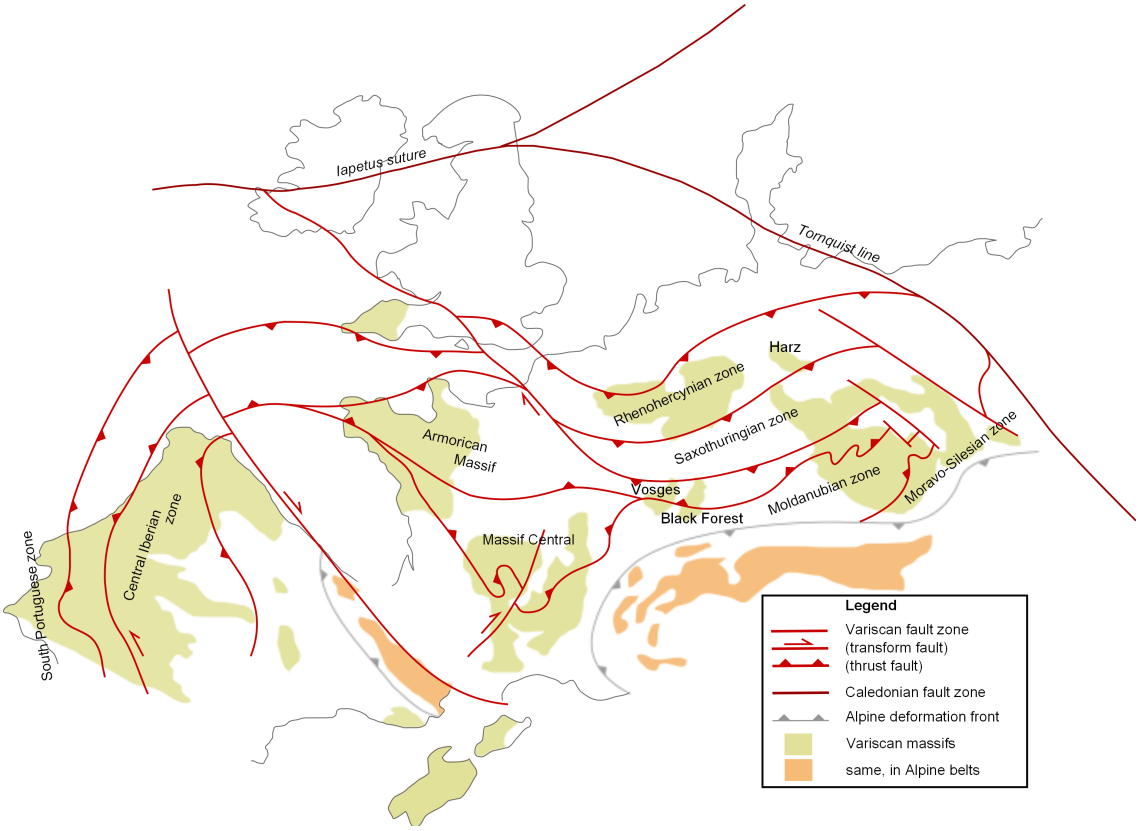

Figure 1.1: Location of Variscan outcrops and sutures in Europe, and (deformed) European shorelines. Modified from Wikipedia, the free encyclopedia, http://en.wikipedia.org-/wiki/File:Hercynian_structures_Europe_EN.svg.

1.1 Geology

From the geological[1] point of view the Bohemian Massif is an interesting region where all three basic types of rocks are abundant:

Sedimentary rocks consist of material that was detached from its original site by surface processes, such as water or wind erosion, transported and later deposited. Their location and volume, shape of the sedimentary layers, and size and shape of their constituents provide information on the environment where they were created, on the climate and topography. Historically, the fossils in the sedimentary sequences and organic sediments were used as a basis for establishment of a relative geological time scale. In contrast, the modern dating is based on radioactive decay and it provides absolute ages of different stages of rock formation such as deposition of sediments, crystallization of rock from magma, and metamorphism.

Igneous rocks are made of solidified magma derived from of pre-existing rocks by melting. Melting occurs when the temperature exceeds the solidus of the parent rock e.g. due to an increase of temperature on site, burial of fertile rocks to a

[1]We note that this section is not comprehensive and summarizes only the basic characteristics of the geology of the Bohemian Massif. The scientific literature on the topic is extensive and we mostly cite overviews. The geological terminology is rather complicated and we try to avoid it, which may in some cases lead to a simplification of the problem. Necessary terms are written in *italics* and explained in a short dictionary at the end of this chapter, together with a geological time-scale.

greater depth with higher temperature, an increase of fluid content, or decompression. Melt then usually percolates upward, and depending on the place where it solidifies igneous rocks can be further divided into **volcanic** and **plutonic** groups. In the former group, the melt reached the surface and formed for example different kinds of lavas, while in the latter, it remained trapped within the crust, and either cooled slowly in large bodies (typical extent of several km in each dimension) or more quickly in planar bodies such as dykes. The composition of magma depends on the composition of rocks that were primarily melted, but it can be significantly influenced by contributions from rocks along the path of the melt. The igneous rocks bring information about deep crustal levels, which are otherwise hardly accessible.

Rocks that underwent changes in their mineral composition and structure are called **metamorphic**. In contrast to the igneous rocks that are formed by melting and solidification, the metamorphic changes take place in the solid state. The metamorphism mostly results from increased pressure and temperature (P–T) conditions, determination of which is the subject of petrological studies. Certain P–T conditions in general, and the temperature gradient with depth in particular, are typical for different kinds of tectonic settings. A high pressure attained at low-temperature conditions indicates a subduction setting, where a relatively cold lithospheric material is dragged into the mantle. A contrasting example is a rifted region above an asthenospheric updoming, where high temperatures can be reached at low pressures. Changes in the mineral composition due to evolving P–T conditions are accompanied by changes in the rock structure at various spatial scales (sub-grain size to kilometers). From the resulting structure the rock strain can be determined, which is a basic step towards deciphering individual stages of a tectonic process.

1.1.1 Tectonic units

The Bohemian Massif (Fig. 1.2) can be divided into several tectonic domains or terranes (Saxothuringian, Teplá-Barrandian, Moldanubian, Lugian, Moravo-Silesian, Brunovistulian; for original definitions see Suess, 1912; Kossmat, 1927; Dudek, 1980) separated by zones of major deformation. Besides the characteristics of these tectonic domains and their boundaries, we will pay attention to several rock types that are specific for the Bohemian Massif and that play an important role in assessment of a scenario of its Variscan evolution.

- The **Saxothuringian** domain is an elongated region between the Rhenohercynian Zone to the north-west and the Teplá-Barrandian to the south-east. Its basement is formed by Neoproterozoic (580–550 Ma) rocks with sequences of volcanics and sediments characteristic for an active continental margin. After a gap in sedimentation at the beginning of the Cambrian (540 Ma, corresponds to the so-called Cadomian orogeny) the character of sediments changed pointing to lithospheric extension and rifting. The corresponding high thermal regime has also been deduced from bimodal volcanism and magmatism interpreted as a result of updoming of the lithosphere. Since the Ordovician, the sedimentation typical for passive margin environment continued until 350 Ma. (For overview of the Saxothuringian sedimentary record see Linnemann et al., 2004.)

  During the subsequent Variscan orogeny, the rocks were deformed and metamorphosed with intensity increasing towards the contact with the Teplá–

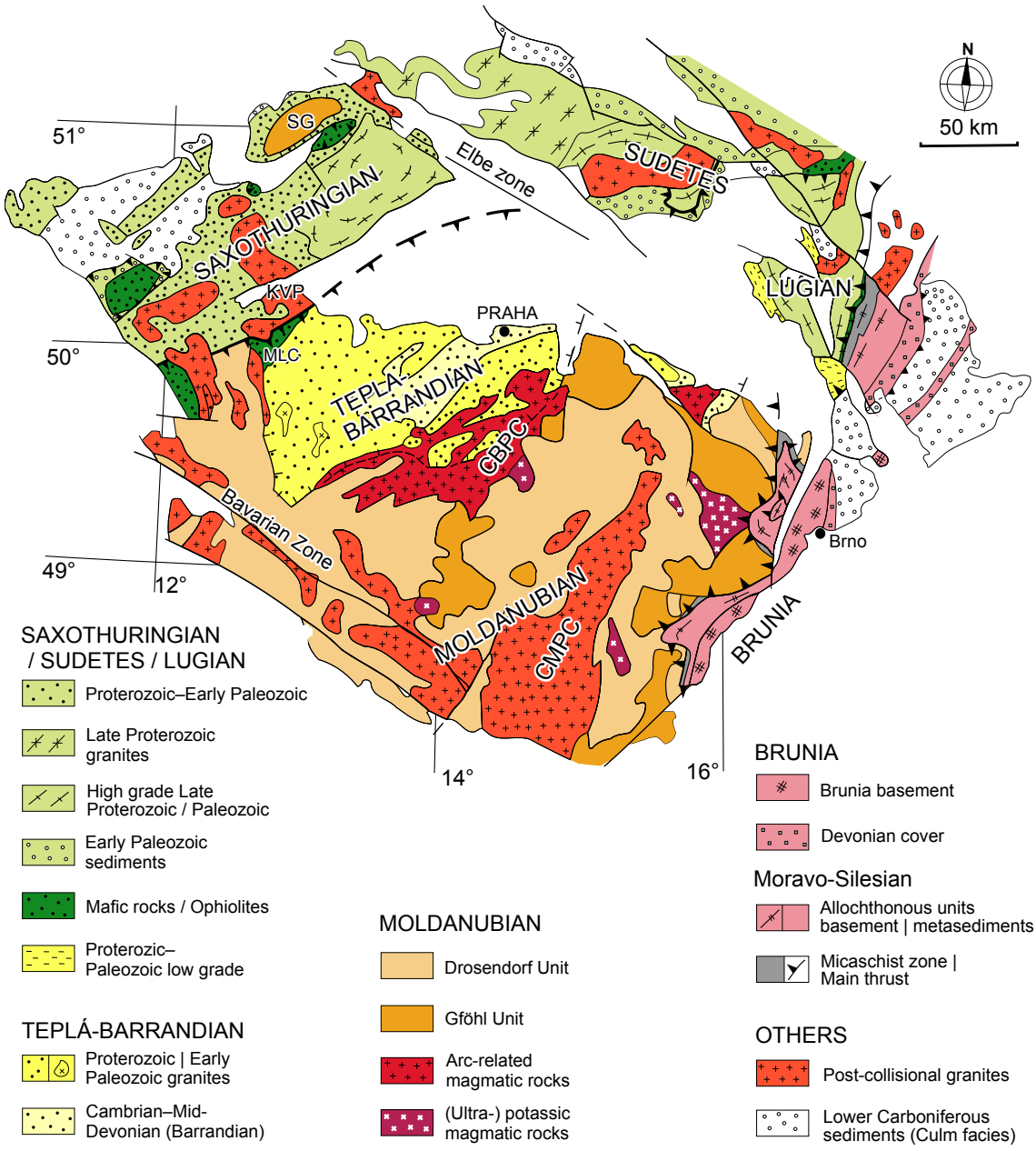

Figure 1.2: Simplified geological map of the Bohemian Massif (modified after Franke, 2000; Schulmann et al., 2009). Red and violet colors correspond to plutonic rocks. White areas are covered by post-Variscan sediments and volcanics. CBPC=Central Bohemian Plutonic Complex, CMPC=Central Moldanubian Plutonic Complex, KVP=Karlovy Vary Pluton, MLC=Mariánské Lázně Complex, SG=Saxon Granulite Massif.

Barrandian to the south-east. On top of the sediments relics of flat thrust sheets (*nappes*) which sustained a high degree of metamorphism at ∼340 Ma are located. The original lateral extent of the *nappes* may have been tens to hundreds of kilometers and their thickness a few kilometers. Their relics, now partly eroded and/or folded to steep position, can be classified into two groups showing contrasting metamorphic conditions (Konopásek and Schulmann, 2005, and references therein). The first group is composed of sediments metamorphosed under *eclogite facies* and *mafic eclogites*. The occurrence of this rock type points to burial to large depths with relatively low-temperature

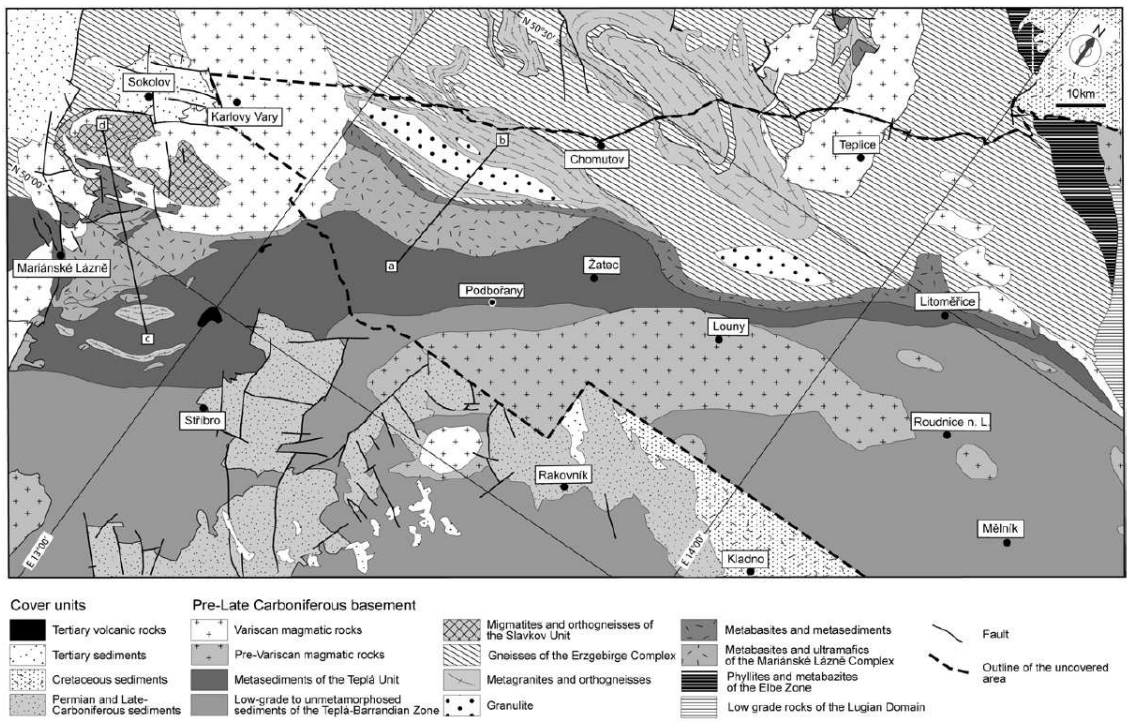

Figure 1.3: Stripped contact of the Saxothuringian and Teplá-Barrandian domains after Mlčoch and Konopásek (2010).

conditions corresponding to a cold geotherm. The rocks belonging to the second group reveal burial along hotter geotherm (*granulites*, ∼800 °C at ∼2 GPa) and bear evidence of partial melting. These high-temperature conditions are recorded for example in a large body of *granulite* rocks, the Saxon Granulite Massif (Rötzler and Romer, 2001).

The contact of the Saxothuringian and Teplá-Barrandian domains sustained intense deformation and metamorphism. The region is characterized by juxtaposition of slices of rocks with contrasting composition and metamorphism, including rocks that underwent high pressures, high temperatures or partial melting (*eclogites*, *gneiss*, *granulites*, *migmatites*). The high-pressure conditions have been confirmed by the finding of micro-diamonds, which are assumed to be stable at pressures higher than ∼4 GPa (Kotková et al., 2011). Directly at the boundary, units with a high content of (ultra)*mafic* rocks (e.g. the Mariánské Lázně Complex, MLC) are located. The MLC contains rocks metamorphosed under conditions suggesting burial and exhumation along a cold geotherm (*serpentinites, amphibolites, eclogites* and meta-*gabbros*).

A major part of the contact is hidden under younger sedimentary and volcanic rocks, but continuation of a belt of highly metamorphosed units and MLC-type rocks is confirmed from borehole samples (Mlčoch and Konopásek, 2010, see the reconstruction of the contact in Fig. 1.3). In the **Sudetes** region east of the Elbe (Labe) Zone rocks of a similar type as in the Saxothuringian domain continue, including units with (ultra)*mafic* composition (Mazur et al., 2006).

- The **Teplá-Barrandian** domain is a well spatially defined crustal block in the center of the Bohemian Massif which was only affected by low-grade Variscan metamorphism. It consists of Neoproterozoic volcanics and sediments (ages

of about 620–560 Ma) whose characteristics point to an active-margin setting (for overview see Drost et al., 2004). The discontinuity in sedimentation at the end of the Proterozoic (∼540 Ma) is interpreted to be a result of the Cadomian orogeny. Similarly to the Saxothuringian domain, a high thermal regime during the Late Cambrian (∼500 Ma) is recorded in volcanic and magmatic rocks. The sedimentation continued until the mid-Devonian (∼380 Ma), and culminated by *flysh* sediments related to closing of an oceanic basin. The resulting Cambrian–Devonian sedimentary sequence is particularly well preserved in the Prague basin (Chlupáč, 1993). During the Devonian, the rocks were folded and metamorphosed with intensity and age increasing towards the contact with the Saxothuringian domain in the north-west.

- A large association of plutonic bodies, the **Central Bohemian Plutonic Complex** (CBPC), is located along the south-eastern margin of the Teplá-Barrandian. The composition of magmas in the CBPC is variable and suggests that the source of the melt evolved in time (for overview see Janoušek et al., 2000). The oldest rocks of CBPC are dated to ∼370 Ma, but two slightly older plutons (375–373 Ma) in the Teplá-Barrandian crust some 20 and 50 km to the west have been interpreted to genetically belong to the CBPC (Venera et al., 2000; Žák et al., 2011). The composition of the plutonic rocks placed during the Late Devonian (∼355 Ma) indicates that they originate from a slightly depleted mantle mixed with crustal rocks. In the Early Carboniferous (∼349–346) plutonic rocks, the composition of the mantle source is observed to be more enriched in incompatible elements.
  A large shear zone separating the Teplá-Barrandian and Moldanubian domains coincides with the location of the CBPC. It is about 2 km wide and it records a downward displacement of the Teplá-Barrandian downwards with respect to the Moldanubian domain by about 10 km. Based on the age of plutonic bodies which intruded along the shear zone, the time when the zone operated has been constrained to 343–337 Ma (for overview see Dörr and Zulauf, 2010).
- The **Moldanubian** domain is a region to the south-east from the Teplá-Barrandian, continuing further south-west to Austria and Germany. The Moldanubian rocks show medium to high grade of metamorphism (see Schulmann et al., 2008, and references therein). The *protoliths* of the metamorphosed rocks were dated to Proterozoic and Early Paleozoic age. According to the degree of metamorphism, the Moldanubian domain is divided into the **Drosendorf** and **Gföhl** Units. The Drosendorf Unit consists of rocks that underwent medium metamorphic conditions, which reached regionally pressures of 0.5–1.2 GPa (∼15–35 km depth) at temperatures of 600–750 °C (Racek et al., 2006; Petrakakis, 1997). Higher grade of metamorphism is typical for the Gföhl Unit, where some rocks (*granulites, eclogites*) bear witness of peak P–T conditions of 800–1000 °C and 1.6–2.2 GPa (∼50–65-km depth) (O'Brien and Rötzler, 2003; Štípská and Powell, 2005). The timing of formation of the *granulites* is very well defined and the data from different locations all yield similar ages around 340 Ma.
  Locally the *granulites* contain lenses (∼100-m to 2-km long) of *peridotites* (rocks with mantle composition) pointing to an interaction of the crust and the mantle during the tectonic process. The peak-pressure conditions (more than ∼3 GPa) recorded by these *peridotites* suggest that they were originally

located deeper than the surrounding *granulites*. *Peridotites* are also present in Saxothuringian *granulites* and their characteristics are similar to those in the Moldanubian domain (Schmädicke et al., 2010).
At ∼340–335 Ma, a number of plutons of (ultra-)potassic composition called *durbachites* were emplaced in a close spatial association with the *granulites* of the Gföhl Unit. The specific composition of *durbachites* requires melting of a mantle source contaminated by crustal material. The relationship between the Moldanubian *durbachites* and *granulites* is underlined by their complementary enrichment and depletion, respectively, in trace elements such as uranium, lead and thorium (Janoušek and Holub, 2007).
The rocks in the Moldanubian domain have a complex structure, which can be interpreted as a result of a succession of several stages of deformation (Schulmann et al., 2008). The stage of vertical motion of material is recorded in vertical *fabrics*. These were later reworked by subhorizontal *fabrics*, that can be attributed to a flow at medium- to low-pressure and high-temperature conditions. The vertical *fabrics* were dated to 350–340 Ma, while the ages of the subhorizontal *fabrics* are 330–325 Ma. The intensity of the reworking varies within the Moldanubian domain suggesting that the horizontal deformation was more prominent at its eastern margin.

- In the central part of the Moldanubian domain, numerous plutonic bodies form the **Central Moldanubian Plutonic Complex** (CMPC). The age of emplacement of the CMPC is significantly younger than that of the CBPC, and its composition is pointing to a crustal origin of the melt. The oldest ages (about 325 Ma) are recorded in the northern part of the CMPC, while southern and eastern bodies are typically younger (about 320–310 Ma) (Finger et al., 2009). A number of other plutons of similar composition and age are scattered in the south-western part of the Moldanubian domain along faults in the Bavarian Zone. Finger et al. (2009) suggested that not only the CMPC and plutons in the Bavarian Zone, but also late *granites* in the Saxothuringian domain including a large body of the Karlovy Vary Pluton, result from the same tectonic process.

- The **Lugian** domain (a part of the Sudetes region) is located north of the Moldanubian domain, from which it is separated by the Elbe Zone. It is significantly smaller than the Moldanubian domain, but they share several similarities (Schulmann et al., 2008). The core of the Lugian domain is formed by rocks (*gneisses*) that sustained medium-grade metamorphism and a belt (∼1×10 km) of *granulites* (maximum pressure 1.8–2 GPa, temperature 800–900 °C). These metamorphic rocks are considered to be an equivalent of the Moldanubian Gföhl Unit, which is further supported by their coeval peak metamorphism at 340 Ma. The core is surrounded by a few kilometers thick belt of mafic rocks interpreted to be a relic of a Cambro-Ordovician rift. In contrast to the Moldanubian domain, the steep fabrics associated with the vertical flow of material are well preserved in the Lugian domain, and the horizontal flow is not recorded (Schulmann et al., 2008; Štípská et al., 2012).

- The rocks at the eastern margin of the Moldanubian domain are thrusted over the Brunia domain to the east, in the form of *nappes* containing pieces of high-pressure metamorphs (*eclogites*, pressure ∼1.6 GPa, temperature ∼650 °C,

granulites and *peridotites*). The thrusting affected also the underlying Brunian rocks leading to the development of a 50-km wide zone of deformation and metamorphism — the **Moravo-Silesian Zone**. The metamorphic conditions in this zone (0.5–1 GPa, 550–650 °C) show inverse metamorphic gradient, i.e. increase towards the contact of the two domains. The cooling after the metamorphism was constrained to 340–325 Ma (Schulmann et al., 2009, and references therein).

- The **Brunia** (also called Brunovistulian) domain consists of a Neoproterozoic basement, intruded by 550-Ma-old *granites*. The basement is overlain by a thick pile of Devonian sediments. During the Early Carboniferous (∼345 Ma) a foreland basin developed, where the sediments were deposited for about 20 Ma now forming an up to 7.5-km thick sedimentary sequence. In the sediments, pebbles of highly metamorphosed rocks were identified, and the earliest age of their deposition was dated to 330 Ma (see Hartley and Otava, 2001, and references therein).

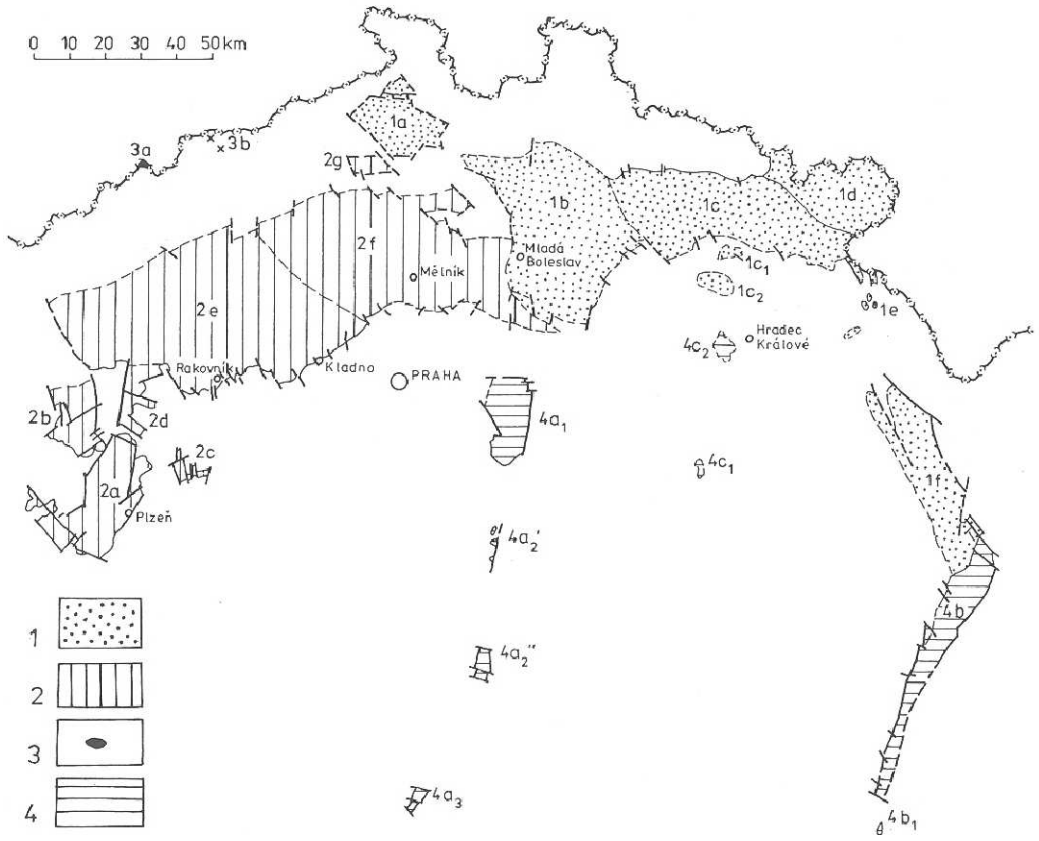

Figure 1.4: Permo-Carboniferous sedimentary cover in the area of the Czech republic after Chlupáč and Štorch (1992). 1) Sudetic Basins, 2) Central and Western Bohemian basins, 3) Late Paleozoic of the Erzgebirge, 4) sediments in graben structures (4a–Blanice graben, 4b–Boskovice graben, 4c–Jihlava graben).

1.1.2 Post-Variscan sediments and volcanics

A large portion of the surface of the Bohemian Massif is covered by post-Variscan sediments and accompanying volcanics. The Permo-Carboniferous (∼320–250 Ma) extensional basins (Fig. 1.4) are aligned along structural discontinuities, such as the Saxothuringian–Teplá-Barrandian boundary and the Moravo-Silesian Zone (see e.g. Ulrych et al., 2006). The upper part of their sedimentary infill, deposited in a continental environment, often contains coal-bearing layers.

The largest area is covered by Cretaceous sediments (∼90 Ma) located along Elbe and Odra Zones. Younger (mostly 35 Ma and later) sedimentary basins are located in the České Budějovice and Třeboň regions. At ∼20–12 Ma, a Carpathian foreland basin developed at the eastern margin of the Bohemian Massif and was being filled with marine sediments.

A system of Tertiary rift-related sedimentary basins and volcanics is located along the southern rim of the Krušné hory Mountains (Erzgebirge) in the region of the Eger (Ohře) Rift (Fig. 1.5). It extends from the Cheb basin (younger, 5 Ma) towards Doupovské hory and České středohoří. The volcanic rocks of this system cover an area of ∼1100 km^2. The main phase of the volcanism took place ∼30 Ma ago, but the oldest volcanic rocks in this system were dated to 80 Ma, and the volcanoes near Františkovy Lázně in the western Bohemia are only several hundreds of thousands of years old (see e.g. Ulrych et al., 1999).

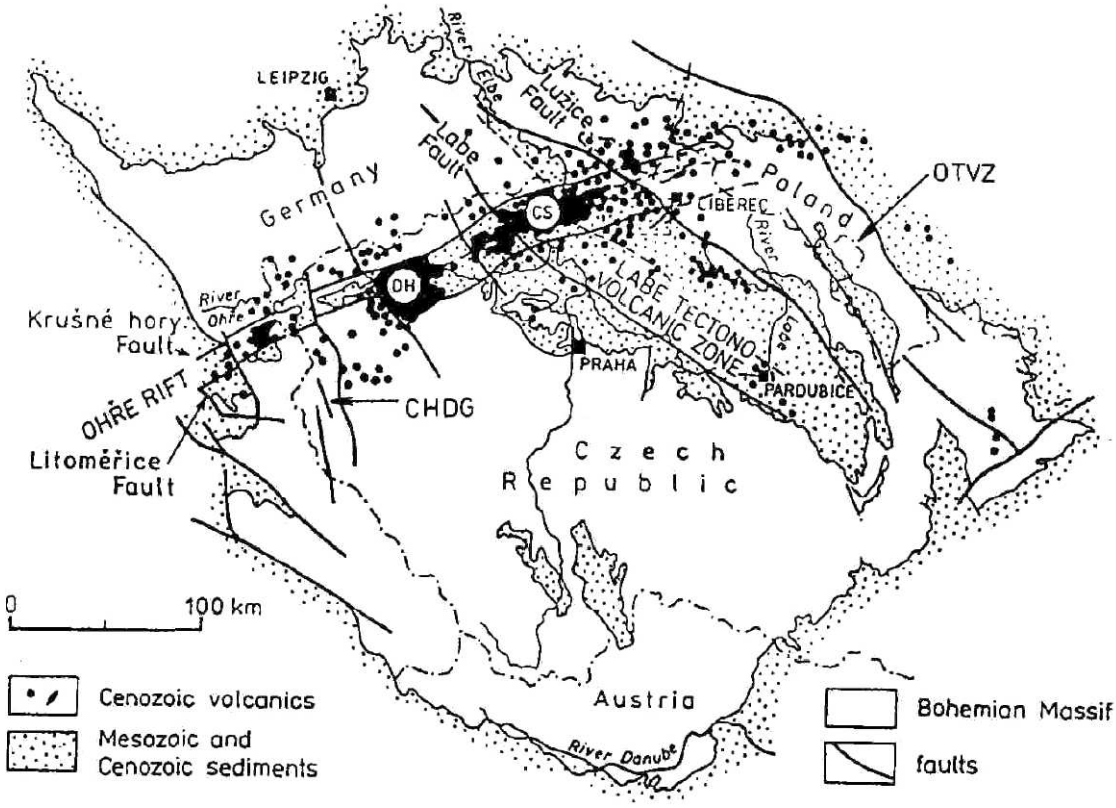

Figure 1.5: Cenozoic sediments and volcanics in the Bohemian Massif. After Kopecký (1978), adapted by Ulrych et al. (1999). DH=Doupovské hory, CS=České středohoří.

1.2 Geophysics

There is a broad spectrum of geophysical methods which can be used to constrain the crustal and lithospheric structure. In the following short and incomplete overview, we will focus on studies that help to reveal the deep crustal structure, especially the sub-surface equivalent of the geological domains described in the previous section.

The most important source of information about the lithospheric structure are **seismic waves**. The velocity of seismic waves is sensitive to the material through which they propagate, namely its density and elastic properties. Seismic studies can detect both abrupt and continuous changes in the velocity, but different methods are sensitive to different features, or they visualize them in a different manner. For example, steeply dipping velocity discontinuities are not directly observable in reflected seismic waves from a standard seismic profiling. The zones where the velocity decreases with depth are difficult to examine by seismic rays, but they can be identified by surface waves. In all methods of inversion of seismic data in order to obtain a model of velocity distribution in the Earth's interior, a good coverage of the studied domain by seismic waves is essential.

The Bohemian Massif is a well consolidated and therefore seismically relatively quiet region. An exception is the area of the Eger Rift in the western Bohemia, where swarms of earthquakes with magnitudes up to ∼5 occur (e.g. Fischer and Horálek, 2003; Fischer et al., 2010), and the Sudetic Marginal Fault in the north-eastern Bohemia (Štěpančíková et al., 2010). The earthquakes in the western Bohemia are suitable for studies of the local crustal structure (e.g. Novotný, 1996; Málek et al., 2004). For determination of a regional structure, either teleseismic waves or active seismic experiments are used.

The area of the Bohemian Massif is crossed by a number of profiles along which experiments with actively generated seismic waves were performed. A steep-angle reflection profile 9HR passes through the Krušné Hory Mountains in the Saxothuringian domain, the Teplá-Barrandian and Moldanubian domains (see red line "9HR" in the geological map in Fig. 1.8). In this experiment, a high seismic energy produced by explosive sources permitted to study features in a depth of up to ∼60 km. Tomek et al. (1997) interpreted the obtained seismic sections (Fig. 1.6) in terms of individual reflectors or reflexive zones. The upper crust (above 10-km depth) of the Saxothuringian domain shows flat reflectors interrupted by a low-reflectivity zone corresponding to the Karlovy Vary Pluton. Below this depth, there is a number of reflectors dipping towards south-east. Another series of inclined reflectors starts underneath the MLC and continues to the center of the Teplá-Barrandian domain. Between the Teplá-Barrandian and Moldanubian domains, a main change in the character of reflectors occurs, interpreted as a steep fault. The Moho (i.e. the boundary between the crust and the mantle) appears to be shallower beneath the Saxothuringian and Teplá-Barrandian crust (minimum depth ∼33 km) than beneath the Moldanubian crust (up to 40-km depth). Several important reflexions of unknown origin were observed also in the lithospheric mantle approximately below the MLC.

The depth of the Moho was determined by several methods, and the results generally agree that the crustal thickness is larger in the Moldanubian domain and decreases towards the west and north. A compilation and interpolation of the results of active seismic experiments shows that the Moho depth varies between ∼40 km

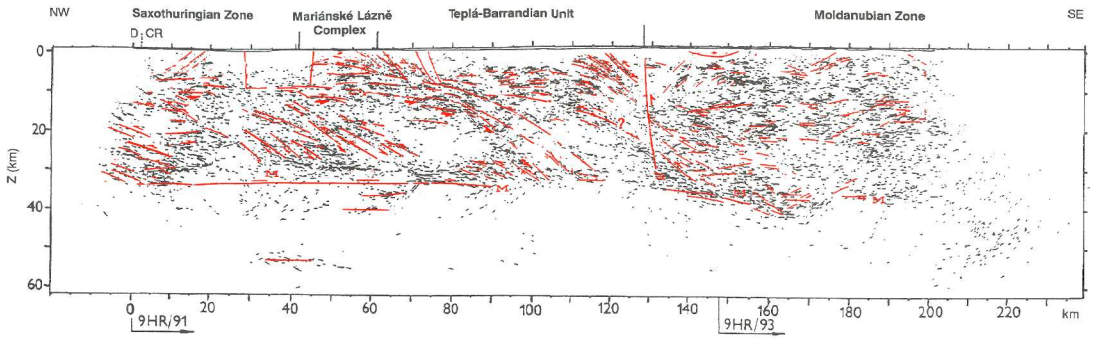

Figure 1.6: Ray-tracing migrated section (black) of the 9HR profile and its geological interpretation (red). Modified after Tomek et al. (1997). Reflexions "M" were interpreted to correspond to the Moho discontinuity.

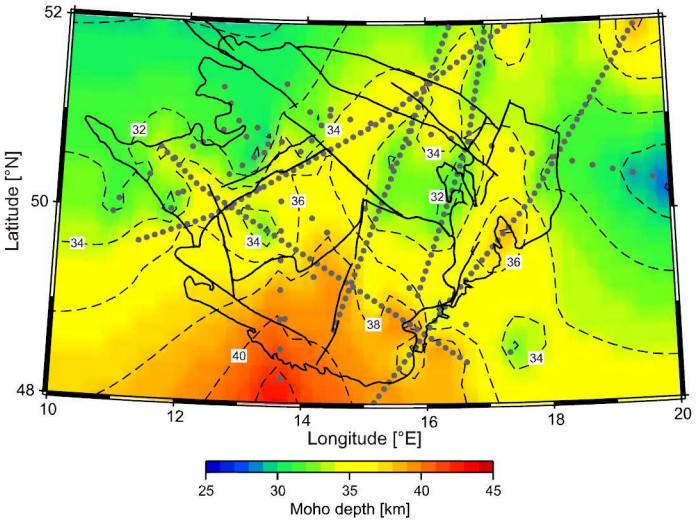

Figure 1.7: Moho depth below the Bohemian Massif after Karousová et al. (2012), who compiled and interpolated results of inversions of active seismic experiments along several profiles (gray dots). Solid lines show boundaries of the tectonic domains and main faults.

beneath the Moldanubian and ∼28–30 km beneath the Saxothuringian domain (see Fig. 1.7, Karousová et al., 2012).

The crustal structure was also studied using data acquired during a series of refraction and wide-angle reflexion experiments, such as CELEBRATION 2000 and SUDETES 2003. The distribution of P-wave velocities along the profiles CEL09 and CEL10 was modeled by Hrubcová et al. (2005) and Hrubcová et al. (2008), respectively, who used seismic tomography combined with ray-tracing modeling (for their results and locations of the profiles, see Fig. 1.8). The profiles CEL09 and CEL10 are practically perpendicular. The profile CEL09 is passing through a similar region as the profile 9HR but it continues further to the south-east. The profile CEL10 intersects the Moravo-Silesian and Brunia domains in the south-west–north-east direction and continues further to Poland.

The lowest P-wave velocity is observed near the surface and corresponds to

weakly consolidated sedimentary layers (see e.g. the northern part of the CEL10 profile in Fig. 1.8). Within the crust, only a few reflectors were detected and most of them are (nearly) horizontal; the several major moderately inclined reflectors identified by Tomek et al. (1997) were not confirmed by Hrubcová et al. (2005).

Along the profile CEL09, a sharp velocity discontinuity interpreted as Moho is observed only in the center of the Bohemian Massif (eastern part of the Teplá-Barrandian and western part of the Moldanubian domain). In the rest of the profile, a zone of a vertical velocity gradient below ∼25-km depth is detected. This feature, possibly interpreted as a laminated lower crust, continues more than 200 km to the north-east along the profile CEL10. In the Moldanubian domain, the Moho is deflected downwards and reaches the depth of ∼40 km compared to ∼30 km at the contacts with the two zones of the velocity gradient.

A different method of inversion of data from active seismic experiments was applied by Růžek et al. (2007). In their study, they first established a low-parametric velocity model based on Pg, Pn and PmP phases, and in the final stage they applied a tomographic refinement. This approach yields qualitatively different results than those reported by e.g. Hrubcová et al. (2005). They both observe similar near-surface features related to sedimentary layers, and a homogeneous middle crust with a P-velocity around 6 $\mathrm{km\,s^{-1}}$ at 10–15-km depth. In contrast to the velocity model by Hrubcová et al. (2005), Růžek et al. (2007) reported a highly heterogeneous lower crust (depths of 20–30 km) on most of the analyzed profiles. In the central (Moldanubian) part of the profile CEL09, Růžek et al. (2007) identified a prominent low-velocity anomaly (velocities less than 6.5 $\mathrm{km\,s^{-1}}$ compared to more than 7 $\mathrm{km\,s^{-1}}$ in the surrounding regions) almost reaching the Moho depth. The location of this anomaly coincides with that of the thick crust calculated by Hrubcová et al. (2005). However it should be noted that Růžek et al. (2007) did not attempt to interpret the acquired crustal models in terms of crustal composition and rock types. Moreover, the largest variations of velocities in the lower crust coincide with a relatively low resolvability and their significance may be debatable. Interestingly, Růžek et al. (2007) observe a high-velocity lower crust and inverted velocity gradient at approximately the same places where Hrubcová et al. (2005) reported velocity gradient instead of a sharp Moho (compare Fig. 1.8, left, and Fig. 1.9).

Another model of the P-velocity distribution within the upper and middle crust along the profile CEL09 was set up by Novotný (2011) (Fig. 1.10). This tomographic model shows highly variable velocities in the marginal parts of the Bohemian Massif, and anomalous low-velocity zones approximately at the supposed boundaries of the crustal domains. Similar features were reported by Novotný et al. (2009) along the profile S01 crossing the Saxothuringian domain in the south-west–north-east direction. Despite the significant differences among the models by Hrubcová et al. (2005), Růžek et al. (2007) and Novotný (2011), they all point a contrasting character of the Moldanubian with respect to the marginal Teplá-Barrandian and Brunian domains. For a detailed discussion of differences between the methods of inversion we refer to Novotný et al. (2009).

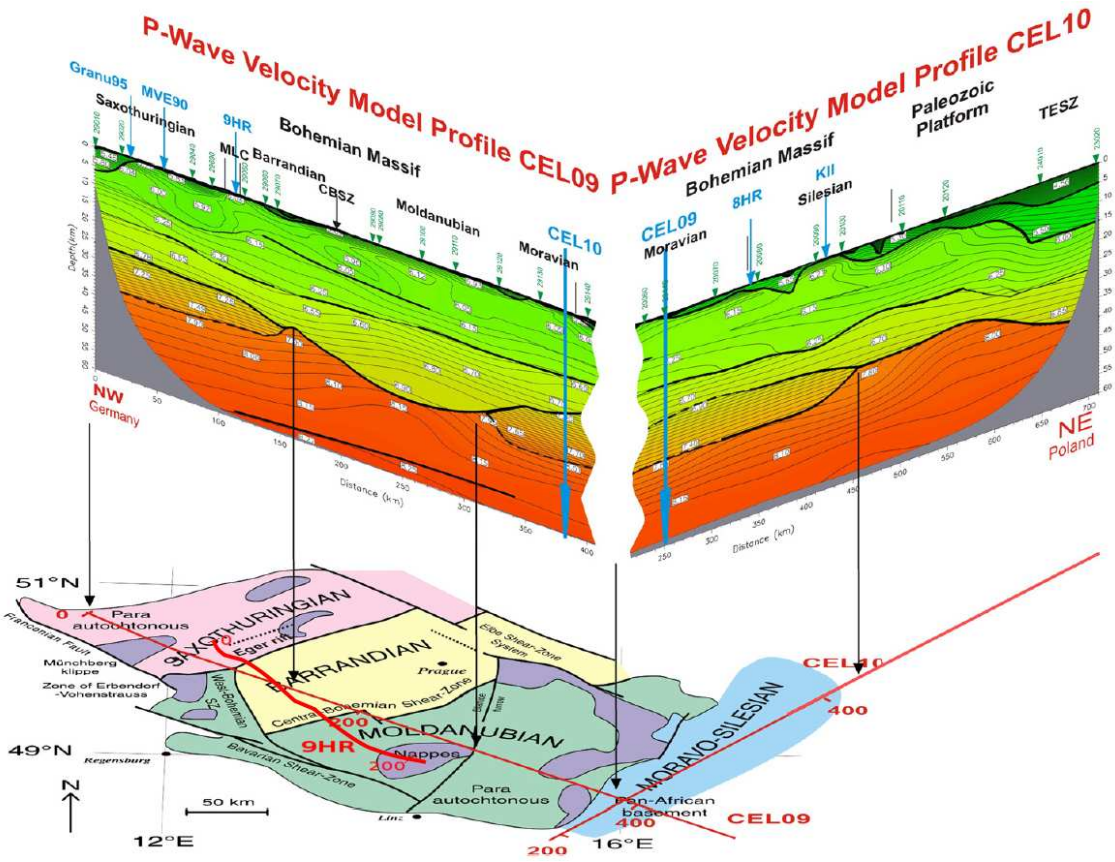

Figure 1.8: Model of P-wave velocities along the profiles CEL09 and CEL10 and a schematic geological map of the region plotted below, modified after Hrubcová et al. (2008). The position of the profiles CEL09, CEL10 and 9HR is plotted in red.

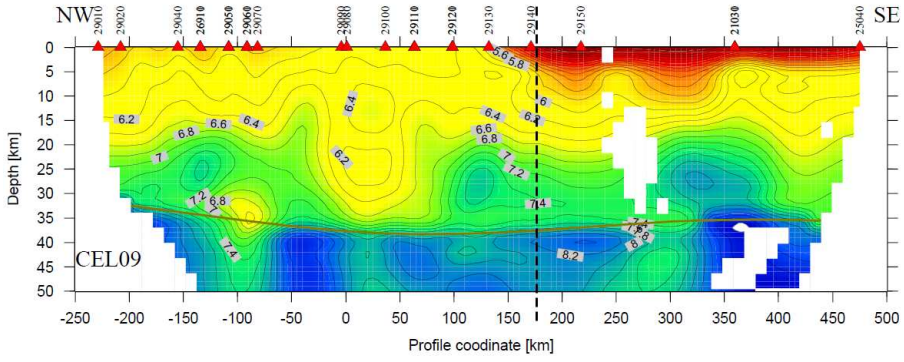

Figure 1.9: Distribution of P-wave velocities along the profile CEL09 by Růžek et al. (2007). The vertical dashed line corresponds to the right end of the profile CEL09 plotted in Fig. 1.8.

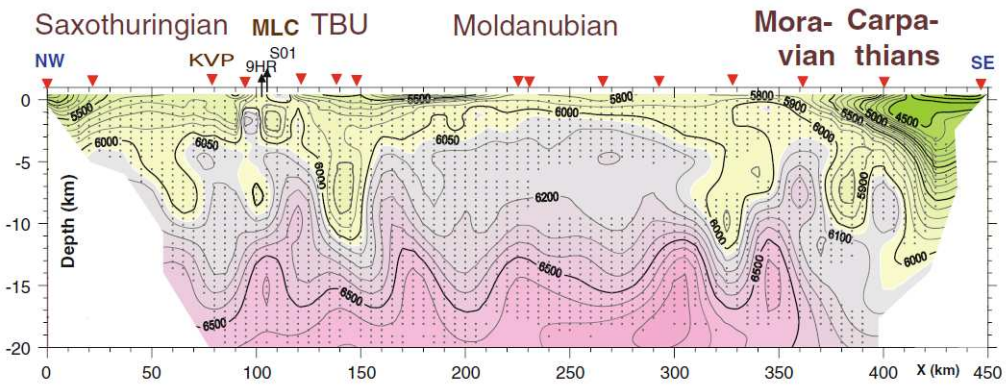

Figure 1.10: Tomography model along the profile CEL09 after Novotný (2011). KVP=Karlovy Vary Pluton, TBU=Teplá-Barrandian Unit (domain), MLC=Mariánské-Lázně Complex. Note that the depth extent is only up to 20 km.

Passive seismic experiments are another source of data for studies of the crustal structure. Wilde-Piórko et al. (2005) applied receiver function method on teleseismic waves and determined S-wave velocities below seismic stations located in the Bohemian Massif. They reported a low-velocity zone in the middle crust (10–15-km depth) of the Saxothuringian domain and attribute this feature to the tectonic and magmatic activity of the Eger Rift. The anomalous character of the crust beneath the Eger Rift was suggested by other authors who used various methods (e.g. Heuer et al., 2006; Hrubcová and Geissler, 2009).

Plomerová et al. (2007) observed a broad low-velocity anomaly beneath the Eger Rift using a 3D tomography from teleseismic waves, and interpreted this feature as an upwelling of the lithosphere–asthenosphere boundary. On the other hand, no columnar low-velocity anomaly which could correspond to a mantle plume was identified there.

Kolínský et al. (2011) studied dispersion of surface Love waves from Aegean-Sea earthquakes in order to determine the S-wave velocity vs. depth in different domains in the western part of the Bohemian Massif. Their results show a fast increase of velocity in shallow depths (less than 5 km). Below, at ∼10–30-km depth, the velocity is slowly increasing in the Saxothuringian domain, but it is constant or even slightly decreasing with depth in the Moldanubian and Teplá-Barrandian domains. Underneath the Eger Rift, the velocity gradient with depth is almost the same in the whole middle and lower crust and no sharp increase of velocity at the Moho is observed. Kolínský et al. (2011) suggest that the missing Moho discontinuity is a result of asthenospheric updoming.

The uplift of the lithosphere–asthenosphere boundary was indicated by a study of seismic anisotropy by Babuška and Plomerová (2001). These authors processed teleseismic data and estimated the depth of the lithosphere–asthenosphere boundary to 120–140 km in the Moldanubian domain and 90–120 km in the Saxothuringian domain, with the smallest depth beneath the Eger Rift. The lithospheric anisotropy further shows that the preferred dip of fabrics is different in these two domains.

According to Babuška et al. (2008), not only the Moldanubian and Saxothurin-

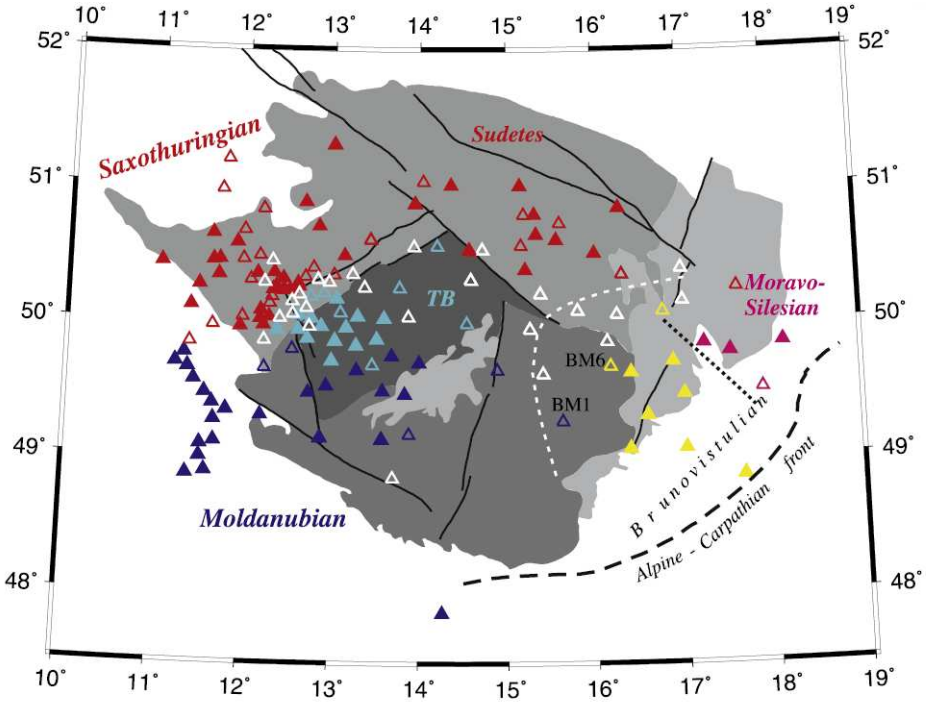

Figure 1.11: Stations included in the passive seismic experiments evaluated by Plomerová et al. (2012) colored according to the calculated pattern of P-wave velocity anisotropy. Redrafted after Plomerová et al. (2012). The dashed white line is supposed to mark the minimum westward extent of the mantle lithosphere corresponding to the Brunia (Brunovistulian) crustal domain. Abbreviation TB stands for the Teplá-Barrandian domain.

gian domains differ in their lithospheric anisotropy, but also the Teplá-Barrandian domain exhibits a distinct anisotropy pattern (Fig. 1.11). Different anisotropy of the lithosphere of the Teplá-Barrandian domain is more easily detectable by the P-wave velocity anisotropy, because it is smaller in depth-extent and requires smaller wavelengths to be resolved. Further, differences in the anisotropy of the Moldanubian and Brunian lithospheres were distinguished by Plomerová et al. (2012) and Babuška and Plomerová (2012). The lithospheric boundary between the two domains is shifted by about 100 km to the west with respect to their contact at the surface (see Fig. 1.11). In addition, the Brunian (Brunovistulian) block can be subdivided into two regions with a different P-velocity anisotropy (yellow and violet triangles in Fig. 1.11). Based on their observations, these authors conclude that the lithosphere of the Bohemian Massif still consists of blocks separated by sharp boundaries. Each of the blocks has a different anisotropy which remained from the pre-Variscan times and have not been significantly modified by asthenospheric flow.

Apart from waves associated with a certain earthquake, ambient seismic noise can be used for determination of crustal structure. For example, Růžek et al. (2012) applied a joint inversion of teleseismic P-waveforms and local group velocities of surface waves obtained from seismic noise. In line with other methods, their analysis points to systematic variations of crustal characteristics within the Bohemian Massif.

Variations of the **gravity** field are related to the density structure of the subsurface material. The density within the crust mostly depends on the rock type. *Mafic* rocks, such as *basalt* and *amphibolite*, have a higher density than *felsic* rocks, such as *granite*. A very low density is typical for weakly consolidated sediments, where porosity plays an important role. The sensitivity of the gravity field to a density anomaly decreases with distance. For this reason, interpretation of gravity data in terms of local features such as plutonic bodies (*felsic* or *mafic*) in a shallow depth is most common.

For geophysical purposes, the gravity field measured at the Earth's surface is usually reduced to the Bouguer anomaly. The Bouguer anomaly is the difference between the observed and calculated gravity field, which is corrected for the gravitational effect of the topography. In the Bohemian Massif, the gravity anomalies (Fig. 1.12) are smaller in magnitude than those observed in active orogenic belts, such as the large gravity low associated with the Alpine orogenic belt located to the south-west and south-east of the Bohemian Massif (see e.g. Bielik et al., 2006) (blue area in the south-west corner in Fig. 1.12). Within the Bohemian Massif the Bouguer anomaly has maximum variations of ∼100 mGal and shows a long-wavelength undulation in the north-west–south-east direction. In the north—west, gravity lows coincide with low-density rocks in the Saxothuringian domain and in the Sudetes. The lowest anomaly is observed in the area of the Karlovy Vary Pluton, whose vertical extent was estimated to approximately 10 km based on gravity data (e.g. Blecha et al., 2009).

A chain of local positive anomalies starts at the MLC and continues further east. These anomalies were interpreted to belong to high-density bodies at the Saxothuringinan–Teplá-Barrandian boundary hidden below sediments of the Elbe Zone (Sedlák et al., 2009). A positive gravity anomaly is typical for the whole Teplá-Barrandian, and it increases towards its north-western margin. By means of inverse modeling Guy et al. (2011) and Švancara and Chlupáčová (1997) interpreted this gravity increase as a signal from an inclined high-density body coinciding with the MLC at the surface and dipping to the south-east. Their agreement on this result is likely related to the fact that they used the same seismic study by Tomek et al. (1997) as a basis for determination of boundaries separating bodies with continuous density.

The Moldanubian domain can be divided into two parts: the western part up to the eastern rim of the CMPC shows a low gravity anomaly, while east of the CMPC the gravity is significantly higher, similar to that above the adjacent Brunia basement. The high anomaly in the eastern part of the Moldanubian domain was interpreted as a signal from a relatively dense tip of the Brunian block covered by a thin layer of light Moldanubian rocks (Guy et al., 2011).

The low anomaly of the western Moldanubian domain was interpreted by Guy et al. (2011) to originate from a low-density material in the Moldanubian lower crust. However, the study by Švancara and Chlupáčová (1997) gives a contradictory result. This difference is not surprising, as the solution of this inverse problem is non-unique due to the integral character of the gravity field, and the signal from density anomalies in the lower crust is relatively weak.

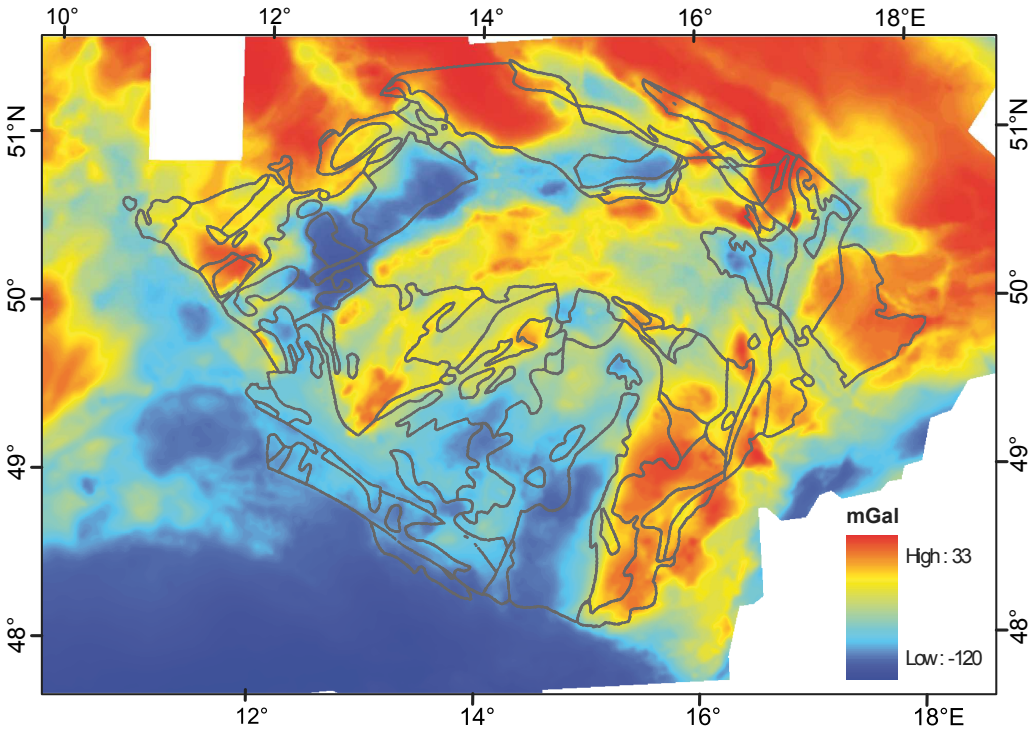

Figure 1.12: Map of Bouguer gravity anomalies in the Bohemian Massif after Lexa et al. (2011) (data were provided by the Czech Geological Survey). Lines are boundaries of the tectonic domains (cf. Fig. 1.2). White areas are not covered with data.

Additional information on crustal structure can be retrieved from electric and **magnetic anomalies**. The area of the Bohemian Massif is weakly magnetized compared to the East European Craton (former Baltica continent). Positive magnetic anomalies usually correspond to igneous rocks while negative anomalies occur above regions with a thick pile of weakly magnetized sediments. In the Bohemian Massif, the most prominent anomalies (green and blue in Fig. 1.13) are located along the boundaries of the crustal domains (along the Eger Rift, the CBPC) and at the contact with the Carpathian foreland (e.g. Šalanský, 1994).

Sources of most anomalies are exposed at the surface, or they are in a shallow depth, e.g. covered by a layer of sediments. A local magnetic field along the Teplá-Barrandian–Saxothuringian boundary was discussed by Sedlák et al. (2009). These authors interpreted a belt of positive anomalies along the Teplá suture and further east below the sediments of the Elbe Zone as a continuation of MLC-type rocks with high susceptibility.

A crustal-scale model of magnetic susceptibility along the profile 9HR, constrained from seismic and gravity data, was set up by Pokorný and Beneš (1997). The magnetic anomalies along the western part of the profile were interpreted as a combination of a signal from several near-surface highly magnetized bodies and an inclined mafic layer 3–5 km thick dipping to the south-east underneath the Teplá-Barrandian domain. In the easterly Moldanubian domain, the magnetic anomalies are much less pronounced and a simple layered structure of the crust was sufficient to explain the data.

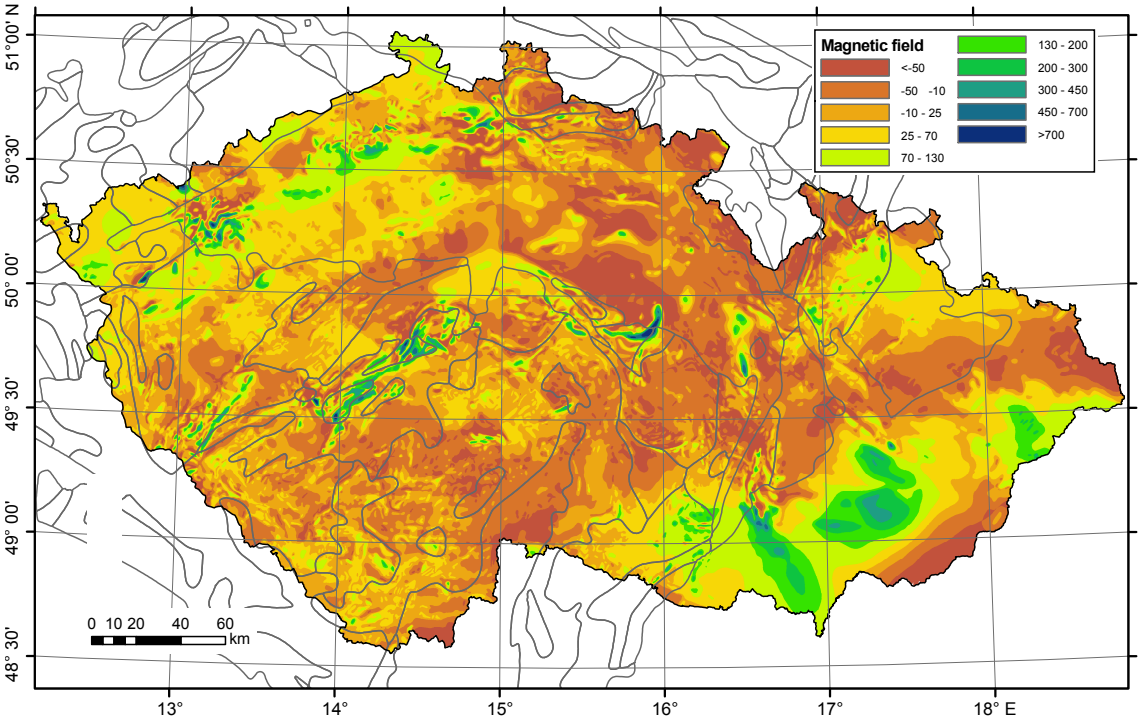

Figure 1.13: Map of magnetic anomalies in the area of the Czech Republic. Data were provided by the Czech Geological Survey. Lines are boundaries of the tectonic domains (cf. Fig. 1.2).

Measurements of the near-surface **heat flow** show its systematic variation within the Bohemian Massif (Čermák, 1994, Fig. 1.14). The lowest values (50–60 mW m^{-2}) coincide with a higher crustal thickness in the central part of the Bohemian Massif. Towards north-west and north-east, the heat flow increases and attains values of ∼70–80 mW m^{-2} in some parts along the Eger Rift and Elbe Zone.

Together with the heat coming from the mantle, natural **radioactivity** of rocks (see Fig. 1.15) contributes significantly to the surface heat flow. High and low radioactivity is typical for *felsic* and *mafic* rocks, respectively, although exceptions may occur. A typical example of highly radioactive *felsic* rocks are *granitic* plutons in the Saxothuringian domain, which increase the local heat flow by up to 40 mW m^{-2}. In contrast, the *felsic granulite* bodies in the Moldanubian domain show relatively low radioactivity compared to the neighbouring (mostly *mafic*) *durbachites*.

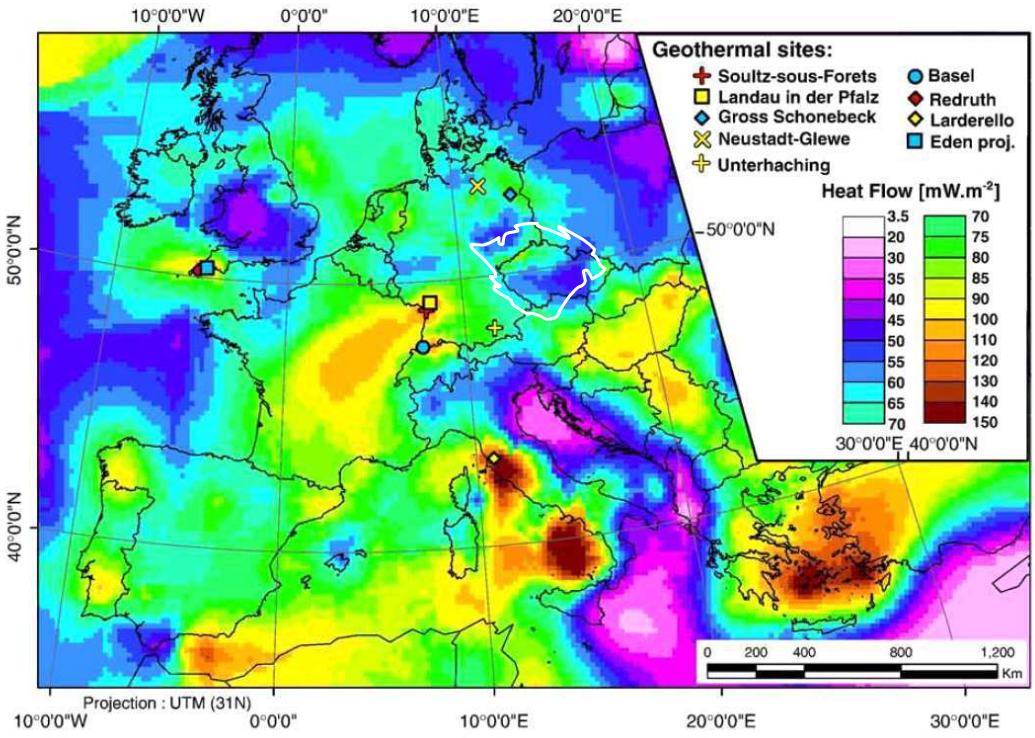

Figure 1.14: Map of the surface heat flow in Europe after Cloething et al. (2010). The boundaries of the Bohemian Massif are plotted in white.

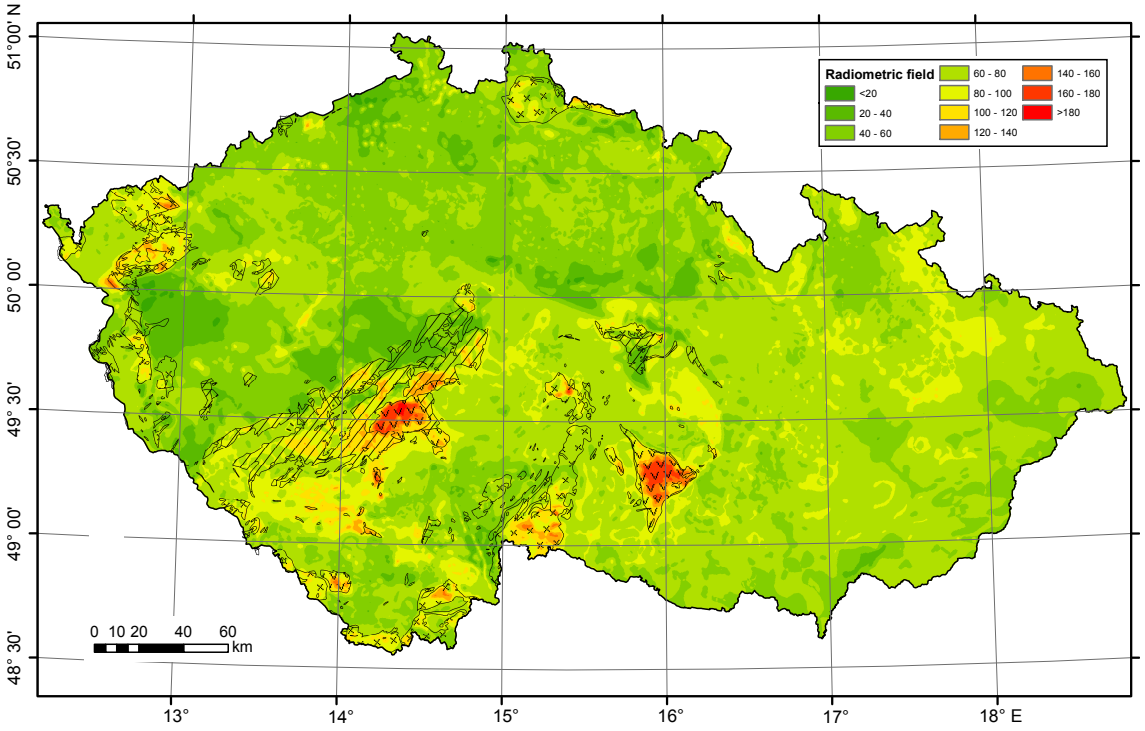

Figure 1.15: Map of the radiometric field in the area of the Czech Republic. Data were provided by the Czech Geological Survey. Hatched areas are plutons belonging to the Central Bohemian Plutonic Complex, areas with "x" symbols are late Variscan plutons. The highest values of the radiometric field coincide with durbachitic plutons ("v" symbols).

1.3 Tectonic evolution

The motion of lithospheric plates in the past is mostly inferred from paleomagnetic and paleobiogeographic data. The paleomagnetisation can reveal the position of individual plates with respect to the Earth's magnetic dipole in the past, while the mutual distance of plates can be inferred from the distribution of different kinds of fossils. The contact between the plates, their deformation and associated tectonic stresses are studied by geological methods as described at the beginning of Section 1.1. Based on a combination of these observations, a scenario of drift and tectonic evolution of lithospheric plates and terranes, such as those that form the Bohemian Massif, can be assessed (see e.g. Tait et al., 1997; Pharaoh, 1999; Franke, 2000; Matte, 2001; Winchester et al., 2002; Linnemann et al., 2004).

1.3.1 Pre-Variscan

Although the dating from the radioactive decay reveals the existence of a recycled ∼2.5 Ga-old crust (see references in Franke, 2000), the oldest relatively well established tectonic event recorded in the area of the Bohemian Massif is the Cadomian orogeny (about 650–550 Ma). The Cadomian orogeny took place on the margin of the Gondwana continent, and it involved accretion of material at a subduction zone and collision with volcanic arcs. In the Bohemian Massif, the corresponding active-margin setting is recorded in the sediments and volcanics of the Saxothuringian and Teplá-Barrandian domains.

After this stage of continental convergence, the orientation of plate motion changed. In the Ordovician (∼500–430 Ma), rifting of the northern Gondwana margin occurred and led to separation of a terrain called Avalonia and opening of the Rheic ocean (Fig. 1.16, left). Relics of Avalonia are now in England and Belgium, but it is supposed to extend further to Germany and Poland, where it is covered by layers of sediments. Later another assemblage of small continental terranes or micro-plates called Armorica detached from Gondwana, and drifted to the north towards Laurasia, a supercontinent formed by closing of the Iapetus ocean between Laurentia and Baltica (Fig. 1.16). The maximum distance between Armorica and Gondwana remains debated (Linnemann et al., 2004). The individual micro-plates forming Armorica were probably also separated by oceanic domains, but their exact relationship is uncertain (Tait et al., 1997; Matte, 2001). Based on the associated magmatism, an interaction of the lithosphere with a mantle plume has been proposed as a mechanism of the influx of heat, rifting of Gondwana, and fragmentation of Armorica (Winchester et al., 2002).

The Saxothuringian and Teplá-Barrandian blocks were a part of the Armorica terrane assemblage, and they record the rifting and asthenospheric upwelling. Based on geological evidence and paleomagnetic data showing a post-Silurian pre-380 Ma rotation of the Teplá-Barrandian block, its oceanic separation from the Saxothuringian block was proposed (Franke, 2000; Tait et al., 1997). The position of the Moldanubian block is difficult to constrain because of the lack of sedimentary sequences, but it is assumed to be also a part of Armorica. Mafic mantle rocks along the eastern margin of the Moldanubian domain can point to the existence of another oceanic domain there (Tait et al., 1997). The Brunia domain (or so-called Moravo-Silesian Terrane) is usually considered to be another Gondwana-derived block or a

continuation of the Rhenohercynian Zone (see Pharaoh, 1999, for discussion).

The formation of the Bohemian Massif from several micro-plates is supported by geophysical data. The seismic profiling shows differences between the deep crustal structure of individual domains and discontinuities at their boundaries (e.g. Hrubcová et al., 2005; Tomek et al., 1997). Seismic anisotropy in the lithosphere also reveals individual domains, but the boundaries between the lithospheric domains are shifted with respect to those in the crust (e.g. Plomerová et al., 2012).

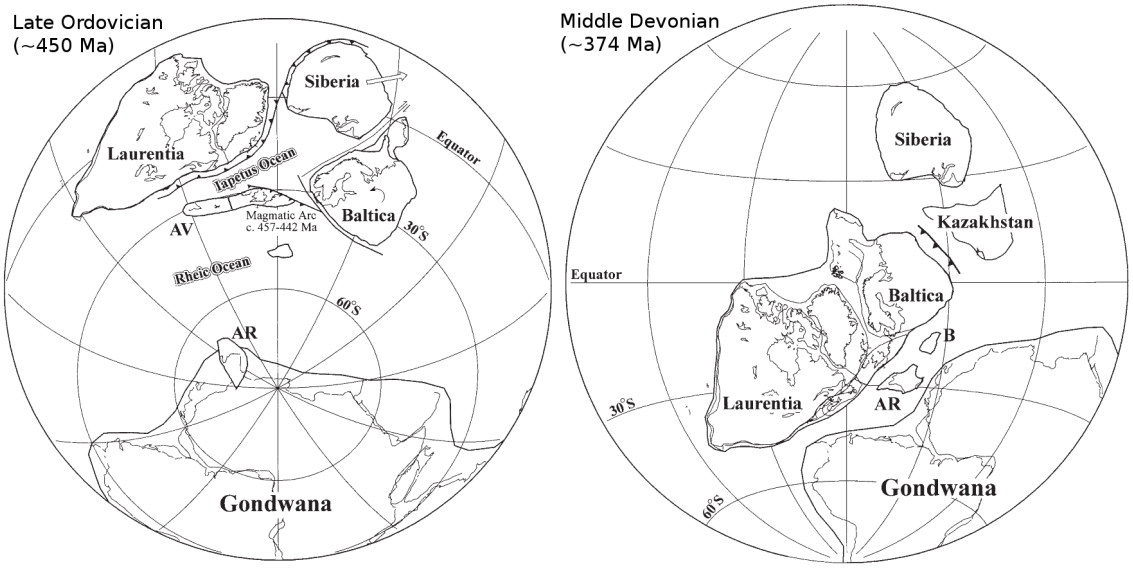

Figure 1.16: Reconstruction of position of main terranes involved in the Variscan orogeny reproduced from Torsvik (1998). In the late Ordovician (left), Avalonia (AV) had drifted apart from Gondwana towards Laurentia and Baltica, and Armorica (AR) was about to separate from Gondwana. In the Middle Devonian (right), the Rheic ocean between Avalonia and Armorica closed again and the plates, including the Bohemian Massif (B), collided.

1.3.2 Variscan

The Variscan orogeny was a result of collision of Laurasia, smaller terranes like Avalonia and Armorica, and Gondwana. Avalonia was accreted to Laurasia during the Silurian, and by that time it was separated from Armorica and Gondwana by the Rheic ocean (cf. Fig. 1.16, left). In late Silurian/early Devonian times the plate motion changed towards convergence between Laurasia and Gondwana. The convergent motion was accommodated by subduction leading to the closing of the Rheic ocean, and later collision of individual blocks (Fig. 1.16, right). Besides the subduction of the Rheic ocean, other subductions most probably operated as well, such as that of the Saxothuringian ocean.

The convergence between the Saxothuringian and Teplá-Barrandian is recorded in the metamorphism and deformation of the Teplá-Barrandian domain and MLC at about 410–370 Ma. In the scenario of subduction of the Saxothuringian ocean, the MLC represents a relic of an oceanic crust. The polarity of the subduction of the Saxothuringian ocean is debated, but the scenario of eastward subduction of

the Saxothuringian below the Teplá-Barrandian domain is mostly accepted (Franke, 2000; Mazur et al., 2006; Schulmann et al., 2009). This is supported by inclined reflectors in the Saxothuringian and below the Teplá-Barrandian crust (Tomek et al., 1997, Fig. 1.6). The structure of inclined bodies of mafic composition starting approximately at the MLC and dipping below the Teplá-Barrandian domain is confirmed by gravity and magnetotelluric inverse modeling (Švancara and Chlupáčová, 1997; Guy et al., 2011; Pokorný and Beneš, 1997).

The magmatic arc corresponding to the Saxothuringian subduction is commonly identified with the CBPC (Schulmann et al., 2009). The composition of the CBPC is typical for magmatism above a subducting plate, and it shows a temporal shift consistent with the evolution from young towards mature subduction. However, the composition of the CBPC does not necessarily require oceanic subduction, as it may be obtained by re-melting of mafic material for example from the previous rifting of Gondwana (Janoušek et al., 2000). As an alternative to the hypothesis of a magmatic arc above a subduction zone, Dörr and Zulauf (2010) attribute most of the magmatism of the CBPC to post-collisional processes.

During the oceanic subduction, the back-arc region was subject to extension, the Moldanubian crust was thinned, and a small oceanic basin may have been created (Schulmann et al., 2009). Alternatively, a wide oceanic separation between the Teplá-Barrandian and the Moldanubian domains has been proposed by Franke (2000).

After the consumption of the Saxothuringian ocean, and possibly another ocean in the east, the continental lithospheres collided. The collision was accompanied by crustal thickening and growth of the topography. As a result, the surface in the center of the newly growing orogen was uplifted, and marine sedimentation in the Teplá-Barrandian domain ceased at ∼380 Ma. At 340 Ma, peak P–T conditions were reached inside the Moldanubian crust and led to the formation of *granulites*, *gneiss* and *migmatites* of the Gföhl Unit. At about the same time, the sediments in the Saxothuringian domain underwent metamorphism and highly metamorphosed *nappes* were thrusted on top of them.

The topographic load caused bending of the lithosphere and growth of a foreland sedimentary basin in the Brunia domain. Shortly after the peak metamorphism in the Moldanubian domain, the metamorphosed rocks were exhumed from the lower-crustal depth (∼60 km) to mid-crustal levels or even to the surface. Their exhumation to the surface is documented in the foreland basin, where starting from ∼330 Ma, i.e. ∼10 Ma after the peak metamorphism, sediments derived from highly metamorphosed rocks were deposited. At some places, the exhumation of the rocks is accompanied by emplacement of *durbachitic* plutons.

The exhumation was a multi-stage process, as witnessed by P–T evolution and deformational *fabrics* of the Moldanubian rocks. Lexa et al. (2011) proposed that the vertical *fabrics* recorded in the Moldanubian rocks correspond to a stage of diapiric upwelling of the lower crust accompanied by a simultaneous burial of the middle crust. This vertical exchange was later followed by a horizontal flow resulting into horizontal *fabrics*, which are most prominent in the Moldanubian *nappes* and the underlying Moravo-Silesian Zone. The position of the *nappes* led some authors to propose a model of the far-travelling Gföhl Unit (Franke, 2000). In their model, the *nappes* were rooted below the Teplá-Barrandian and travelled several hundreds of kilometers to the Moravo-Silesian Zone, and also to the west above Saxothurin-

gian rocks. In contrast, e.g. Schulmann et al. (2008) interpreted the *nappes* as a result of underthrusting of the Moldanubian thickened crust by the Brunia block. The underthrusting of the Brunia could be also regarded as a result of oceanic and later continental subduction. Supporting evidence for such westward oceanic subduction can be found in the metamorphic rocks derived from mid-ocean ridge *basalts* within the Gföhl Unit and *eclogites* located along the eastern Moldanubian boundary (Kalvoda et al., 2008). The Brunian promontory covered by a thin layer of Moldanubian rocks was revealed by interpretation of the gravity data (Guy et al., 2011), and further supported by the westward shift of the Brunian lithosphere with respect to the surface contact of the two blocks (Plomerová et al., 2012).

The lack of horizontal reworking of the vertical *fabrics* in the Lugian domain in comparison to the Moldanubian domain suggests a significant difference in their tectonic evolution. The absence of the low-gravity anomaly in the Lugian domain compared to the Moldanubian domain again points to the importance of the underthrusting event on the formation of the horizontal *fabrics* (Schulmann et al., 2008).

Dörr and Zulauf (2010) proposed that the continental collision induced the growth of a large Tibetan-style plateau consisting of the Teplá-Barrandian and Moldanubian blocks. At ∼340 Ma, the crust of the plateau was disrupted, and due to unequal denudation lower orogenic levels were exposed in the Moldanubian domain, while the surface of the Teplá-Barrandian domain is largely preserved until today.

At ∼325–310 Ma, numerous granitic plutons were emplaced within the Moldanubian and Saxothurigian domains. Different mechanisms have been considered to provide the heat source needed for this episode of crustal melting. Due to (partial) delamination of the mantle lithosphere, the ascending asthenosphere can increase the heat flow from the mantle and induce widespread melting (e.g. Finger et al., 2009). Alternatively, enough heat can be generated by radioactive elements in a significantly thickened crust (Gerdes et al., 2000).

1.3.3 Post-Variscan

After cessation of the collision-related compression, the thickened orogenic crust started to flow laterally in order to equilibrate the differences in the crustal load. Around 300 Ma, this extensional movement activated a system of faults and basins. During and after this orogenic collapse, the Variscan mountains were gradually leveled by denudation processes. The early stage of the erosion and deposition of Variscan material is preserved in abundant Permo-Carboniferous sediments, but only a few sedimentary records document the later Triassic and Jurassic times.

The next important tectonic event was the onset of the Alpine–Carpathian orogeny, which operated at ∼70–3 Ma as a result of closing of the Tethys ocean between Africa and Europe. Due to the compressional forces, faults in the Elbe and Odra Zones were activated during the Late Cretaceous leading to subsidence and filling of the resulting basins. At 40–30 Ma, a long system of rifts was activated in the Alpine foreland. This system extended from the Pyrenees to the North Sea and its activity is attributed to the lithospheric folding and thinning, probably due to an interaction with a mantle plume (Dèzes el al., 2004). The Eger Rift, activated at ∼30 Ma, is considered a part of this system. Although the volcanism in that region ceased before some ∼200 ka (e.g. Ulrych et al., 1999), the area of the Eger

Rift is still geodynamically active, as documented by seismic swarms and thermal springs. The thinned lithosphere below the Eger Rift shows that it is a rheologically weakened zone, but no plume have been detected below the lithosphere (Plomerová et al., 2007).

At ∼20–10 Ma, the growth of the Carpathian topography loaded and bent the lithosphere in the eastern part of the Bohemian Massif. The resulting foreland basin and adjacent Carpathian *nappes* covered a part of the Moldanubian and Brunia domains. In the Quaternary, the intra-plate tectonic forces reactivated pre-existing crustal discontinuities and caused uplift of the marginal parts of the Bohemian Massif leading to its current topography (Ziegler and Dèzes, 2007).

1.4 Achievements and challenges of numerical modeling

The scenarios of the tectonic evolution of the Bohemian Massif are mostly conceptual, and verification of their feasibility with respect to dynamics of the processes is rare. Numerical modeling can help to discriminate between different scenarios and improve our understanding of the nature of the tectonic processes. Due to the large complexity of orogenic systems, it is generally not possible to capture in detail the whole evolution of any orogen, and its individual stages (e.g. oceanic subduction, continental collision, continental underthrusting) have to be modeled separately. Moreover, many discrepancies between different models occur, because the freedom in the choice of model parameters is relatively large, and initial conditions are mostly unknown.

Generic models of oceanic subduction are applicable to the early Variscan evolution of the Bohemian Massif. The oceanic-subduction models show burial and exhumation of material along a cold geotherm which corresponds to the high-pressure low-temperature metamorphism recorded by the rocks along the Saxothuringian–Teplá-Barrandian boundary.

The collision during the Variscan orogeny was investigated by Arnold et al. (2001), who simulated the building of the orogenic root and its subsequent reduction due to slab break-off and delamination. Arnold et al. (2001) pointed out that asthenospheric upwelling after lithospheric delamination provides an efficient heat supply for extensive post-collisional melting, and related this process to the formation of the Moldanubian *granites*. However, their models have a relatively low resolution, and they do not provide a direct comparison to geological data. In contrast to Arnold et al. (2001), Gerdes et al. (2000) preferred increased radioactive heating in the thickened crust as a likely mechanism of the post-collisional melting.

The delamination of the over-thickened lithosphere was invoked by Willner et al. (2002) as a mechanism of (syn-collisional) exhumation of the high-pressure metamorphic rocks that are found e.g. in the Saxothuringian domain. In their model, the material of the thickened orogenic crust is first pulled into large depths by the negatively-buoyant mantle lithosphere, and after detachment of the lithosphere it is exhumed again. The P–T paths achieved by Willner et al. (2002) agree only approximately with those measured for the Saxothuringian rocks, and the authors had to apply a better-constrained one-dimensional modeling in order to obtain a closer fit.

The late stage of the Variscan continental collision was studied by Duretz et al. (2011), who set up a crustal-scale numerical (and analogue) models of underthrusting of the Brunian promontory into the Moldanubian crust. The models reproduce emplacement of the *nappe* of the Moldanubian lower-crustal material into the middle crust accompanied by the development of a topographic plateau above the *nappe*. However, the exhumation of the lower-crustal rocks to the surface was not achieved in their models. This can be due to the neglecting of the buoyancy forces that could lead to the Rayleigh-Taylor instability in the system and increase the efficiency of exhumation. Also the rheology (linear viscous in combination with plasticity) was simplified, and surface processes were neglected completely.

The growth of the Rayleigh-Taylor instability leading to diapiric exhumation of the lower crust was addressed by Lexa et al. (2011). These authors assumed temperature- and composition-dependent rheology, density and radioactive heat sources. Lexa et al. (2011) concluded that once relatively high radioactive heating is prescribed, the P–T evolution in the exhumed lower crust fits well the P–T paths observed for the Moldanubian *granulite* bodies.

In some of the models mentioned above (Gerdes et al., 2000; Arnold et al., 2001; Duretz et al., 2011; Lexa et al., 2011) it is assumed that the continental crust of the subducting plate was emplaced into lower-crustal levels of the overriding plate. Such subduction of continental material was discussed e.g. by Hacker et al. (2011), but numerical models of this process are still rare. Faccenda et al. (2008) simulated the continental collision including the subduction of the continental crust. The model by Faccenda et al. (2008) successfully reproduced several characteristics of metamorphism and lithospheric structure of orogens like the Andes, Himalayas and Alps. The Variscan orogeny was in some respects comparable to that in the modern Himalayas, and the model of Faccenda et al. (2008) thus can be applicable for the evolution of the Bohemian Massif as well. However, a numerical model of continental subduction which would take into account the specific features of the Variscan orogeny, such as a large number of accreted microplates, has not been set up yet.

Besides the continental subduction, there is a number of episodes of the Bohemian-Massif evolution that remain to be addressed by means of numerical modeling. The accretion and collision of the microplates, juxtaposition of contrasting metamorphic units along the Saxothuringian–Teplá-Barrandian boundary, formation of a crustal-scale vertical shear zone in the center of the orogen, and multi-stage deformation within the Moldanubian domain are only a few examples.

In the following chapters, we focus on the last episode of the Variscan collision, and we elaborate the models of lower-crustal exhumation by Duretz et al. (2011) and Lexa et al. (2011). This late Variscan evolution is well preserved in the geological record, and we can compare the results of the numerical model with petrological and structural data. In order to obtain a high resolution of the studied area, and at the same time to reduce the number of free parameters, we set up a crustal-scale model only. On the other hand, we take into account some of the aspects of crustal deformation, which have been neglected so far.

1.5 Geological terminology and time scale

- *amphibolite* – a metamorphic rock type, medium- to coarse-grained, typically high-density and dark-colored due to presence of mineral amphibole
- *basalt* – a common type of mafic volcanic rock, fine-grained, dark grey, composed mainly of the minerals plagioclase and pyroxene
- *durbachite* – potassium-rich mostly mafic plutonic rock
- *eclogite* – mafic metamorphic rock, forms at pressures higher than those in the normal ∼35-thick crust, typically contains garnet (red color) in a matrix of pyroxene (green)
- *fabric* – a spatial structure of the rock's constituents, including orientation of grains and crystals, and planar or linear structures made of minerals of the same type
- *felsic* – rich in light elements. Felsic rocks contain more than 75% of felsic minerals such as quartz and feldspar, are usually light-colored and have relatively low density.
- *flysh* – a sequence of sedimentary rocks that is deposited in a deep marine environment in a foreland basin of a growing orogen
- *gabbro* – mafic plutonic rock, dark, coarse-grained, compositionally equivalent to basalt
- *granite* – felsic plutonic rock, light-colored, medium- to coarse-grained, composed mainly of the minerals quartz, feldspar and mica
- *granulite* – rock that underwent high-temperature metamorphism. The mineral composition of granulites varies depending on the protolith and metamorphic conditions, and it can be both felsic and mafic.
- *gneiss* – a type of rock formed by high-grade regional metamorphic processes. Due to deformation, the minerals are typically arranged into darker and lighter bands.
- *mafic* – rich in magnesium and iron. Mafic minerals (e.g. olivine, pyroxene and amphibole) are usually dark-colored and have high density.
- *metamorphic facies* – areas in the pressure-temperature space where metamorphism leads to formation of a typical assemblage of minerals, see Fig. 1.17
- *migmatite* – rock which experienced very high temperature conditions resulting into partial melting. Migmatites often record intense deformation leading to separation of different mineral types into thin light and dark bands.
- *nappe* – a large planar body of rock that has been displaced over a long distance from its original position
- *peridotite* – mafic plutonic rock consisting mostly of the minerals olivine and pyroxene, dark and dense, coarse-grained. The composition of peridotite is typical of the Earth's upper mantle.
- *protolith* – the original rock from which a metamorphic rock was formed
- *serpentinite* – rock composed of minerals formed by serpentinization, i.e. hydration and metamorphism, of the mantle material

Table 1.1: Simplified geological time scale after Odin (1994).

Phanerozoic	Cenozoic	Quaternary		1.8
		Neogene		23.5
		Paleogene		65
	Mesozoic	Cretaceous		135
		Jurassic		200
		Triassic		250
	Paleozoic	Permian	Late	258
			Early	295
		Carboniferous	Late	320
			Early	355
		Devonian	Late	375
			Middle	390
			Early	410
		Silurian		435
		Ordovician		500
		Cambrian	Late	510
			Middle	520
			Early	540
Proterozoic	Neoproterozoic			1000
	Mesoproterozoic			1600
	Paleoproterozoic			
Archean				>2500 (Ma)

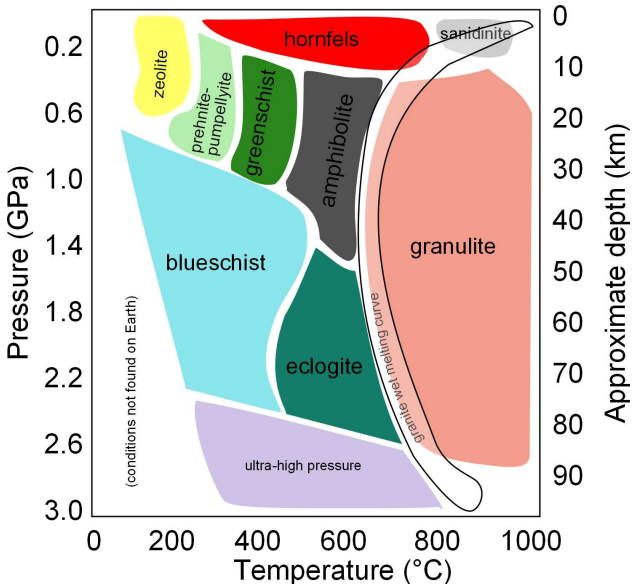

Figure 1.17: Metamorphic facies, after Bentley (2010) and Bousquet et al. (2008).


19.0 Myr

Chapter 2

Numerical model setup

We set up a model of continental collision (Fig. 2.1) that takes into account the basic characteristics of crustal deformation: brittle-ductile behavior including the material weakening due to sustained strain, body forces due to density variations, growth of the topography and its coupling with surface processes. In a number of respects we follow the strategy developed by Fullsack (1995) and applied in models of large collisional orogens (e.g. Beaumont et al., 2001). We use a two-dimensional plane-strain approximation of the generally three-dimensional problem. The model domain is divided into crustal and mantle parts. The flow of material is solved only in the crustal part, and therefore we neglect the dynamic effect of the mantle flow on the crustal deformation. The computational domain is initially rectangular but its shape evolves with time due to a growing topography of the upper free surface and due to isostatic compensation of the crustal load. For discretization of the solved equations we use a finite element approach with structured mesh of bilinear quadrilateral elements. The model is implemented in the open-source software Elmer (http://www.csc.fi/english/pages/elmer), which we have extended by a number of procedures dealing with the specific features of crustal deformation as described in more details below in this chapter.

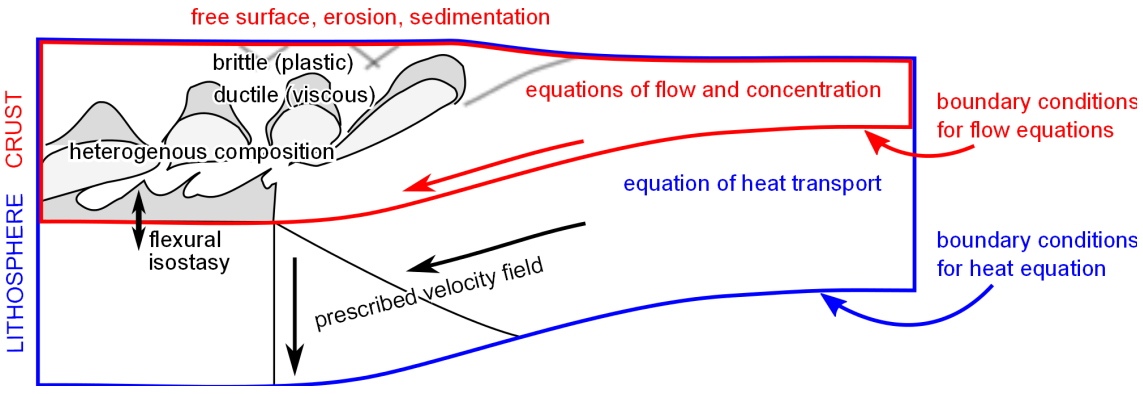

Figure 2.1: Sketch of the numerical model.

2.1 Equations

2.1.1 Governing equations

We model deformation of heterogeneous material coupled with heat transport (cf. Gerya and Yuen, 2003; Beaumont et al., 2009). We use the following primary variables: the velocity $\mathbf{v}$, the pressure p, the temperature T, the concentration c_i of the material with the composition i, and derived variables: the deviatoric stress tensor $\boldsymbol{\sigma}$ and the strain-rate tensor $\dot{\boldsymbol{\epsilon}}$. The flow of incompressible material with negligible inertia (the Stokes problem) can be described by the following equations expressing the conservation of momentum and mass:

$$\nabla p - \nabla\cdot\boldsymbol{\sigma} = -\rho g \mathbf{e}_z \,, \tag{2.1}$$

$$\nabla\cdot\mathbf{v} = 0 \,, \tag{2.2}$$

where ρ is the density, g is the gravity acceleration and $\mathbf{e}_z$ is the unit vector in the direction of the $z-$axis. For the meaning of symbols see also Notation on pages 147–148. In the heat equation, we take into account terms of advection and diffusion, heating by viscous dissipation and additional heat sources Q:

$$\rho c_p \frac{\mathrm{D}T}{\mathrm{D}t} - \nabla\cdot k\nabla T = \boldsymbol{\sigma} : \dot{\boldsymbol{\epsilon}} + Q \,, \tag{2.3}$$

where c_p is the specific heat capacity at constant pressure and k is the thermal conductivity. We assume that the evolution of material composition has a non-diffusive character on geological scales:

$$\frac{\mathrm{D}c_i}{\mathrm{D}t} = 0 \quad \text{for every } i \,. \tag{2.4}$$

The full set of equations (2.1)-(2.4) is solved only in the crustal part of the model domain (red in Fig. 2.1). In the lithospheric mantle (below the red border in Fig. 2.1) we solve only equation (2.3) without the terms on the right-hand side and assume a prescribed velocity field (see Section 2.1.5).

The deviatoric stress tensor is a function of the strain rate, temperature, pressure and composition,

$$\boldsymbol{\sigma} = \boldsymbol{\sigma}(\dot{\boldsymbol{\epsilon}}, T, p, \{c_i\}), \tag{2.5}$$

and its form is defined in Sections 2.1.2-2.1.3. The parameters in the equations (2.1)-(2.3) are assumed to be constant (g, c_p and k), or depend on the material composition,

$$\rho = \rho(\{c_i\}), \quad Q = Q(\{c_i\}). \tag{2.6}$$

In a more general case, the parameters may depend also on temperature, pressure, phase transitions and other factors. In particular, we neglect variations of density due to the thermal expansivity[1].

[1]The variations of temperature at a certain crustal depth may reach up to a few hundreds of Kelvins at maximum. Thermal expansivity of rocks is approximately $3\cdot10^{-5}\mathrm{K}^{-1}$ and density of crust is about 2500–3000 $\mathrm{kg\,m}^{-3}$ (e.g. Guy et al., 2011). The resulting density variations $\rho\alpha\Delta T$ are up to $\sim 10^1\,\mathrm{kg\,m}^{-3}$ that is by one order of magnitude less than the density differences among different crustal rock types ($\sim 10^2\,\mathrm{kg\,m}^{-3}$).

2.1.2 Rheology

We assume non-linear visco-plastic rheology as a description of the response of the crustal material to stress. Plastic deformation is an approximation of brittle failure that dominates at low temperatures and high strain rates, while at relatively low strain rates and high temperatures the crustal material flows viscously. Viscous flow is characterized by immediate irreversible deformation of material with a rate dependent on the applied stress. Plastic deformation is also irreversible, but it occurs only after reaching a certain differential stress σ_{yield}, called the yield strength of material. The functional dependence (2.5) for the visco-plastic material can be expressed in terms of the effective viscosity, η_{eff}:

$$\boldsymbol{\sigma} = 2\eta_{\text{eff}}\dot{\boldsymbol{\epsilon}}\,. \tag{2.7}$$

In the viscous regime, i.e. when the second invariant of the deviatoric stress tensor σ_{II} is smaller than σ_{yield}, we consider dislocation creep which is characterised by a non-linear relation between the stress and strain-rate tensors,

$$\dot{\boldsymbol{\epsilon}} = \tilde{A}{\sigma_{\text{II}}}^{n-1}\exp\left(-\frac{E_{\text{A}}}{RT}\right)\boldsymbol{\sigma}\,, \tag{2.8}$$

where R is the gas constant and parameters $\tilde{A}$, n and E_{A} are determined experimentally. Typically, the parameter $\tilde{A}$ is not a direct output of experiments, because a simpler relation between scalar quantities is measured:

$$\dot{\epsilon} = A\sigma^n\exp\left(-\frac{E_{\text{A}}}{RT}\right)\,, \tag{2.9}$$

where the exact meaning of σ and $\dot{\epsilon}$ depends on the experimental setup. In the common case of a uniaxial stress experiment, the conversion from measured A to $\tilde{A}$ is (Ranalli, 1995)

$$\tilde{A} = A\frac{3^{\frac{n+1}{2}}}{2}\,. \tag{2.10}$$

From the comparison of (2.7) and (2.8) we observe that the effective viscosity depends on the temperature, pressure and second invariant of the strain rate, $\dot{\epsilon}_{\text{II}}$:

$$\eta_{\text{eff}} = \frac{1}{2}\left(\tilde{A}\right)^{-1/n}\dot{\epsilon}_{\text{II}}^{1/n-1}\exp\left(\frac{E_{\text{A}}}{nRT}\right)\,. \tag{2.11}$$

After substituting (2.10) into (2.11) we get

$$\eta_{\text{eff}} = \eta_0\dot{\epsilon}_{\text{II}}^{1/n-1}\exp\left(\frac{E_{\text{A}}}{nRT}\right), \quad \text{where} \quad \eta_0 = \frac{1}{2}\left(A\right)^{\frac{-1}{n}}\frac{2^{\frac{1-n}{n}}}{3^{\frac{n+1}{2n}}}\,. \tag{2.12}$$

In the plastic regime, the relation $\sigma_{\text{II}} = \sigma_{\text{yield}}$ holds, and the effective viscosity can be expressed from (2.7):

$$\eta_{\text{eff}} = \frac{\sigma_{\text{yield}}}{2\dot{\epsilon}_{\text{II}}}\,. \tag{2.13}$$

2.1.3 Yield criterion

The yield strength is not constant, but it depends on intrinsic and extrinsic parameters. There are several empirical criteria on the yield strength (for overview see Ranalli, 1995), out of which the pressure-dependent Drucker-Prager criterion is commonly used as an approximation of behavior of rocks:

$$\sigma_{\text{yield}} = p \sin\phi + C \cos\phi \,, \tag{2.14}$$

where the angle of internal friction ϕ and the cohesion C are parameters. To show the meaning of these two parameters, we will derive the Drucker-Prager criterion from the Mohr-Coulomb(-Navier) criterion in two dimensions. The Mohr-Coulomb criterion gives a linear relation between the shear stress $T_{\mathbf{t}}$ and the normal stress $T_{\mathbf{n}}$ at a given plane at which the material yields:

$$T_{\mathbf{t}} = T_{\mathbf{n}} \tan\phi + C \,. \tag{2.15}$$

The criterion means that the shear stress which can be sustained by the material without yielding is proportional to the confining normal stress. Higher shear stresses than that given by the criterion can not be reached, as the material yields (i.e. is fractured) beforehand. In Fig. 2.2 the Mohr-Coulomb criterion is represented by a line separating admissible stresses in the material (below the line) from non-admissible stresses (above the line). We can see that the cohesion is the maximum possible shear stress when a zero normal stress is applied and the angle ϕ corresponds to the slope of the line.

The shear and normal stresses are the parallel and perpendicular components of the traction $\mathbf{T}$ at a given plane corresponding to a stress tensor $\boldsymbol{\tau}$, respectively. The stress tensor in the Cartesian basis $\{\mathbf{e}_x, \mathbf{e}_z\}$ has the form

$$\boldsymbol{\tau} = \begin{pmatrix} \tau_{xx} & \tau_{xz} \\ \tau_{zx} & \tau_{zz} \end{pmatrix} \mathbf{e}_x \otimes \mathbf{e}_z \,, \tag{2.16}$$

and we define the principal stresses σ_1, σ_3 as its eigenvalues:

$$\sigma_{1,3} = \frac{\tau_{xx} + \tau_{zz}}{2} \pm \sqrt{\left(\frac{\tau_{xx} - \tau_{zz}}{2}\right)^2 + \tau_{xz}^2} \,. \tag{2.17}$$

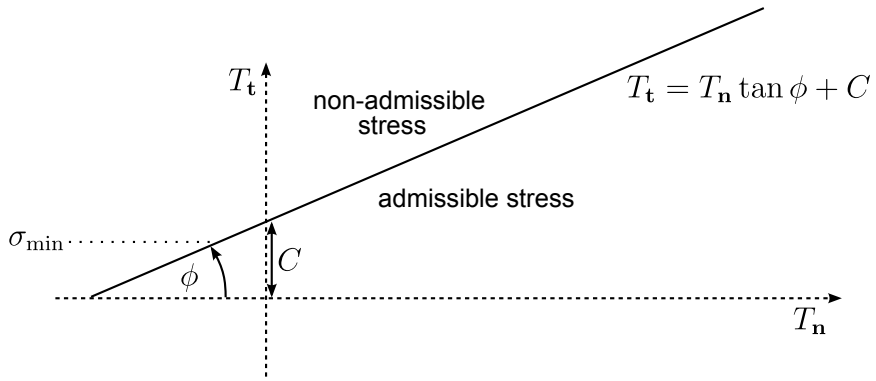

Figure 2.2: Yield strength of material.

Let us first express the components of the traction on a plane with a normal vector $\mathbf{n} = (\cos\beta, \sin\beta)$ and a tangent vector $\mathbf{t} = (-\sin\beta, \cos\beta)$ in the Cartesian basis:

$$T_x = \tau_{xx}\cos\beta + \tau_{xz}\sin\beta\,, \tag{2.18}$$
$$T_z = \tau_{xz}\cos\beta + \tau_{zz}\sin\beta\,, \tag{2.19}$$

and then in the basis $\{\mathbf{n}, \mathbf{t}\}$:

$$\begin{aligned} T_\mathbf{n} &= \mathbf{n}\cdot(T_x, T_z) = T_x\cos\beta + T_z\sin\beta = \\ &= \tau_{xx}\cos^2\beta + 2\tau_{xz}\cos\beta\sin\beta + \tau_{zz}\sin^2\beta = \\ &= \frac{\tau_{xx}+\tau_{zz}}{2} + \frac{\tau_{xx}-\tau_{zz}}{2}\cos 2\beta + \tau_{xz}\sin 2\beta\,, \end{aligned} \tag{2.20}$$

$$\begin{aligned} T_\mathbf{t} &= \mathbf{t}\cdot(T_x, T_z) = -T_x\sin\beta + T_z\cos\beta = \\ &= -\tau_{xx}\sin\beta\cos\beta + \tau_{xz}\left(\cos^2\beta - \sin^2\beta\right) + \tau_{zz}\sin\beta\cos\beta = \\ &= -\frac{\tau_{xx}-\tau_{zz}}{2}\sin 2\beta + \tau_{xz}\cos 2\beta\,. \end{aligned} \tag{2.21}$$

Without loss of generality, we choose the coordinate system so that the principal axis of the stress tensor is parallel to $\mathbf{e}_x$, and β is the angle between the principal axis and the vector $\mathbf{n}$. In this case $\tau_{xz} = 0$, and

$$T_\mathbf{n} = \frac{\tau_{xx}+\tau_{zz}}{2} + \frac{\tau_{xx}-\tau_{zz}}{2}\cos 2\beta\,, \tag{2.22}$$
$$T_\mathbf{t} = -\frac{\tau_{xx}-\tau_{zz}}{2}\sin 2\beta\,. \tag{2.23}$$

After introducing the mean stress $\bar{\sigma}$ and the differential stress $\Delta\sigma$,

$$\bar{\sigma} = \frac{\sigma_1+\sigma_3}{2}\,, \tag{2.24}$$
$$\Delta\sigma = \frac{\sigma_1-\sigma_3}{2}\,, \tag{2.25}$$

the normal and shear stresses are

$$T_\mathbf{n} = \bar{\sigma} + \Delta\sigma\cos 2\beta\,, \tag{2.26}$$
$$T_\mathbf{t} = -\Delta\sigma\sin 2\beta\,. \tag{2.27}$$

Geometrically we can represent the stress state given by equations (2.26) and (2.27) as a circle in the Mohr-Coulomb diagram (Fig. 2.3). We see that yielding first occurs on a plane inclined to the principal axis at an angle $\beta = \pi/4 + \phi/2$. (The same result can be obtained by minimizing the yield function $F(\beta) = T_\mathbf{n}(\beta)\tan\phi + C - T_\mathbf{t}(\beta)$.) Reinserting this angle into (2.26) and (2.27), we can express the Mohr-Coulomb criterion (2.15) in the form

$$\Delta\sigma = \bar{\sigma}\sin\phi + C\cos\phi\,, \tag{2.28}$$

which is in two dimensions equivalent to the Drucker-Prager yield criterion,

$$\sigma_\text{yield} = \sigma_\text{II} = p\sin\phi + C\cos\phi\,. \tag{2.29}$$

The type of relation between the shear and normal stresses (2.15) has been experimentally observed during reactivation of pre-existing faults in rocks (Byerlee,

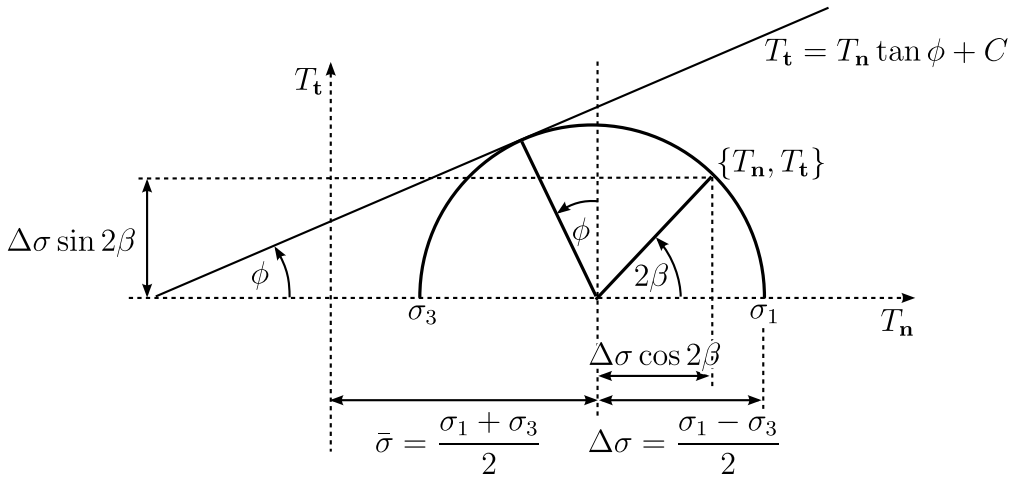

Figure 2.3: Mohr-Coulomb diagram.

1978), formation of new faults, but also in localized shear zones operating by means of various mechanisms. The measured angle of internal friction is approximately 30° for dry rocks independently on their composition. The friction required for formation of new faults is higher, but crustal rocks are usually pre-fractured at different spatial scales, e.g. due to cooling or past deformation. The reactivation of pre-existing faults is thus a more likely mechanism of brittle failure than formation of new cracks (Ranalli, 1995).

The crustal material often contains a certain amount of water or other fluids. The pressure exerted by the fluid on the walls of the pores in rocks counteracts the confining pressure p, and effectively reduces the yield strength (2.14). In the case of a vertical column of "wet" rocks, i.e. rocks with an interconnected network of fluid, the pore-fluid pressure can be estimated by the hydrostatic pressure. The yield strength is then decreased by about one third, corresponding to the ratio between the hydrostatic and lithostatic pressures. This effect can be approximated by an appropriate reduction of the angle of internal friction ϕ.

In the tensional domain ($T_{\mathbf{n}} < 0$), there is a singularity where material yields at any shear stress (left from the intersection point of the line with the $x-$axis in Fig. 2.2). In numerical simulations, a certain minimum value of the yield stress $\sigma_{\min}$ is often used (e.g. Lemiale et al., 2008; Kaus, 2009),

$$\sigma_{\text{yield}} = \max(\sigma_{\min}, p \sin\phi + C \cos\phi)\,, \tag{2.30}$$

as depicted by the dotted line in Fig. 2.2. However, the experimentally observed behavior of rocks is different, showing a steeper slope of the stress envelope in the tensional domain and its flattening in the compressional domain (Ranalli, 1995).

Observations and theoretical models (Dieterich, 1979; Ruina, 1983) point to a more complex behavior of the stress at yield. The friction between the sliding surfaces is different when initiating the motion from a static situation than in a dynamic case. An important mechanism observed in experiments (e.g. Bos and Spiers, 2001) and appropriate for crustal deformation at long time scales (e.g. Holyoke and Tullis, 2006) is strain weakening: A local accumulation of strain causes changes in the characteristics of the material at yield and a subsequent decrease of friction. As an approximation of this process, we consider a linear decrease of the angle of internal friction (or cohesion) with strain (e.g. Huismans and Beaumont, 2003; Buiter et al.,

2006; Gerya, 2010):

$$\begin{aligned} \phi &= \phi_0 && \text{if} \quad \epsilon_{\mathrm{II}} \leq \epsilon_0 \,, \\ \phi &= \phi_0 + (\phi_\infty - \phi_0) \left(\frac{\epsilon_{\mathrm{II}} - \epsilon_0}{\epsilon_\infty - \epsilon_0} \right) && \text{if} \quad \epsilon_0 < \epsilon_{\mathrm{II}} < \epsilon_\infty \,, \\ \phi &= \phi_\infty && \text{if} \quad \epsilon_{\mathrm{II}} \geq \epsilon_\infty \,, \end{aligned} \tag{2.31}$$

where ϕ_0, ϕ_∞, ϵ_0 and ϵ_∞ are parameters and ϵ_{II} is the plastic strain obtained by integrating the second invariant of the plastic strain rate along the material trajectory.

2.1.4 Material treatment

The evolution of material composition (2.4) is treated using the particle-in-cell method (e.g. Gerya and Yuen, 2003). A cloud of material particles, which are initially regularly or randomly distributed, is advected by the velocity field obtained by solving the governing equations. For the advection of the particles, the velocity field is evaluated using an appropriate element basis (i.e. bilinear interpolation on bilinear elements in our case). The particles are then displaced using the fourth-order Runge-Kutta method; methods of lower order (explicit Euler, mid-point and Heun's method) are implemented as well (see Section 2.3.3 for details).

The number of particles in an element is initially set to a certain value, but it changes during the time evolution. If it drops below a certain level in an element, new particles are injected at random positions in the element. The material composition i of a newly injected particle is set randomly with a probability proportional to the material composition $\{c_i\}$ averaged from the particles that are currently in the element (Běhounková, 2007). The plastic strain of the new particle is evaluated using an arithmetic average of ϵ_{II} stored by the particles in the element.

For the solution of the governing equations (2.1)-(2.3), evaluation of parameters that depend on the material composition is required. Each material particle stores information about its composition (i.e. identifier i of a rock-type it represents) and the accumulated plastic strain (ϵ_{II}). The values of parameters in a selected spatial point can be inferred from properties stored by nearby particles, but different schemes of evaluation can be applied. In the presence of sharp boundaries between materials with different properties, the scheme can play an important role (Deubelbeiss and Kaus, 2008; Schmeling et al., 2008), particularly in the case of the viscosity that varies by several orders of magnitude at crustal conditions. We use an approach where the parameters are evaluated at integration points of elements by averaging over all particles in the element. The effective viscosity is then computed using geometric averaging:

$$\log\left(\eta_{\mathrm{eff}}\right) = \frac{\sum_i w_i \log\left(\eta_{\mathrm{eff},i}\right)}{\sum_i w_i}, \tag{2.32}$$

while the arithmetic average is used to evaluate other quantities F:

$$F = \frac{\sum_i w_i F_i}{\sum_i w_i}, \tag{2.33}$$

where index i denotes a particle in the element and w_i are weights (cf. Gerya and Yuen, 2003):

$$w_i = \frac{1}{\Delta x^{\max} \Delta z^{\max}} \left(1 - \frac{\Delta x_i}{\Delta x^{\max}}\right) \left(1 - \frac{\Delta z_i}{\Delta z^{\max}}\right). \tag{2.34}$$

Symbols Δx_i and Δz_i are the distances along the $x-$ and $z-$axis, respectively, of the particle from the point $\{x, z\}$ where the quantity is evaluated, and $\Delta x^{\max}$ and $\Delta z^{\max}$ are respectively the maxima of Δx_i and Δz_i over all particles in the element.

2.1.5 Boundary conditions, free surface treatment and surface processes

Besides the equations that are to be solved in the model domain, we have to specify the interaction of the model with the surrounding space. At the boundaries of the model, we prescribe velocities, forces and thermal conditions that are appropriate for a collision of two lithospheric blocks. At the boundaries of the lithosphere (blue in Fig. 2.1) we specify the condition for the heat equation (2.3): at the top of the crust we prescribe the temperature, at the bottom of the lithospheric mantle the heat flux at the direction normal to the boundary ($\mathbf{q_n} = -k\nabla_{\mathbf{n}} T = \mathbf{q}_{\mathrm{BC}}$), and the sides are insulated ($\mathbf{q_n} = 0$).

The boundary conditions for flow equations (2.1)-(2.2) are specified only for the crustal part of the domain (red in Fig. 2.1). On the sides, we prescribe the normal velocity ($v_{\mathbf{n}} = v_x = v_{\mathrm{BC}}$) and leave the tangential velocity free, i.e. the tangential traction is zero. At the boundary between the crust and the mantle lithosphere, the velocity in the normal direction is zero, and the tangential velocity is set to be different beneath the left and the right parts of the model (Fig. 2.1). This setup involves a velocity discontinuity at one point at the bottom of the crust, which leads to formation of two colliding blocks.

In the lithospheric mantle, we have to fully specify the velocity field, because we do not solve the equations of flow there, but we still take into account the advection of heat in equation (2.3). The velocity field in the mantle is prescribed in agreement with the condition at the crust–mantle boundary, and it corresponds to a lithospheric wedge moving along with the right colliding block and pushing a part of the lithospheric material down into the mantle (Fig. 2.1). The velocity in this downward-moving wedge is calculated so that the mass is conserved at the contact of the lithospheric blocks.

The upper boundary of the domain is a free surface with zero traction ($\boldsymbol{\sigma} \cdot \mathbf{n} = 0$) and its shape follows the deformation of the material. The advection of the free surface is implemented by shifting the mesh nodes by an explicit Euler step followed by a linear interpolation of the advected surface to a priori known positions of the nodes in the $x-$direction (Fig. 2.4). In such a scheme, the $x-$positions of the free-surface nodes have to be either fixed or prescribed analytically.

The shape of the free surface is then corrected for the effect of surface processes: erosion and sedimentation. From the wide range of phenomenological descriptions of erosion on geological timescales (e.g. Martin and Church, 1997; Montgomery and Brandon, 2002) we choose the slope-dependent rate of erosion,

$$v_{\mathrm{e}}(x) = E|\tan\alpha(x)|\,, \tag{2.35}$$

where E is a parameter and the slope $\tan\alpha$ is computed from the topography $h(x)$ of the surface using a linear approximation of its slope on a finite interval (see Fig. 2.5). The slope-dependent erosion corresponds to the material removal by a network of rivers incising into bedrock (e.g. Willet et al., 2001; Montgomery and Brandon, 2002). This type of erosion is non-conservative with respect to the mass

in the model, because the eroded material is assumed to be transported over a large distance and deposited outside the studied domain. Besides the river-incision erosion, other processes leading to removal and deposition of material may operate, and they are usually simulated by a conservative diffusive law (e.g. Willet et al., 2001; Montgomery and Brandon, 2002).

The rate of sedimentation of material into topographic lows is proportional to the topography:

$$v_{\mathrm{s}}(x) = S\,h(x) \qquad \text{for } h(x) < 0\,, \tag{2.36}$$

$$v_{\mathrm{s}}(x) = 0 \qquad \text{for } h(x) \geq 0\,, \tag{2.37}$$

where S is a parameter. A small amount of local diffusive smoothing is employed in order to omit grid-scale oscillations of the free surface. The rate of this process is computed from the "roughness" of the surface: The difference d of the position of a node with respect to the position of the free surface interpolated from the surrounding nodes is evaluated, as shown in Fig. 2.5. The rate of local smoothing of the surface is then proportional to this difference:

$$v_{\mathrm{d}}(x) = E_d\,d(x)\,. \tag{2.38}$$

The total correction of the position of the free surface at a time step of length Δt is:

$$\Delta h(x) = -\Delta t\Big(v_{\mathrm{e}}(x) + v_{\mathrm{s}}(x) + v_{\mathrm{d}}(x)\Big)\,. \tag{2.39}$$

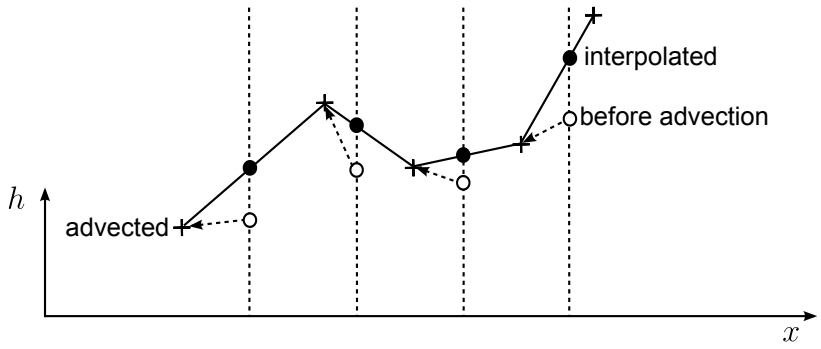

Figure 2.4: Advection of free surface. Vertical dashed lines are (fixed) $x-$positions of mesh nodes. Arrows pointing from open circles towards crosses show the displacement of the material. Filled circles show position of the boundary nodes after advection and interpolation.

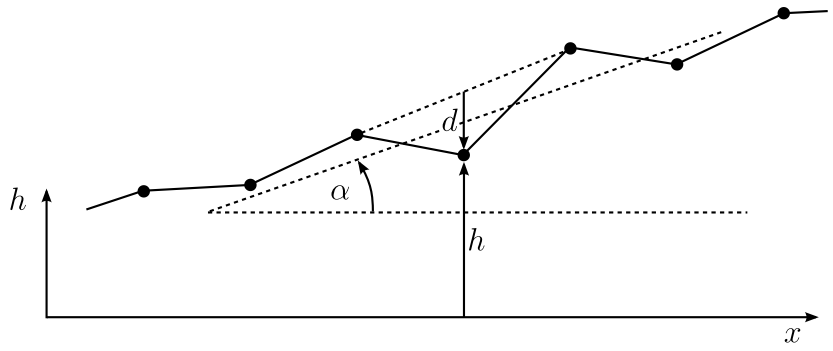

Figure 2.5: Parameters for evaluation of erosion and sedimentation.

2.1.6 Mesh deformation, ALE description

Due to the deformation of the free surface, the shape of the computational mesh has to vary with time. The major role of convection does not allow the use of purely Lagrangian methods, as they would lead to large mesh distortion, or they would require remeshing. The numerical framework developed for the treatment of large deformations of material in a domain with a shape evolving with time is called an Arbitrary Lagrangian–Eulerian (ALE) approach (for overview see Donea and Huerta, 2003; Scovazzi and Hughes, 2007; Duran, 2000). In the ALE description, the computational mesh is moving (unlike in the Eulerian description) and its motion is independent of the material motion (unlike in the Lagrangian description). Besides the spatial and material configurations that are used in the Eulerian and Lagrangian descriptions, respectively, we define the referential configuration. In the spatial configuration, the frame of reference is fixed with respect to the "laboratory". In contrast, the material frame of reference coincides with the position of the material particles. In the ALE approach, the referential configuration is defined so that the positions of mesh nodes are constant. The spatial, material and referential coordinates, $\mathbf{x}$, $\mathbf{X}$ and $\boldsymbol{\chi}$, respectively, can be converted one to another using the following invertible mappings:

$$\mathbf{x} = \varphi(\mathbf{X}, t)\,, \quad \mathbf{x} = \psi(\boldsymbol{\chi}, t)\,, \quad \mathbf{X} = \varphi^{-1}\left(\psi(\boldsymbol{\chi}, t)\right)\,, \tag{2.40}$$

as shown in Fig. 2.6.

We will now outline the basic kinematic equations in the ALE description and their application to the studied problem. An arbitrary property $\mathbf{F}$ can be expressed in any of the coordinate systems (2.40):

$$\mathbf{F}(\mathbf{x}, t) = \mathbf{F}(\psi(\boldsymbol{\chi}, t), t) = \mathbf{F}(\varphi(\mathbf{X}, t), t)\,. \tag{2.41}$$

Keeping in mind that the functional form of the property $\mathbf{F}$ is different in different coordinate systems we will simplify the notation:

$$\mathbf{F}(\boldsymbol{\chi}, t) \equiv \mathbf{F}(\psi(\boldsymbol{\chi}, t), t)\,, \tag{2.42}$$

$$\mathbf{F}(\mathbf{X}, t) \equiv \mathbf{F}(\varphi(\mathbf{X}, t), t)\,. \tag{2.43}$$

In the following, we will need to express the velocity of material with respect to the spatial frame:

$$\mathbf{v} \equiv \left.\frac{\partial \mathbf{x}}{\partial t}\right|_{\mathbf{x}}\,, \tag{2.44}$$

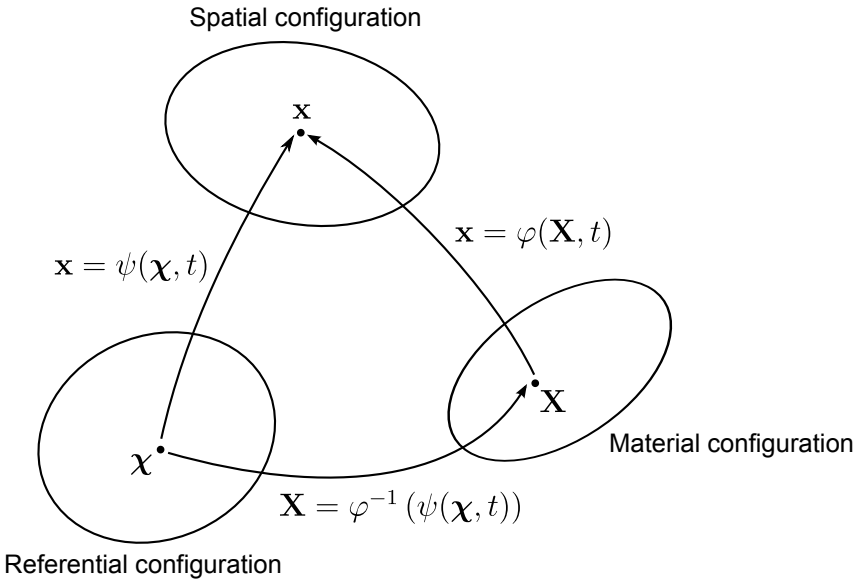

Figure 2.6: Spatial, material and referential configuration.

the velocity of material with respect to the referential frame (i.e. with respect to the mesh):

$$\mathbf{w} \equiv \left.\frac{\partial \boldsymbol{\chi}}{\partial t}\right|_{\mathbf{X}}, \tag{2.45}$$

and the velocity of the mesh with respect to the spatial frame:

$$\hat{\mathbf{v}} \equiv \left.\frac{\partial \mathbf{x}}{\partial t}\right|_{\boldsymbol{\chi}}. \tag{2.46}$$

Besides the property $\mathbf{F}$ and its spatial derivatives, the governing equations usually contain the material-time derivatives of $\mathbf{F}$, which is defined in the material configuration:

$$\frac{\mathrm{D}\mathbf{F}}{\mathrm{D}t} \equiv \left.\frac{\partial \mathbf{F}(\mathbf{X}, t)}{\partial t}\right|_{\mathbf{X}}. \tag{2.47}$$

In the spatial configuration, the material-time derivative can be expressed using the chain rule:[2]

$$\begin{aligned} \frac{\mathrm{D}\mathbf{F}}{\mathrm{D}t} &= \left.\frac{\partial \mathbf{F}(\mathbf{x}, t)}{\partial t}\right|_{\mathbf{x}} + \left.\frac{\partial \mathbf{x}}{\partial t}\right|_{\mathbf{X}} \cdot \frac{\partial \mathbf{F}(\mathbf{x}, t)}{\partial \mathbf{x}} = \\ &= \left.\frac{\partial \mathbf{F}(\mathbf{x}, t)}{\partial t}\right|_{\mathbf{x}} + \mathbf{v} \cdot \frac{\partial \mathbf{F}(\mathbf{x}, t)}{\partial \mathbf{x}}, \end{aligned} \tag{2.48}$$

and analogously in the referential configuration with coordinates $\boldsymbol{\chi}$:

$$\begin{aligned} \frac{\mathrm{D}\mathbf{F}}{\mathrm{D}t} &= \left.\frac{\partial \mathbf{F}(\boldsymbol{\chi}, t)}{\partial t}\right|_{\boldsymbol{\chi}} + \left.\frac{\partial \boldsymbol{\chi}}{\partial t}\right|_{\mathbf{X}} \cdot \frac{\partial \mathbf{F}(\boldsymbol{\chi}, t)}{\partial \boldsymbol{\chi}} = \\ &= \left.\frac{\partial \mathbf{F}(\boldsymbol{\chi}, t)}{\partial t}\right|_{\boldsymbol{\chi}} + \mathbf{w} \cdot \frac{\partial \mathbf{F}(\boldsymbol{\chi}, t)}{\partial \boldsymbol{\chi}}. \end{aligned} \tag{2.49}$$

[2]For a vector $\mathbf{F}$, the components of $\frac{\partial \mathbf{F}}{\partial \mathbf{x}}$ in the Cartesian coordinates are $\left(\frac{\partial \mathbf{F}}{\partial \mathbf{x}}\right)_{ij} = \frac{\partial F_j}{\partial x_i}$.

As the property $\mathbf{F}$ is arbitrary, we can apply equation (2.49) also to spatial coordinates $\mathbf{x}$:

$$\frac{\partial \mathbf{x}}{\partial t}\Big|_{\mathbf{x}} = \frac{\partial \mathbf{x}}{\partial t}\Big|_{\boldsymbol{\chi}} + \mathbf{w} \cdot \frac{\partial \mathbf{x}}{\partial \boldsymbol{\chi}}\,, \tag{2.50}$$

and after rearrangement we obtain:

$$\frac{\partial \mathbf{x}}{\partial t}\Big|_{\mathbf{x}} - \frac{\partial \mathbf{x}}{\partial t}\Big|_{\boldsymbol{\chi}} = \mathbf{w} \cdot \frac{\partial \mathbf{x}}{\partial \boldsymbol{\chi}}\,, \tag{2.51}$$

$$\mathbf{v} - \hat{\mathbf{v}} = \mathbf{w} \cdot \frac{\partial \mathbf{x}}{\partial \boldsymbol{\chi}}\,, \tag{2.52}$$

where the difference of velocities at the left hand side,

$$\mathbf{c} \equiv \mathbf{v} - \hat{\mathbf{v}}\,, \tag{2.53}$$

is called the convective velocity. The convective velocity arises in the equation (2.49) when the last term is further expanded:

$$\begin{aligned} \frac{\mathrm{D}\mathbf{F}}{\mathrm{D}t} &= \frac{\partial \mathbf{F}(\boldsymbol{\chi}, t)}{\partial t}\Big|_{\boldsymbol{\chi}} + \left(\mathbf{w} \cdot \frac{\partial \mathbf{x}}{\partial \boldsymbol{\chi}}\right) \cdot \frac{\partial \mathbf{F}(\boldsymbol{\chi}, t)}{\partial \mathbf{x}} = \\ &= \frac{\partial \mathbf{F}(\boldsymbol{\chi}, t)}{\partial t}\Big|_{\boldsymbol{\chi}} + \mathbf{c} \cdot \frac{\partial \mathbf{F}(\boldsymbol{\chi}, t)}{\partial \mathbf{x}}\,. \end{aligned} \tag{2.54}$$

Comparing the material-time derivative in the ALE (2.54) and Eulerian descriptions (2.48) we make three important observations: In both cases the spatial gradient $\frac{\partial}{\partial \mathbf{x}}$ occurs in the convective term. The velocity $\mathbf{v}$ is replaced by the convective velocity $\mathbf{c}$ in the ALE description. The time derivative is not evaluated at a fixed spatial point, but at a fixed point with respect to the mesh, e.g. fixed node or integration point. All these three features are particularly convenient for numerical implementation. The form of the material-time derivative (2.54) can be substituted into the governing equations while keeping the classical Eulerian form of the remaining terms, which is an approach widely used in the modelling of flow with free surface and fluid–structure interaction (see e.g. Donea and Huerta, 2003).

Apart from the solved equations, we have to specify the position of the computational mesh at each time step. The position of the mesh boundaries usually conforms with the boundaries of the material body, or it is prescribed in spatial coordinates. Inside the model domain, the mesh deformation is not constrained, although a certain regularity of the mapping ψ (2.40) is required. There are several methods of mesh adaptation to the prescribed shape of the boundaries. One possibility is to formally describe the mesh as a compressible elastic body stretched in between the boundaries. On a structured mesh, also geometrical methods can be used, where the positions of the inner nodes are calculated analytically from the positions of the boundary nodes (for overview of mesh adaptation methods see Donea et al., 2004).

2.1.7 Flexural isostasy

The evolving topography of the free surface and the redistribution of density within the crust induces a non-uniform and time-dependent loading of the lithosphere. The crustal load should be compensated by flexure of the lithosphere leading to an equilibrium between the load and the buoyancy and elastic forces. However, when the flow equations (2.1)-(2.5) are solved only in the crustal part, the equilibrium can not be achieved self-consistently and the flexure of the lithosphere has to be imposed artificially (Fullsack, 1995). For this purpose, the position of the boundary between the crust and the mantle is adjusted so that it satisfies an analytical equation for flexure u of a thin elastic beam with the flexural rigidity D (Watts, 2001, for notation see Fig. 2.7):

$$D\frac{\partial^4 u(x,t)}{\partial x^4} + B(x,t) = L(x,t)\,. \tag{2.55}$$

The buoyancy B acting on the crustal root is proportional to the flexure, mantle density and gravity acceleration:

$$B(x,t) = u(x,t)\rho_m g\,. \tag{2.56}$$

The load L is computed from the mass of the column of material above the loaded point $\{x,z\}$ at the crust–mantle boundary,

$$L(x,t) = \int_{u_0-u(x,t)}^{h(x,t)} \rho(x,z,t)g\mathrm{d}z - L_{\mathrm{ref}}\,, \tag{2.57}$$

where L_{ref} is the load at a given reference point x_{ref} at the beginning of the time evolution,

$$L_{\mathrm{ref}} = \int_{u_0}^{0} \rho(x_{\mathrm{ref}},z,t_0)g\mathrm{d}z\,, \tag{2.58}$$

and $x_{\mathrm{ref}} = x_{\mathrm{max}}$ in our case.

Equation (2.55) is solved analytically using the Fourier method in the spatial domain. We assume a symmetrical boundary condition at the left end of the beam ($\frac{\partial u}{\partial x}|_{x_{\mathrm{min}}} = 0$) and keep the right end of the beam fixed ($u(x_{\mathrm{max}}) = 0$). For these boundary conditions, only cosine terms with

$$\tilde{l} = \frac{2l+1}{2}, \quad l = 0,1,2,\ldots \tag{2.59}$$

are non–zero in the Fourier series:

$$L(\tilde{l}) = \frac{2}{x_{\mathrm{max}}-x_{\mathrm{min}}}\int_{x_{\mathrm{min}}}^{x_{\mathrm{max}}} L(x)\cos\left(\pi\tilde{l}\frac{(x-x_{\mathrm{min}})}{(x_{\mathrm{max}}-x_{\mathrm{min}})}\right)\mathrm{d}x \tag{2.60}$$

(we omit time in the notation). In the Fourier domain, we can express the flexure from equation (2.55):

$$u(\tilde{l}) = \frac{L(\tilde{l})g}{D\left(\pi\tilde{l}/(x_{\mathrm{max}}-x_{\mathrm{min}})\right)^4 + \rho_m g}\,, \tag{2.61}$$

and then transform it back to the spatial domain:

$$u(x) = \sum_{\tilde{l}} u(\tilde{l})\cos\left(\pi\tilde{l}\frac{(x-x_{\mathrm{min}})}{(x_{\mathrm{max}}-x_{\mathrm{min}})}\right)\,. \tag{2.62}$$

At a given time step, we evaluate the difference between the flexure u satisfying equation (2.55) and the actual shape of the bottom crustal boundary and shift the computational mesh and particles in the z–direction by this difference to a new position z_{corr}:

$$z_{\mathrm{corr}}(x,t) = z(x,t) + u(x,t) - u_{\mathrm{prev}}(x,t)\,. \tag{2.63}$$

The mesh is shifted not only in the crust, but also in the mantle lithosphere. The bottom boundary of the model thus deforms in the same way as the boundary between the crust and the mantle (see Fig. 2.1).

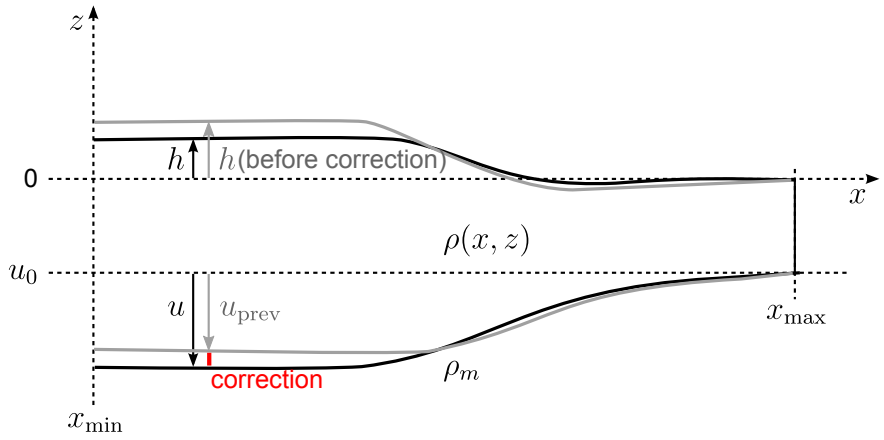

Figure 2.7: Evaluation of flexural isostatic compensation.

2.2 Numerical implementation

We use the following computational scheme:

0. initialization of temperature field and particles
1. evaluation of time step
2. interpolation of viscosity and density from particles to integration points and iterative solution of the Stokes problem, equations (2.1)-(2.5)
3. interpolation of heat sources and density from particles to integration points and solution of the heat equation (2.3)
4. advection of free surface and correction for erosion and sedimentation
5. mesh deformation
6. advection of material particles, integration of plastic strain in particles
7. computation of isostatic flexure and appropriate adjustment of mesh and particles
8. output and return to step 1

The simulation is implemented using the open-source finite-element software Elmer (http://www.csc.fi/english/pages/elmer). Elmer contains several modules, called solvers, designed for the solution of different types of partial differential equations, in particular for thermo-mechanical convection in a domain with a free surface. The setup of a numerical simulation (i.e. time stepping, order of solvers, parameters in the solved equations, numerical methods, initial and boundary conditions) is specified in an input text file, which also serves as an interface for linking of user-written procedures to Elmer. These external procedures can either provide parameters in the solved equations or they can be separate solvers. We use both possibilities in order to implement the specific properties of the crustal deformation.

The solution of the partial differential equations in steps 2, 3 and 5 is implemented in the Elmer software, but we evaluate some of the parameters in the equations (viscosity, density and heat sources) in external procedures. The visco-plastic rheology is defined in Sections 2.1.2 and 2.1.3 and the evaluation of composition-dependent properties is described in Section 2.1.4. The composition-dependent parameters can be evaluated either in mesh nodes or inside elements in points of integration over elements. We prefer the latter possibility, because it avoids secondary interpolation from nodes to integration points performed by Elmer during assembly of the local representation of the solved equations.

We developed solvers to compute the advection of the free surface and surface processes (step 4, Section 2.1.5), the advection of particles (step 6, Section 2.1.4) and crustal flexure (step 7, Section 2.1.7). During the advection of particles, several additional procedures are used for a fast search of particles contained in an element.

The partial differential equations are discretized using bilinear quadrilateral elements. The low order of elements ensures fast solution and assembly, but the choice of equal-order elements requires additional stabilization of the solution of the Stokes equations (see e.g. Donea and Huerta, 2003). There are several stabilization methods implemented in Elmer, two of which can be used with bilinear elements, as will be discussed in Section 2.3. For the solution of the discretized system we use direct methods, namely the package UMFPACK (Davis, 2004), which is robust

and fast for a relatively small number of unknowns. For the time integration of the heat equation we use the backward differentiation of the first order. The time-step length is given by the Courant criterion with the Courant number typically between 0.1 and 0.2.

2.2.1 Output and postprocessing

There are several different types of output data. Nodal values of primary variables (velocity, pressure, temperature and mesh deformation) are a part of the standard Elmer output. In addition, Elmer can store boundary values of variables or their fluxes through the boundaries (e.g. heat flow) and scalar characteristics of the model (e.g. kinetic energy and mean temperature) which are calculated from the finite-element solution. The free-surface solver saves topography, rate of sedimentation and rates of different types of erosion.

The properties stored by particles (e.g. material, total strain, plastic strain, strain rate, viscosity) are saved during particle advection. Selected particles also record pressure and temperature along their trajectories, and the resulting pressure–temperature–time paths then can be used for comparison with geological data.

The density field is post-processed in order to obtain a gravitational anomaly comparable to the Bouguer gravity anomaly (for definition see e.g. Watts, 2001). We calculate the gravitational effect of density anomalies within the model domain. The density anomalies $\Delta\rho$ are taken with respect to some one-dimensional reference density profile, which can be chosen arbitrarily. In order to simplify the calculations, we use the density profile at the right boundary of the model domain followed downwards by mantle density ρ_m. The density anomalies are assumed to be non-zero only inside the model domain and zero elsewhere. During the calculation of the Bouguer anomaly, the gravitational effect of topography is removed from the gravity field. For that reason, we integrate the density anomalies only below the zero-topography level $h = 0$.

We transform the model domain into a part of a sphere with the radius r_E equal to the radius of the Earth, see Fig. 2.8. The model domain is placed south of the equator so that $\theta = \pi/2$ at $x = x_{\min}$, and it is symmetrically reflected north of the equator. The transformation of the Cartesian coordinates $\{x, z\}$ into the polar coordinates $\{r, \theta\}$ is then:

$$r = z + r_E\,, \quad \theta = \frac{\pi}{2} + \frac{x - x_{\min}}{r_E}\,. \tag{2.64}$$

We express the density anomaly using spherical harmonics. Because the density is independent of longitude δ, we use Legendre polynomials of degree j instead of full spherical harmonics:

$$\Delta\rho(r,\theta) = \sum_{j=0}^{\infty} \Delta\rho_j(r) P_j(\cos\theta)\,, \tag{2.65}$$

$$\text{where} \quad \Delta\rho_j(r) = \int_0^{2\pi}\int_0^{\pi} \Delta\rho(r,\theta) P_j(\cos\theta)\sin\theta\,\mathrm{d}\theta\,\mathrm{d}\delta\,. \tag{2.66}$$

From the symmetry around the equator ($\Delta\rho(r,\theta) = \Delta\rho(r,\pi-\theta)$) and integrating

over δ we get:

$$\Delta\rho_j(r) = 4\pi \int_0^{\pi/2} \Delta\rho(r,\theta) P_j(\cos\theta) \sin\theta \mathrm{d}\theta \text{ for } j = 0, 2, \ldots \quad (2.67)$$

$$\Delta\rho_j(r) = 0 \text{ for } j = 1, 3, \ldots \quad (2.68)$$

The gravitational potential due to the density anomaly $\Delta\rho_j(r)$ is (Burša and Pěč, 1988):

$$v_j(r_E) = \frac{4\pi G r_E}{2j+1} \int_0^{r_E} \left(\frac{r}{r_E}\right)^{j+2} \Delta\rho_j(r) \mathrm{d}r \,, \quad (2.69)$$

and the corresponding gravitational acceleration is:

$$g_j(r_E) = (j-1)\frac{v_j(r_E)}{r_E} \,. \quad (2.70)$$

Finally, combining equations (2.67)-(2.70) we get the following formula:

$$g_j(r_E) = \frac{16\pi^2 G(j-1)}{2j+1} \int_0^{r_E} \int_0^{\pi/2} \left(\frac{r}{r_E}\right)^{j+2} \Delta\rho(r,\theta) P_j(\cos\theta) \sin\theta \,\mathrm{d}\theta \,\mathrm{d}r \,, \quad (2.71)$$

which can be used for the calculation of the Bouguer gravity anomaly at a given colatitude θ:

$$g(r_E, \theta) = \sum_j g_j(r_E) P_j(\cos\theta) \,. \quad (2.72)$$

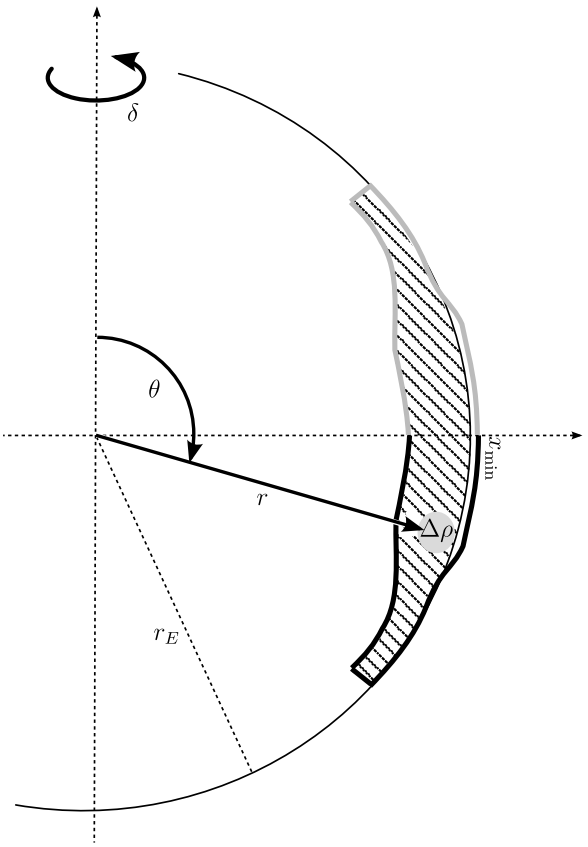

Figure 2.8: The transformation of the model domain to a part of a sphere. The model domain (thick black boundaries) is positioned south of the equator and symmetrically reflected north of it (thick gray boundaries). Density anomalies $\Delta\rho$ are integrated over the hatched domain.

2.3 Tests

Prior to the application of the software to the continental-collision modeling, we tested its numerical behavior on several simple setups. Because the original version of the Elmer software has been tested on a number of physical problems, we focus on the newly implemented features (non-linear visco-plastic rheology, advection of material particles, advection of free surface and isostasy), and on the effect of the mesh resolution and particle density.

Elmer provides several schemes for the specification of material properties. The viscosity and density can be prescribed at mesh nodes and then interpolated to integration points of elements. Another possibility is to prescribe them directly at integration points. In that case, we may either interpolate the values from material particles directly to the position of the integration points (i.e. the value differs at different integration points of an element), or we can use one value per element calculated at the element center. The latter possibility was recommended by Deubelbeiss and Kaus (2008) as numerically more accurate, but their study does not apply to equal-order stabilized elements that we deal with.

Besides the location where the viscosity and density are specified also the applied averaging scheme influences the result. Here we test arithmetic, geometric and harmonic averaging evaluated analogously as in equations (2.32)-(2.33). For a detailed discussion on averaging schemes and their physical interpretation see Schmeling et al. (2008).

Another numerical issue is the solution of the incompressible Stokes equations (2.1)-(2.2) (see Donea and Huerta, 2003, and references therein). The solution of the weak formulation of the incompressible Stokes equations is numerically stable only for certain combinations of finite-element spaces for the velocity and pressure. The elements that are bilinear both in velocity and pressure are not stable, which may for example result into spurious pressure oscillations. Different methods can be applied to stabilize the solution. For bilinear elements, there are two stabilization methods available in Elmer: residual-free bubbles (see e.g. Russo, 1996; keyword "bubbles" will be used to refer to this method in the following text) and Galerkin-least-squares (Franca and Frey, 1992; keyword "stabilized").

Bubble stabilization is based on enrichment of the finite-element space by element-wise defined functions. The name "bubbles" refers to the additional nodes by means of which these functions are specified. The bubble functions are of higher order than the standard finite elements, and they vanish on element boundaries. They capture the fine-scale part of the exact solution which is not resolved on the standard mesh.

In the Galerkin-least-squares method, special terms defined over the element interiors are added to the weak formulation. The choice of the terms is not unique, but they have to depend on the residual of the momentum equation, so that they equal to zero when exact solution is reached. The main drawback of this method is that spatial derivatives of viscosity occur in the stabilization terms. In the presence of large viscosity contrasts (several orders of magnitude), the evaluation of spatial derivatives of viscosity may yield large errors. We were not able to use this method in some of the numerical tests, but we used an incomplete stabilization, where these derivatives are set to zero. The result of this kind of incomplete stabilization is not consistent when the viscosity varies. Nevertheless, we present the results of two tests

(circular inclusion in pure shear and initiation of shear bands) calculated using this stabilization, because they can provide interesting insight into the effect of pressure oscillations on the deformation of material of Drucker-Prager type.

When examining the accuracy of different numerical settings, we mostly rely on cases where analytical solutions are available, but we also reproduce results for different kinds of numerical setups reported in literature. In the majority of the tests, we use dimensionless formulation of equations.

2.3.1 Thermal convection

A series of classical tests on coupling of thermal and flow equations was described by Travis et al. (1990). We solve equations (2.3) and (2.1)-(2.2) without heating by viscous dissipation in a rectangular domain $\Omega = (0, W) \times (0, 1)$. Free slip is prescribed at all four boundaries, constant temperature at the upper boundary, and zero heat flux at vertical boundaries. At the bottom boundary, either temperature (cases B1 and B4) or heat flux (cases B2 and B3) is specified (for values of parameters see Travis et al., 1990). The cases B1-B3 lead to a steady-state solution, that can be quantified by the kinetic energy, Nusselt number and average temperature at the bottom boundary as follows:

$$\mathrm{KE} = \frac{1}{2W} \int_\Omega \left(v_x^2 + v_z^2\right) \mathrm{d}\Omega \,, \tag{2.73}$$

$$\mathrm{Nu} = \frac{1}{W} \int_0^W \left(v_z T - \frac{\partial T}{\partial z}\right) \mathrm{d}x \,, \tag{2.74}$$

$$\bar{T}(0) = \frac{1}{W} \int_0^W T(x, z = 0) \, \mathrm{d}x \,. \tag{2.75}$$

For the summary of the results see Table 2.1.

In the case B4, a mode with periodically growing thermal instabilities is reached. The time of onset of this periodic mode depends on the prescribed length of the time step. When a too long time step is applied, the thermal instabilities are not resolved properly and a spurious steady state is reached (Fig. 2.9).

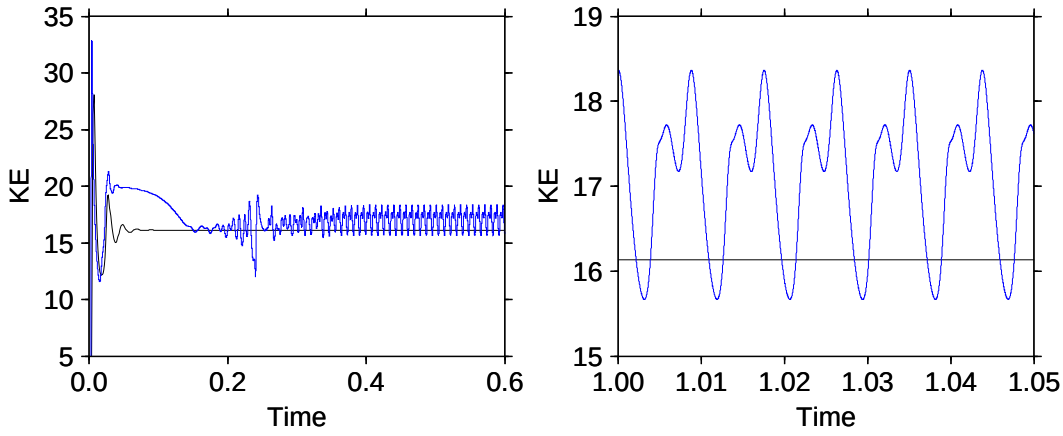

Figure 2.9: Time evolution of the kinetic energy (KE) in the test case B4. Blue and black lines are calculated for time steps of 10^{-5} and 10^{-3}, respectively. Right panel shows the periodic evolution of kinetic energy (blue line) in more detail. For a long time-step length (black line), the periodic state is not observed.

Table 2.1: Results for four test cases for thermal convection. For simplicity we report absolute values. Time-step length was 10^{-4}. The reference values along with a detailed description of the four testing cases can be found in Travis et al. (1990).

B1	32×32	64×64	128×128	reference
KE	13550	13561	13566	13558
Nu	9.7091	9.7119	9.7141	9.7143
$v_z(0, 0.5)$	303.51	303.70	303.83	303.86
$v_x(0.5, 0)$	227.98	227.65	227.58	227.49
$v_x(0.5, 1)$	227.98	227.65	227.58	227.50
max $v_z\|_{x=0}$	305.38	305.80	305.95	305.99
max $v_x\|_{z=0}$	228.61	228.26	228.18	228.09
max $v_x\|_{x=1}$	228.61	228.26	228.18	228.11

B2	32×32	64×64	128×128	reference
KE	322.73	323.97	324.28	324.30
$\bar{T}(0)$	0.12244	0.12230	0.12226	0.12225
$v_z(1, 0.5)$	50.053	50.174	50.172	50.182
$v_x(0.5, 0)$	32.843	32.849	32.851	32.851
$v_x(0.5, 1)$	36.815	36.800	36.797	36.795
max $v_z\|_{x=1}$	51.221	51.375	51.422	51.436
max $v_x\|_{z=0}$	33.381	33.389	33.391	33.392
max $v_x\|_{x=1}$	40.496	40.588	40.598	40.602

B3	32×32	64×64	128×128	reference
KE	935.41	938.08	938.74	938.63
$\bar{T}(0)$	0.095079	0.095019	0.095006	0.095987
$v_z(1, 0.5)$	103.18	103.32	103.36	103.38
$v_x(0.5, 0)$	53.051	53.029	53.024	53.017
$v_x(0.5, 1)$	55.993	55.834	55.793	55.776
max $v_z\|_{x=1}$	106.93	107.20	107.28	107.31
max $v_x\|_{z=0}$	56.191	56.175	56.185	56.187
max $v_x\|_{x=1}$	71.521	71.542	71.545	71.550

2.3.2 Channel flow

Implementation of non-linear rheology is tested on a flow in an infinitely long channel parallel to the $z-$axis. The flow is driven by a constant pressure gradient $\partial p/\partial z$ and slowed down due to a zero velocity prescribed at the side-walls. The material in the channel is viscous with the following non-linear relation between stress and deformation:

$$\sigma_{xz} = \eta_0 \left(\frac{\partial v_z}{\partial x} \right)^{\frac{1}{3}}, \tag{2.76}$$

where η_0 is a reference value of viscosity. The analytical solution of the problem (Turcotte and Schubert, 2002; Gerya and Yuen, 2003) is then

$$v_z = -\frac{W^4}{64} \left(\frac{\partial p/\partial z}{\eta_0} \right)^3 \left(1 - \left(\frac{2x}{W} - 1 \right)^4 \right), \tag{2.77}$$

where W is the width of the channel. The comparison of the analytical and numerical solutions (Fig. 2.10) shows that the software deals well with this type of non-linear rheology.

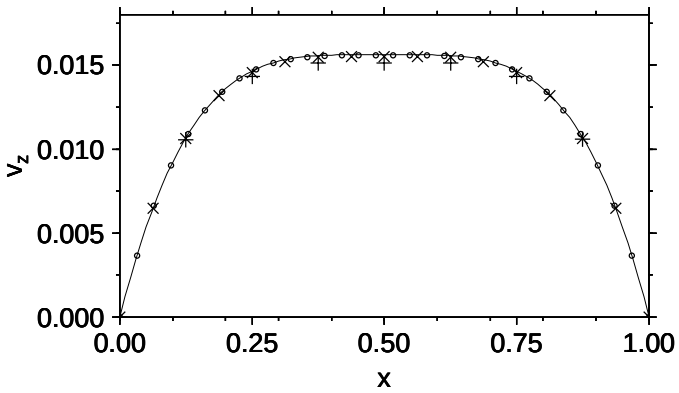

Figure 2.10: A comparison of analytical (line) and numerical (crosses and circles) solutions of the channel-flow problem with $W = 1$, $\partial p/\partial z = 1$, and $\eta_0 = 1$. The solutions were obtained on a two-dimensional $(0, 1) \times (0, 1)$ domain. Circles, "x" and "+" crosses correspond to a discretization by 32×32, 16×16 and 8×8 elements, respectively.

2.3.3 Vortex flow

Different schemes of advection of material particles were tested on the case of the vortex flow described by Fullsack (1995). In a vortex, material rotates around a center with an angular velocity dependent on the distance from the center. In this test case, the angular velocity is prescribed analytically:

$$\omega(r) = \omega_0 \frac{r}{r_0} \exp\left(-\frac{r}{r_0}\right), \tag{2.78}$$

where $r = \sqrt{x^2 + z^2}$ is the distance from the center, $r_0 = 0.25$ and $\omega_0 = 0.3$. Initially, 60×60 particles are regularly positioned in a $(-0.3, 0.3) \times (-0.3, 0.3)$ square. Each particle is assigned a scalar quantity $F(x, z, t)$ defined as a homogeneous gradient in the $x-$direction at $t = 0$:

$$F(x, z, 0) = x\,. \tag{2.79}$$

The particles are then advected by the velocity field (2.78), and we evaluate their position at selected time steps (Figs 2.11-2.12), and the time evolution of F at selected spatial points (Fig. 2.13). The analytical solution for the time evolution of F is

$$F(x, z, t) = x \cos(\omega(r)t) + z \sin(\omega(r)t)\ . \tag{2.80}$$

For advection of particles, we use four different schemes. In each scheme, the position of a particle $\mathbf{x}^{it}$ is evaluated from the velocity field $\mathbf{v}$ and from the position of the particle at the previous time-step t^{it-1}, $\mathbf{x}^{it-1}$. The simplest is the explicit one-step Euler method,

$$\mathbf{x}^{it} = \mathbf{x}^{it-1} + \Delta t \mathbf{v}^{it-1}(x^{it-1})\,, \tag{2.81}$$

where it is the index of the time step, and $\Delta t = t^{it} - t^{it-1}$. We use two different second-order Runge-Kutta schemes: the midpoint method,

$$\begin{aligned} \mathbf{v}_1 &= \mathbf{v}^{it-1}\left(\mathbf{x}^{it-1}\right), \\ \mathbf{v}_2 &= \mathbf{v}^{it-1/2}\left(\mathbf{x}^{it-1} + \frac{\Delta t}{2}\mathbf{v}_1\right), \\ \mathbf{x}^{it} &= \mathbf{x}^{it-1} + \Delta t \mathbf{v}_2\,, \end{aligned} \tag{2.82}$$

and Heun's method,

$$\begin{aligned} \mathbf{v}_1 &= \mathbf{v}^{it-1}\left(\mathbf{x}^{it-1}\right), \\ \mathbf{v}_2 &= \mathbf{v}^{it}\left(\mathbf{x}^{it-1} + \Delta t \mathbf{v}_1\right), \\ \mathbf{x}^{it} &= \mathbf{x}^{it-1} + \frac{\Delta t}{2}\left(\mathbf{v}_1 + \mathbf{v}_2\right). \end{aligned} \tag{2.83}$$

Higher precision can be attained using the fourth-order Runge-Kutta scheme:

$$\begin{aligned} \mathbf{v}_1 &= \mathbf{v}^{it-1}\left(\mathbf{x}^{it-1}\right), \\ \mathbf{v}_2 &= \mathbf{v}^{it-1/2}\left(\mathbf{x}^{it-1} + \frac{\Delta t}{2}\mathbf{v}_1\right), \\ \mathbf{v}_3 &= \mathbf{v}^{it-1/2}\left(\mathbf{x}^{it-1} + \frac{\Delta t}{2}\mathbf{v}_2\right), \\ \mathbf{v}_4 &= \mathbf{v}^{it}\left(\mathbf{x}^{it-1} + \Delta t \mathbf{v}_3\right), \\ \mathbf{x}^{it} &= \mathbf{x}^{it-1} + \frac{\Delta t}{6}\left(\mathbf{v}_1 + 2\mathbf{v}_2 + 2\mathbf{v}_3 + \mathbf{v}_4\right). \end{aligned} \tag{2.84}$$

Apart from the explicit Euler method, the velocity field is required not only at t^{it-1}, but also at other times ($t^{it-1/2}$, t^{it}). The velocity field (2.78) is stationary, so we can use:

$$\mathbf{v}^{it} = \mathbf{v}^{it-1/2} = \mathbf{v}^{it-1} \,. \tag{2.85}$$

In non-stationary problems, we will still use this approximation assuming that the spatial variability of the field is large compared to the temporal variability between time steps (cf. Fullsack, 1995). In some cases it may, however, deteriorate the accuracy of the result.

The $(-0.5, 0.5) \times (-0.5, 0.5)$ model domain is discretized by 60×60 elements and the time step is $\Delta t = 1$. The results obtained for the second- and fourth-order schemes are comparable to those presented by Fullsack (1995). The shape of the area covered by the particles changes due to the variation of the angular velocity, but the particles still follow circular trajectories (Fig. 2.11, Fig. 2.12A-C). The sinusoidal time evolution of F (2.80) is better reproduced far from the center of rotation (blue dots in Fig. 2.13) than in its vicinity (black dots in Fig. 2.13). In the case of the Euler method (Fig. 2.12D), the circular shape of the trajectories is not preserved, particles migrate away from the center of rotation and some of them leave the model domain. This corresponds to a decrease of amplitudes of F with time (gray circles in Fig. 2.14).

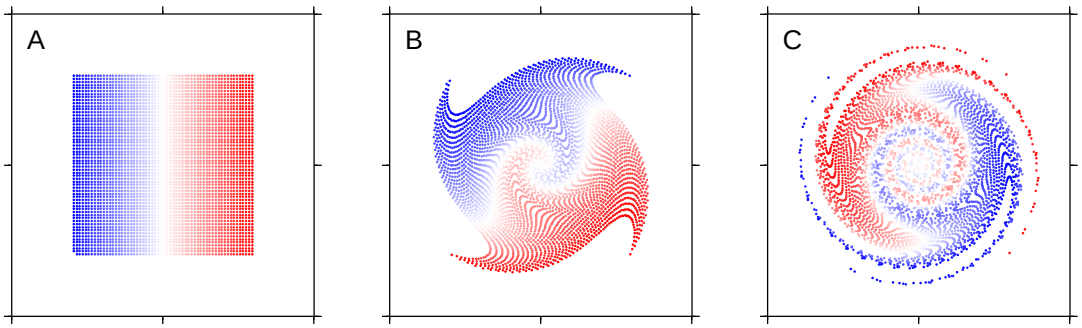

Figure 2.11: Model domain with particles colored according to the quantity F at three different time-steps: (A) $t = 0$ (initial position of particles), (B) $t = 50$, and (C) $t = 200$. The advection is computed using the fourth-order Runge-Kutta scheme.

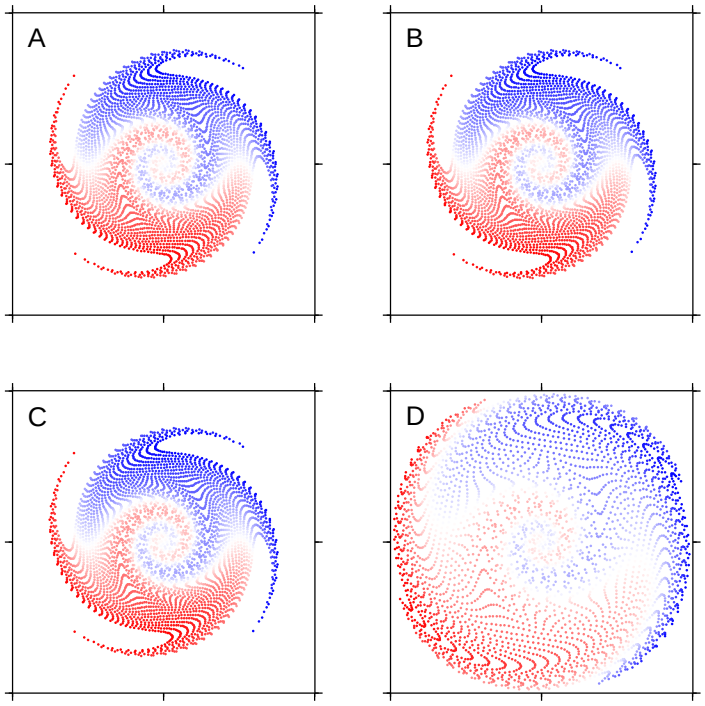

Figure 2.12: The same plot as Fig. 2.11, but for different advection schemes at $t = 100$. Advection was computed using (A) the fourth-order Runge-Kutta scheme, (B) the mid-point method, (C) Heun's method and (D) the explicit Euler method.

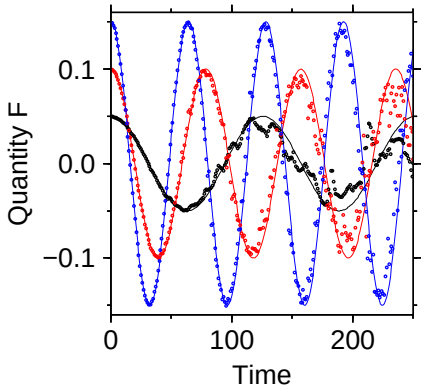

Figure 2.13: Time evolution of the scalar quantity F interpolated at different distances from the center of the vortex (circles) compared to the analytical solution (lines). Black, red and blue colors correspond to the distances $r = 0.2r_0$, $r = 0.4r_0$ and $r = 0.5r_0$, respectively. Advection was computed using the fourth-order Runge-Kutta scheme.

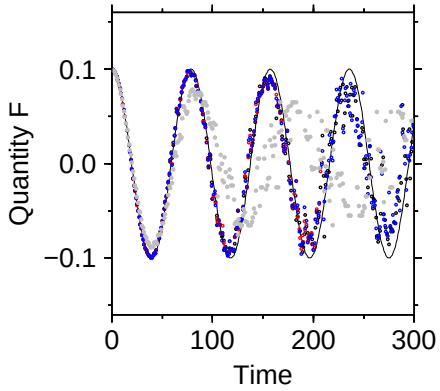

Figure 2.14: Time evolution of the scalar quantity F interpolated at the distance $r = 0.4r_0$ from the center of the vortex calculated using different advection schemes (circles) compared to the analytical solution (black line). Black, red, blue and gray circles correspond to advection using the fourth-order Runge-Kutta scheme, the mid-point method, Heun's method and the explicit Euler method, respectively.

2.3.4 Circular inclusion

The solution of flow equations in the presence of sharp viscosity contrasts can be tested on a problem concerning small-scale rock deformation: strain and rotation of a rock clast in a weaker matrix. We approximate the clast and the matrix by a high-viscosity ($\eta_1 = 1000$) circular inclusion of radius $r_1 = 0.1$ embedded in relatively low-viscosity ($\eta_2 = 1$) material. We consider a pure shear with a background value of strain rate $\dot{\epsilon} = 1$:

$$v_x = \dot{\epsilon}x, \quad v_z = -\dot{\epsilon}z \tag{2.86}$$

in the far field. The analytical solution of the problem was described by Schmid and Podladchikov (2003) and used by Deubelbeiss and Kaus (2008) as a testing case for accuracy of numerical schemes of viscosity interpolation. According to the analytical solution (Fig. 2.15) the pressure in the inclusion is zero, and the velocity is

$$v_x = \frac{\eta_2}{\eta_1 + \eta_2} 2\dot{\epsilon}x\,, \quad v_z = -\frac{\eta_2}{\eta_1 + \eta_2} 2\dot{\epsilon}z\,. \tag{2.87}$$

In the surrounding matrix, the pressure is

$$p = -2\frac{\eta_2(\eta_1 - \eta_2)}{\eta_1 + \eta_2} \left(\frac{r_1}{r}\right)^2 2\dot{\epsilon} \cos\left(2 \arctan\left(\frac{x}{z}\right)\right)\,, \tag{2.88}$$

where $r = \sqrt{x^2 + z^2}$.

At the boundaries of the model domain $\Omega = (-1, 1) \times (-1, 1)$ we prescribe the condition (2.86). We use 10×10 particles per element and two mesh resolutions (100×100 elements, 200×200 elements). For a quantitative comparison of the results we use the same error estimates as Deubelbeiss and Kaus (2008):

$$\text{velocity error} = \sqrt{\frac{\int \left(v_x^{\text{computed}} - v_x^{\text{analytic}}\right)^2 \mathrm{d}\Omega}{\int \left(v_x^{\text{analytic}}\right)^2 \mathrm{d}\Omega}}\,, \tag{2.89}$$

$$\text{pressure error} = \sqrt{\frac{\int \left(p^{\text{computed}} - p^{\text{analytic}}\right)^2 \mathrm{d}\Omega}{\int \left(p^{\text{analytic}}\right)^2 \mathrm{d}\Omega}}\,. \tag{2.90}$$

Our results agree with those presented by Deubelbeiss and Kaus (2008) only partly. Similarly to them, we obtain relative errors in the velocity more than one order of magnitude lower than those in the pressure (Table 2.2). However, the comparison between interpolation schemes yields different results, presumably because the numerical method (e.g. the type of finite elements) is different.

The velocity errors show only minor variations for different numerical setups (see Table 2.2). Besides resolution, they mostly depend on averaging scheme, yielding smallest errors for harmonic and largest for arithmetic averaging (compare different rows in Fig. 2.16). The errors in pressure are more variable and depend mostly on stabilization method. Best results were obtained for the "stabilized" method and arithmetic averaging to element centers. The source of errors can be observed in Fig. 2.17. The pressure near the rim of the circular inclusion is not well reproduced especially when harmonic averaging and/or bubble stabilization are used. For a lower resolution, the pressure overshoot near the rim is even more pronounced (Fig. 2.18). The interpolation of viscosity to integration points yields slightly higher errors than using a constant viscosity in each element.

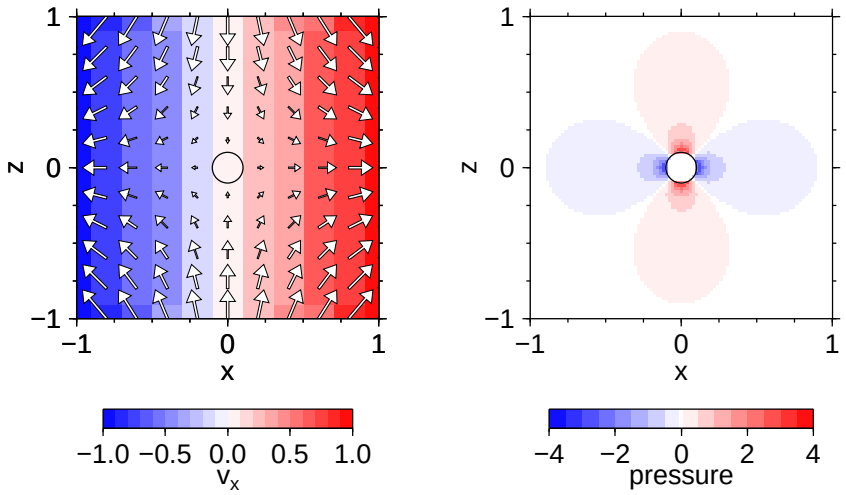

Figure 2.15: Analytical solution for the circular inclusion under pure shear. Velocity field (left) and pressure (right).

Table 2.2: Velocity and pressure errors

resolution	stabilization	element or integration points	averaging	velocity error ($\times 10^{-2}$)	pressure error
200×200	bubbles	integration points	arithmetic	2.766	0.7570
200×200	bubbles	integration points	geometric	2.625	1.1836
200×200	bubbles	integration points	harmonic	2.450	1.0111
200×200	bubbles	element	arithmetic	2.744	0.5975
200×200	bubbles	element	geometric	2.632	0.7421
200×200	bubbles	element	harmonic	2.476	0.7874
200×200	stabilized	integration points	arithmetic	2.869	0.4208
200×200	stabilized	integration points	geometric	2.715	0.4721
200×200	stabilized	integration points	harmonic	2.541	0.4724
200×200	stabilized	element	arithmetic	2.835	0.3783
200×200	stabilized	element	geometric	2.701	0.4317
200×200	stabilized	element	harmonic	2.547	0.4760
100×100	bubbles	integration points	arithmetic	3.069	1.1216
100×100	bubbles	element	arithmetic	3.054	0.8627
100×100	stabilized	integration points	arithmetic	3.233	0.6060
100×100	stabilized	element	arithmetic	3.202	0.5194

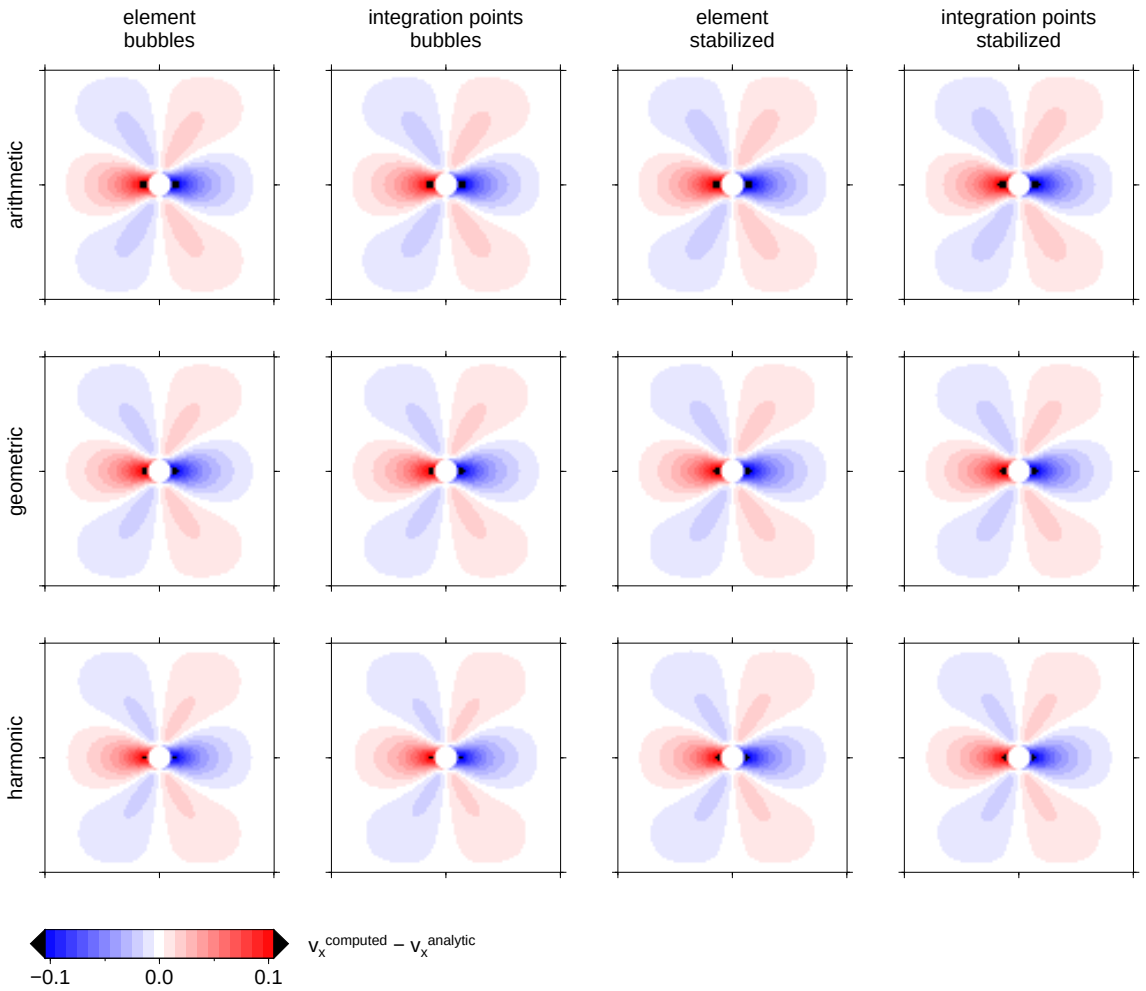

Figure 2.16: Circular-inclusion test. Difference between numerical and analytical solutions for velocity. The stabilization method and interpolation (element-wise constant, or variable at integration points) is noted to the top of the panels. The averaging schemes used are noted to the left of the panels. The resolution of 200×200 elements and 10×10 particles per element is used. The whole $(-1, 1) \times (-1, 1)$ model domain is plotted.

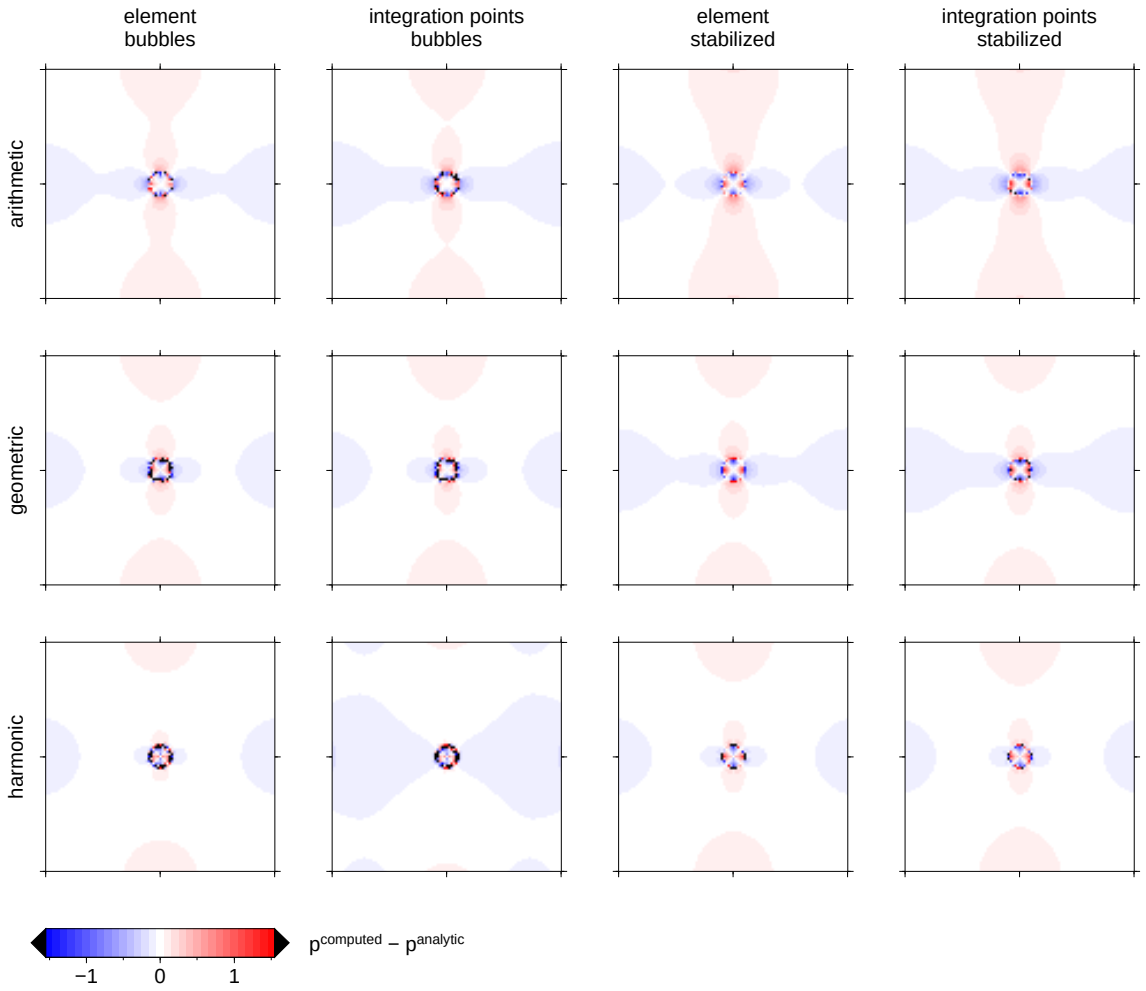

Figure 2.17: Circular-inclusion test. Difference between numerical and analytical solutions for pressure. The setups are the same as in Fig. 2.16.

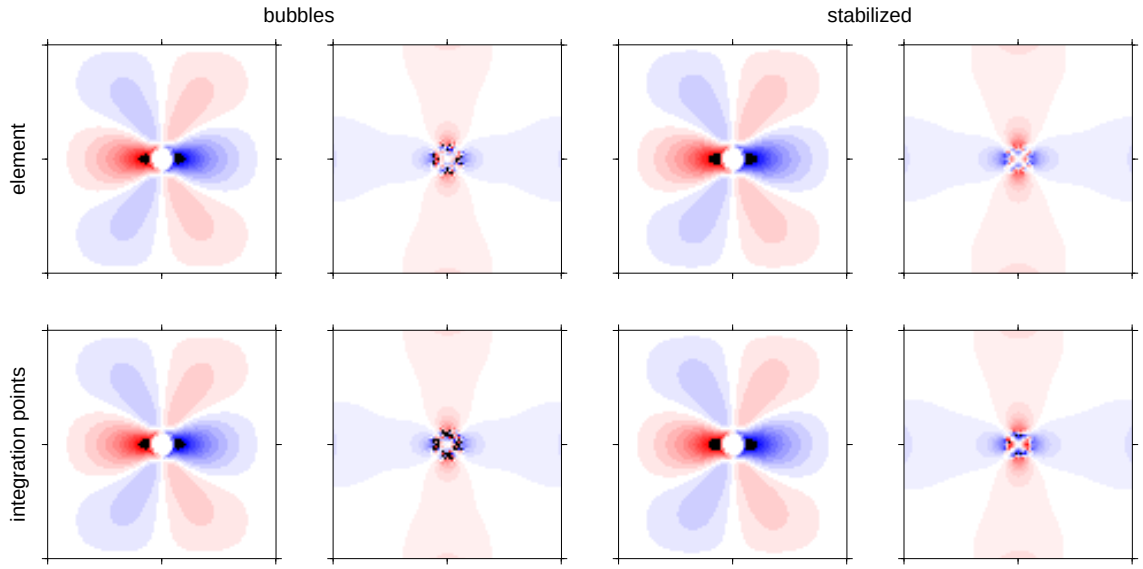

Figure 2.18: Circular-inclusion test with a resolution of 100×100 elements. Difference between numerical and analytical solutions for velocity (first and third columns) and pressure (second and fourth columns). Arithmeticl averaging of viscosity is used. The color scales for velocity and pressure are the same as in Figs 2.16 and 2.17, respectively.

2.3.5 Growth rate of the Rayleigh-Taylor instability

Following Deubelbeiss and Kaus (2008), we use a model of the Rayleigh-Taylor instability to estimate the precision of averaging schemes for viscosity and density. The term Rayleigh-Taylor instability refers to an unstable layering of material in the gravity field, where material with lower density resides beneath that having higher density. In a simple case with two layers, the amplitude of the initial perturbation of the interface grows with a rate v dependent on densities, viscosities, gravity and geometry of the layers (for definition of symbols see Fig. 2.19):

$$v = -\Delta z_0 K\left(\lambda, \eta_1, \eta_2, h_1, h_2\right) \frac{\rho_1 - \rho_2}{2\eta_2} h_2 g\,, \tag{2.91}$$

where the form of the factor K can be found in Ramberg (1981). The model domain is discretized using 100×100 elements each containing 10×10 regularly distributed material particles. We use an initial undulation of the interface $\Delta z_0 = 0.0025$, which is less than mesh resolution, but it is still resolved by the cloud of particles. In the model, we identify the rate of growth of this undulation with the maximum velocity in the $z-$direction.

The results (Fig. 2.20, Table 2.3) show that the velocity is well reproduced only for a limited viscosity contrast. The arithmetic averaging of viscosity yields the most stable results and the correct value of the growth rate is obtained even for the viscosity contrast of 10^6. With the geometric averaging, we can reproduce the velocity for the contrast of up to 10^5, and using the harmonic averaging this threshold is $\sim 10^3$. This behavior has been reported by Deubelbeiss and Kaus (2008) for certain combinations of interpolation and averaging schemes. The interpolation of viscosity (variable or constant at element) does not influence the result significantly. For the evaluation of density, we use mostly arithmetic averaging and the geometric

averaging gives similar results (see last row in Table 2.3). In contrast, the growth rate is sensitive to the density interpolation, showing an overshoot when element-wise constant density is assumed.

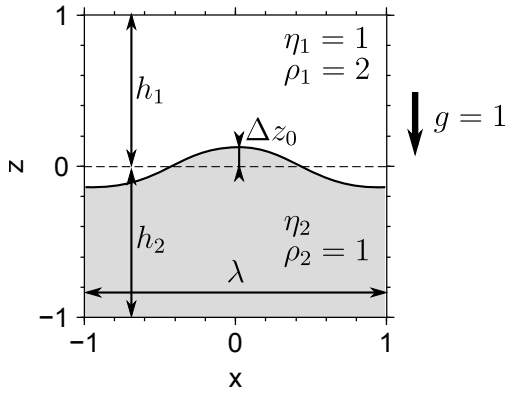

Figure 2.19: Model setup. The amplitude of undulation Δz_0 is not in scale. The viscosity of the lower layer varies between 10^0 and 10^6. We prescribe free-slip and no-slip conditions at vertical and horizontal boundaries, respectively.

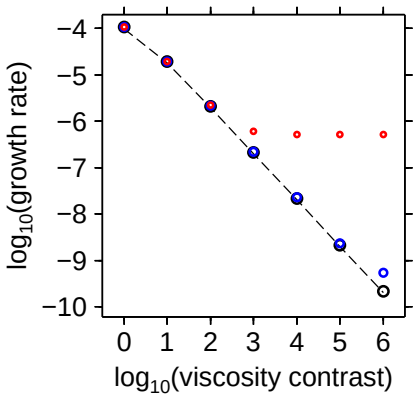

Figure 2.20: Analytically (dashed line) and numerically (circles) computed growth rates of the Rayleigh-Taylor instability. Black, blue and red circles are values calculated for arithmetic, geometric and harmonic averaging, respectively. Results were obtained for the resolution of 200×200 elements and interpolation to integration points.

Table 2.3: Growth rate of the Rayleigh-Taylor instability for viscosity contrast of 10^6

η: element or integration points	η: averaging	ρ: element or integration points	growth velocity ($\times 10^{-10}$)
integration points	arithmetic	integration points	2.1365
integration points	geometric	integration points	5.4489
integration points	harmonic	integration points	5231.5
element	arithmetic	integration points	2.1053
element	geometric	integration points	102.89
element	harmonic	integration points	6541.4
element	arithmetic	element	3.4569
integration points	arithmetic	element	3.4569
integration points	arithmetic	integration points, geometric	2.1079
analytical solution			**1.9882**

2.3.6 Time evolution of the Rayleigh-Taylor instability

The analytical solution (2.91) is valid only for small perturbations of the interface between the two layers with different density. The time evolution of the Rayleigh-Taylor instability with large deformations was modeled by van Keken et al. (1997) using various numerical approaches. We reproduced their results using different averaging schemes, points of interpolation and particle densities (for the model setup see Fig. 2.21). The plotted results (Figs 2.22–2.24) were obtained using the mesh resolution of 50×50 elements, geometric averaging of viscosity, and element-wise constant viscosity. The results mostly depend on the particle density. A relatively high density of material particles (approximately 10×10 particles per element) was needed to reproduce the results of van Keken et al. (1997). Small particle resolution leads to earlier initiation and growth of small–scale secondary instabilities (Fig. 2.23). The calculated velocity is highly variable in time (Fig. 2.24) and space. For this reason, the time-step length was evaluated using the Courant criterion.

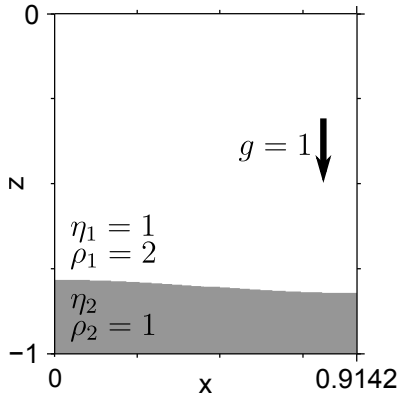

Figure 2.21: Model domain and initial material distribution. The viscosity of the lower layer varies between 1 and 10^{-2}. We prescribe zero velocity at the horizontal boundaries and free slip at the sides.

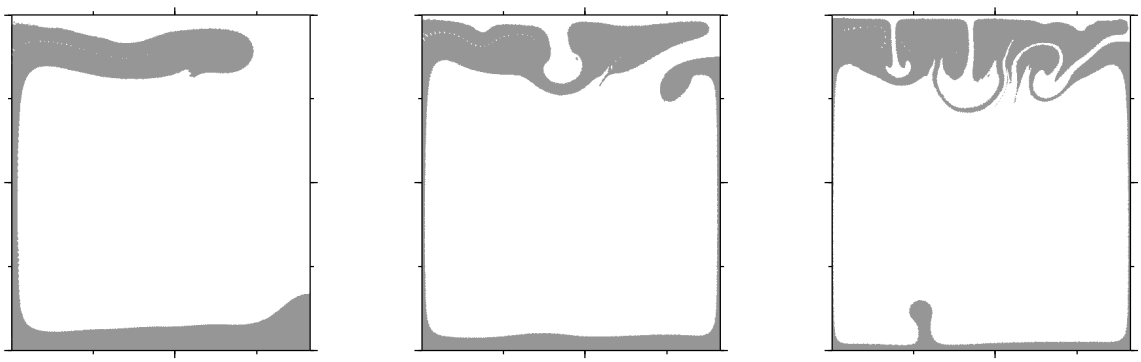

Figure 2.22: Material distribution for $\eta_1 = \eta_2 = 1$ at $t = 500$, 1000 and 2000 (from left to right).

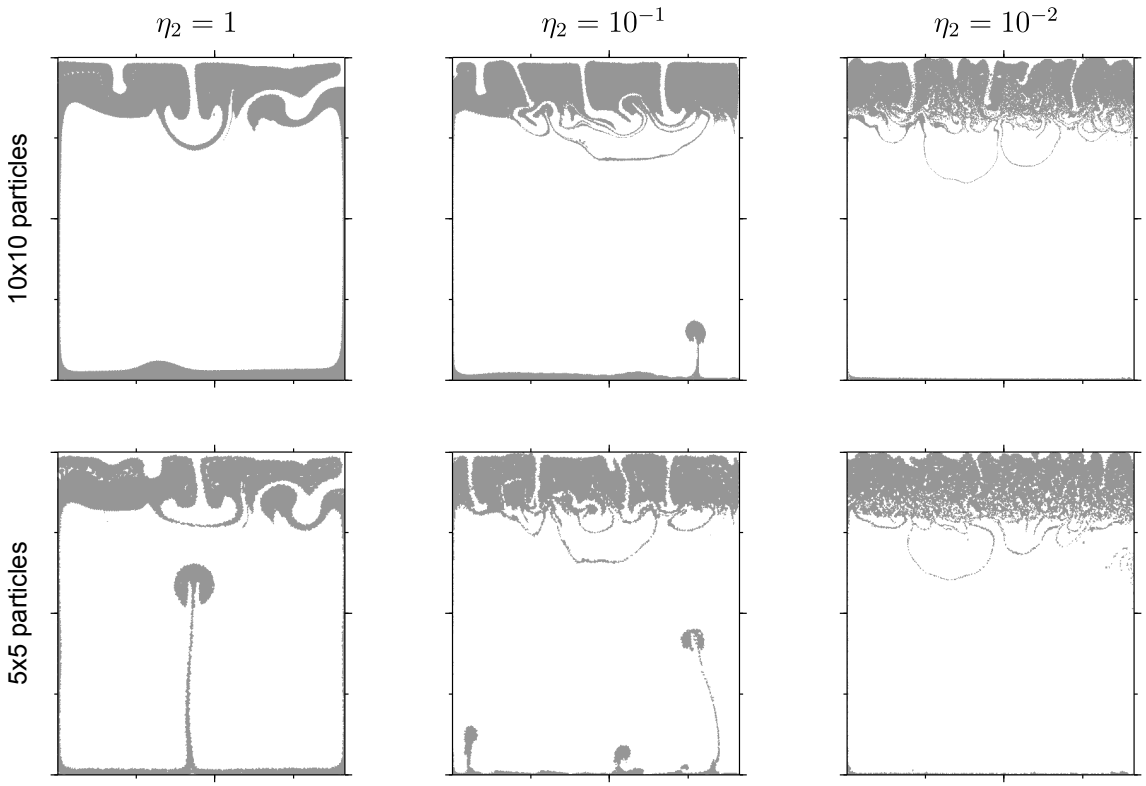

Figure 2.23: Material distribution at $t = 1500$ for different viscosity of the buoyant (gray) material (noted to the top of the panels). The initial number of particles per element is noted to the left of the panels.

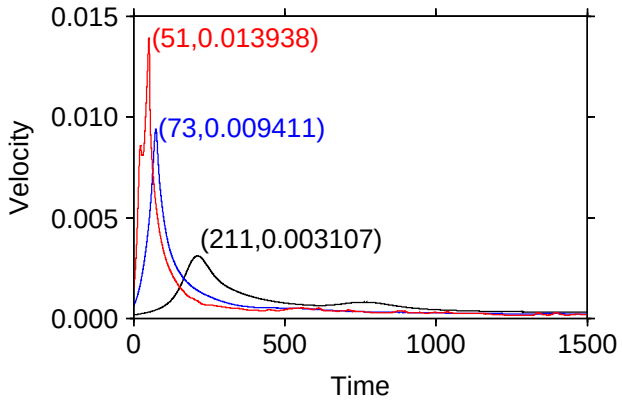

Figure 2.24: Time evolution of the root-mean-square velocity during the growth of the Rayleigh-Taylor instability. The black, blue and red lines show the results for $\eta_2 = 1$, 10^{-1} and 10^{-2}, respectively. The pairs of numbers are the peak values and times, when they were achieved. The rise of a low-viscosity buoyant material is faster and earlier.

2.3.7 Sinking cube

The effect of density and viscosity evaluation was also tested on the sinking cube experiment (Gerya and Yuen, 2003). In this experiment, an initially cubic body made of material with a high density is sinking through a less dense fluid (Fig. 2.25). The model domain (Fig. 2.25, left panel) was discretized to 50×50 elements, each of them initially containing 5 × 5 regularly distributed material particles. When the viscosity of the cube is similar to that of the surrounding fluid, the shape of the sinking body evolves (Figs 2.25 and 2.26, left). For the viscosity contrast higher than approximately 3 orders of magnitude, the original cubic shape remains unchanged during its motion through the fluid (Fig. 2.26, right). However, even for the viscosity contrast of 6 orders of magnitude, the harmonic averaging of viscosity leads to slight deformation of the edges of the cube, where some particles are detached by the surrounding fluid (see the right panels in Fig. 2.27). For all viscosity contrasts, the averaging scheme of viscosity influences the sinking velocity: the harmonic averaging leads to the fastest, geometric to an intermediate and arithmetic to the slowest sinking of the dense body (compare the position of the cube in different columns in Fig. 2.27), as discussed by Schmeling et al. (2008). Variable vs. constant viscosity in elements has only a minor effect on the shape and velocity of the sinking body.

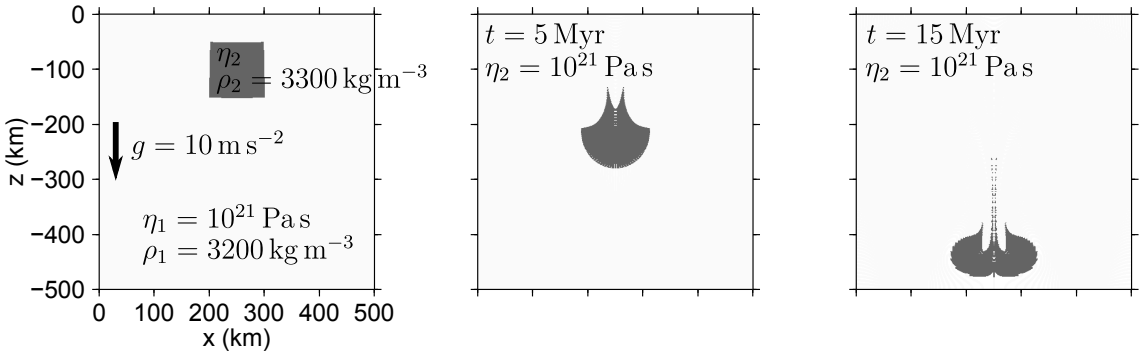

Figure 2.25: Setup of the model showing the initial position of the material particles (left), and material distribution at two time steps (middle and right panels) in an isoviscous model.

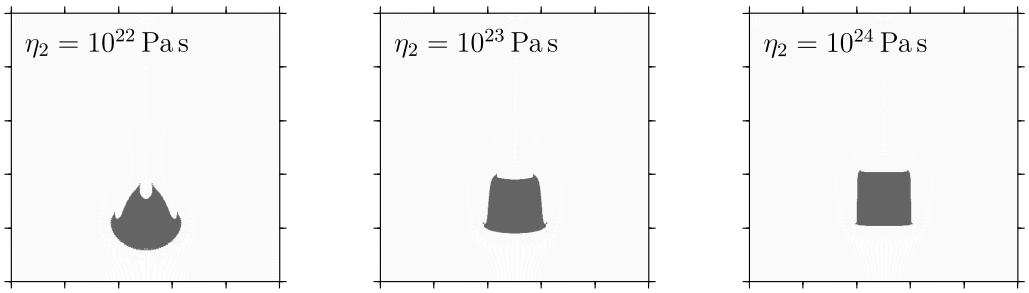

Figure 2.26: Material distribution after 15 Myr of evolution for three different viscosity contrasts between the sinking body and the surrounding material. Geometrically averaged constant viscosity per element and arithmetically averaged density at integration points was used. The plotted domain is the same as in Fig. 2.25.

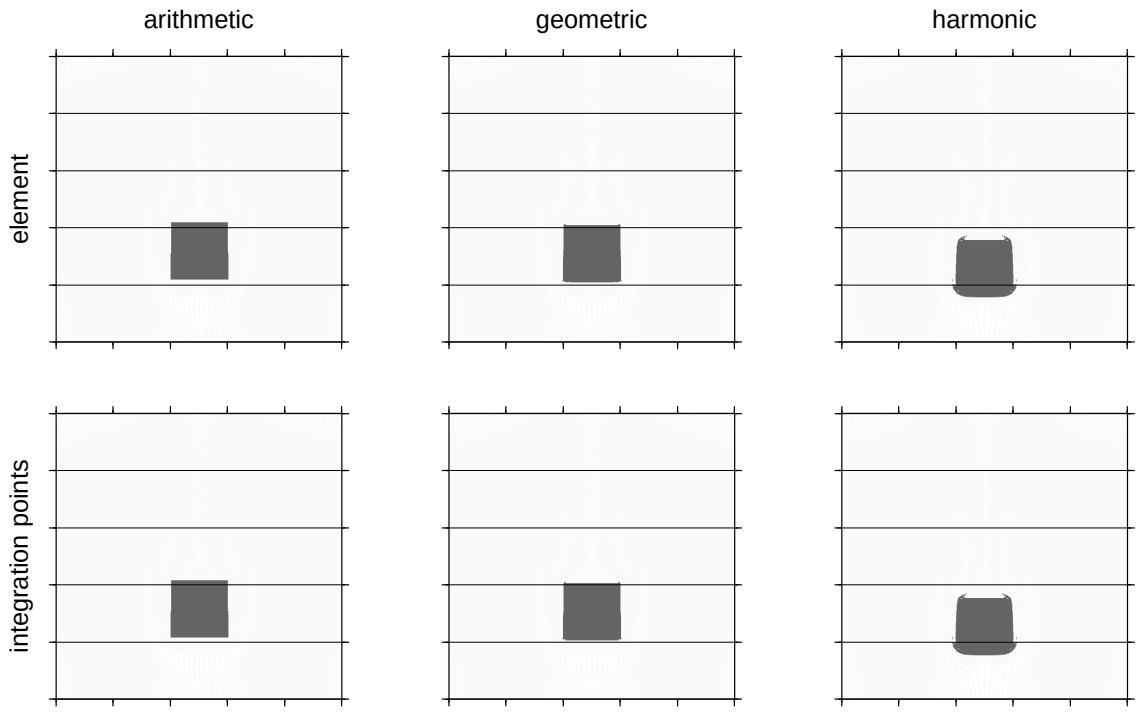

Figure 2.27: Material distribution after 15 Myr of evolution for the viscosity contrast of 10^6 between the sinking body and the surrounding material. The interpolation (element-wise constant or variable at integration points) is noted to the left of the panels. The averaging schemes used for viscosity is noted to the top of the panels. The plotted domain is the same as in Fig. 2.25.

2.3.8 Initiation of shear bands

As a basic test of the plasticity implementation we used a similar setup as Lemiale et al. (2008) and Kaus (2009). We examined inclination of shear bands initiated near a weak impurity in otherwise homogeneous material due to compression or extension (Fig. 2.28). Panels in Fig. 2.29 show the second invariant of strain rate in the domain after 0.5% of shortening or extension. The strain rate is concentrated into narrow bands forming a certain angle near the weak inclusion. The contrast between the strain rate in the bands and that in the surrounding area is more than 3 orders of magnitude, and the width of the bands is only a few elements. This concentration of strain into narrow bands is related to the strain weakening due to a prescribed decrease of cohesion with increasing strain (Lemiale et al., 2008).

Theoretically, angles of shear bands measured from the main stress axis attain values between the Coulomb angle $\frac{\pi}{4} - \frac{\phi}{2}$ (black lines in Figs 2.29-2.31, see also Section 2.1.3) and the Roscoe angle $\frac{\pi}{4}$ (Lemiale et al., 2008). Similarly to Kaus (2009), we obtained angles close to the Coulomb angle for a high resolution and angles getting closer to the Roscoe angle for a low resolution (Fig. 2.30). In Fig. 2.30, we observe that the use of the "stabilized" method effectively reduces the resolution. In this test, the number of particles per element, interpolation and averaging schemes play only a minor role.

The reason for inefficient localization of the strain rate when using the "stabi-

lized" method can be seen in the pressure field (Fig. 2.31). The bubble stabilization causes a pressure overshoot near the band with the high strain rate. This is in line with the results of the circular-inclusion test, where the bubble stabilization caused large pressure oscillations (see Fig. 2.17). This high pressure contrast helps to focus the strain rate into narrow bands where pressure is low, because the yield strength (and effective viscosity) of the material decreases with pressure: $\sigma_{\text{yield}} = p \sin\phi + C \cos\phi$.

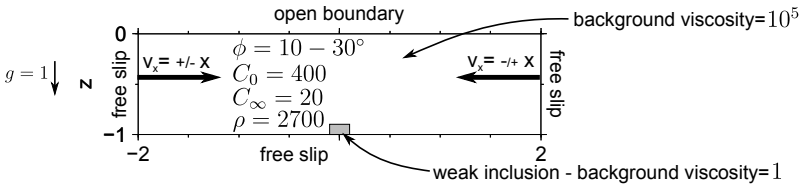

Figure 2.28: Model domain and boundary conditions. Material parameters are the same in the whole model domain, except the background viscosity of ductile flow, which is by 5 orders of magnitude smaller in the weak inclusion than in the surrounding matrix. The size of the inclusion is 0.04×0.02 (not in scale with the plotted domain).

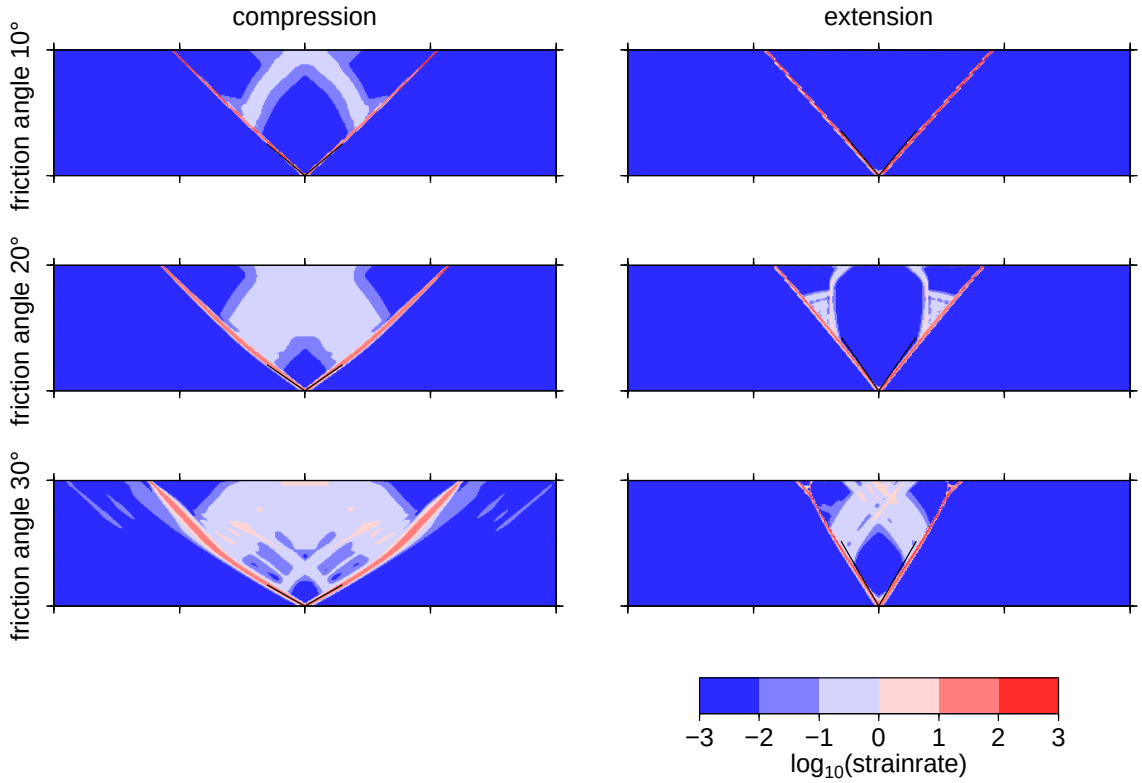

Figure 2.29: Initiation of shear bands for different model setups. Shortening (left) or extension (right) of the model domain is prescribed at the vertical boundaries. The angle between the shear bands and the main stress axis depends on the angle of internal friction ϕ (noted to the left of the panels). The black line shows the Coulomb angle $\frac{\pi}{4} - \frac{\phi}{2}$. Mesh resolution is 400×100 elements with 3×3 particles per element.

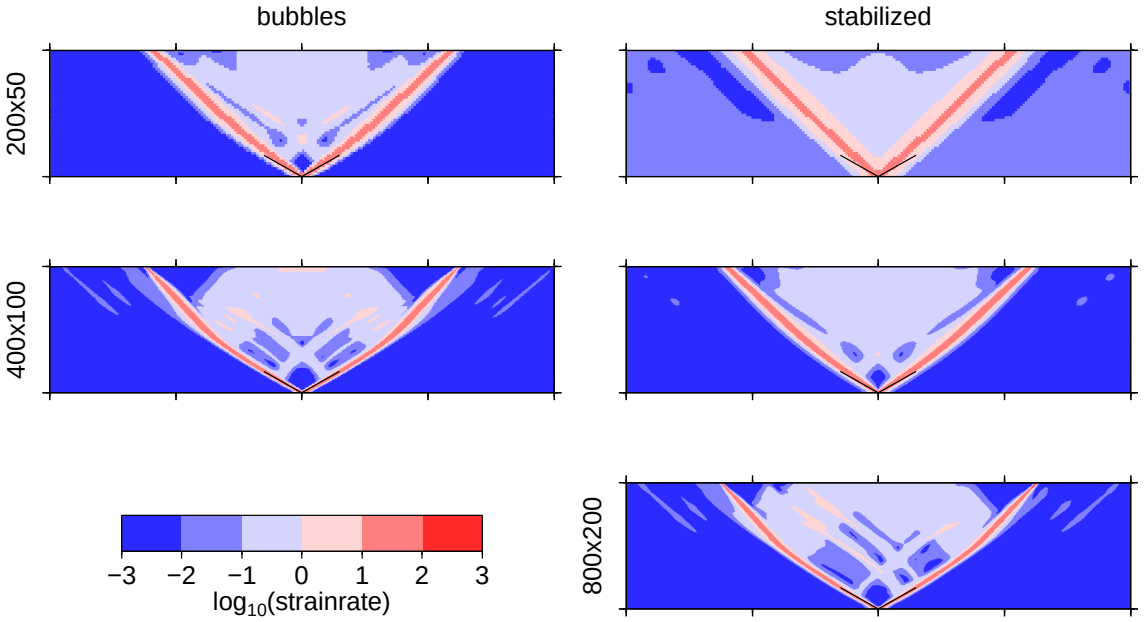

Figure 2.30: Initiation of shear bands — effects of mesh resolution (noted to the left) and stabilization method (noted on top). The results obtained using the incomplete "stabilized" method have effectively smaller resolution compared to those computed using residual-free bubble stabilization. The angle of internal friction is 30°. The particle density is 3×3 per element.

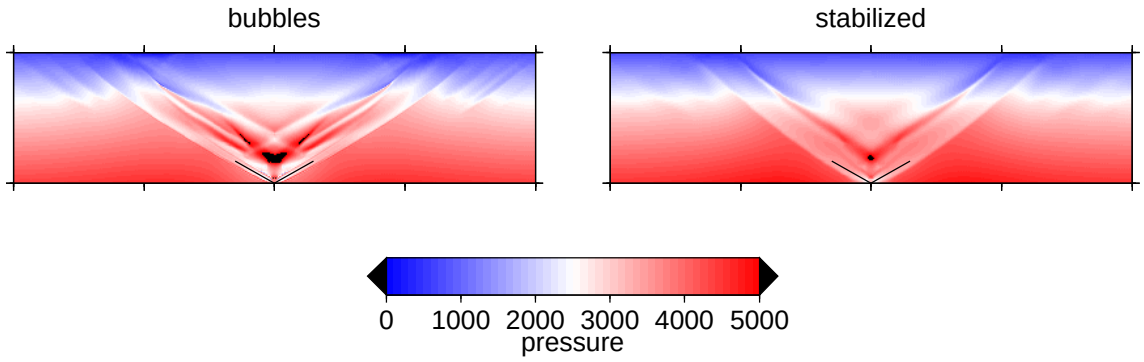

Figure 2.31: Pressure field during the formation of shear bands in two cases with different stabilization methods (noted to the top of the panels). Resolution is 400×100 elements, 3×3 particles per element. The angle of internal friction is 30°.

2.3.9 Numerical sandbox

A more complicated setup requiring not only plasticity, but also free surface and large mesh deformations in both vertical and horizontal directions, was described by Buiter et al. (2006). It simulates a box filled with layers of plastic (brittle) material shortened from one side. The overall dynamic evolution of the model as well as quantitative characteristics were compared among results from different numerical codes and analogue experiments. Our result (Fig. 2.32) is well within the range of the reported results achieved by other numerical codes.

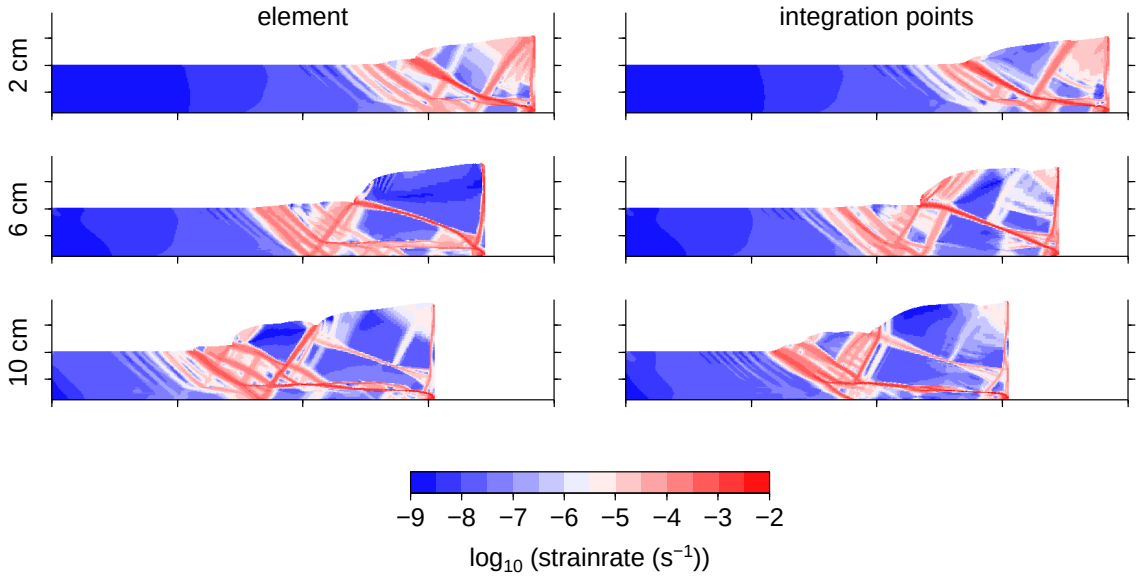

Figure 2.32: The strain-rate field in the numerical sandbox. The model domain is shortened from the right side, causing activation of shear bands and deformation of the upper free surface. The amount of shortening is indicated to the left of the panels. The model description is detailed in Buiter et al. (2006). The resolution is 400×70 elements, 5×5 particles per element. Different interpolation of viscosity (to the element center or to integration points) affects the distribution of the shear bands, but the overall evolution is similar.

2.3.10 Collisional orogen

The general setup of our model of continental collision follows the approach of Fullsack (1995), that was applied by e.g. Vanderhaeghe et al. (2003) for the modeling of orogenic wedges and their transition to continental plateaux. In order to test the implementation of the free surface and its coupling with material flow and isostasy, we reproduced the results presented by Vanderhaeghe et al. (2003) for several simple cases (isoviscous, purely brittle-plastic, with and without flexural isostatic compensation). In this setup, the deformation of two colliding crustal blocks is modeled. The velocity of convergence of the two blocks is prescribed through a boundary condition at the bottom of one of the blocks and at the adjacent vertical boundary.

The top boundary is a free surface and the bottom of the crust deforms due to isostasy. The resulting evolution of the model (velocity field, shape of the domain and material distribution, in Figs 2.33 and 2.34) is in a good agreement with the results of Vanderhaeghe et al. (2003), although the isostatic flexure is evaluated analytically in our model (see Section 2.1.5), while Fullsack (1995) and Vanderhaeghe et al. (2003) use a 1D finite-element approach.

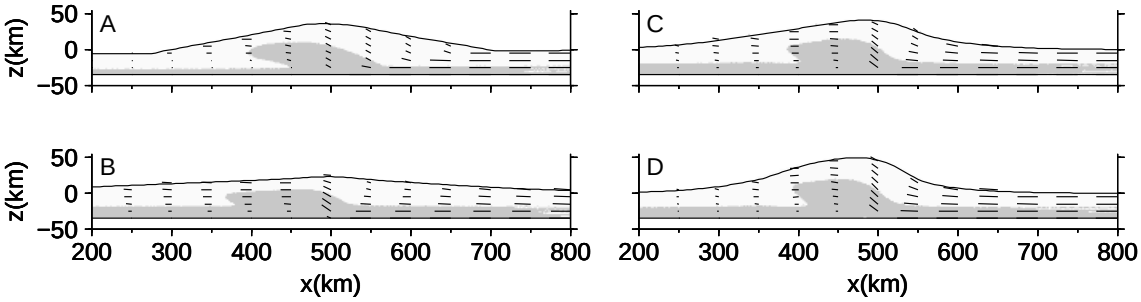

Figure 2.33: Shape of the free surface, velocity and material distribution in the model after 30 Myr of evolution for different viscosity of material: (A) brittle-plastic rheology with $\phi = 11.3$, (B) $\eta = 10^{21}\,\mathrm{Pa\,s}$, (C) $\eta = 10^{22}\,\mathrm{Pa\,s}$, and (D) $\eta = 10^{23}\,\mathrm{Pa\,s}$. Sticks show the magnitude and direction of flow. The upper free surface and the material layers are initially flat, the bottom boundary is rigid. At the bottom boundary, the prescribed tangential velocity changes from 0 to $-1\,\mathrm{cm\,yr^{-1}}$ at $x = 500$ km. The model description is detailed in Vanderhaeghe et al. (2003).

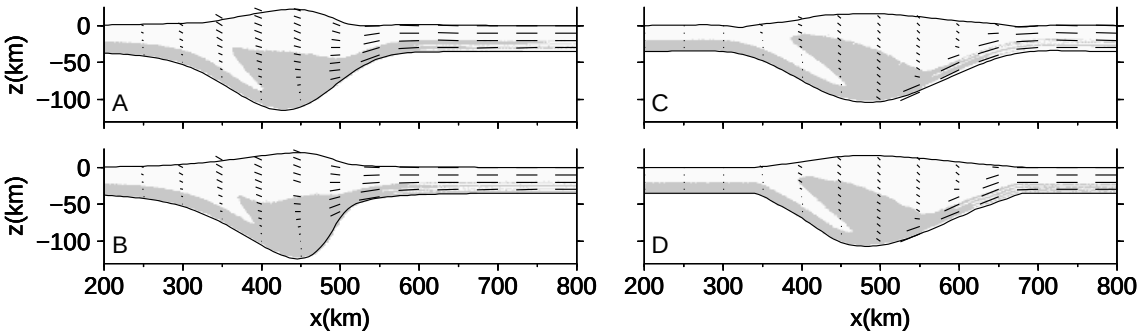

Figure 2.34: Comparison of models with the flexural rigidity of $10^{22}\,\mathrm{Nm}$ (panels A, C) and with Airy isostasy ($D = 0$, panels B, D) after 45 Ma of evolution. The viscosity is either constant $10^{23}\,\mathrm{Pa\,s}$ (panels A, B) or follows brittle-plastic rheology with $\phi = 11.3$ (panels C, D). The plotted properties are the same as in Fig. 2.33. We observe that the difference between the results obtained using the flexural isostatic compensation with $D = 10^{22}\,\mathrm{Nm}$ and those using Airy isostasy are relatively minor, as already discussed by Vanderhaeghe et al. (2003).

2.3.11 Summary of numerical tests

The performed numerical tests show that the software successfully treats thermal convection, advection of heterogeneous material, non-linear rheology and brittle-plastic deformation in a domain with moving boundaries. The accuracy of the simulations depends on several aspects, and the optimal numerical setup can be different for different modeled problems. Nevertheless, we made the following observations:

- At least second-order schemes shall be used for advection of material particles (see the vortex experiment).
- The velocity field exhibits large errors when harmonic averaging of viscosity is applied, as was shown in the Rayleigh-Taylor instability and sinking-cube experiments.
- The geometric averaging of viscosity is a compromise between the accuracy of the calculated pressure and velocity field calculated in the circular-inclusion experiment.
- The interpolation of viscosity to integration points or using element-wise constant viscosity does not have a large effect on the results of the tests.
- Interpolation of density to integration points gives a more accurate solution of the Rayleigh-Taylor instability test. Arithmetic averaging of density is appropriate.
- The mesh resolution influences not only the accuracy of the solution (see e.g. the circular-inclusion test), but also the angle of the shear bands in a model of Drucker-Prager plastic material.
- The particle density should be set according to the modeled problem (compare 3×3 particles per element in the model of shear-band initiation and 10×10 particles per element in the model of the Rayleigh-Taylor instability).
- Stabilization influences the calculated pressure near boundaries with large viscosity contrasts. Residual-free-bubble stabilization leads to a larger pressure overshoot compared to the incomplete "stabilized" method. Pressure contrasts play important role during initiation of shear bands, and the bubble stabilization leads to more focused shear zones. For some applications, both stabilization methods can be used. However, if the brittle-plastic rheology is modeled, an effective decrease of resolution in the case of the incomplete "stabilized" method has to be taken into account.


34.0 Myr

Chapter 3

A numerical model of exhumation of the orogenic lower crust in the Bohemian Massif during the Variscan orogeny

Published in Studia Geophysica et Geodaetica,
Volume 56, 595–619, doi: 10.1007/s11200-011-0455-x, 2012.

Petra Maierová[1], Ondřej Čadek[1], Ondrej Lexa[2] and Karel Schulmann[3]

[1]Department of Geophysics, Faculty of Mathematics and Physics, Charles University, Prague, Czech Republic
[2]IPSG, Faculty of Science, Charles University, Prague, Czech Republic
[3]EOST, Université de Strasbourg, Strasbourg, France

Abstract

We present a numerical model of the main phase (370–335 Ma) of the Variscan orogeny in the central part of the Bohemian Massif. The crustal deformation in our model is driven by radiogenic heating in the felsic lower crust, the lateral contraction of the Moldanubian domain due to convergence with the Saxothuringian plate (in the early stage of orogeny), and the indentation of the Brunovistulian basement into the weakened orogenic root (in the late stage). Our model explains the main geological events inferred from the geological record in the Moldanubian domain: formation of the orogenic plateau and onset of sedimentation at about 345 Ma, rapid exhumation of the orogenic lower crust at about 340 Ma and subsurface flow of crustal material (∼335 Ma and later). The results of our modeling suggest that delamination of the lithosphere, often invoked to explain the high temperature metamorphism in the orogenic lower crust of the Bohemian Massif, is not the only physical mechanism which can transfer a sufficient amount of heat to the crust to trigger its overturn.

Keywords: felsic granulites, Moldanubian zone, radiogenic heating, delamination

3.1 Introduction

Despite the large amount of geophysical and geological data collected in central Europe in the past decades, our knowledge of the formation of the Bohemian Massif is still rather limited and a number of key details remain elusive. It is mostly accepted that the Bohemian Massif is a collage of microplates assembled during the Variscan orogeny in Devonian and Carboniferous (Franke, 2000; Winchester et al., 2002). The amalgamation process was probably initiated by collision of the Saxothuringian microplate with a Gondwana-derived lithospheric block in the east (in present geographic coordinates) which was subsequently thickened and its central part (Moldanubian domain) was intensely reworked. These tectonic events were accompanied by the release of a large amount of heat leading to high-temperature metamorphism and voluminous magmatism. The final stage of the orogeny was marked by a change of the convergence direction from east-west to north-south resulting in collision of the orogen with the Brunovistulian domain and the development of a sedimentary basin along the eastern margin of the Bohemian Massif.

From the physical point of view, a fundamental question related to the scenario described above is the source of the heat that was needed, together with plate tectonic forces, to drive the processes of crustal deformation, magmatism and metamorphism. Steltenpohl et al. (1993) have suggested that the collision with the Saxothuringian microplate was followed by delamination of the underthrust lithosphere which enhanced the heat transfer from the asthenosphere and resulted in widespread deformation and granite plutonism (see also Arnold et al., 2001; Willner et al., 2002; Massonne, 2006; Dörr and Zulauf, 2010). An alternative explanation has been proposed by Gerdes et al. (2000) who pointed out the possibility that a sufficient amount of heat may have been produced by radiogenic heating. This concept has been further developed by Lexa et al. (2011) who suggested that a part of the Saxothuringian upper crust, rich in radioactive elements, was pulled into the mantle and emplaced at the base of the crust of the overriding plate. The subsequent overheating of this material in synergy with the collisional process in the east led to a dramatic turnover, marked by exhumation of the orogenic lower crust, crustal indentation and widespread crustal melting.

In the present paper, we examine the latter hypothesis by means of a numerical simulation, mimicking the evolution of two adjacent crustal blocks subject to a compression. Our simulation begins at the time when the radiogenic material is already emplaced at the base of the Moldanubian crust. The simulation itself represents $\sim$35 Ma of geological evolution and can be divided into two stages: In the first one, the model imitates the processes related to the collison of the blocks with the Saxothuringian unit, while the other stage represents indentation of the Brunovistulian block into the thickened Moldanubian crust. In evaluating the admissibility of our models, we consider only the geological data. The geophysical aspects, including seismic information (e.g. Hrubcová et al., 2005; Babuška et al., 2008), gravity field measurements (e.g. Bielik et al., 2006; Guy et al., 2011) and others, will be discussed in a subsequent paper.

The number of modeling efforts which have directly addressed the geological evolution of the Bohemian Massif is still rather limited (cf. Gerdes et al., 2000; Arnold et al., 2001; Willner et al., 2002; Lexa et al., 2011; Duretz et al., 2011). The present work is thus one of the first attempts to explain the processes that

led to exhumation of the orogenic lower crust using a complex numerical modeling approach. The structure of the paper is as follows. In the Section 3.2 we summarize the basic geological information that can be used to constrain our numerical model and we briefly discuss possible scenarios of the Variscan evolution of the Bohemian Massif. The equations governing the deformation and heat transfer in the crust as well as the numerical method used for the simulations are detailed in Section 3.3. In Section 3.4, we present the results of our numerical modeling and, in Section 3.5, we compare them with the geological data. Potential feedback of the numerical model on the current geological concepts of the Bohemian Massif is outlined in the final section.

3.2 Geological constraints

The last few years have seen remarkable progress in the numerical modeling of geological processes (e.g. Gerya et al., 2008; Beaumont et al., 2001; Sobolev and Babeyko, 2005; Burov and Yamato, 2008). Used in conjunction with traditional geological and geophysical approaches, numerical modeling now appears to be a powerful tool to verify geological concepts and provide insight into the processes that formed the Earth's crust. Although the present-day numerical models of crustal deformation are significantly more complex than the usual models of mantle convection (as they often include several mineralogical phases, complicated visco-plastic rheology and free upper surface, shaped not only by crustal flows but also by erosion and sedimentation), they are still too simplified to capture all details of the geological record. Nevertheless, some geological data can be directly used as constraints on the numerical models, namely (i) the petrological data, which provide information about the pressure and temperature (P–T) history of rocks, (ii) the data on the time scales of principal tectonic and thermal events based on U-Pb zircon and ^{40}Ar-^{39}Ar ages, and (iii) the structural data which can be considered as a proxy for deformation regime, prevailing orientation of stress, rate of deformation and possible tectonic setting. In the following overview, we will focus on the above three types of data.

3.2.1 Variscan orogeny in the Bohemian Massif

The Bohemian Massif is an eastern part of a large orogenic belt formed during the Variscan mountain-building event in the Devonian and Carboniferous (400–300 Ma). It consists of four basic geological units (Saxothuringian, Teplá-Barrandian, Moldanubian and Brunovistulian, see Fig. 3.1) which probably played the role of microplates in the process of closing the Rheic Ocean between Laurentia and Baltica in the north and Gondwana in the south (Franke, 2000; Winchester et al., 2002). The tectonic structure of the Bohemian Massif established during the Variscan orogeny is only mildly affected by later geological events, which involve Cretaceous and Cenozoic sedimentation and Tertiary volcanism to name the most important ones.

The record of early evolution of the Variscan orogeny is well preserved in the Teplá-Barrandian domain and along its boundary with the Saxothuringian domain, where the low-temperature eclogites of the Mariánské Lázně Complex (MLC in Fig. 3.1) are considered to be a relic of the oceanic crust subducted beneath the Teplá-Barrandian domain (e.g. Beard et al., 1995). Most rocks in this region pre-

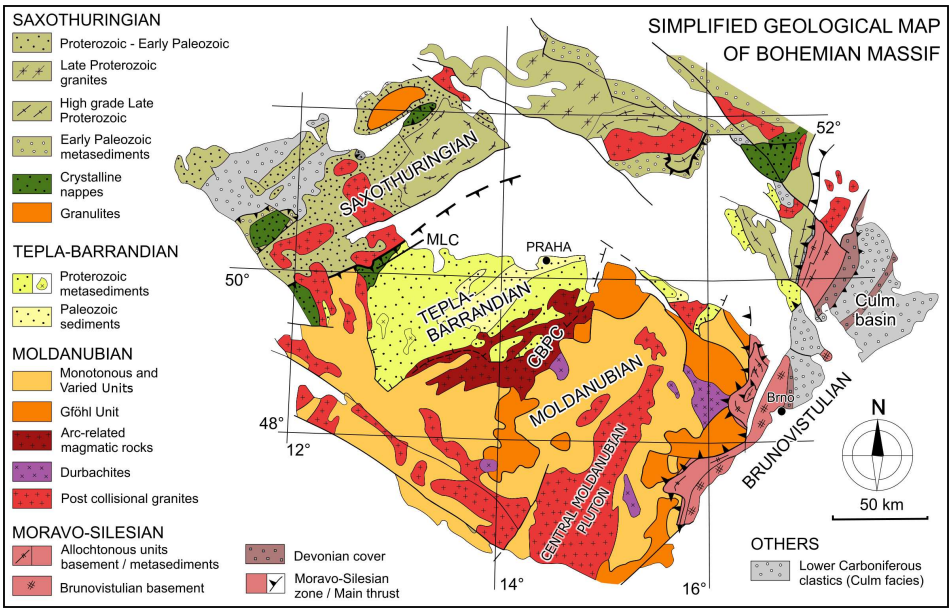

Figure 3.1: Simplified geological map of the Bohemian Massif (modified after Franke, 2000).

serve fabrics and structures related to east-west oriented convergence (e.g. Zulauf, 2001) and reveal Upper Devonian (380–360 Ma) metamorphic and cooling ages (e.g. Dallmayer and Urban, 1998; Timmermann et al., 2006). This concept is further supported by the magmatic history of the Central Bohemian Plutonic Complex (CBPC in Fig. 3.1) located along the border between the Teplá-Barrandian and the Moldanubian domains and interpreted by some authors as a continental magmatic arc (e.g. Janoušek at al., 2000; Žák et al., 2005). A different view has been presented by Dörr and Zulauf (2010) who relate most of the plutons along the Barrandian-Moldanubian boundary to post-collisional processes.

The main collisional stage is characterized by crustal thickening in the Moldanubian domain leading to the development of an orogenic root. The lower crust of the orogenic root is now exposed in the Gföhl Unit (see Fig. 3.1) which is composed of high-grade rocks including felsic granulites and boudins of meta-peridotites and eclogites. All these rocks exhibit equilibration at temperatures of 800–1000 °C and pressures of 16–20 kbar at about 340 Ma ago followed by isothermal decompression. The orogenic middle crust is represented by medium grade rocks (Monotonous and Varied Units in Fig. 3.1) which experienced metamorphism at 8–12 kbar and 600–700 °C with the maximum temperature attained during decompression. Recent studies (e.g. Schulmann et al., 2008) have revealed that the early exhumation of the lower crust, the emplacement of mantle-derived melts (durbachites) and the peak metamorphism of the middle crust were accompanied by the development of subvertical fabrics (for a complete list of citations relevant to orogenic processes in the Moldanubian domain, see Schulmann et al., 2008).

The final stages of the Variscan orogeny are manifested by the development of a major deformation zone along the boundary between the Moldanubian and Brunovistulian domains. This zone is characterized by intense subhorizontal shearing and metamorphism related to an inverted temperature gradient which have been interpreted as a result of continental indentation occurring between ∼340–325 Ma (Štípská and Schulmann, 1995; Fritz et al., 1996). During this event (between

about 335 and 325 Ma) the subvertical fabrics in the orogenic root are reworked by a subhorizontal flow at high-temperature and intermediate-pressure (7–5 kbars) conditions associated with significant partial melting (e.g. Central Moldanubian Pluton, for review see Finger et al., 1997). This period of deformation coincides with the break-up of the brittle upper crust and exposure of deeper orogenic levels (Dörr and Zulauf, 2010). At about 345 Ma, a foreland basin (Culm) develops along the north-eastern margin of the orogenic plateau. Deposition of sediments continues in this region until about 315 Ma. The high-grade rocks are detected in the sediment record starting from ca. 330 Ma (Hartley and Otava, 2001).

3.2.2 Goals of the present study

The details of the evolution scenario outlined above remain unclear and they are hotly debated. The nature of the collision process in the east, the tectonic affinity between the Teplá-Barrandian and Moldanubian blocks as well as the character and timing of the oceanic and continental subduction in the west are just a few examples of problems that require further study. Another important question concerns the role of mantle convection and, in general, the source of heat needed to accomplish the processes described above. Delamination of the thickened lithosphere is a physical mechanism providing a large amount of heat within a time scale of a few million years and therefore a tempting explanation for the rapid high temperature metamorphism and extensive volcanism observed in the Bohemian Massif (e.g. Massonne, 2006; Dörr and Zulauf, 2010). The other possibility is to invoke radiogenic heating (Gerdes et al., 2000). This mechanism does not require any supply of additional heat from the mantle but it is usually considered to be only effective on larger (∼10–100 Ma) time scales (for comparison of different heating mechanisms, see Arnold et al., 2001). Schulmann et al. (2008, 2009) have proposed a scenario for the evolution of the Bohemian Massif (Fig. 3.2, modified) in which a part of the felsic material of the Saxothuringian upper crust was emplaced under or near the Moldanubian crust (stage 2 in Fig. 3.2, cf. Kotková et al., 2011). This material, possibly rich in radioactive elements, could be an important source of heat influencing the thermal evolution of the orogen (stages 3–5 in Fig. 3.2). Invoking the concept of relamination (Hacker et al., 2011) and following the study by Faccenda et al. (2008), Lexa et al. (2011) have demonstrated that this type of heating can increase the temperature of the lower crust to 900–1000 °C within a time period of 15–25 Ma and, therefore, it is a likely candidate for explaining the high-temperature metamorphism and durbachite magmatism in the Variscan orogenic root.

In this study, we aim to examine the scenario proposed for exhumation of the lower crust by Schulmann et al. (2008, 2009) and later developed by (Lexa et al., 2011). With the aid of a numerical model comparable with those used today to study hot orogens (e.g. Beaumont et al., 2001), we will attempt to reproduce the main phase of the Variscan orogeny in the Bohemian Massif, sketched as stages 3–5 in Fig. 3.2. Our goal is to predict:
(i) the P–T conditions typical for the formation of the Moldanubian granulites (depths of upto 60 km and temperatures of ∼850 °C);
(ii) a rapid turnover occurring some 20–40 Ma after the emplacement of the Saxothuringian upper crust underneath the Moldanubian crust, and the subsequent channel flow deformation, observed in the geological record in the eastern part of

the Moldanubian unit;
(iii) the fast exhumation of the granulites in P–T conditions consistent with the observed P–T paths, and, finally,
(iv) the evolution of surface topography compatible with the sediment record from the Culm Basin.
This study does not have the ambition to provide an explanation of the process that was responsible for underplating of the Moldanubian crust by the Saxothuringian upper crustal material (stages 1–2 in Fig. 3.2). For a general discussion of this problem, the reader is referred to the review paper by Hacker et al. (2011).

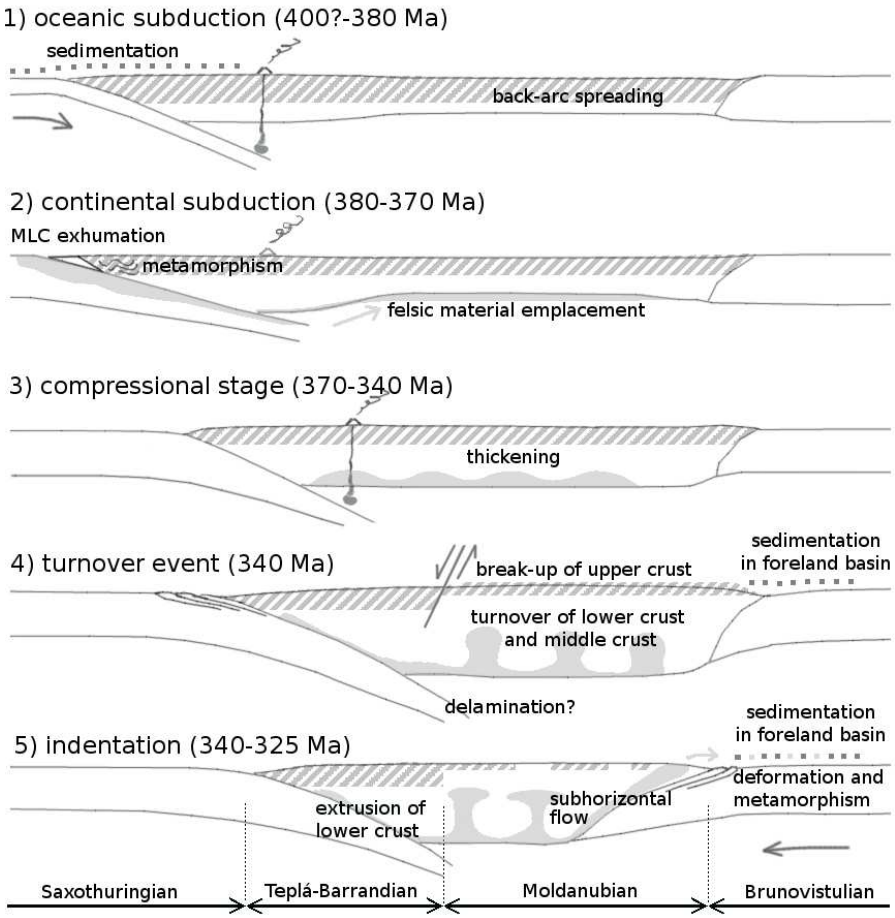

Figure 3.2: Conceptual model of tectonic evolution of the Bohemian Massif during the Variscan orogeny. Modified after Schulmann et al. (2008, 2009) and Lexa et al. (2011) and simplified for the purpose of numerical simulation. 1) Eastward subduction of the Saxothuringian ocean and back-arc spreading in the future Moldanubian domain. 2) Underthrusting of the Saxothuringian continental crust and relamination of the felsic crust in the region of the future Moldanubian domain. 3) The main thickening event and formation of the orogenic root. 4) Laterally forced gravity overturns of the buyoant felsic lower crust and break-up of the upper crustal lid. 5) Indentation of the Brunovistulian associated with channel flow and subhorizontal flow of extruded lower crust.

3.3 Numerical model

3.3.1 Model setting

Our numerical model simulates the compressional and indentation events of the scenario proposed in Section 3.2.2. Although the direction of compression changed from about east-west in the former to about north-south in the latter (or, to be more accurate, from NW-SE to NNE-SSW), we simulate the whole process in two dimensions, that is, we impose the same direction of compression during the whole simulation. This simplification has been adopted to avoid the computational difficulties associated with three-dimensional modeling. The initial geometry of the domain is shown in Fig. 3.3a. The domain consists of two lithospheric blocks representing respectively the Teplá-Barrandian and Moldanubian domains ("orogenic root", left) and the Brunovistulian domain ("indentor", right). In the crustal part of the model domain we solve the full set of equations governing the heat transfer and deformation of chemically heterogeneous visco-plastic crustal material, while in the lower part (lithospheric mantle) we evaluate the temperature field using a kinematically prescribed velocity. Our modeling strategy follows the approach proposed for studying hot orogenes by Beaumont and co-workers (see e.g. Beaumont et al., 2006). This approach allows to study in detail the crustal processes but it simplifies the thermal and mechanical coupling between the crust and mantle and does not properly involve mantle dynamics (the details of which are, however, largely unknown in our case). A discussion of advantages and pitfalls of the crustal models as well as their comparison with upper mantle models can be found in the appendix of Beaumont et al. (2006).

For the solution of the governing equations we use an extended version of the finite element software Elmer (http://www.csc.fi/english/pages/elmer). The computational mesh consists of 20500 bilinear quadrilateral elements, 13000 of which being in the crustal part of the domain. The resolution in the crustal part is approximately 0.7×4 km at the beginning and 1×2 km at the final stage of the time evolution. The left boundary of the model domain is fixed. The right boundary is moving with a constant velocity, mimicking the compression due to the collison with the Saxothuringian plate (stages 3 and 4 in Fig. 3.2) and subsequently the indentation of the orogenic root by a promontory of the Brunovistulian plate (stage 5). The upper boundary of the model is freely deformable which allows the topographic relief resulting from orogenic processes to be predicted. In our model, the topography reflects not only the crustal deformation but also erosion, sedimentation and the isostatic response of the lithosphere to internal and surface loading (for more details, see Section 3.3.3).

The initial lithological stratification (Fig. 3.3b) corresponds to the end of stage 2 in Fig. 3.2, i.e. prior to the thickening of the orogenic root. In the indentor (the Brunovistulian plate), we assume a simple stratification with a strong and dense mafic lower crust, typical of stable continental crust (for values of model parameters, see Table 3.1). In the orogenic root corresponding to the Teplá-Barrandian and the Moldanubian, we consider a more complex structure consisting of three layers. The middle layer corresponds to a relatively stiff and dense mafic rocks that presumably underplated the thinned crust during the Devonian rifting (stage 1 in Fig. 3.2). Below the mafic middle crust, we place an anomalous layer of felsic material characterized by low density, weak rheology and a high content of radiogenic

elements (stage 2 in Fig. 3.2). We assume no lithological differences between the Teplá-Barrandian and the Moldanubian, partly for the sake of simplicity but also because the tectonic relationship between these two domains in the period preceding the main phase of the Variscan orogeny is still unclear. Between the root and the indentor, we prescribe a transition region consisting of an ordinary upper and middle crust. During the evolution of the model, this region helps to accommodate the sharp differences in material properties in the two domains, and thus to reach a more natural state of the system. Most of the material of the transition region is eroded during the thickening stage and it does not influence the indentation stage significantly.

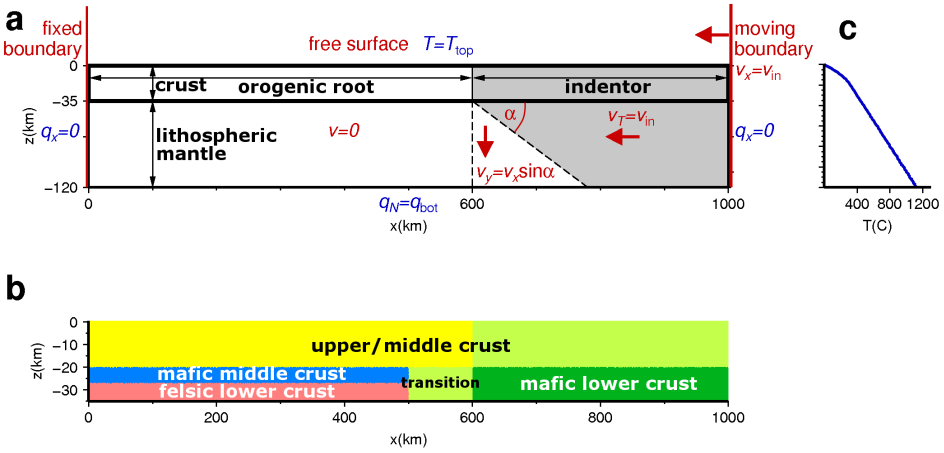

Figure 3.3: **a** Model domain geometry and boundary conditions. The upper boundary is stress-free and it deforms during the evolution of the model. Both left and right boundaries are impermeable. The left boundary is fixed, the right boundary moves to the left with velocity $v_x = v_{\text{in}}$. This velocity is prescribed also at the base of the crust of the indentor, while the velocity is zero at the base of the crust of the orogenic root. The crust-mantle boundary deforms due to isostatic flexure and the shape of the lithospheric mantle follows this deformation. The velocity in the mantle is prescribed as follows: In the indentor, the velocity is tangential to the crust-mantle boundary and its magnitude equals v_{in}. In the wedge below the indentor, $v_x = 0$ and $v_y = \tilde{v}_x \sin\alpha$, where α is 30° and $\tilde{v}_x$ is the x-coordinate of the velocity at the crust-mantle boundary. In the heat equation (2.3), we prescribe temperature T_{top} at the top boundary, heat flux q_{bot} through the bottom boundary and zero heat flux at the side boundaries. **b** Initial material distribution. The total crustal thickness is 35 km, the thickness of the upper/middle crust (yellow and light green), mafic middle crust (blue), felsic lower crust (pink) and mafic lower crust (dark green) is 20 km, 7 km, 8 km and 15 km, respectively. **c** Initial geotherm. It results from a steady-state simulation of heat conduction with heat sources prescribed only in the upper/middle crust and using the same boundary conditions as used for the time evolution – see panel **a**.

Table 3.1: Parameters of the model

Parameter	Symbol	Value
thermal conductivity	k	$2.5\,\mathrm{W m^{-1} K^{-1}}$
specific heat	c_p	$800\,\mathrm{J\,kg^{-1} K^{-1}}$
gravity acceleration	g	$9.81\,\mathrm{m s^{-2}}$
gas constant	R	$8.314\,\mathrm{J K^{-1} m^{-1}}$
mantle density	ρ	$3300\,\mathrm{kg\,m^{-3}}$
flexural rigidity	D	$3 \cdot 10^{22}\,\mathrm{Nm}$
velocity of indentor	v_{in}	$1.5\,\mathrm{cm\,a^{-1}}$
erosion parameter	E	$2.5\,\mathrm{cm\,a^{-1}}$
sedimentation parameter	S	$0.2\,\mathrm{cm\,a^{-1}}$
temperature at the top boundary	T_{top}	273 K
heat flux at the bottom boundary	q_{bot}	$20\,\mathrm{mW\ m^{-2}}$
switch–off temperature of heat sources	T_{off}	1170 K
minimum and maximum viscosity	η_{min}, η_{max}	$10^{18}\,\mathrm{Pa\,s}$, $10^{26}\,\mathrm{Pa\,s}$
reference values of plastic strain	ϵ_0, ϵ_∞	0, 1
cohesion	C	1 MPa
upper/middle crust, sediments:		
initial angle of internal friction	ϕ_0	15°
final angle of internal friction	ϕ_∞	7.5°
mafic middle crust, felsic lower crust, mafic lower crust:		
initial angle of internal friction	ϕ_0	30°
final angle of internal friction	ϕ_∞	15°
upper/middle crust, sediments — quartzite (Hirth et al., 2001):		
viscosity stress exponent	n	4
pre-exponential parameter	B	$1.89 \cdot 10^8\,\mathrm{Pa\,s^{1/n}}$
activation energy	E_A	$135\,\mathrm{kJ\,mol^{-1}}$
density	ρ	$2800\,\mathrm{kg\,m^{-3}}$
heat production	r	$2\,\mu\mathrm{W\,m^{-3}}$
mafic middle crust — plagioclase (Ranalli, 1995):		
viscosity stress exponent	n	3.2
pre-exponential parameter	B	$3.69 \cdot 10^6\,\mathrm{Pa\,s^{1/n}}$
activation energy	E_A	$238\,\mathrm{kJ\,mol^{-1}}$
density	ρ	$3000\,\mathrm{kg\,m^{-3}}$
felsic lower crust — granite (Ranalli, 1995):		
viscosity stress exponent	n	1.9
pre-exponential parameter	B	$2.75 \cdot 10^7\,\mathrm{Pa\,s^{1/n}}$
activation energy	E_A	$137\,\mathrm{kJ\,mol^{-1}}$
density	ρ	$2700\,\mathrm{kg\,m^{-3}}$
heat production	r	$4\,\mu\mathrm{W\,m^{-3}}$
mafic lower crust — basalt (Mackwell et al., 1998, viscosity decreased 10×):		
viscosity stress exponent	n	4.7
pre-exponential parameter	B	$1.91 \cdot 10^4\,\mathrm{Pa\,s^{1/n}}$
activation energy	E_A	$485\,\mathrm{kJ\,mol^{-1}}$
density	ρ	$2900\,\mathrm{kg\,m^{-3}}$

3.3.2 Governing equations, rheological description and material advection

The incompressible flow of crustal material can be described by the following equations:

$$\nabla p - \nabla\cdot\boldsymbol{\sigma} = \rho\mathbf{g}\,, \tag{3.1}$$
$$\nabla\cdot\mathbf{v} = 0\,, \tag{3.2}$$

where p is the pressure, $\boldsymbol{\sigma}$ is the deviatoric stress, ρ is the density, $\mathbf{g}$ is the gravity acceleration and $\mathbf{v}$ is the flow velocity. The density ρ only depends on the material composition c,

$$\rho = \rho(c), \tag{3.3}$$

and the deviatoric stress is a function of the strain-rate $\dot{\boldsymbol{\epsilon}}$, temperature T, pressure and composition,

$$\boldsymbol{\sigma} = \boldsymbol{\sigma}(\dot{\boldsymbol{\epsilon}}, T, p, c). \tag{3.4}$$

The transfer of heat is governed by the following equation:

$$\rho c_p \frac{\mathrm{D}T}{\mathrm{D}t} - \nabla\cdot k\,(\nabla T) = \boldsymbol{\sigma} : \dot{\boldsymbol{\epsilon}} + r\,, \tag{3.5}$$

where $\mathrm{D}/\mathrm{D}t$ denotes the material time derivative, c_p is the heat capacity at constant pressure, t is the time, k is the thermal conductivity and r are additional heat sources. The initial geotherm is plotted in Fig. 3.3c.

We assume non-linear visco-plastic rheology, where plastic deformation approximates brittle failure. The admissible stress in the visco-plastic material is enclosed by the stress envelope defined by

$$\sigma_{\mathrm{II}} = \sigma_{\mathrm{yield}}\,, \tag{3.6}$$

where σ_{yield} is the yield strength of the material and the subscript II denotes the second invariant of a tensor. The functional dependence (3.4) for the visco–plastic material can be expressed in terms of an effective viscosity η_{eff} which depends on temperature, pressure and the second invariant of strain-rate,

$$\boldsymbol{\sigma} = 2\eta_{\mathrm{eff}}\dot{\boldsymbol{\epsilon}}. \tag{3.7}$$

In the viscous regime, i.e. $\sigma_{\mathrm{II}} < \sigma_{\mathrm{yield}}$, we consider non-linear dislocation creep with

$$\eta_{\mathrm{eff}} = B\dot{\epsilon}_{\mathrm{II}}^{1/n-1}\exp\left(\frac{E_{\mathrm{A}}}{nRT}\right)\,, \tag{3.8}$$

where R is the gas constant and B, n and E_{A} are experimentally determined parameters. In the plastic regime, $\sigma_{\mathrm{II}} = \sigma_{\mathrm{yield}}$ and the effective viscosity is

$$\eta_{\mathrm{eff}} = \frac{\sigma_{\mathrm{yield}}}{2\dot{\epsilon}_{\mathrm{II}}}\,. \tag{3.9}$$

For the yield strength of the material we assume the Drucker-Prager yield criterion,

$$\sigma_{\mathrm{yield}} = p\sin\phi + C\cos\phi\,, \tag{3.10}$$

where C is the cohesion and ϕ is the effective angle of internal friction which includes the effect of internal pore-fluid pressure. Both parameters in the Drucker-Prager criterion may depend on strain in a rather complex way. For simplicity, we consider strain-softening characterized by a linear decrease of the effective angle of internal friction with strain (e.g. Buiter et al., 2006)

$$\begin{aligned} \phi &= \phi_0 && \text{if} \quad \epsilon_{\mathrm{II}} \leq \epsilon_0 \,, \\ \phi &= \phi_0 + (\phi_\infty - \phi_0) \left(\frac{\epsilon_{\mathrm{II}} - \epsilon_0}{\epsilon_\infty - \epsilon_0} \right) && \text{if} \quad \epsilon_0 < \epsilon_{\mathrm{II}} < \epsilon_\infty \,, \\ \phi &= \phi_\infty && \text{if} \quad \epsilon_{\mathrm{II}} \geq \epsilon_\infty \,, \end{aligned} \tag{3.11}$$

where ϕ_0, ϕ_∞, ϵ_0 and ϵ_∞ are parameters and ϵ_{II} is the plastic strain obtained by integrating the second invariant of plastic strain-rate along the material trajectory.

The evolution of material composition is treated using the particle-in-cell method in which the material properties are stored in particles advected by the velocity field. Each particle contains information about its composition (which does not change during the evolution) and the accumulated plastic strain (ϵ_{II}). The displacement of the particles from the velocity field is computed by the fourth–order Runge-Kutta method. The material properties in each mesh element are evaluated at integration points by averaging over the particles in the element. The effective viscosity is computed using geometric averaging

$$\log\left(\eta_{\mathrm{eff}}\right) = \sum_{\mathrm{i}} c_i \log\left(\eta_{\mathrm{eff},i}\right), \tag{3.12}$$

while the arithmetic average

$$P = \sum_{\mathrm{i}} c_i P_i \,, \tag{3.13}$$

is used to evaluate the other quantities. In eqs. (3.12) and (3.13), index i denotes the i-th component and c_i is the fraction of the i-th component. To evaluate c_i and the strain $\epsilon_{\mathrm{II},i}$ of the i-th fraction at a point with coordinates $\{x, z\}$ we use the following formulas (cf. Gerya and Yuen, 2003):

$$c_i = \frac{\sum_{mi} w_{mi}}{\sum_m w_m} \,, \quad \epsilon_{\mathrm{II},i} = \frac{\sum_{mi} \epsilon_{\mathrm{II},m_i} w_{mi}}{\sum_{mi} w_{mi}} \,, \tag{3.14}$$

where w are weights, index m_i denotes the particles containing the i-th component and index m is used when summing over all particles in the element. The weight w_m of the particle is computed as follows

$$w_m = \frac{1}{\Delta x^{\max} \Delta z^{\max}} \left(1 - \frac{\Delta x_m}{\Delta x^{\max}} \right) \left(1 - \frac{\Delta z_m}{\Delta z^{\max}} \right) , \tag{3.15}$$

where Δx_m and Δz_m are the distances of the particle from point $\{x, z\}$, and $\Delta x^{\max}$ and $\Delta z^{\max}$ are respectively the maxima of Δx_m and Δz_m over all particles in the element.

3.3.3 Boundary conditions, surface processes and flexural isostasy

At each domain boundary, we impose boundary conditions describing the interaction of the model with the surrounding region. The boundary conditions used in our

model are specified in Fig. 3.3a. The upper boundary of the domain is a free surface: Its shape changes according to the velocity field computed at the surface and is affected by erosion and sedimentation. From the wide range of phenomenological descriptions of erosion on geological timescales (e.g. Montgomery and Brandon, 2002; Martin and Church, 1997) we choose the slope-dependent one,

$$v_{\mathrm{e}}(x) = E|\tan\alpha(x)|\,, \tag{3.16}$$

where v_{e} is the rate of erosion, E is a parameter and the slope $\tan\alpha$ is computed from the topography $h(x)$ of the surface using a linear approximation of its slope on a finite interval. The sedimentation is imposed only in topographic lows and its rate, v_{s}, is proportional to topography:

$$v_{\mathrm{s}}(x) = S\,h(x) \qquad \text{for } h(x) < 0\,, \tag{3.17}$$

$$v_{\mathrm{s}}(x) = 0 \qquad \text{for } h(x) \geq 0\,, \tag{3.18}$$

where S is a parameter. A small amount of local diffusive erosion is employed in order to omit grid-scale oscillations of the free surface. We note that the erosion-sedimentation law used in this study is non-conservative which is in agreement with the use of a two-dimensional model and the assumption that only a part of the eroded material was deposited in the Culm basin while the rest was transported out of the model domain (Hartley and Otava, 2001).

During the time evolution, the shape of the model domain changes significantly and the computational mesh has to be adjusted not only at the boundaries but also inside the domain. For this purpose, the mesh is formally described as a compressible elastic body with the boundaries attached to the model domain boundaries (for review of mesh adaptation methods, see Donea et al., 2004). As the shape of the model domain evolves, the mesh deforms and the positions of its nodes change.

Since the flow equations (3.1)-(3.4) are solved only in the crustal part, the flexure of the lithosphere due to topographic and internal loads cannot be evaluated in a self-consistent manner and it has to be approximated by the deformation of the boundary between the crust and the mantle (Fullsack, 1995). This deformation is computed as a flexure u of a thin elastic beam (Watts, 2001),

$$D\frac{\partial^4 u(x,t)}{\partial x^4} + B(x,t) = L(x,t)\,, \tag{3.19}$$

where D is the flexural rigidity, B is the buoyancy of the crustal root

$$B(x,t) = -u(x,t)\rho g\,, \tag{3.20}$$

with ρ being the density of the lithospheric mantle, and L is the load of the beam,

$$L(x,t) = \int \rho(x,y,t)g\mathrm{d}y - \int \rho(x = x_{\max}, y, t = 0)g\mathrm{d}y\,, \tag{3.21}$$

where $x_{\max}$ is the point at the right end of the beam, and the integrals are evaluated over the whole crustal thickness at times t and 0, respectively. Equation (3.19) is solved analytically using the Fourier method for a beam fixed at the right end. At the end of each time step, we evaluate the difference Δz between the calculated flexure u and the actual shape z_{bot} of the bottom crustal boundary,

$$\Delta z(x,t) = u(x,t) - [z_{\mathrm{bot}}(x,t) - z_{\mathrm{bot}}(x,0)]\,, \tag{3.22}$$

and shift the position of all mesh nodes and particles in the z–direction by this difference, depending on their x–coordinates. As a result, the shape of the crust–mantle boundary satisfies equation of elastic flexure (3.19) at the beginning of the next time step.

3.3.4 Numerical implementation

We use the following computational scheme:

0. initialization of temperature field and particles
1. evaluation of time step
2. interpolation of viscosity and density from particles to integration points and iterative solution of the Stokes problem, eqs. (3.1)-(3.4)
3. interpolation of heat sources and density from particles to integration points and solution of heat equation (3.5)
4. advection of free surface and correction for erosion and sedimentation
5. mesh deformation
6. advection of material particles, integration of plastic strain in particles
7. computation of isostatic flexure and appropriate adjustment of mesh and particles
8. output and return to step 1

For the simulation we use Elmer, an open–source finite–element software suitable for modeling of thermo–mechanical convection in the domain with deforming boundaries using ALE method (Fullsack, 1995; Donea et al., 2004). Elmer itself contains several modules, called solvers, designed for the solution of different types of partial differential equations. The setup of a numerical simulation (i.e. time–stepping, order of solvers, parameters in the solved equations, numerical methods, initial and boundary conditions) is specified in an input text-file. The text-file also serves as an interface for the linking of user-written procedures to Elmer. These external procedures can either provide parameters in the solved equations or they can be separate solvers. In our simulation, we use both possibilities in order to implement the specific properties of crustal deformation (chemical convection, visco-plastic rheology, surface erosion and isostatic compensation). The solution of the partial differential equations in steps 2, 3 and 5 is implemented in the Elmer software, but we evaluate some of the parameters in the equations (viscosity, density and heat sources) in external procedures. We have also developed our own solvers to compute the advection of the free surface and the effects of erosion and sedimentation in step 4, the advection of particles (step 6) and the crustal flexure (step 7). In calculating the advection of particles, several additional procedures are used for a fast search of particles contained in an element. For the time integration of the heat equation we use the backward differentiation scheme of the first order with a variable time-step evaluated using the Courant criterion with a Courant number of 0.1.

The Elmer software has been tested on a number of physical problems in flow dynamics and heat transport, including a series of classical tests for thermal convection with an infinite Prandtl number (e.g. Blankenbach et al., 1989). The main modification of the software, namely the implementation of the compositional convection, was tested on the growth of an isothermal Rayleigh-Taylor instability (e.g. van Keken et al., 1997) and by the sinking cube experiment (Gerya and Yuen, 2003). As a test of our plasticity implementation we used a simple setup described by Lemiale et al. (2008) and Kaus (2009), and a more complicated setup requiring not only plasticity, but also free surface and large mesh deformations described by Buiter et al. (2006). The general setup of our model of a collisional orogen follows the approach of Fullsack (1995). This approach was applied by Vanderheaghe et al. (2003) for the modeling of orogenic wedges and their transition to continental plateaux. We reproduced the results presented by Vanderhaeghe et al. (2003) for several simple cases. The detailed description of the benchmarks together with their results can be found on the web-page http://geo.mff.cuni.cz/∼maipe/research.

3.4 Results

The results of our modeling are presented in Figs 3.4 and 3.5. The series of snapshots in Fig. 3.4a illustrates the evolution of the temperature and composition fields while the corresponding strain rate and flow velocity are depicted in Fig. 3.4b. The model is shown at five unevenly spaced times (t = 16, 26, 29, 33 and 34 Ma after the beginning of the simulation) reflecting the accelerating evolution of the system. The plots zoom in on the crustal part of the model domain and laterally span 500 km (counted from the left fixed boundary). The topographic relief and the lateral variations of erosion and sedimentation rates are detailed in Figs 3.5a-c. In Fig. 3.5d the typical P–T paths predicted by our model are compared with the petrological data published by Schulmann et al. (2008).

We now describe the results in more detail. After 16 Ma of evolution (top panel in Figs 3.4a and b), the right block has moved by more than 200 km to the left, which induced the thickening of the left block to about 45 km and the growth of topography. The topographic plateau is 2-km high on average, with a 4-km peak at the contact of the two blocks (Fig. 3.5a, violet line). The compression of the left block is accommodated by folding of the mafic middle crust (Fig. 3.4a, blue), by motion on several shear zones developed in the upper crust and by viscous flow in the felsic lower crust (Fig. 3.4b). At this stage, the felsic lower crust is heated to about 600 °C mostly due to the internal heat sources, as it is indicated by the geometry of isotherms following the shape of the layer (Fig. 3.4a).

At 26 Ma (second panel in Figs 3.4a and b), the orogenic root at the left is 60-km thick and it has a 5-km high plateau (Fig. 3.5a, green line). A part of the orogenic root is loading the left end of the right crustal block and causes its bending, which leads to the development of a topography low some 100–200 km to the right from the peak topography (Fig. 3.5a, green line) and deposition of first sediments (Fig. 3.5c, green line). The erosion pattern (Fig. 3.5b, green line) at this stage is rather complex and shows large lateral variations. The maximum erosion rates are obtained at the contact of the two crustal blocks, while the orogenic plateau is characterized by low erosion. This spatial distribution of erosion rates is also typical for the subsequent stages of the evolution. The internal deformation of the root concentrates in the

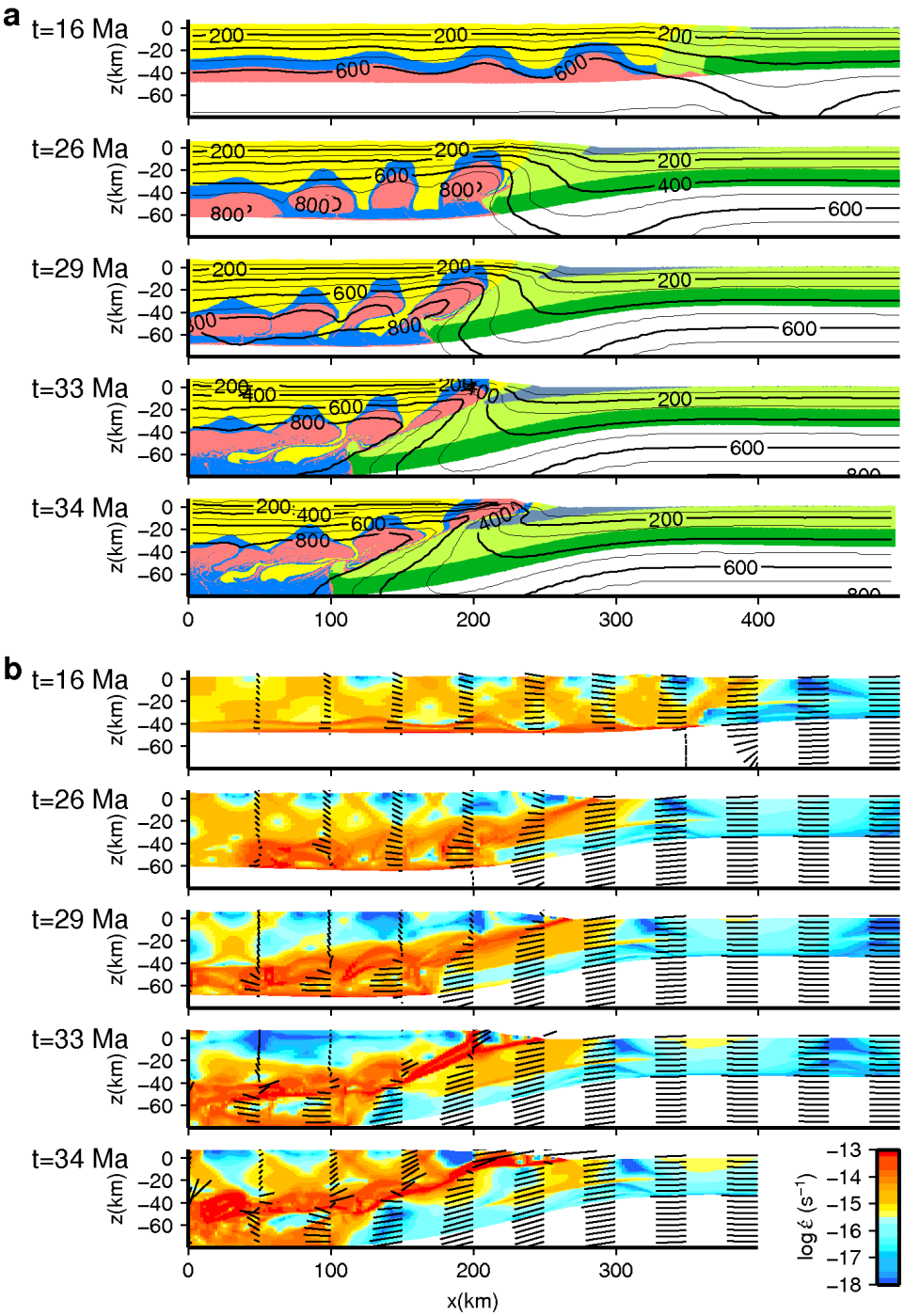

Figure 3.4: Model evolution in five representative time steps. **a** Composition and temperature fields. The colors are the same as in Fig. 3.3, sediments are plotted in gray. The isotherms are plotted every 100 °C and labeled every 200 °C. **b** Strain-rate and flow velocity fields. Sticks show the magnitude and direction of velocity.

lower and middle part of orogenic root where the dense middle crustal material sinks to regions originally occupied by light felsic rocks, forming a new mafic layer at the base of the crust, while "blobs" of the felsic material gradually rise up to shallow crustal levels. The temperature in the felsic lower crust increases up to 800 °C in some points.

In the next stage (29 Ma, third panel in Figs 3.4a and b), the indentation process begins to play an important role. The tip of the right block plunges beneath the orogenic root and causes flattening of the upwellings of felsic material and their mechanical decoupling from the lower part of the root. The material above the felsic lower crust is not involved in the deformation and forms a stiff lid (blue in Fig. 3.4b). The temperature field is characterized by progressive heating of the felsic lower crust and the development of an inverse temperature gradient in the indentor due to a lateral flow of hot material towards the right at middle crustal levels.

Around 33 Ma (fourth panel from top in Figs 3.4a and b, red line in Fig. 3.5a), the orogenic root reaches the maximum thickness exceeding 70 km and its evolution speeds up. A subhorizontal channel of flowing material connects the depths of about 40 km inside the root with the surface and the upwellings of the felsic lower crust are about to reach the surface. At 34 Ma (bottom panels in Figs 3.4a and b), the flow in the channel is accompanied by disruption of the crustal lid into several independently moving blocks. The blocks near the right edge of the orogenic plateau start moving quickly in the opposite direction than the indentor (see the velocity field in Fig. 3.4b) which results in the shift of the edge and the adjacent foredeep to the right with respect to the previous snapshot (Fig. 3.5a, black vs. red line). The process is accompanied by deepening of the sedimentary basin and intense sedimentation (Fig. 3.5c). The basin is now about 2-km deep and the thickness of the sediments reaches to 5–10 km. A part of the sediments is pushed down under the exhumed lower crustal material and deformed.

At the final stage of the simulation we can recognize three lens-shaped regions of the former felsic lower crust. One of them has reached the surface, the second one is being exhumed along a ramp formed by the indentor, and the third one remains at a depth of 40–50 km in the left part of the orogenic root. Most of the former mafic middle crust is now located above the crust-mantle boundary, while the rest of it can still be found on top of the three felsic regions described above. A part of the former felsic upper crust is trapped at a depth of 50–60 km and its temperature exceeds 800 °C. The temperature at the contact between the indentor and the orogenic root is about 600 °C at 20-km depth and 700 °C at 30-km depth. The temperature of the orogenic root below a depth of 40 km is ∼800 °C.

Figure 3.5d shows several P–T paths typical of the orogenic crust in our model. The green, red and blue paths correspond to felsic rocks originally forming the lower crust which are eventually found in the first, second and third felsic region from the right, respectively, discussed in the previous paragraph. All these P–T paths show an initial increase of pressure and temperature due to the thickening and warming of the orogenic root, followed by fast decompression associated with exhumation during the indentation stage. The green path bears witness of complete exhumation to the surface, with a maximum pressure of 14 kbar and maximum temperature of 800 °C attained during the ascent phase.

The red path, illustrating the P–T history of the second felsic region, records higher peak pressure conditions (16 kbar) followed by nearly isothermal (840 °C)

decompression to 9 kbar. At this point, the green and red paths meet, and we may expect that if the evolution continued, the "red" particle would be decompressed along a similar path as the "green" one. In the deepest felsic region, the peak pressure and temperature are even higher (18 kbar and 900 °C, respectively), but the decompression stage is short and the final pressure is relatively high (12 kbar). The black path depicts the evolution of a middle crustal rock which first moves down and plunges into the felsic lower crust and then is captured by the subhorizontal flow above the indentor. After reaching the peak conditions of 9 kbar and 750 °C, the pressure and temperature in this rock slightly decrease to 8 kbar and 700 °C. At these P–T conditions, the black and green paths meet, similarly to the red and green paths which, however, meet at somewhat higher pressure and temperature. The pressure and temperature of about 8–9 kbar and 700–800 °C, respectively, thus can be regarded as typical P–T conditions of the flow above the indentor, independently of the type of rock and its origin.

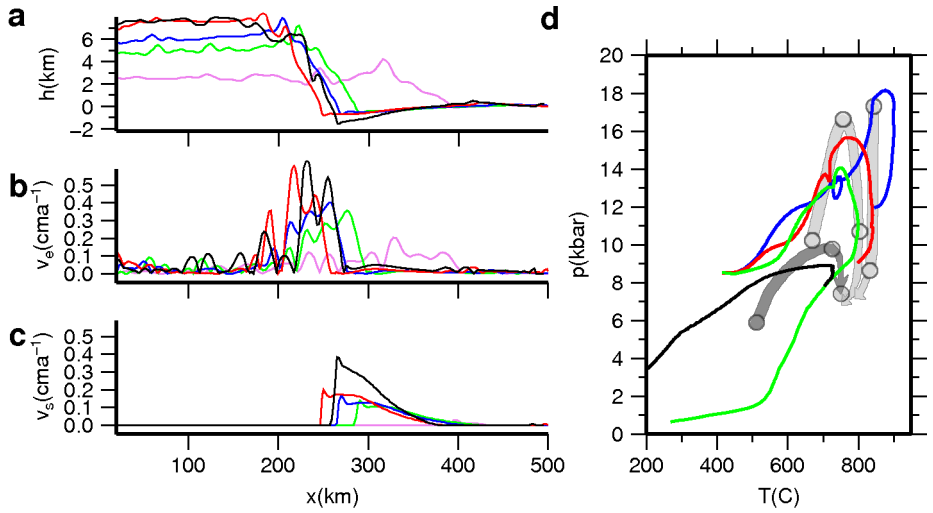

Figure 3.5: Profiles of topography (**a**), rate of erosion (**b**) and rate of sedimentation (**c**) for the same times as in Fig. 3.4. Violet, green, blue, red and black lines correspond to 16, 26, 29, 33 and 34 Ma of evolution, respectively. **d)** P–T paths for selected material particles of felsic lower crust (green, red and blue line) and middle crust (black). The observed P–T paths for rock samples from the orogenic lower and middle crust (Schulmann et al., 2008) are shown in light and dark gray, respectively.

3.5 Discussion

We now compare the basic characteristics of our model with the geological constraints discussed in Section 3.2 and assess how much our modeling effort meets the goals set up in Subsection 3.2.2. Our numerical simulation covers some 35 Ma of geological evolution and the initial setting of our model corresponds to the geological situation in the Bohemian Massif at the beginning of the compressional phase at about 370 Ma ago. In our model the compression phase takes about 25 Ma and thus can be identified with an age range of 370–345 Ma on the geological time scale. The turnover period occurring in the Moldanubian between about 345 Ma and 335 Ma (with a peak activity at about 340 Ma) then corresponds to model times of 25–35 Ma.

As follows from comparison of modelled and measured P–T paths in Fig. 3.5d, the model described in the previous section predicts rather well the P–T conditions of the formation of granulites and their fast exhumation. After some 20–25 million years of compression, during which the Moldanubian domain is gradually thickened (up to about 60 km) and its bottom felsic layer is heated up (to more than 800 °C) and significantly weakened, the modelled system reaches a critical point in its evolution and its unstable density layering is reversed. This turnover is characterized by avalanche-like downwellings of the upper and middle crustal material and fast ascent of the lower crust leading to the redistribution of the mass to a gravitationally more stable position. The time needed for the granulites to get from a depth of 50–60 km to shallow crustal levels is just a few millions of years. This time is comparable with that predicted for the delamination process (Arnold et al., 2001) which is often considered to be the only effective mechanism for granulite exhumation.

The material structure during the turnover event is rather complex showing large lateral variations in material composition. A part of the mafic middle crust is passively carried by the lower-crustal bodies up to near the surface while blobs of the upper crustal material are pulled into the deep crust and heated up to 700–850 °C, thus to temperatures near the partial melting point. This pattern is consistent with the P–T paths of the granulites and the middle crustal material presented in Schulmann et al. (2008) and also with the structure of the Moldanubian domain which shows two NNE-SSW trending belts of high-grade metamorphic rocks with the Central Moldanubian Pluton located in between them.

As demonstrated in the previous section, the flow of the crustal material was further boosted by indentation of the Brunovistulian lower crust. This process leads to a gradual change of relative flow direction from vertical, prevailing at the beginning of the turnover event, to horizontal, characteristic of its later phase. This change of the flow direction is in agreement with the deformation history of the Moldanubian domain inferred from structural data.

The evolution of topographic relief in our model roughly agrees with the geological record from the Culm Basin containing sediments younger than about 345 Ma. This age is likely to correspond to the beginning of the rapid topographic uplift of the Moldanubian domain accompanied by intense erosion at the eastern slope of the topographic plateau. In our model, the initial compression of the domain leads to intense crustal thickening but to only limited erosion and sedimentation. During most of the compression phase, the slope of the topography remains rather small and there is no pronounced depression where sediments could be deposited. The situation changes after about 25 Ma of evolution ($\sim$345 Ma on the geological time scale) when a topographic plateau with a steep eastern slope develops. This leads to intense erosion and sedimentation which is enhanced due to the rapidly descending foredeep formed at the western margin of the Brunovistulian domain.

It is worth noting that the western block of the model domain does not deform uniformly. The upper crust in the left part of this block, roughly corresponding to the present Teplá-Barrandian domain, remains basically untouched by the processes taking place in the lower-crustal levels. The composition and temperature structures of this region are only weakly affected by the material upwellings evolving deep in the orogenic root and by the deformation zone developed at the contact with the Brunovistulian plate. It is tempting to speculate that this dichotomy reflects the observed differences in geological characteristics between the Teplá-Barrandian and

the Moldanubian as mentioned in Section 3.2.

The physical process simulated by our model is strongly non-linear and depends on a large number of model parameters as well as the initial and boundary conditions. Besides the parameters used in the model run discussed in this section, we have tested several other combinations of model parameters to better understand the behaviour of the system and to determine those physical characteristics that are crucial for its evolution. From the physical point of view, the process can be split into three major stages: folding, diapirism and indentation. The stages build on each other with the processes in earlier stages determining the subsequent evolution. In general, different sets of model parameters can produce models which significantly differ in timing and geometry. Figure 3.6 illustrates the role of three parameters that can strongly influence the evolution of the modelled system, namely the heat productivity of the lower crust, the rate of erosion and the velocity of shortening and indentation. The dependence of the model on the rheological properties of the individual layers will be discussed in more details in a further study.

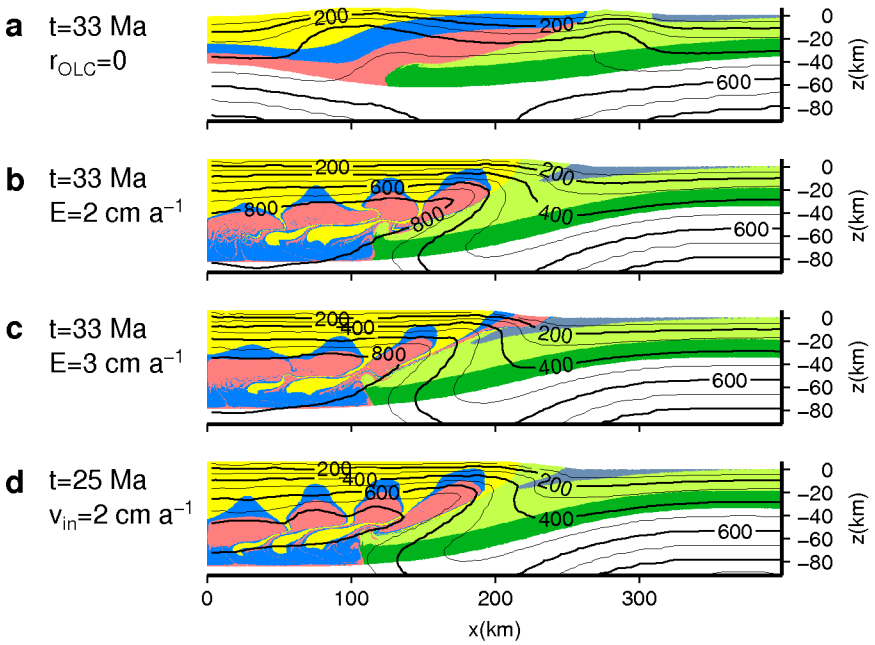

Figure 3.6: Examples of models with different parameters. In model **a**, the radiogenic heating in the felsic lower crust is switched off and rheological parameters are the same as for upper crust. As a consequence, the lower crust is colder and stronger, the mafic middle crust is only gently folded and a simple doubly vergent wedge is developped. Models (**b**) with lower and (**c**) higher erosion rate differ in the overall thickness of the crust and in the timing of exhumation of the lower crust. While in the model with $E = 2\,\mathrm{cm/a}$ the felsic lower crust stays deeper than 20 km after 33 Ma of evolution, in the model with $E = 3\,\mathrm{cm/a}$ one of the felsic bodies is already exhumed and almost eroded (see the thin pink layer at the surface at the contact of the two crustal blocks). In model **d**, the effect of a higher velocity of shortening ($v_{\mathrm{in}} = 2\,\mathrm{cm/a}$) is illustrated. The model is shown already after 25 Ma of evolution when the displacement of the indenting crustal block is approximately the same as in the reference model (with $v_{in} = 1.5\,\mathrm{cm/a}$) after 33 Ma. The faster model is slightly colder and the exhumation is less efficient than in the reference model. All parameters that were not mentioned here are the same as in the reference model (see Table 3.1).

We will now briefly discuss the basic physical mechanisms controlling the individual stages of the model evolution. The folding of a viscous layer embedded in a medium of lower viscosity and subject to layer-parallel shortening is a classical problem of continuum physics. In the simplest case of a single layer, the wavelength of folding is proportional to the layer thickness and increases with the viscosity contrast between the layer and the medium (e.g. Turcotte and Schubert, 2002). In our model, the formal analysis of the folding process is complicated by the fact that the viscosities of the layers vary in time due to the evolution of temperature and strain rate and the uppermost layer exhibits plastic (brittle) behavior. Nevertheless, the results of our runs indicate that the above rule is still more or less valid and it can help us to guide our intuition in analyzing the first stage of evolution of our system. The folding in our model is mostly controlled by the viscosity and the thickness of the layer forming the mafic middle crust, and by the viscosity contrast between this layer and the felsic lower crust. If we switch off the radiogenic heating in the lower crust and use the same rheological properties for the felsic lower crust as for the upper crust, the viscosity contrast between the lower and the middle crust remains rather small during the whole evolution and the middle crustal layer is not folded (Fig. 3.6a). In contrast, if we increase the viscosity of the mafic layer and keep the radiogenic heating in the bottom layer, we obtain a model with even more pronounced folds than in the case presented in Fig. 3.4 but with longer wavelengths. The results of our numerical experiments (not shown here because of the lack of space) clearly show that the initial folding stage is crucial for the further evolution of the system. In the absence of compression (and hence folding), the Rayleigh-Taylor instability of the light felsic lower crust overlain by the denser middle crust is still present. However, the rate of its growth is low because of small (zero) perturbation of the interface between the two layers (cf. also equation 6-156 in Turcotte and Schubert, 2002). As a consequence, the time necessary for the lower crust to reach the surface is much larger than the time scale of the observed geological events.

The Rayleigh-Taylor instabilities developed during the folding stage promote the subsequent diapirism of the light lower crust which is further boosted by continuing lateral shortening of the domain. The geometry of diapirs depends on the size of the previously developed folds, on the material properties of the visco-plastic upper crust and, in the later stage, also on the rate of shortening and erosion (which draws the lower crustal material to areas with the steepest topographic slope).

The final stage is characterized by interaction of the diapirs with a moving crustal wedge. The wedge is relatively stiff and its tip penetrates into the bottom part of the thickened domain. The behavior of the system at this stage is very complex and depends on the choice of the model parameters in a non-trivial way. The shear zone developed at the contact between the wedge and the orogenic root is usually transformed to a subhorizontal low-viscosity channel connecting the lower crust with the surface. The flow in this channel is further enhanced by surface erosion and may take the form of a few pulses characterized by strikingly high exhumation rates. The results of simulations with different rates of erosion and shortening velocity are shown in Fig. 3.6b-d. The flow velocity field in the vicinity of the channel has a large rotational component which induces intense mixing of the uprising crustal material, resulting in a complex compositional pattern at the surface.

3.6 Concluding remarks

The Variscan structure of the Bohemian Massif is characterized by the presence of numerous felsic granulite bodies which presumably originate from the same protolith (Saxothuringian upper crust) and show similar metamorphic ages (∼340 Ma). Petrological analysis of the granulites from the Moldanubian zone of the Bohemian Massif suggests that these rocks were buried to deep crustal levels (50–60 km), heated up (to 750–850 °C) and then rapidly exhumed. The timing of the exhumation event roughly coincides with the initial stage of orogenic uplift as well as the durbachitic magmatism, bearing evidence of melting in the upper mantle. These processes clearly required a large amount of energy and an effective physical mechanism of its transfer to the crust. For many researchers, delamination of the lithosphere is the only process which could provide a sufficient amount of heat in a short time scale and trigger the crustal overturn documented in the geological record of the Bohemian Massif. In the present paper, we demonstrate that the overturn event may have different causes and could be induced by the combined effects of radiogenic heating in the (relaminated) felsic lower crust, the lateral contraction of the domain due to the collision with the Saxothuringian plate and the later indentation of the Brunovistulian basement. Although the radiogenic heating plays a crucial role in our model, it is worth emphasizing that the system is mainly deformed due to the contraction and indentation. In other words, the radiogenic heat is only a part of the energy needed for the overturn event to occur, and the other part is the mechanical energy of plate tectonic origin.

Our model is simplified in a number of respects: The complex three-dimensional process of the Variscan orogeny is simulated in two dimensions and the contraction of the domain is controlled "by the hand of God." The thermal evolution of the system includes neither convective heat transfer in the mantle lithosphere, nor temporal and lateral variations of the heat flux from the asthenosphere. Melting processes and associated latent heat release and absorption, as well as magma percolation can also influence the resultant temperature field in a non-negligible way. It is possible that the initial temperature field was significantly affected by the processes responsible for the emplacement of the Saxothuringian upper crustal material under or near the base of the Moldanubian crust. The temperature predicted by our model in the mantle lithosphere is obviously too low to account for partial melting of mantle material which has been suggested by the petrological analysis of durbachites. This indicates that the role of convective processes in the mantle, including, for example, partial delamination or anomalous heat flux from the subduction wedge, may have been substantial. These issues will be addressed in a future study.

Acknowledgments:
The work was supported by grants GAUK No. 432911 and SVV-2012-265308. Ondrej Lexa was also supported by the research grant from the Czech Science Foundation GACR 205/09/1041 and the Ministry of Education, Youth and Sports of the Czech Republic Research Plan No. MSM0021620855. Finite-element computations were performed using the Elmer software developed by the CSC—IT Center for Science (http://www.csc.fi/english/pages/elmer). The authors thank Taras Gerya and an anonymous reviewer for critical comments, Susanne Buiter for helpful suggestions on numerical model setup, and Craig Bina for careful reading of the manuscript.

3.7 References

Arnold J., Jacoby W.R., Schmeling H. and Schott B., 2001. Continental collision and the dynamic and thermal evolution of the Variscan orogenic crustal root - numerical models. *J. Geodyn.*, **31**, 273–291.

Babuška V., Plomerová J. and Vecsey L., 2008. Mantle fabric of western Bohemian Massif (central Europe) constrained by 3D seismic P and S anisotropy. *Tectonophysics*, **462**, 149–163.

Beard B.L., Medaris L.G., Johnson C.M., Jelínek E., Tonika J. and Riciputi L.R., 1995. Geochronology and geochemistry of eclogites from the Marianske Lazne Complex, Czech Republic - Implications for Variscan orogenesis. *Geol. Rundsch.*, **84**, 552–567.

Beaumont C., Jamieson R.A., Nguyen M.H. and Lee B., 2001. Himalayan tectonics explained by extrusion of a low-viscosity crustal channel coupled to focused surface denudation. *Nature*, **414**, 738–742.

Beaumont C., Jamieson R.A., Nguyen M.H. and Ellis S., 2006. Crustal flow models in large hot orogens. *Geological Society, London, Special Publications*, **268**, 91–145, doi: 10.1144/GSL.SP.2006.268.01.05.

Bielik M., Kloska K., Meurers B., Švancara J., Wybraniec S., Fancsik T., Grad M., Grand T., Guterch A., Katona M., Krolikowski C., Mikuška J., Pašteka R., Petecki Z., Polechońska O., Ruess D., Szalaiová V., Šefara J. and Vozár J., 2006. Gravity anomaly map of the CELEBRATION 2000 region. *Geol. Carpath.*, **57**, 145–156.

Blankenbach B., Busse F., Christensen U., Cserepes L., Gunkel D., Hansen U., Harder H., Jarvis G., Koch M., Marquart G., Moore D., Olson P., Schmeling H. and Schnaubelt T., 1989. A benchmark comparison for mantle convection codes. *Geophys. J. Int.*, **98**, 23–38.

Buiter S.J.H., Babeyko A.Y., Ellis S., Gerya T.V., Kaus B.J.P., Kellner A., Schreurs G. and Yamada Y., 2006. The numerical sandbox: Comparison of model results for a shortening and an extension experiment. In: Buiter S.J.H. and Schreurs G. (Ed.), *Analogue and Numerical Modelling of Crustal–Scale Processes*. Geological Society, London, 29–64.

Burov E. and Yamato P., 2008. Continental plate collision, P–T–t–z conditions and unstable vs. stable plate dynamics: Insights from thermo-mechanical modelling. *Lithos*, **103**, 178–204.

Dallmeyer R.D. and Urban M., 1998. Variscan vs Cadomian tectonothermal activity in northwestern sectors of the Tepla-Barrandian zone, Czech Republic: constraints from Ar-40/Ar-39 ages, *Geol. Rundsch.*, **87**, 94–106.

Donea J., Huerta A., Ponthot J.-P. and Rodríguez–Ferran A., 2004. Arbitrary Lagrangian–Eulerian Methods. In: Stein E., de Borst R. and Hughes T. (Ed.), *Encyclopedia of Computational Mechanics, Volume 1: Fundamentals*. Wiley, 413–437.

Dörr W. and Zulauf G., 2010. Elevator tectonics and orogenic collapse of a Tibetan-style plateau in the European Variscides: the role of the Bohemian shear zone. *Int. J. Earth Sci. (Geol. Rundsch.)*, **99**, 299–325.

Duretz T.M., Kaus B.J.P., Schulmann K., Gapais D. and Kermarrec J.-J., 2011. Indentation as an extrusion mechanism of lower crustal rocks in the Eastern Bohemian Massif: Insight from analogue and numerical modelling. *Lithos*, **124**, 158–168.

Faccenda M., Gerya T.V. and Chakraborty S., 2008. Styles of post-subduction collisional orogeny: Influence of convergence velocity, crustal rheology and radiogenic heat production. *Lithos*, **103**, 257–287.

Finger F., Roberts M.P., Haunschmid B., Schermaier A. and Steyrer H.P., 1997. Variscan granitoids of central Europe: their typology, potential sources and tectonothermal relations. *Mineral. Petrol.*, **61**, 67–96.

Franke W., 2000. The mid-European segment of the Variscides: tectonostratigraphic units, terrane boundaries and plate tectonic extension. In: Franke W., Altherr R., Haak V., Oncken O. and Tanner D. (Eds.), *Orogenic Processes: Quantification and Modelling in the Variscan Belt*. Geol. Soc. London, Spec., **179**, 35–61.

Fritz H., Dallmeyer R.D. and Neubauer F., 1996. Thick-skinned versus thin-skinned thrusting: Rheology controlled thrust propagation in the Variscan collisional belt (The Southeastern Bohemian Massif, Czech Republic - Austria). *Tectonics*, **15**, 1389–1413.

Fullsack P., 1995. An arbitrary Lagrangian-Eulerian formulation for creeping flows and its application in tectonic models. *Geophys. J. Int.*, **120**, 1–23.

Gerdes A., Worner G. and Henk A., 2000. Post-collisional granite generation and HT-LP metamorphism by radiogenic heating: the Variscan South Bohemian Batholith. *J. Geol. Soc.*, **157**, 577–587.

Gerya T.V. and Yuen D.A., 2003. Characteristics-based marker-in-cell method with conservative finite-differences schemes for modeling geological flows with strongly variable transport properties. *Phys. Earth Planet. Inter.*, **140**, 293–318.

Gerya T.V., Perchuk L.L. and Burg J.-P., 2008. Transient hot channels: Perpetrating and regurgitating ultrahigh-pressure, high-temperature crust-mantle associations in collision belts. *Lithos*, **103**, 236–256.

Guy A., Edel J.-B., Schulmann K., Tomek, Č. and Lexa O., 2011. A geophysical model of the Variscan orogenic root (Bohemian Massif): Implications for modern collisional orogens. *Lithos*, **124**, 144–157.

Hacker B.R., Kelemen P.B. and Behn M.D., 2011. Differentiation of the continental crust by relamination. *Earth Planet. Sci. Lett.*, **307**, 501–516.

Hartley A.J. and Otava J., 2001. Sediment provenance and dispersal in a deep marine foreland basin: the Lower Carboniferous Culm Basin, Czech Republic. *J. Geol. Soc. London*, **158**, 137–150.

Hirth G., Teyssier C. and Dunlap W.J., 2001. An evaluation of quartzite flow laws based on comparisons between experimentally and naturally deformed rocks. *Int. J. Earth Sci.*, **90**, 77–87.

Hrubcová P., Sroda P., Špičák A., Guterch A., Grad M., Keller G.R., Brueckl E. and Thybo, H., 2005. Crustal and uppermost mantle structure of the Bohemian Massif based on CELEBRATION 2000 data. *J. Geophys. Res.*, **110**, B11305.

Janoušek V., Bowes D.R., Rogers G., Farrow C.M. and Jelínek E., 2000. Modelling diverse processes in the petrogenesis of a composite batholith: the Central Bohemian Pluton, Central European Hercynides. *J. Petrol.*, **41**, 511–543.

Kaus B., 2009. Factors that control the angle of shear bands in geodynamic numerical models of brittle deformation. *Tectonophysics*, **484**, 36–47.

Kotková J., O'Brien P.J. and Ziemann M.A., 2011. Diamond and coesite discovered in Saxony-type granulite: Solution to the Variscan garnet peridotite enigma. *Geology*, **39**, 667–670.

Lemiale V., Mühlhaus H.-B., Moresi L. and Stafford J., 2008. Shear banding analysis of plastic models formulated for incompressible viscous flows. *Phys. Earth Planet. Inter.*, **171**, 177–186.

Lexa O., Schulmann K., Janoušek V., Štípská P., Guy A. and Racek M., 2011. Heat sources and trigger mechanisms of exhumation of HP granulites in Variscan orogenic root. *J. Metamorph. Geol.*, **29**, 79–102.

Mackwell S.J., Zimmerman M.E. and Kohlstedt D.L., 1998. High-temperature deformation of dry diabase with application to tectonics on Venus. *J. Geophys. Res.*, **103**, 975–984.

Martin Y. and Church M., 1997. Diffusion in landscape development models: On the nature of basic transport relations. *Earth Surf. Process. Landf.*, **22**, 273–279.

Massonne H.J., 2006. Early metamorphic evolution and exhumation of felsic high-pressure granulites from the north-western Bohemian Massif. *Mineral. Petrol.*, **86**, 177–202.

Montgomery D.R. and Brandon M.T., 2002. Topographic controls on erosion rates in tectonically active mountain ranges. *Earth Planet. Sci. Lett.*, **201**, 481–489.

Ranalli G., 1995. *Rheology of the Earth, 2nd Edn.* Chapman and Hall, London, United Kingdom.

Schulmann K., Konopásek J., Janoušek V., Lexa O., Lardeaux J.-M., Edel J.-B., Štípská P. and Ulrich S., 2009. An Andean type Palaezoic convergence in the Bohemian Massif. *C. R. Geoscience*, **341**, 266–286.

Schulmann K., Lexa O., Štípská P., Racek M., Tajčmanová L., Konopásek J., Edel J.-B., Peschler A. and Lehmann J., 2008. Vertical extrusion and horizontal channel flow of orogenic lower crust: key exhumation mechanisms in large hot orogens? *J. Metamorph. Geol.*, **26**, 273–297.

Sobolev S.V. and Babeyko A.Y., 2005. What drives orogeny in the Andes? *Geology*, **33**, 617–620.

Steltenpohl M.G., Cymerman Z., Krogh E.J. and Kunk M.J., 1993. Exhumation of eclogitized continental basement during Variscan lithospheric delamination and gravitational collapse, Sudety Mountains, Poland. *Geology*, **21**, 1111–1114.

Štípská P. and Schulmann K., 1995. Inverted metamorphic zonation in a basement-derived nappe sequence; eastern margin of the Bohemian Massif. *Geol. J.*, **30**, 385–413.

Timmermann H., Dörr W., Krenn E., Finger F. and Zulauf G, 2006. Conventional and in situ geochronology of the Teplá crystalline unit, Bohemian Massif: implications for the processes involving monazite formation. *Int. J. Earth Sci.*, **95**, 629–647.

Turcotte D.L. and Schubert G., 2002. *Geodynamics, 2nd Edn.* Cambridge University Press. Cambridge, United Kingdom.

van Keken P.E., King S.D., Schmeling H., Christensen U.R., Neumeister D. and Doin M.-P., 1997. A comparison of methods for the modeling of thermomechanical convection. *J. Geophys. Res.*, **102**, 22477–22495.

Vanderhaeghe O., Medvedev S., Fullsack P., Beaumont C. and Jamieson R.A., 2003. Evolution of orogenic wedges and continental plateaux: insights from crustal thermal-mechanical models overlying subducting mantle lithosphere. *Geophys. J. Int.*, **153**, 27–51.

Watts A.B., 2001. *Isostasy and Flexure of the Lithosphere.* Cambridge University Press. Cambridge, United Kingdom.

Willner A.P., Sebazungu E., Gerya T.V., Maresch W.V. and Krohe A., 2002. Numerical modelling of PT-paths related to rapid exhumation of high-pressure rocks from the crustal root in the Variscan Erzgebirge Dome (Saxony, Germany). *J. Geodyn.*, **33**, 281–314.

Winchester J.A. and PACE TMR Network Team, 2002. Palaeozoic amalgamation of Central Europe: new results from recent geological and geophysical investigations. *Tectonophysics*, **360**, 5–21.

Zulauf G., 2001. Structural style, deformation mechanisms and paleodifferential stress along an exposed crustal section: constraints on the rheology of quartzofeldspathic rocks at supra- and infrastructural levels (Bohemian Massif). *Tectonophysics*, **332**, 211–237.

Žák J., Holub F. and Verner K., 2005. Tectonic evolution of a continental magmatic arc recorded by multiple episodically emplaced magma pulses: the Central Bohemian Plutonic Complex (Bohemian Massif, Czech Republic). *Int. J. Earth Sci.*, **94**, 385–400.

Chapter 4

Contrasting tectono-metamorphic evolution of orogenic lower crust in the Bohemian Massif: a numerical model

Published in Gondwana Research, doi: 10.1016/j.gr.2012.08.020, 2012.

Petra Maierová[1], Ondrej Lexa[2], Karel Schulmann[3,4] and Pavla Štípská[3,4]

[1]Department of Geophysics, Faculty of Mathematics and Physics, Charles University, Prague, Czech Republic
[2]IPSG, Faculty of Science, Charles University, Prague, Czech Republic
[3]Center for Lithospheric Research, Czech Geological Survey, Prague, Czech Republic
[4]EOST, Université de Strasbourg, Strasbourg, France

Abstract

The Bohemian Massif, located at the eastern margin of the European Variscan belt, is characterised by an exceptional accumulation of felsic high-pressure granulites. The petrological, structural and geochronological studies of this region revealed systematic differences between the tectonometamorphic evolution of the southern (Moldanubian) and northern (West Sudetes) parts of the orogen. Two contrasting tectonic scenarios have been proposed: gravity-driven vertical mass exchanges followed by continental indentation in the Moldanubian domain, and crustal-scale folding leading to gneiss dome formation in the West Sudetes. We present a numerical model in order to correlate the apparent differences between these two regions with the variations in the dynamics of the modelled system. We model two colliding blocks: an orogenic root, where a felsic lower crust is overlain by a mafic layer and a middle crust, and a continental indentor. We examine the role of the rate of convergence of the two blocks, radiogenic heat production within the felsic lower crust and efficiency of erosion. The prograde part of the metamorphic evolution is controlled by the rate of convergence and the peak temperature depends on the heat production. The retrograde evolution is controlled mostly by erosional processes. In the models, where the material is weakened due to the heating in the

felsic lower crust, the gravitational instability of the mafic and felsic layers causes their complete vertical exchange followed by a flow above the indentor. In colder and/or faster models, the thickening is dominated by the buckling of the mafic layer. These two styles of deformation, i.e. gravity-dominated and fold-dominated models, correspond to the structures observed in the Moldanubian and the West Sudetes. Moreover, the calculated pressure-temperature paths of the felsic lower crust are in agreement with available data.

Keywords: felsic lower crust, PT evolution, numerical model, Bohemian Massif

Graphical abstract

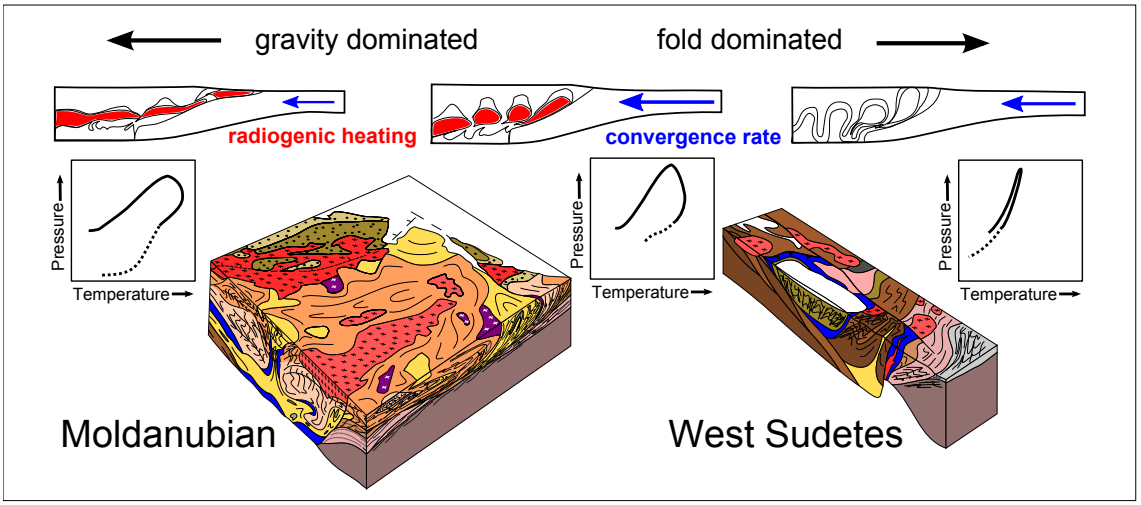

4.1 Introduction

Recent progress in mineral equilibria modelling and geochronological methods allowed more accurate determination of pressure–temperature–time (P–T–t) paths. The P–T–t paths represent the basic tool for understanding orogenic processes and constraining thermal evolution as well as time-scales of deformation and metamorphism in orogens (England and Thompson, 1984). The P–T evolutions observed in different orogenic systems exhibit common features that are characteristic for distinct types of orogens, such as large hot collisional orogens (Jamieson et al., 2004), paired metamorphic belts (Brown, 2010) or subduction-related cold orogenic systems (Duchene et al., 1997). In addition, Brown (2006, 2007) pointed out systematic differences between P–T arrays of Archean, Proterozoic and Phanerozoic orogenic systems. Rocks related to high- to ultra-high-temperature (HT–UHT) metamorphism are granulites which occur since the Archean and are dominant metamorphic rocks in Proterozoic orogens. The granulites typical for the Archean to Early Proterozoic period are characterized by average dP/dT trends (Harley, 2008). Since the late Proterozoic new branches of high- and low-pressure granulitic rocks have developed, suggesting a major change in plate tectonic dynamics. While the low-pressure granulites are attributed to backarcs and continental or oceanic magmatic arcs (Brown, 2007), the mechanism of formation of high-pressure (HP) granulites remains debated. The HP granulites are chiefly described from fossil orogenic belts, such as the Proterozoic Grenville orogeny in Canada (Jamieson et al., 2007), the Paleozoic European Variscan belt (Pin and Vielzeuf, 1983), and only recently from the Tertiary Namche Barwa syntaxis of the Himalayan orogen (Guilmette et al., 2011; Zeng et al., 2012). In all three cases the granulites have experienced high temperatures typical for large hot orogens, but the tectonic models that were suggested for these orogens differ: tectonic stacking in the case of the Grenville orogen (Indares et al., 1998), deep continental underthrusting in the Variscan belt (O'Brien and Rötzler, 2003; Babuška and Plomerová, 2012) and lower crustal flow in Tibet (Henry et al., 1997).

The eastern termination of the European Variscan belt, exemplified by the Bohemian Massif (Fig. 4.1), represents an ideal source of constraints on the HP granulites formation and exhumation (e.g. Faryad et al., 2012). This is due to exceptional accumulation of felsic HP granulite massifs and well studied P–T evolution, geochronology and structural evolution (e.g. Schulmann et al., 2008) of these rocks. Recently, a new conceptual model of formation of these rocks has been proposed (Schulmann et al., 2009; Lexa et al., 2011) which calls for testing by means of numerical modelling.

Since 1980s (England and Thompson, 1984), numerical modelling has been used as a unique tool for simulation of P–T evolutions in a number of subduction and collisional regions (Allemand and Lardeaux, 1997; Jamieson et al., 2004). The modern numerical parametric studies examine the effect of the rate and geometry of subduction, the age of the subducting slab, etc., on subduction dynamics (e.g. Gerya and Stockhert, 2006; Burov and Yamato, 2008), or they focus on the role of lithological stratification, radiogenic heat production, erosion and other processes important in evolution of orogenic systems (e.g. Babeyko et al., 2006; Beaumont et al., 2006; Faccenda et al., 2008). However, a dynamically consistent model of felsic HP granulite formation is still missing.

For the felsic HP rocks in the Bohemian Massif a large geological database is

available, but only a few attempts to model their formation have been made. Duretz et al. (2011) compared numerical and analogue models of extrusion of lower crustal material induced by a stiff indentor. Gravity-driven exhumation of felsic rocks from lower crustal levels was numerically studied by Lexa et al. (2011). The concepts of continental indentation and diapirism were combined in a model by Maierová et al. (2012). Based on their model setup, we perform a parametric study with special emphasis on the comparison of the calculated structural and P–T evolution with the corresponding geological data. We examine the role of the rate of continental convergence, syn-tectonic erosion and radiogenic heat sources on the model evolution, and correlate the results with the observed systematic variations in metamorphism and tectonic setting of granulite rocks in the Bohemian Massif.

4.2 Geodynamic model of the Bohemian Massif and tectonic setting of granulitic rocks

The Bohemian Massif tectonic model is based on eastward Devonian oceanic subduction followed by underthrusting of Saxothuringian continent below the Teplá-Barrandian and the Moldanubian domains (Schulmann et al., 2009; Keppie et al., 2010). The latter one was subsequently indented by the Brunia promontory advancing to SW during the Early Carboniferous (Schulmann et al., 2008). The granulite-facies rocks of the Bohemian Massif occur in three distinct regions (Fig. 4.1): 1) a narrow belt extruded over the imbricated Saxothuringian continent from the SE (Kotková et al., 1996; Konopásek and Schulmann, 2005), 2) as bodies which together with other lower crustal and deeply buried rocks form a NE–SW trending belt in the central part of the orogen (Machek et al., 2009; Franěk et al., 2011a, 2011b), and 3) as dismembered lenses surrounded by migmatites forming a wide NE–SW trending belt along the margin with the Brunia promontory (Racek et al., 2006; Tajčmanová et al., 2006; Štípská et al., 2008). In the central part of the orogen, the granulite bodies coincide with gravity lows and with a vertical domain of low seismic reflectivity (Franěk et al., 2011a). These geophysical arguments along with generally preserved vertical fabrics formed under granulite-facies conditions and retrograded mineral assemblages within subhorizontal fabrics led Franěk et al. (2011a) to propose a model of vertical extrusion of granulites from the bottom of the thickened crust. Lexa et al. (2011) further suggested that this process was accompanied by synchronous burial of mid-crustal rocks (see also Racek et al., 2006; Skrzypek et al., 2011; Štípská et al., 2012). The lower crustal rocks were finally reworked at mid-crustal conditions due to vertical shortening below a rigid crustal lid (Schulmann et al., 2005). The eastern granulite belt shows a similar succession of steep and subhorizontal metamorphic fabrics but the latter reworking is much more intensively developed. The assemblage of HP granulites and mid-crustal rocks embedded in migmatites (Hasalová et al., 2008) was interpreted as channel flow resulting from indentation of the hot and thick crustal root by the Brunia promontory (Schulmann et al., 2008; Štípská et al., 2008).

The vertical gravity-driven redistribution of a low-density lower crust and a high-density middle crust followed by indentation of a continental promontory are the salient features of a tectonic scenario proposed by Schulmann et al. (2009) for the Moldanubian part of the Bohemian Massif (Fig. 4.1, left block). A slightly differ-

ent scenario has been proposed for the West Sudetes part north of the Elbe zone (Fig. 4.1, right). In the West Sudetes, the HP granulites form a core of a high-grade gneiss body further surrounded by a coherent layer of Early Ordovician mafic rocks and low-grade Proterozoic metasediments. Chopin et al. (2012) and Mazur et al. (2012) suggest that this is a surface expression of a large mantled gneiss dome emerging through the Teplá-Barrandian crust. Štípská et al. (2012) and Chopin et al. (2012) proposed that crustal-scale folding was the dominating mechanism of gneiss dome formation. They also argue that the effect of indentation by the Brunia promontory on the final exhumation of the high-grade rocks is negligible compared to the southerly Moldanubian region.

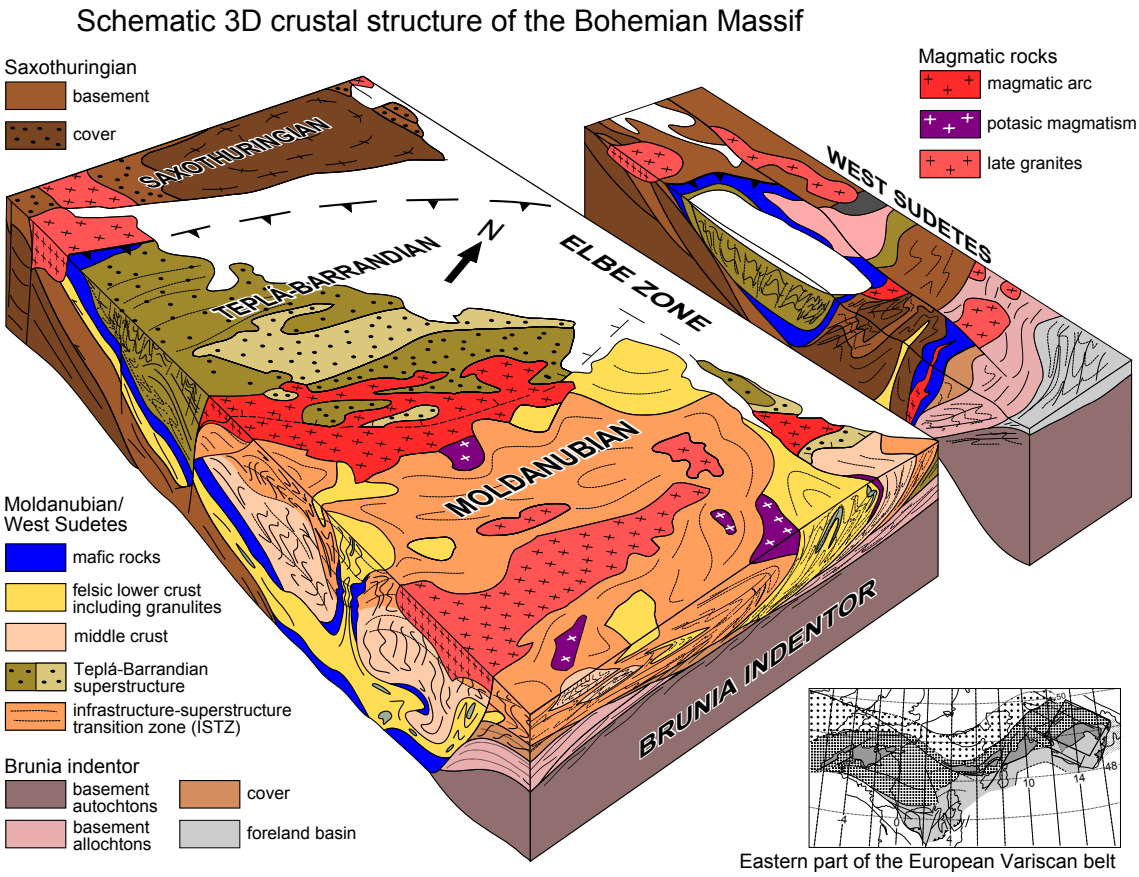

Figure 4.1: Schematic 3D block-diagram showing major structural features of the Bohemian Massif. Two separate blocks represent southern part (Moldanubian) and northern part (West Sudetes) of the orogen. Occurrences of the felsic lower crust including granulite massifs according to surface geology and gravity modelling (Chopin et al., 2012; Guy et al., 2011) are shown in yellow. The mafic rocks (blue) represent Ordovician magmatic underplate originally located above the felsic lower crust. The infrastructure–superstructure transition zone (ISTZ) is highlighted by orange colour and includes channel of partially molten rocks above the Brunia indentor. See text for details. The location of the studied area is marked by a rectangle in the map of the Eastern Variscan belt in the lower right corner. Map view is based on Franke (2000) and N–S section is redrawn after Schulmann et al. (2008).

4.3 Bohemian Massif granulites and their P–T–t paths

The Bohemian Massif granulites represent mylonites of a coarse-grained protolith of granitic composition developed under HT to UHT conditions (Behr, 1978; Franěk et al., 2011b). A typical felsic granulite consists of garnet, quartz, ternary feldspars, kyanite and accessory rutile, zircon, apatite, and ilmenite ± monazite (O'Brien and Rötzler, 2003). Janoušek et al. (2004), based on low zircon and monazite saturation temperatures (750 °C) and preservation of an Ordovician–Silurian principal inherited component in zircons, argued that these felsic granulites do not represent high-pressure Variscan granitic liquids (as proposed by Kotková and Harley, 1999; Vrána, 1989). Instead, he suggested that they originate from limited HP melting of an Ordovician–Silurian rhyolite to granite protolith (e.g. Fiala et al., 1987).

Inferring P–T–t paths for a granulite body is not a straightforward task and for the Bohemian granulites there are only several attempts to correlate P–T paths, geochronology and structural evolution (Štípská et al., 2004; Tajčmanová et al., 2006; Tajčmanová et al., 2010). A rock is supposed to progressively equilibrate in the presence of fluid (melt), but the equilibration may take place at different scales causing earlier assemblages and/or mineral chemistry to be locally preserved. In addition, to preserve granulite-facies assemblages, melt loss (and therefore H_2O loss) must occur leading to changes in the whole-rock composition along the P–T paths. In mineral equilibria modelling, the P–T paths must be therefore traced backwards, starting with the last equilibration that is supposed to occur just above the solidus and affects commonly rims of large porphyroblasts and matrix. In the Bohemian granulites, the last metamorphic stage reflects amphibolite-facies overprint and commonly involves the assemblage garnet-rim–biotite–sillimanite–plagioclase–K-feldspar–quartz. The corresponding P–T conditions have been estimated to 700–850 °C and 4–12 kbar (Petrakakis, 1997; Kröner et al., 2000; Štípská and Powell, 2005b; Štípská et al., 2008; Verner et al., 2008; Nahodilová et al., 2012) using thermobarometry and pseudosection modelling.

Tracing the P–T paths to the metamorphic peak may be more difficult and it involves interpretation of equilibrium among mineral relics like kyanite, ternary feldspars, Zr-rich rutile and garnet core chemistry. Using conventional thermobarometry peak metamorphic conditions have been estimated to 750–1100 °C and 18–28 kbar (e.g. Carswell and O'Brien, 1993; Cooke, 2000; O'Brien and Rötzler, 2003; Vrána, 1989) while mineral equilibria modelling yields a maximum of 850–900 °C and 16–20 kbar (Štípská et al., 2004; Štípská and Powell, 2005b; Tajčmanová et al., 2006; Racek et al., 2008). However, it has been shown that some granulites contain two generations of garnets, and some of the garnets preserve in their core chemistry that may have been achieved on the prograde path, or these garnets may have grown in a rock with different whole-rock composition (Štípská and Powell, 2005a; Racek et al., 2008; Nahodilová et al., 2012). Combination of such high-Ca garnet core and ternary feldspar then leads to results as high as 28 kbar and 1100 °C, but it is not clear if these minerals were in equilibrium. Even if the recent finding of microdiamonds confirms the UHP conditions of some granulites (Kotková et al., 2011), it is not clear at which temperature they were achieved. Therefore, tracing the P–T paths beyond the major equilibration at 850–1000 °C and 17–20 kbar is still questionable. Some attempts to interpret mineral inclusions in garnet and garnet

chemical zoning point to prograde P–T paths, but their slope is highly uncertain (Štípská and Powell, 2005a,b; Tajčmanová et al., 2010; Nahodilová et al., 2012).

There is only limited amount of geochronological data that allows us to constrain the time scales of prograde evolution of the Bohemian granulites. There are several Late Devonian U-Pb zircon ages as well as an Early Visean Sm-Nd age of garnet from the granulites in the central part of the Moldanubian domain (Prince et al., 2000), which suggest that the age range 360–350 Ma reflects the end of burial and onset of exhumation (van Breemen et al., 1982; Schulmann et al., 2005; Tajčmanová et al., 2010; Nahodilová et al., 2012). This corroborates with Lu–Hf and Sm–Nd study of granulites from the West Sudetes indicating that (U)HP conditions were attained already between c. 387 and 360 Ma (Anczkiewicz et al., 2007). The onset of exhumation of most granulites is well dated by the U-Pb zircon method which yields an almost uniform age of ∼340 Ma (Kröner et al., 2000; Štípská et al., 2004; Schulmann et al., 2005), while their mid-crustal emplacement occurred at 340–323 Ma (Štípská et al., 2004; Tajčmanová et al., 2006; Tajčmanová et al., 2010; Friedl et al., 2011). Finally, the cooling varies from 335 to 325 Ma based on a range of available Ar^{40}–Ar^{39} data (Dallmeyer et al., 1992; Svojtka et al., 2002). In general, the burial and crustal thickening were probably rather slow (several mm yr^{-1}), while exhumation rates may vary between 1 cm yr^{-1} and 5 cm yr^{-1} (Štípská et al., 2004; Tajčmanová et al., 2006; Tajčmanová et al., 2010).

4.4 Numerical model setup

We follow the modelling strategy of Beaumont and co-workers developed for studying hot orogens (Fullsack, 1995). The deformation of the crust is obtained by solving the full set of equations governing the heat transfer and flow of a chemically heterogeneous incompressible visco-plastic material. In the lithospheric mantle, the velocity of flow is explicitly prescribed and we only evaluate the temperature field by solving the heat transfer equation. This approach allows simulating in detail the processes in the crust, and testing the conceptual models derived on the basis of geological data. A potential drawback of this approach is that it may oversimplify the mechanical coupling between the crust and the mantle: the flow of mantle lithosphere is reduced to plate motion, the role of thermal convection in the upper mantle is suppressed, and the vertical motion of the crust must be artificially corrected for the effect of isostasy or elastic flexure. For a more detailed comparison of different modelling strategies, the reader is referred to the appendix in Beaumont et al. (2006) and to Beaumont et al. (2010).

The initial setup of the model is shown in Fig. 4.2. We simulate convergence of two crustal blocks in 2D Cartesian geometry. The block on the left represents a precursor of the Moldanubian domain which was originally stretched and thinned (Fig. 4.2a, plotted in yellow, see also Schulmann et al., 2005), underplated by a mafic material (blue), and then, in the process of relamination (Hacker et al., 2011), underlain by a felsic lower crust (FLC) rich in radioactive elements (pink). This felsic material is assumed to originate from the upper crust of the subducting Saxothuringian continent (Lexa et al., 2011) which is located to the left from the model domain and is not a subject of the present study. The block on the right represents a tectonically stable area which was not affected by the subduction process. It consists of a felsic upper layer (light green) and a mafic lower crust (dark green) with miner-

alogical compositions and rheological properties typical of stable continental crust (see Table 4.1 for values of the model parameters). The two blocks are separated by a 100 km long transition region consisting of an ordinary upper and lower crust which represents a proximal passive margin of the Brunia microcontinent stretched during the Devonian basin formation. Although the existence of such a transition region has not yet been confirmed by geological or geophysical data, we include it in our model because it helps to smooth large contrasts in material properties between the two domains at the beginning of the model evolution. Most of the material of this region is eroded already during an early stage of evolution and it has little effect on the final deformation.

At the beginning, the crustal part of the model domain is 35-km thick and its horizontal size is 1000 km. The convergence of the two crustal blocks is simulated by imposing a constant horizontal velocity $v_{\rm in}$ at the right-side boundary of the model domain while the left-side boundary is kept fixed (see Fig. 4.2b). The same velocity $v_{\rm in}$ is prescribed as a boundary condition at the base of the right crustal block. The bottom boundary of the left crustal block is assumed to be stagnant and its vertical position is only corrected for the effect of isostasy at each time step (Fullsack, 1995). The upper boundary of the model domain is a free surface and its shape thus directly corresponds to the surface topography. Erosion and sedimentation are included using a non-conservative formulation, which means that the mass of eroded material is not necessarily the same as the mass of sediments. This choice is justified by the two-dimensional nature of the model and the assumption that a certain amount of eroded material could be deposited outside the model domain. The rate of erosion, $v_{\rm e}$, is proportional to the topographic slope, $\tan\alpha$,

$$v_{\rm e}(x) = E\,|\tan\alpha(x)|\ , \tag{4.1}$$

and the rate of sedimentation, $v_{\rm s}$, is proportional to topography h (in km),

$$v_{\rm s}(x) = S\,h(x) \qquad \text{for } h(x) < 0\,, \tag{4.2}$$

$$v_{\rm s}(x) = 0 \qquad \text{for } h(x) \geq 0\,, \tag{4.3}$$

where E and S are parameters. The topography elevation h is measured with respect to the top right corner of the model domain.

The boundary conditions for the heat equation involve an influx of heat at the base of the lithosphere, a constant temperature at the surface, and zero heat flux at the side boundaries (Fig. 4.2b). The heat sources are prescribed in the upper layers of both blocks and in the bottom layer of the left block. The thermal evolution is started from a conductive steady state which is obtained for the boundary conditions described above and the heat sources prescribed only in the upper layers.

The deformation properties of the crustal material are approximated by non-linear visco-plastic rheology. For stresses smaller than the yield strength, $\sigma_{\rm yield}$, the material behaves like a viscous fluid with effective viscosity

$$\eta_{\rm eff} = B\dot{\epsilon}_{\rm II}^{1/n-1} \exp\left(\frac{E_{\rm A}}{nRT}\right)\ , \tag{4.4}$$

where $\dot{\epsilon}_{\rm II}$ is the second invariant of the strain-rate tensor, T is the temperature, R is the gas constant, and B, n and $E_{\rm A}$ are material parameters (see Table 4.1). If $\sigma_{\rm II} = \sigma_{\rm yield}$, material enters a plastic regime and its effective viscosity is

$$\eta_{\rm eff} = \frac{\sigma_{\rm yield}}{2\dot{\epsilon}_{\rm II}}\,. \tag{4.5}$$

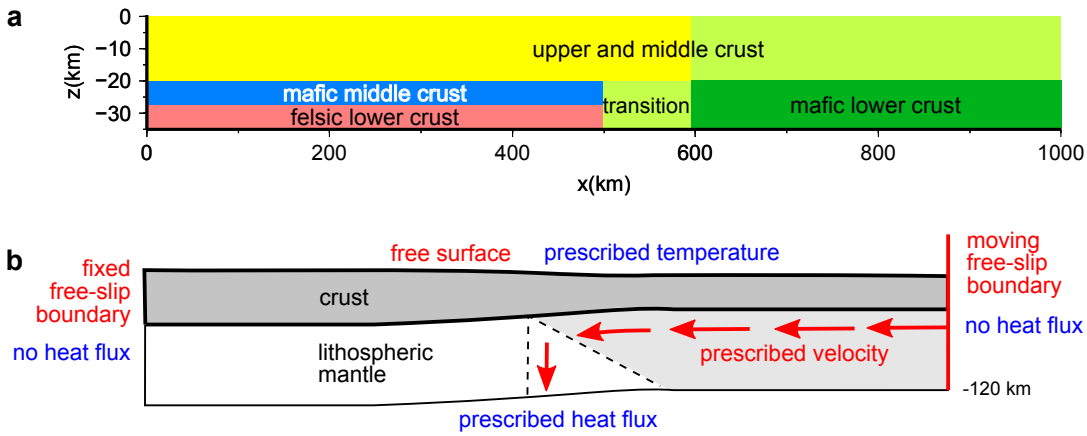

Figure 4.2: Model configuration with initial material distribution (a) and boundary conditions (b).

Table 4.1: Material parameters

Parameter	Symbol	Value
upper and middle crust, sediments — quartzite (Hirth et al., 2001):		
viscosity stress exponent	n	4
pre-exponential parameter	B	$1.89 \cdot 10^8$ Pa s$^{1/n}$
activation energy	E_A	135 kJ mol^{-1}
density	ρ	2800 kg m^{-3}
heat production	r	2 μW m^{-3}
mafic middle crust — plagioclase (Ranalli, 1995):		
viscosity stress exponent	n	3.2
pre-exponential parameter	B	$3.69 \cdot 10^6$ Pa s$^{1/n}$
activation energy	E_A	238 kJ mol^{-1}
density	ρ	3000 kg m^{-3}
felsic lower crust — granite (Ranalli, 1995):		
viscosity stress exponent	n	1.9
pre-exponential parameter	B	$2.75 \cdot 10^7$ Pa s$^{1/n}$
activation energy	E_A	137 kJ mol^{-1}
density	ρ	2700 kg m^{-3}
heat production	r	0, 2 μW m^{-3} or 4 μW m^{-3}
mafic lower crust — basalt (Mackwell et al., 1998, viscosity decreased 10×):		
viscosity stress exponent	n	4.7
pre-exponential parameter	B	$1.91 \cdot 10^4$ Pa s$^{1/n}$
activation energy	E_A	485 kJ mol^{-1}
density	ρ	2900 kg m^{-3}
reference values of plastic strain	ϵ_0, ϵ_∞	0, 1
cohesion	C	1 MPa
upper and middle crust, sediments:		
initial and final angle of internal friction	ϕ_0, ϕ_∞	15°, 7.5°
mafic middle crust, felsic lower crust, mafic lower crust:		
initial and final angle of internal friction	ϕ_0, ϕ_∞	30°, 15°

In the present study, the plastic regime mimics brittle deformation and the yield strength is obtained from the Drucker-Prager yield criterion,

$$\sigma_{\text{yield}} = p \sin\phi + C \cos\phi \,, \tag{4.6}$$

where p is the pressure, C is the cohesion and ϕ is the effective angle of internal friction. Strain-softening is included via a linear decrease of ϕ with strain (e.g. Buiter et al., 2006): When the plastic strain increases from ϵ_0 to ϵ_∞, the material softens as ϕ decreases linearly from ϕ_0 to ϕ_∞. The governing equations are solved using the extended version of the finite element software Elmer (http://www.csc.fi-/english/pages/elmer). The resolution in the crust is approximately 0.7×4 km at the beginning and 1×2 km at the final stage of the time evolution. For a detailed description of the numerical implementation the reader is referred to Maierová et al. (2012).

4.5 Results

We examine the role of three basic parameters: the velocity of shortening of the model domain v_{in}, rate of erosion (parameter E) and the radiogenic heat production within the felsic lower crust, r_{FLC}. The velocity of shortening, i.e. the velocity of the right block, varies between 1 and $2\,\text{cm}\,\text{yr}^{-1}$ in different models. Correspondingly, we change the total time of the model evolution in order to keep the same final shortening in all models (i.e. models with velocity of shortening $1\,\text{cm}\,\text{yr}^{-1}$ span twice longer time than those with $v_{\text{in}} = 2\,\text{cm}\,\text{yr}^{-1}$). For each value of v_{in} we test three values of erosion parameter E (2, 2.5, and $3\,\text{cm}\,\text{yr}^{-1}$). The third tested parameter is the heat production in the felsic lower crust, r_{FLC}. Besides a reference value of $4\,\mu\text{Wm}^{-3}$, we consider heat productivity that is reduced by one half, $r_{\text{FLC}} = 2\,\mu\text{Wm}^{-3}$, and a model where $r_{\text{FLC}} = 0$. A complete list of models with values of the tested parameters, together with output characteristics, is given in Table 4.2.

4.5.1 Modelled crustal deformation

The general evolution of all investigated models can be divided into three stages. At the beginning of the shortening, folding governed by the competent mafic middle crust occurs inside the left block. Subsequently, the mafic middle crust and the felsic lower crust vertically exchange, and finally the thickened orogenic root is underthrusted by the right block (see e.g. model v15e25r4 with parameters $v_{\text{in}} = 1.5\,\text{cm}\,\text{yr}^{-1}$, $E = 2.5\,\text{cm}\,\text{yr}^{-1}$, $r_{\text{FLC}} = 4\,\mu\text{Wm}^{-3}$ in Fig. 4.3). However, the internal structure and evolution of individual models differ in many respects. We classify the models according to three basic criteria: 1) the relative importance of folding and diapirism as a mechanism of thickening, 2) the existence of the infrastructure–superstructure transition zone (ISTZ) and its characteristics, and 3) the time of exhumation of the felsic lower crust to the surface. The characteristics of the models according to these three criteria are summarized in Table 4.2, and described in more detail on four representative models shown in Figs 4.3–4.6.

In all of the models, the shortening and thickening in the domain of the future orogenic root are initially accommodated by crustal-scale folding. This is due to a large viscosity contrast between the mafic middle crust and the felsic material

above and below this layer. While in some models the folding remains the governing mechanism during most of the model evolution (v15e25r0, Fig. 4.4), in others it gradually becomes less important and the Rayleigh-Taylor instability prevails (v15e25r4, Fig. 4.5). In the fold-dominated models, the whole competent mafic layer is buckled (blue layer in Fig. 4.6a, top panel). In the models, where the Rayleigh-Taylor instability prevails, it grows independently on lateral stresses. The originally continuous layer of the buoyant FLC evolves into circular or lense-shaped bodies, while the dense middle crust is dismembered and sinks in between them (pink and blue areas in Fig. 4.5a). In some models, the Rayleigh-Taylor instability, leading to diapirism, dominates the deformation soon after the onset of compression (v10e20r4, Fig. 4.5a). The relative importance of diapirism vs. folding is indicated in Table 4.2, showing that folding is more important in models with high v_{in} and/or small r_{FLC}.

In the gravity-dominated models, the FLC emplaced to mid-crustal levels forms a weak zone which accommodates most of the deformation induced by the lateral shortening (Fig. 4.5b). As it separates the upper crust, traditionally named orogenic superstructure, from the deep crustal levels — orogenic infrastructure (Wegmann, 1935; Culshaw et al., 2006) — we call it here infrastructure-superstructure transition zone (ISTZ). According to the character of the ISTZ, we observe two main groups of models. In the first group ("n" in the ISTZ column, Table 4.2), the ISTZ is a flat, well defined and relatively narrow (∼10–20 km thick) zone of intense deformation. It is always developed from the internal part of the orogen towards the surface contact between the root and the indentor (Figs 4.3b, 4.5b). In some models, the deformation along the indentor front is localized into a very thin zone (Fig. 4.5b) corresponding to highly deformed low-viscosity FLC material, which decouples the underthrusting block from the material of the root. Another observed feature is the channel flow ("c" in the ISTZ column, Table 4.2), defined here as a flow between the relatively rigid lower block and the upper lid, that has opposite direction than the motion of the underthrusting block (Fig. 4.5b, bottom panel). The second group of models ("w" in the ISTZ column, Table 4.2), is characterized by a wide and diffuse zone of deformation (ISTZ) in the middle crust (e.g. v20e25r4, Fig. 4.6b). The FLC bodies are not interconnected and therefore the horizontal flow within the ISTZ is not developed and the crustal lid remains mechanically coupled with deeper levels. In the model without radiogenic heat sources in the FLC, the ISTZ can hardly be identified and several relatively steep thrusts develop (v15e25r0, Fig. 4.4b).

The occurrence of the FLC at the surface is documented in foreland basin sediments and its onset can constrain the duration and speed of the FLC exhumation (Schulmann et al., 2008). In the model, the time of the FLC exhumation mostly results from the interplay between the velocity of shortening and erosion. Faster shortening of the model domain speeds up the model evolution and thus leads to earlier exhumation (Table 4.2, last column). We note, however, that not all models with high v_{in} predict exhumation: If the rate of erosion is low, the FLC does not reach the surface during the evolution time considered and it remains trapped at mid-crustal levels (e.g. v20e25r4, Fig. 4.6a).

Table 4.2: Description of models. The name of each model is constructed as a combination of values of the three varied parameters, e.g. v10e20r4 is a model with $v_{\text{in}} = 1\,\text{cm yr}^{-1}$, $E = 2\,\text{cm yr}^{-1}$ and $r_{\text{FLC}} = 4\,\mu\text{Wm}^{-3}$. Description of columns: (Folding) the number of "+" signs increases with the importance of folding as a mechanism of deformation, and "-" indicates gravity-dominated deformation. (ISTZ) "n" denotes a well defined narrow zone of deformation between relatively more rigid upper and lower crust, "w" denotes a wide and diffuse zone of deformation, and "c" indicates that channel flow is developed above indentor. (FLC-exhumation time) the time when the felsic lower crustal material reaches the surface.

Model	Velocity v_{in} (cm yr^{-1})	Erosion E (cm yr^{-1})	Heat sources r_{FLC} ($\mu\text{W m}^{-3}$)	Max. time (Myr)	Folding	ISTZ	FLC-exhumation time (Myr)
v10e20r4	1.0	2.0	4	51	-	nc	49
v10e25r4	1.0	2.5	4	51	-	nc	41
v10e30r4	1.0	3.0	4	51	-	nc	37
v10e25r2	1.0	2.5	2	51	+	n	43
v15e20r4	1.5	2.0	4	34	+	nc	-
v15e25r4	1.5	2.5	4	34	+	nc	33
v15e30r4	1.5	3.0	4	34	+	n	30
v15e25r2	1.5	2.5	2	34	++	w	-
v15e25r0	1.5	2.5	0	34	+++	-	34
v20e20r4	2.0	2.0	4	26	+	wc	-
v20e25r4	2.0	2.5	4	26	+	w	-
v20e30r4	2.0	3.0	4	26	+	w	25
v20e25r2	2.0	2.5	2	26	+	w	-

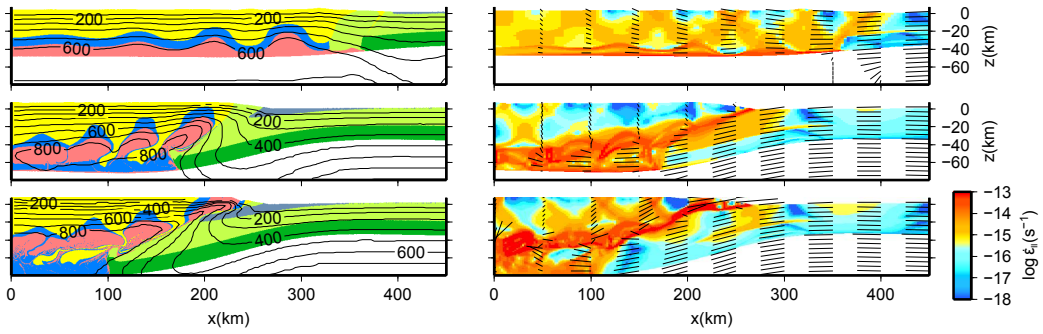

Figure 4.3: Evolution of the model v15e25r4 in three representative time steps (for a detailed discussion see Maierová et al., 2012). a) Composition and temperature fields. The colours are the same as in Fig. 4.2a, sediments are plotted in grey. The isotherms are plotted every 100 °C and labelled every 200 °C. b) Strain-rate and flow velocity fields. Sticks show the magnitude and direction of velocity.

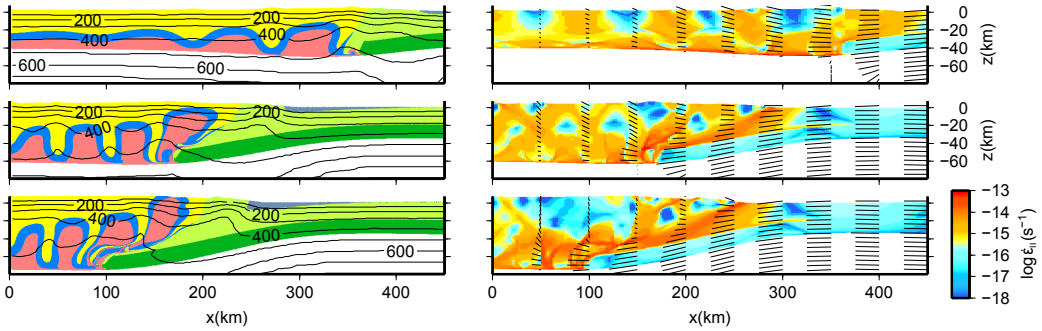

Figure 4.4: Model v15e25r0: a) composition and isotherms, b) strain-rate and flow velocity fields. Description is the same as for Fig. 4.3.

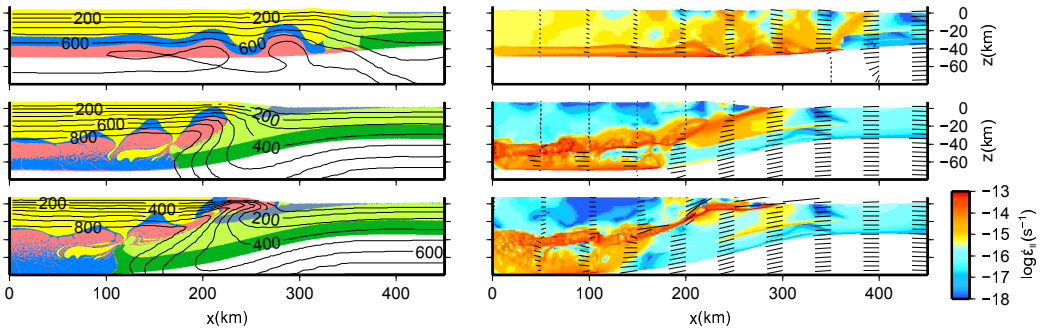

Figure 4.5: Model v10e20r4: a) composition and isotherms, b) strain-rate and flow velocity fields. Description is the same as for Fig. 4.3.

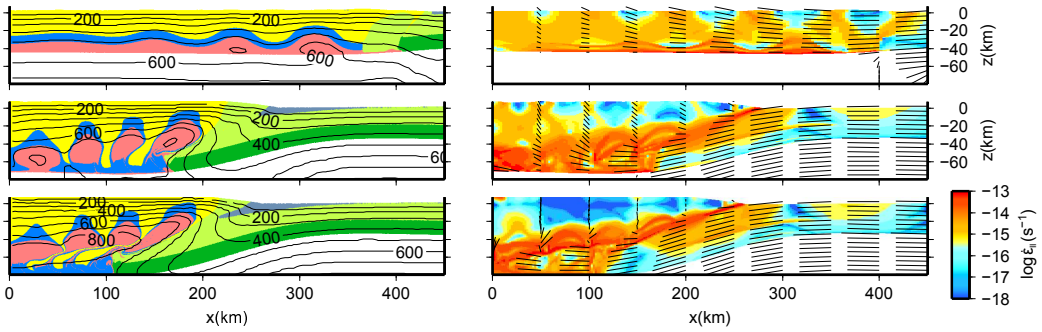

Figure 4.6: Model v20e25r4: a) composition and isotherms, b) strain-rate and flow velocity fields. Description is the same as for Fig. 4.3.

4.5.2 Calculated pressure–temperature–time paths

The metamorphic history of rocks can be approximated by modelled P–T conditions recorded along selected material trajectories. In Fig. 4.7, we show such P–T paths of 1000 material particles regularly distributed in the FLC for each of the models considered (Table 4.2). In the description of the paths, we will restrict ourselves only to the material particles which record pressure less than 10 kbar at the end of the simulation (red, green and blue lines in Fig. 4.7) and neglect those that remain stuck deeper in the orogenic root (cloud of grey lines in Fig. 4.7). We expect that even if the material was not fully exhumed to the surface during the model evolution, it may reach it later due to relaxation of the orogenic root accompanied by erosion and extensional processes. The colour-coding of individual paths of particles corresponds to their x-position at the beginning of the time evolution. The "blue", "green" and "red" particles were initially at x =200–300 km, 300–400 km and 400–500 km, respectively. We will focus on four main characteristics of the recorded P–T paths: 1) the slope of the prograde branch, 2) the peak conditions in pressure and temperature and their relative position, 3) the shape of the retrograde branch, and 4) the area enclosed by the P–T loop, i.e. by the prograde and retrograde branches in the P–T space. As the recorded P–T paths show significant variations within each model, our analysis will be restricted to the most typical evolution imaged by the highest density of paths in the P–T plot.

In all models considered, the prograde path recorded by most particles exhibits linear relation between temperature and pressure. The slope is mainly controlled by the velocity of convergence of the two crustal blocks showing a moderate dP/dT gradient of 1 kbar/40 °C and a high dP/dT gradient of 1 kbar/25 °C for slow ($v_{\mathrm{in}} = 1\,\mathrm{cm\,yr^{-1}}$) and fast convergence ($v_{\mathrm{in}} = 2\,\mathrm{cm\,yr^{-1}}$), respectively. The peak pressure also increases with increasing v_{in}, and with the distance from the front of the indentor. The peak pressure in models with $v_{\mathrm{in}} = 1\,\mathrm{cm\,yr^{-1}}$ and $v_{\mathrm{in}} = 2\,\mathrm{cm\,yr^{-1}}$ is up to 15 kbar and 17 kbar, respectively. For slow convergence and position far from the indentor, oscillating P–T paths reflect complex deformation within the FLC (e.g. blue and green lines in Fig. 4.7, model v10e20r4), while rapid convergence leads to simpler paths (e.g. Fig. 4.7, model v20e20r4).

The parameter v_{in} also controls the shape of the path in the vicinity of the pressure peak. In the case of a high velocity ($v_{\mathrm{in}} = 2\,\mathrm{cm\,yr^{-1}}$, right panels in Fig. 4.7), the peak pressure (up to 17 kbar) is significantly higher than the pressure at the peak temperature (typically 10–12 kbar). Moreover, the angle between the prograde and retrograde paths becomes sharper (right panels in Fig. 4.7). This is because the heat production is practically constant in time but the higher convergence rate causes faster elevation of the fertile rocks, and therefore most of the heat is released in a shallower depth. Slow convergence ($v_{\mathrm{in}} = 1\,\mathrm{cm\,yr^{-1}}$, left panels in Fig. 4.7) favours a small pressure difference between the points with the peak pressure and the peak temperature, open angle between the prograde and retrograde paths and generally more complex shapes of the paths.

The peak temperature is, not surprisingly, controlled by the heat production r_{FLC}. A high production of $4\,\mu\mathrm{Wm^{-3}}$ (three upper rows in Fig. 4.7) leads to the maximum temperature around 850 °C, while a moderate production of $2\,\mu\mathrm{Wm^{-3}}$ (fourth row in Fig. 4.7) leads to the maximum temperature close to 650 °C. When there are no radiogenic heat sources in the FLC, the prograde and retrograde paths follow practically the same geotherm (Fig. 4.7, model v15e25r0). Consequently, the

area enclosed by the P–T loop is roughly proportional to the amount of internal heating.

After reaching the peak temperature, the shape of the retrograde path is chiefly controlled by erosional processes. As erosion operates mostly near the contact of the two colliding blocks, the paths related to exhumation to the surface are recorded only by particles close to the margin of the orogen. The relation between the shape of the retrograde branch and the erosion parameter E is non-linear and reflects the deformation regime at the contact. The geotherm along the contact varies with time due to a highly unsteady velocity of the material outflow. Consequently, even closely spaced particles within a single simulation can record contrasting retrograde P–T paths (e.g. Fig. 4.7, model v15e25r4). A completely different evolution is observed in the central part of the orogen (blue and most of green paths in Fig. 4.7), where the FLC remains stuck in a depth corresponding to ∼10 kbar in all presented models. This depth is related to the base of the effectively rigid part of the upper crust, commonly called the orogenic lid. It should be noted that this level does not coincide with the brittle–ductile transition, which is always located above. In the models where the efficiency of erosion is very low (small E, high v_{in}, e.g. model v20e25r4 in Fig. 4.7) the FLC does not reach the surface at all and the retrograde paths end at mid-crustal level. In the fold-dominated models, the retrograde P–T paths are more homogeneous and show important cooling during decompression (Fig. 4.7, model v10e25r2).

The evolution of pressure and temperature with time for three selected models is shown in Fig. 4.8. For P–t and T–t paths from other models see Supplementary Figs S1 and S2, respectively. In models with a low velocity of shortening ($v_{\mathrm{in}} = 1\,\mathrm{cm\,yr^{-1}}$, e.g. model v10e20r4) the P–t paths have polyphase behaviour. During the early and longest stage (∼30 Myr) pressure increases steadily, afterwards it starts to fluctuate, and finally drops rapidly (Fig. 4.8, v10e20r4, top panel). The rapid pressure drop always starts from pressures of ∼10 kbar, i.e. from the base of the orogenic lid. The timing of the pressure drop depends on the erosion rate and varies between ∼50 Myr for $E = 2\,\mathrm{cm\,yr^{-1}}$ and < 40 Myr for $E = 3\,\mathrm{cm\,yr^{-1}}$ (cf. Table 4.2, last column, showing the time of the first FLC exhumation to the surface). In the T–t paths, the three stages of pressure evolution (gradual increase, fluctuations and sudden drop of pressure) correspond to a slow increase of temperature, a temperature plateau and rapid cooling (Fig. 4.8, v10e20r4, bottom panel).

Models with fast shortening ($v_{\mathrm{in}} = 2\,\mathrm{cm\,yr^{-1}}$) reveal different P–t paths with a short period of burial followed by gradual exhumation (Fig. 4.8, v20e25r4, top panel). The final pressure drop is present only in the model v20e30r4 with efficient erosion (see Supplementary Fig. S1). The T–t paths in the fast models lack the temperature plateau and the final rapid cooling (Fig. 4.8, v20e25r4, bottom panel). The period of fast exhumation and cooling is absent also in models with a low radiogenic heat production (Fig. 4.8, model v15e25r0 with $r_{\mathrm{FLC}} = 0$).

In summary, the early stages of metamorphic evolution (prograde path and pressure peak) are controlled mostly by the rate of convergence, while the peak temperature depends on the heat production. Moreover, an elevated heat production causes overall rheological softening of the FLC allowing focused and fast outflow above the indentor, the timing of which is governed by the efficiency of erosion. The influence of the studied parameters (v_{in}, E, r_{FLC}) on the shape of the P–T, T–t and P–t paths is schematically shown in Fig. 4.9.

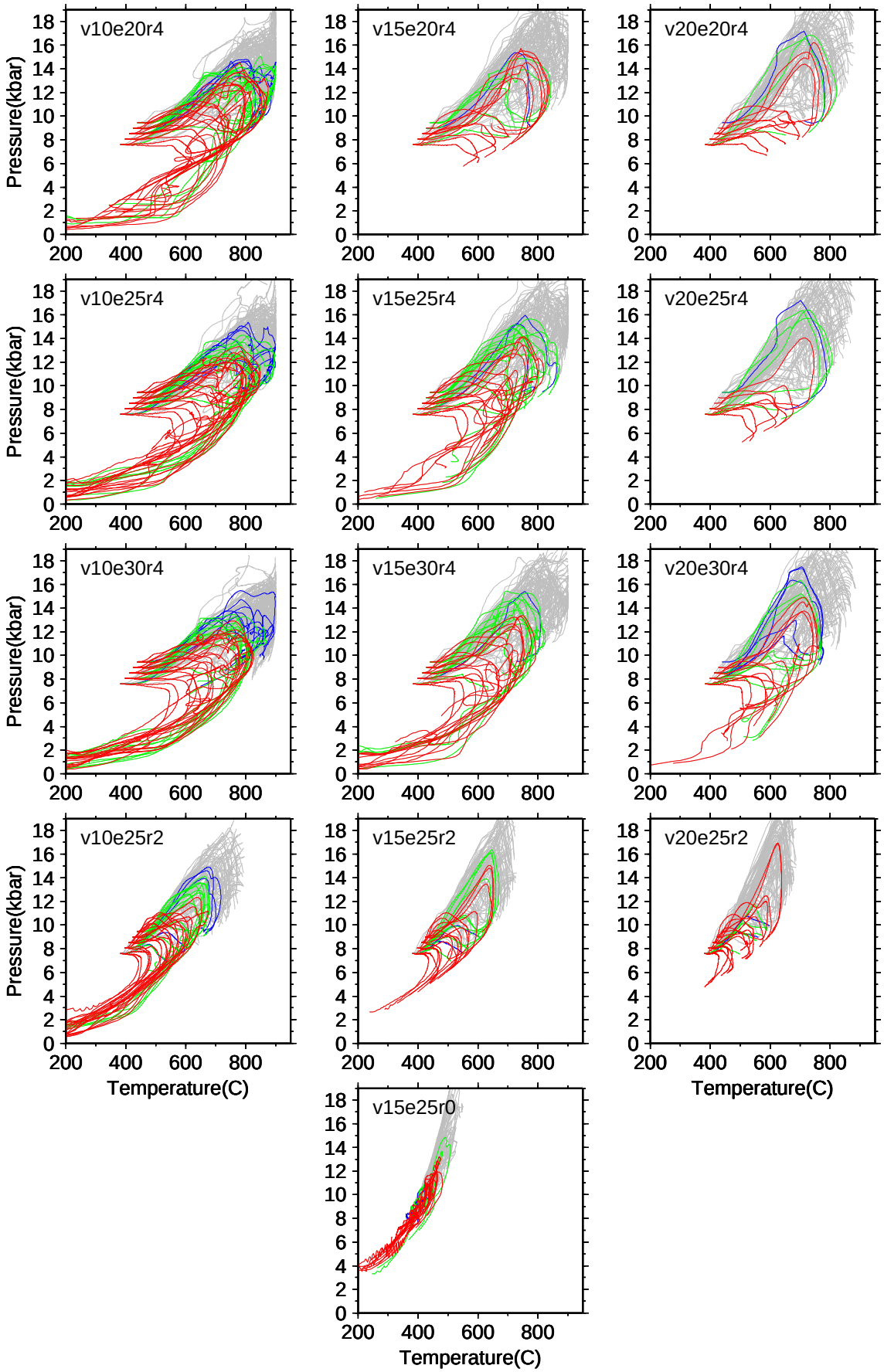

Figure 4.7: P–T paths of material particles of the FLC for all models considered. The name of the model corresponding to the first column in Table 4.2 is written in the top left corner of each panel. For details see Section 4.5.2.

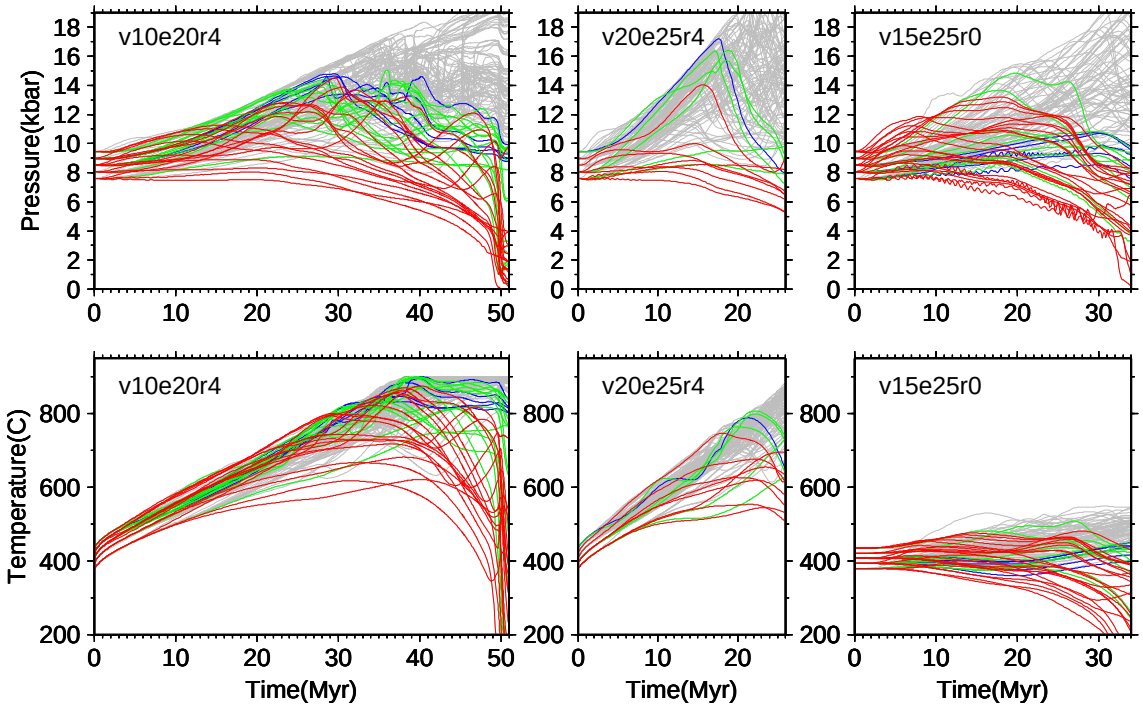

Figure 4.8: Time evolution of pressure (upper row) and temperature (lower row) in three selected models (v10e20r4, v20e25r4, v15e25r0). The colour-coding of individual paths is the same as in Fig. 4.7.

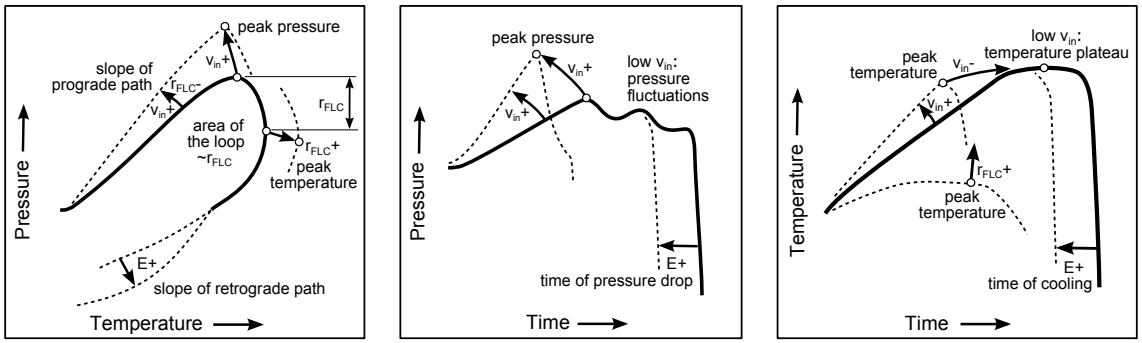

Figure 4.9: Schemes of typical pressure–temperature (left), pressure–time (middle) and temperature–time (right) paths depending on model parameters v_{in} (velocity of convergence), E (rate of erosion) and r_{FLC} (radiogenic heat production within the felsic lower crust).

4.6 Discussion

We have shown that the investigated models can be classified according to their preferred deformational mechanism and typified by two end-members: gravity-dominated and fold-dominated models. In this section, we assess the relative contribution of gravity tectonics, crustal folding, and development of the ISTZ on the metamorphic evolution of the orogenic lower crust expressed in P–T–t paths, and compare the structural and P–T evolution in these two contrasting models with the available data from the Bohemian Massif. Finally, we will compare our results with previous studies and discuss the model limitations.

4.6.1 Geological implications of gravity-dominated and fold-dominated models

The gravity-dominated models result from slow convergence and high internal heating (e.g. model v10e20r4). The characteristic feature of these models is an efficient exchange of the FLC with the mafic crust leading to relatively lower peak pressures recorded by the FLC. The P–T–t paths are characterized by a temperature plateau in the T–t plot and fluctuations of pressure around 14 kbar at the same time interval. From a petrological point of view the long thermal relaxation may imply important diffusion of elements in minerals like garnet, equilibration of mineral textures and coarsening. The subsequent development of the ISTZ and flow of the FLC rocks over the indentor is recorded in the P–T–t paths as a fast exhumation and cooling allowing good preservation of mineral assemblages. The geological expression of the major gravity redistribution is subordinate occurrence of mafic material in the middle crust which is dominated by felsic HP material. The ISTZ would have a form of a well defined layer of migmatites and granulitic gneisses exhibiting intense deformation under high temperature.

The second end-member is the fold-dominated model with a high to intermediate convergence rate and a small radiogenic heat production (e.g. model v15e25r0). As the folding is the dominant mechanism of the thickening, the burial and subsequent exhumation are relatively slow and gradual. The prograde and retrograde P–T paths have high dP/dT slopes and form a narrow P–T loop. The negligible temperature increase in the T–t paths reflects the absence of heat sources. In such an orogen, a continuous mafic layer surrounding the FLC should be preserved and embedded in mid-crustal material. The deformation in the middle crust would not be accompanied by melting implying that HP gneisses and mafic rocks will be surrounded by Barrovian-type schists and not by migmatites.

An intermediate type of behaviour is observed in models with rapid convergence and moderate to high heat production (e.g. model v20e25r4). The orogenic root is build up by buckling of the mafic middle crustal layer leading to exhumation of lower crustal material in cores of large-scale antiforms. The progressive indentation creates a wide zone of deformation including large volumes of hot material that are still internally heated and later sustain gradual cooling and exhumation. This type of orogen is characterized by steep prograde P–T paths, relatively high peak pressures of up to 17 kbar, and a large pressure difference between the peak pressure and peak temperature, which is achieved at pressures of about 10–12 kbar. From the geological point of view, a big portion of mafic crust remains attached to the exhumed FLC in

mid-crustal levels. The large volume of the exhumed FLC efficiently advects heat and together with adjacent partially molten middle crustal rocks forms a wide ISTZ.

4.6.2 Correlation with the tectonic evolution of the Bohemian Massif

In the frame of the Bohemian Massif two regions with contrasting tectonic styles were recognized which can be compared to numerical models presented in this work: 1) The central part of the Bohemian Massif represented by the Saxothuringian subduction system and the overlying Teplá-Barrandian lid and complex Moldanubian infrastructure, and 2) The West Sudetes system, which is significantly smaller and reveals a simple wedge-type geometry with a typical structure of a mantled gneiss dome.

In the central part of the Bohemian Massif, the occurrences of the FLC mostly lack Ordovician gabbroic rims (Racek et al., 2008; Franěk et al., 2011a) even though small relics have been described (Štípská et al., 2008; Tajčmanová et al., 2010). In addition, the seismic imagery indicates a possibility that the deepest part of the Moldanubian domain contains pieces of eclogitized mafic crust just below the seismic Moho (Edel, pers. comm.). This is in agreement with the gravity-dominated models, where almost entire volume of mafic rocks sinks to the deepest orogenic levels. In addition, the ISTZ observed in these models corresponds to the partially molten mid-crustal rocks and granulite massifs exposed today at the surface of the Moldanubian domain (Franěk et al., 2011a). Above the Brunia indentor, the ISTZ has a form of a highly deformed channel of migmatites and high-grade gneisses containing disrupted bodies of granulites and mid-crustal rocks (Schulmann et al., 2008).

In the West Sudetes system, the FLC forming the core of the large gneiss dome is surrounded by a continuous layer of mafic rocks overlain by mid-crustal Barrovian-type schists. The dome-like geometry suggested by Don et al. (1990) is supported by gravity modelling of Chopin et al. (2012). Moreover, the deformation related to the growth of the dome is localized in a shear zone in its upper part. This style of deformation is consistent with the fold-dominated models where the ISTZ is weakly developed and the mafic layer is not disrupted and surrounds the FLC antiforms.

The existing petrological and geochronological data allow only qualitative comparison with numerical modelling results, often due to insufficient precision of the data. It is only recently, when coupled thermodynamic modelling and in-situ geochronology yield more precise constraints on the P–T–t evolution. Nevertheless, there are several robust observations which can be compared with the predictions of the numerical model.

The granulites situated either along the margins of the Moldanubian root or in the West Sudetes are characterized by the presence of prograde zoning in garnets and inclusions of muscovite (phengite) suggesting that the rocks were not entirely equilibrated before exhumation (Štípská et al., 2004; Tajčmanová et al., 2010; Nahodilová et al., 2012). This can be due to insufficient time for thermal maturation, i.e. cooling and exhumation started shortly after peak granulite-facies conditions (at ∼360 Ma) as suggested by Nahodilová et al. (2012). Other explanations are a lack of radioactive heat sources within the FLC or a small thickness of the relaminated felsic crust. The latter interpretation is in line with crustal-scale gravity modelling suggesting that the thickness of a residual felsic layer above Moho is gradually de-

creasing from the core of the orogen to its margins and further north to the West Sudetes (Guy et al., 2011; Chopin et al., 2012). In contrast, granulite samples coming from the central part of the Moldanubian domain show perfectly equilibrated mineral textures, absence of relics of hydrous minerals in cores of garnets and their compositional zoning. In addition, these rocks are marked by migmatitic appearance (Franěk et al., 2011b) indicating high-temperature conditions related to a long residence time (∼30 Myr) at a deep crustal level before exhumation at 340 Ma. Similarly, these two contrasting trends in the temperature evolution are observed in the numerical models. The temperature plateau in the T–t paths is present only in the gravity-dominated models (right panel in Fig. 4.9, low v_{in}), while in the fold-dominated models (high v_{in}), cooling immediately follows the temperature peak. Moreover, the Sudetic granulites are the only samples showing important cooling during exhumation as predicted by the fold-dominated models.

There are also important differences in the depth of the transition from vertical to subhorizontal fabrics. In the West Sudetes granulites, the transition occurs at pressures 7–4 kbar (Skrzypek et al., 2011; Štípská et al., 2012), while pressures 5–4 kbar are documented in the granulite massifs located along the margin of the Moldanubian domain (Tajčmanová et al., 2006, 2010). This contrasts to exhumation P–T paths in the core of the orogen, where the transition to subhorizontal fabrics generally occurs at pressures 10–12 kbar (Štípská and Powell, 2005b). In summary, in the core of the orogen the vertical material transfers occur in the depth range of 70–35 km, while along the margins of the orogen and in the West Sudetes it continues to ∼15-km depth. Regarding our model, the data from the centre and margin of the Moldanubian domain corroborate well with the gravity-dominated model where a part of the FLC is exhumed at the periphery and the rest remains stuck below the orogenic lid.

The Ar^{40}–Ar^{39} cooling age patterns show different trends according to the position in the orogen. The samples from the margin of the Moldanubian domain show prolonged cooling from 340 to 325 Ma. The ages in the core of the orogen suggest a transition of 500 °C isotherm (blocking temperature of amphibole) at about 340 Ma and a transition of 320 °C isotherm (blocking temperature of biotite) at 330–325 Ma (see Schulmann et al., 2008, for review). This contrasts with the T–t evolution of the West Sudetes where amphibole, muscovite and biotite cooling ages are clustered between 340 and 335 Ma. The cooling pattern in the core of the orogen is explained by gravitational emplacement of large volumes of the FLC in mid-crustal levels at 340 Ma, which remained stuck below the orogenic lid until the final cooling period at 330–325 Ma related to either erosional or extensional post-orogenic processes. The continuous cooling path in the West Sudetes fits well with the cooling path predicted by the fold-dominated model.

To test the predictions of the existing model an effort has to be done in a systematic analysis of prograde evolution of granulitic and associated HP rocks using thermodynamic modelling. The first prograde paths presented by Skrzypek et al. (2011), Chopin et al. (2012) and Tajčmanová et al. (2010) indicate prograde dP/dT gradients similar to the modelled P–T evolutions. A diagnostic feature for the folding- or gravity-driven models is also the mutual position of the peak-pressure and the peak-temperature conditions. The thermodynamic modelling combined with in-situ geochronology may provide decisive input in understanding of the orogenic tectonic and thermal evolution.

4.6.3 Numerical modelling aspects

Only few numerical studies of exhumation of felsic material from lower crustal levels have been performed so far. Duretz et al. (2011) explored behaviour of relatively weak material forced by a stiff indentor, as proposed for the eastern margin of the Bohemian Massif. These authors successfully reproduced the geometry of mid-crustal sub-horizontal flow ("hot fold nappe" introduced by Beaumont et al., 2006), and formation of a topographic plateau. However, they neglected the effect of buoyancy, and the vertical motion of material is rather restricted. Despite a good correlation of their numerical- and analogue-modelling results, their model does not explore several important features characteristic for the eastern margin of the Bohemian Massif. It is in particular the P–T evolution of exhumed rocks and the time scales of the indentation event.

Lexa et al. (2011) focused on the growth of the Rayleigh-Taylor instability and diapirism of the felsic lower crust, which is recorded mostly in the central part of the Moldanubian domain. Without lateral forcing, they obtained a typical "mushroom" shape of diapirs, retrograde P–T evolution characteristic for exhumation of felsic granulites located in the core of the Bohemian Massif and time scales of exhumation events corresponding to existing high- and low-temperature geochronology. Their modelling is not related to continental indentation but the growth of crustal diapirs is initiated exclusively due to the existing Rayleigh-Taylor instability induced by a dense mid-crustal gabbroic layer. However, indentation is a key factor for development of a mid-crustal channel and specific P–T evolution of the orogenic lower crust located originally close to the continental indentor.

The model presented by Maierová et al. (2012) incorporated both the gravity and lateral forcing, and reproduced basic geological data available for the Moldanubian part of the Bohemian Massif, including the time scale of the tectonic process, topography evolution and sedimentary record. However, their model is restricted to the lower-crustal exhumation in the Moldanubian domain and does not attempt to explain variations of geological characteristics among different granulite massifs. We followed the modelling strategy of Maierová et al. (2012), but we varied model parameters and obtained a rich family of models applicable to other systems, in particular to the West Sudetes region. However, we investigated only three parameters, and many others may be important. Namely, the applied rock rheology only roughly approximates stress–strain relation of crustal material and we are aware that different choice of rheological description could significantly influence the results. Further, there are several restrictions and uncertainties of the model setup: We neglect the three-dimensional structure of the Bohemian Massif using a 2D modelling approach. The initial and boundary conditions are prescribed, although they are only vaguely indicated by geological and geophysical data. We use a kinematic velocity field in the mantle, and the mechanical coupling between the crust and the mantle is simplified. Further, we neglect the effect of mantle processes on the thermal state of the lithosphere, although a significant perturbation of the lithospheric temperature field during the orogeny can be expected.

The issue of mechanical coupling between the crust and the mantle was studied by several authors in different parts of the Bohemian Massif. Machek et al. (2009), based on similar fabrics of felsic granulites and pyroxenite layers included in garnet peridotites, suggest complete mechanical coupling between the mantle and the lower crust. However, these authors also suggest that the mechanical coupling may be

valid only for early stages of tectonic evolution in the forearc region. The coupling is possibly induced by a localized heat input of a nearby magmatic arc (Nahodilová et al., 2012). In contrast, Kusbach et al. (2012) based on a detailed microstructural study of peridotites and granulites argue that the orogenic lower crust was entirely mechanically decoupled from the underlying mantle during the indentation event. These data are more relevant to our modelling as the study area of Kusbach et al. (2012) is located close to the indentor and records the tectonic evolution related to the indentation process. These authors suggest that only small fragments were mechanically detached from the underlying mantle basement. In agreement with this model we have adapted our modelling strategy and assumed a mechanically strong mantle basement and a weak lower crust.

Models of continental collision often show significant deformation within the mantle (e.g. lithospheric delamination, Gray and Pysklywec, 2012) and of the crust–mantle boundary (e.g. lithospheric folding, Burg and Podladchikov, 1999). However, the wavelength of the lithospheric folding would be presumably significantly larger than that of the folding governed by the mafic middle crust included in our model. In addition, no ultramafic bodies are found in the cores of the observed crustal antiforms (Chopin et al., 2012; Franěk et al., 2011a). The signature of lithospheric delamination is not in agreement with the observed syn-orogenic thermal evolution of the region (Lexa et al., 2011), although it can be related to post-orogenic melting (Finger et al., 2009). Moreover, numerical models by Gray and Pysklywec (2012) suggest that a weak felsic lower crust can reduce the efficiency of lithospheric delamination during continental collision.

Some mechanisms observed in our crustal-scale model appear to be valid also in mantle-scale models. Faccenda et al. (2008) studied the effect of highly radioactive sedimentary material of the subducting plate accreted at the active continental margin during continental collision. Similarly to our results, the P–T paths reported by Faccenda et al. (2008) show that the timing of exhumation increases with lower radiogenic heating.

Despite its limitations, the model well reproduces the basic scenario of laterally forced upwelling of the felsic lower crust and its subsequent sub-horizontal flow over the indentor. For this reason, we consider the model being a good representation of crustal dynamics of such an orogenic system. At the same time we do not preclude other mechanisms of exhumation to operate, especially those related to anomalous heat supply from the mantle.

4.7 Conclusions

The presented numerical model is based on a scenario of formation of felsic HP granulites in the Bohemian Massif during the Variscan orogeny (e.g. Schulmann et al., 2009; Lexa et al., 2011), and simulates the exhumation of felsic lower crustal material during continental collision. Using different values of model parameters, we are able to interpret the contrasting character of the Moldanubian and Sudetic parts of the Bohemian Massif. The gravity-dominated models with a high heat production and a relatively slow convergence of colliding crustal blocks satisfactorily reproduce the structural and metamorphic evolution of the Moldanubian domain. Conversely, the data from the West Sudetes conform to the fold-dominated models characterized by a low heat production and/or rapid convergence.

The main differences between the gravity-dominated and fold-dominated systems are: 1) the proportion of mafic material surrounding felsic HP metamorphs, 2) peak temperatures leading to migmatization of rocks, 3) the presence of a temperature plateau corresponding to thermal equilibration at high pressures and character of subsequent cooling, and 4) the depth of the transition between the vertical and subhorizontal flow. Furthermore, our results predict a direct relation between the prograde P–T paths and the velocity of continental convergence. Even if the modern thermodynamic modelling made progress in determination of prograde metamorphic evolution, the data are still sparse and inaccurate. The possibility to estimate the convergence rate could be tested once such data are available.

The apparent difference between the Moldanubian and Sudetic parts can be related to their position within the Variscan orogenic belt. In a relatively smaller Sudetes domain, a similar closing velocity would lead to higher strain rates and shorter time for thermal maturation. The second key parameter, concentration of radioactive elements, may be smaller in the West Sudetes granulites due to their more mafic composition in comparison to those in the Moldanubian domain (Štípská et al., 2004). The heat budget and the rate of deformation in the model orogen are influenced also by the thickness of the heat-productive lower crust and its lateral extent. A smaller volume of the heat-productive material would lower the total heat budget and the resulting model will presumably favour fold-dominated behaviour. As there are systematic variations in the proportion of the light felsic crust across the Bohemian Massif inferred from gravity anomalies, the influence of the thickness of the heat-productive layer should be systematically studied.

The presented model is only a first step in understanding the HP granulite formation, and improvements shall be introduced in a future study. In particular, the interaction between the crust and the mantle and the role of rheological properties are of major concern.

Acknowledgments:
The Charles University is acknowledged for supporting P. Maierová (projects Nos. GAUK 432911 and SVV-2012-265308) and O. Lexa (SVV-263203). O. Lexa was also supported by the Czech Science Foundation (205/09/0539). Activities of the Center for Lithospheric Research are co-financed by the Czech Ministry of Education, Youth and Sports (LK11202). Finite-element computations were performed using the Elmer software developed by CSC—IT Center for Science (http://www.csc.fi-/english/pages/elmer). We greatly appreciate the contribution of Ondřej Čadek during discussions on the numerical model setup and broader geophysical aspects. We would like to thank Thibault Duretz, Manuele Faccenda and the editor Taras Gerya for their constructive comments.

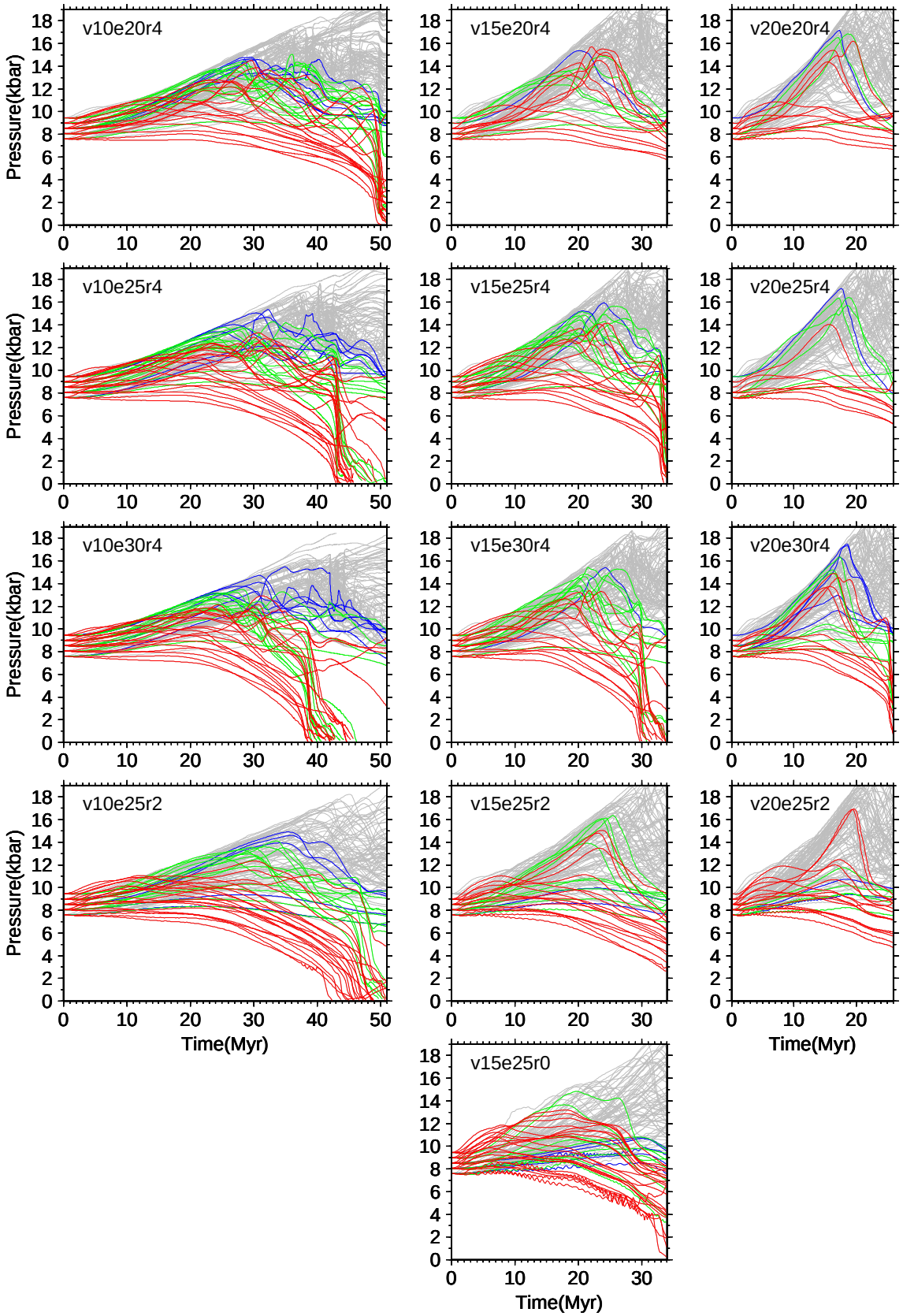

Supplementary Figure S1: P–t paths of material particles of the FLC for all models considered. The name of the model corresponding to the first column in Table 4.2 is written in the top left corner of each panel. The colour-coding of individual paths is the same as in Fig. 4.7.

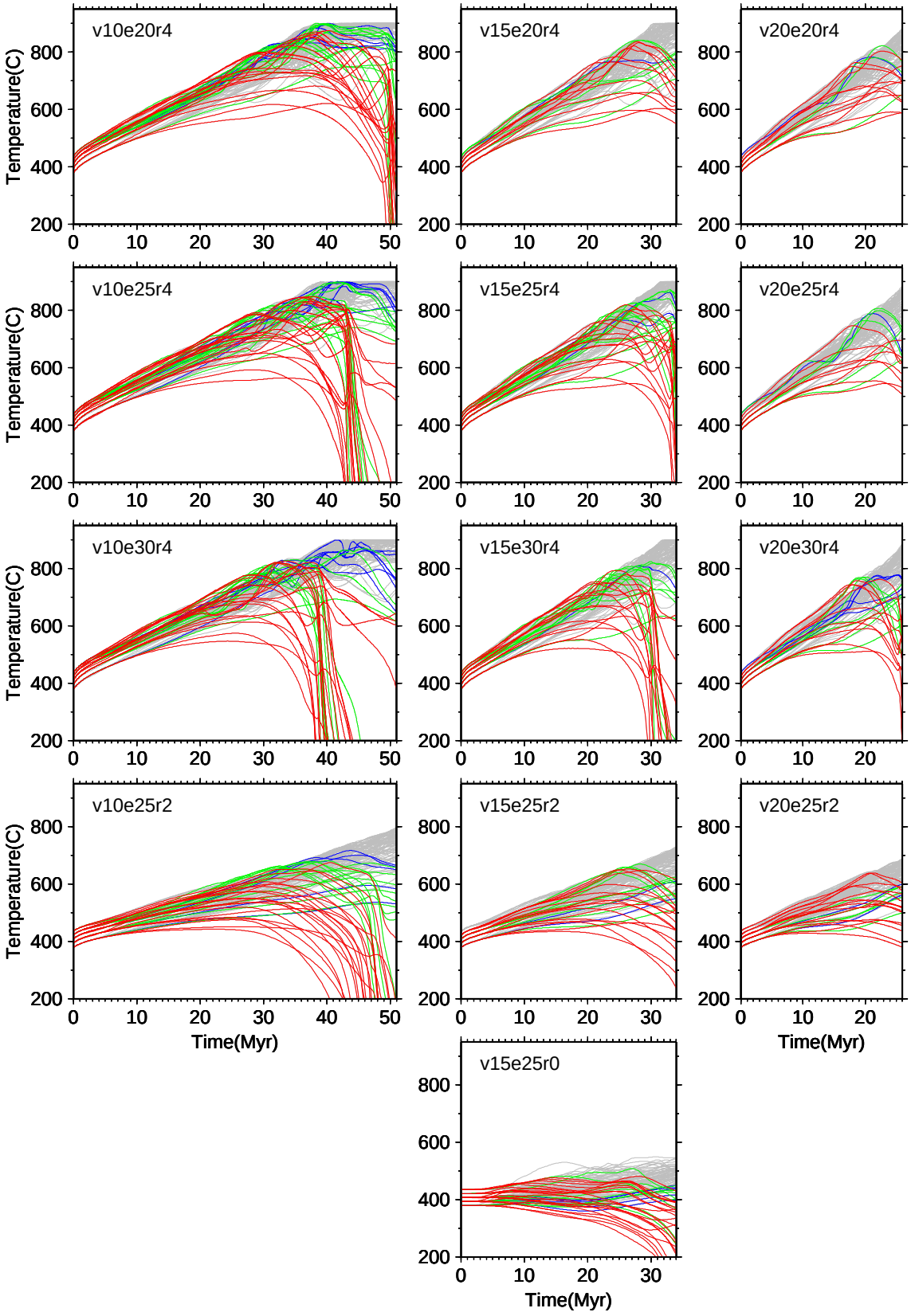

Supplementary Figure S2: T–t paths of material particles of the FLC for all models considered. The name of the model corresponding to the first column in Table 4.2 is written in the top left corner of each panel. The colour-coding of individual paths is the same as in Fig. 4.7.

4.8 References

Allemand, P., Lardeaux, J.M., 1997. Strain partitioning and metamorphism in a deformable orogenic wedge; application to the Alpine belt, In: Schulmann, K. (Ed.), Thermal and mechanical interactions in deep-seated rocks. Elsevier, Amsterdam, Netherlands, pp. 157–169.

Anczkiewicz, R., Szczepański, J., Mazur, S., Storey, C., Crowley, Q., Villa, I., Thirlwall, M., Jeffries, T., 2007. Lu–Hf geochronology and trace element distribution in garnet: Implications for uplift and exhumation of ultra-high pressure granulites in the Sudetes, SW Poland. Lithos 95, 363–380.

Babeyko, A.Y., Sobolev, S.V., Vietor, T., Oncken, O., Trumbull, R.B., 2006. Numerical study of weakening processes in the central Andean back-arc, In: Oncken, O., Chong, G., Franz, G., Giese, P., Götze, H.-J., Ramos, V.A., Strecker, M., Wigger, P. (Eds.), The Andes - Active Subduction Orogeny. Springer, Berlin, pp. 495–512.

Babuška, V., Plomerová, J., 2012. Boundaries of mantle-lithosphere domains in the Bohemian Massif as extinct exhumation channels for high-presssure rocks. Gondwana Research http://dx.doi.org/10.1016/j.gr.2012.07.005.

Beaumont, C., Nguyen, M.H., Jamieson, R.A., Ellis, S., 2006. Crustal flow modes in large hot orogens. Geological Society, London, Special Publications 268, 91–145.

Beaumont, C., Jamieson, R.A., Nguyen, M.H., 2010. Models of large hot orogens containing a collage of reworked and accreted terranes, In: Clowes, R.M., Skulski, T. (Eds.), Lithoprobe Synthesis II, Parameters, Processes and the Evolution of a Continent. Canadian Journal of Earth Sciences 47, 485–515.

Behr, H., 1978. Subfluenz-Prozesse im Grundgebirgs-Stockwerk Mitteleuropas. Zeitschrift der Deutschen Gesellschaft für Geowissenschaften 129, 283–318.

Brown, M., 2006. Duality of thermal regimes is the distinctive characteristic of plate tectonics since the Neoarchean. Geology 34, 961–964.

Brown, M., 2007. Metamorphic conditions in orogenic belts: a record of secular change. International Geology Review 49, 193–234.

Brown, M., 2010. Paired metamorphic belts revisited. Gondwana Research 18, 46–59.

Buiter, S.J.H., Babeyko, A.Y., Ellis, S., Gerya, T.V., Kaus, B.J.P., Kellner, A., Schreurs, G., Yamada, Y., 2006. The numerical sandbox: comparison of model results for a shortening and an extension experiment. Geological Society, London, Special Publications 253, 29–64.

Burg, J.P., Podladchikov, Y., 1999. Lithospheric scale folding: numerical modelling and application to the Himalayan syntaxes. International Journal of Earth Sciences 88, 190–200.

Burov, E., Yamato, P., 2008. Continental plate collision, P–T–t–z conditions and unstable vs. stable plate dynamics: insights from thermo-mechanical modelling. Lithos 103, 178–204.

Carswell, D., O'Brien, P., 1993. Thermobarometry and geotectonic significance in the Moldanubian Zone of the Bohemian Massif in Lower Austria. Journal of Petrology 34, 427–459.

Chopin, F., Schulmann, K., Skrzypek, E., Lehmann, J., Dujardin, J.R., Martelat, J.E., Lexa, O., Corsini, M., Edel, J.B., Štípská, P., 2012. Crustal influx, indentation, ductile thinning and gravity redistribution in a continental wedge: Building a Moldanubian mantled gneiss dome with underthrust Saxothuringian material (European Variscan belt). Tectonics 31, TC1013, doi: 1010.1029/2011TC002951.

Cooke, R., 2000. High-pressure/temperature metamorphism in the St. Leonhard Granulite Massif, Austria: evidence from intermediate pyroxene-bearing granulites. International Journal of Earth Sciences 89, 631–651.

Culshaw, N., Beaumont, C., Jamieson, R., 2006. The orogenic superstructure-infrastructure concept: Revisited, quantified, and revived. Geology 34, 733–736.

Dallmeyer, D., Neubauer, F., Höck, V., 1992. Chronology of late Paleozoic tectonothermal activity in the southeastern Bohemian Massif, Austria(Moldanubian and Moravo-Silesian zones): 40Ar/39Ar mineral age controls. Tectonophysics 210, 135–153.

Don, J., Dumicz, M., Wojciechowska, I., Zelazniewicz, A., 1990. Lithology and tectonics of the Orlica–Snieznik dome, Sudetes—recent state of knowledge. Neues Jahrbuch für Geologie und Paläontologie, Abhandlungen 179, 159–188.

Duchene, S., Lardeaux, J.M., Albarede, F., 1997. Exhumation of eclogites: insights from depth-time path analysis. Tectonophysics 280, 125–140.

Duretz, T., Kaus, B.J.P., Schulmann, K., Gapais, D., Kermarrec, J.-J., 2011. Indentation as an extrusion mechanism of lower crustal rocks: Insight from analogue and numerical modelling, application to the Eastern Bohemian Massif. Lithos 124, 158–168.

England, P.C., Thompson, A.B., 1984. Pressure temperature time paths of regional metamorphism. 1. Heat-transfer during the evolution of regions of thickened continental crust. Journal of Petrology 25, 894–928.

Faccenda, M., Gerya, T.V., Chakraborty, S., 2008. Styles of post-subduction collisional orogeny: Influence of convergence velocity, crustal rheology and radiogenic heat production. Lithos 103, 257–287.

Faryad, S.W., Jedlička, R., Ettinger, K., 2012. Subduction of lithospheric upper mantle recorded by solid phase inclusions and compositional zoning in garnet: example from the Bohemian Massif. Gondwana Research http://dx.doi.org/10.1016/j.gr.2012.05.014.

Fiala, J., Matějovská, O., Vaňková, V., 1987. Moldanubian granulites: source material and petrogenetic considerations. Neues Jahrbuch für Mineralogie, Abhandlungen 157, 133–165.

Finger, F., Gerdes, A., René, M., Riegler, G., 2009. The Saxo-Danubian Granite Belt: magmatic response to postcollisional delamination of mantle lithosphere below the southwestern sector of the Bohemian Massif (Variscan orogen). Geologica Carpathica 60, 205–212.

Franěk, J., Schulmann, K., Lexa, O., Tomek, Č., Edel, J.B., 2011a. Model of synconvergent extrusion of orogenic lower crust in the core of the Variscan belt: implications for exhumation of high-pressure rocks in large hot orogens. Journal of Metamorphic Geology 29, 53–78.

Franěk, J., Schulmann, K., Lexa, O., Ulrich, S., Štípská, P., Haloda, J., Týcová, P., 2011b. Origin of felsic granulite microstructure by heterogeneous decomposition of alkali feldspar and extreme weakening of orogenic lower crust during the Variscan orogeny. Journal of Metamorphic Geology 29, 103–130.

Franke, W., 2000. The mid-European segment of the Variscides: tectonostratigraphic units, terrane boundaries and plate tectonic extension, In: Franke W., Altherr R., Haak V., Oncken O., Tanner D. (Eds.), Orogenic Processes: Quantification and Modelling in the Variscan Belt. Geological Society of London, Special Publication 179, 35–61.

Friedl, G., Cooke, R.A., Finger, F., McNaughton, N.J., Fletcher, I.R., 2011. Timing of Variscan HP-HT metamorphism in the Moldanubian Zone of the Bohemian Massif: U-Pb SHRIMP dating on multiply zoned zircons from a granulite from the Dunkelsteiner Wald Massif, Lower Austria. Mineralogy and Petrology, 1–13.

Fullsack, P., 1995. An arbitrary Lagrangian-Eulerian formulation for creeping flows and its application in tectonic models. Geophysical Journal International 120, 1–23.

Gerya, T., Stockhert, B., 2006. Two-dimensional numerical modeling of tectonic and metamorphic histories at active continental margins. International Journal of Earth Sciences 95, 250–274.

Gray, R., Pysklywec, R.N., 2012. Geodynamic models of mature continental collision:

Evolution of an orogen from lithospheric subduction to continental retreat/delamination. Journal of Geophysical Research 117, B03408, doi:10.1029/2011JB008692.

Guilmette, C., Indares, A., Hébert, R., 2011. High-pressure anatectic paragneisses from the Namche Barwa, Eastern Himalayan Syntaxis: Textural evidence for partial melting, phase equilibria modeling and tectonic implications. Lithos 124, 66–81.

Guy, A., Edel, J.-B., Schulmann, K., Tomek, Č., Lexa, O., 2011. A geophysical model of lower crustal structure of the Palaezoic crustal root (Bohemian Massif): implications for modern collisional orogens. Lithos 124, 144–157.

Hacker, B.R., Kelemen, P.B., Behn, M.D., 2011. Differentiation of the continental crust by relamination. Earth and Planetary Science Letters 307, 501–516.

Harley, S.L., 2008. Refining the P–T records of UHT crustal metamorphism. Journal of Metamorphic Geology 26, 125–154.

Hasalová, P., Štípská, P., Powell, R., Schulmann, K., Janoušek, V., Lexa, O., 2008. Transforming mylonitic metagranite by open-system interactions during melt flow. Journal of Metamorphic Geology 26, 55–80.

Henry, P., Le Pichon, X., Goffé, B., 1997. Kinematic, thermal and petrological model of the Himalayas: constraints related to metamorphism within the underthrust indian crust and topographic elevation. Tectonophysics 273, 31–56.

Hirth, G., Teyssier, C., Dunlap, W.J., 2001. An evaluation of quartzite flow laws based on comparisons between experimentally and naturally deformed rocks. International Journal of Earth Sciences 90, 77–87.

Indares, A., Dunning, G., Cox, R., Gale, D., Connelly, J., 1998. High-pressure, high-temperature rocks from the base of thick continental crust: geology and age constraints from the Manicouagan Imbricate Zone, eastern Grenville Province. Tectonics 17, 426–440.

Jamieson, R.A., Beaumont, C., Medvedev, S., Nguyen, M.H., 2004. Crustal channel flows: 2. Numerical models with implications for metamorphism in the Himalayan-Tibetan orogen. Journal of Geophysical Research 109, B06407, doi: 10.1029/2003JB002811.

Jamieson, R.A., Beaumont, C., Nguyen, M.H., Culshaw, N.G., 2007. Synconvergent ductile flow in variable-strength continental crust: numerical models with application to the western Grenville orogen. Tectonics 26, 1–23.

Janoušek, V., Finger, F., Roberts, M., Frýda, J., Pin, C., Dolejš, D., 2004. Deciphering the petrogenesis of deeply buried granites: whole-rock geochemical constraints on the origin of largely undepleted felsic granulites from the Moldanubian Zone of the Bohemian Massif. Transactions of the Royal Society of Edinburgh, Earth Sciences 95, 141–159.

Keppie, J.D., Nance, R.D., Murphy, J.B., Dostal, J., Braid, J.A., 2010. The high-pressure Iberian-Czech belt in the Variscan orogen: Extrusion into the upper (Gondwanan) plate? Gondwana Research 17, 306–316.

Konopásek, J., Schulmann, K., 2005. Contrasting Early Carboniferous field geotherms: evidence for accretion of a thickened orogenic root and subducted Saxothuringian crust (Central European Variscides). Journal of the Geological Society 162, 463–470.

Kotková, J., Harley, S., 1999. Formation and evolution of high-pressure leucogranulites: experimental constraints and unresolved issues. Physics and Chemistry of the Earth, Part A 24, 299–304.

Kotková, J., Kröner, A., Todt, W., Fiala, J., 1996. Zircon dating of North Bohemian granulites, Czech Republic: further evidence for the Lower Carboniferous high-pressure event in the Bohemian Massif. Geologische Rundschau 85, 154–161.

Kotková, J., O'Brien, P.J., Ziemann, M.A., 2011. Diamond and coesite discovered in Saxony-type granulite: Solution to the Variscan garnet peridotite enigma. Geology 39, 667–670.

Kröner, A., O'Brien, P., Nemchin, A., Pidgeon, R., 2000. Zircon ages for high pressure

granulites from South Bohemia, Czech Republic, and their connection to Carboniferous high temperature processes. Contributions to Mineralogy and Petrology 138, 127–142.
Kusbach, V., Ulrich, S., Schulmann, K., 2012. Ductile deformation and rheology of subcontinental mantle in a hot collisional orogeny: Example from the Bohemian Massif. Journal of Geodynamics 56-57, 108–123, doi: 10.1016/j.jog.2011.06.004.
Lexa, O., Schulmann, K., Janoušek, V., Štípská, P., Guy, A., Racek, M., 2011. Heat sources and trigger mechanisms of exhumation of HP granulites in Variscan orogenic root. Journal of Metamorphic Geology 29, 79–102.
Machek, M., Ulrich, S., Janoušek, V., 2009. Strain coupling between upper mantle and lower crust: natural example from the Běstvina granulite body, Bohemian Massif. Journal of Metamorphic Geology 27, 721–737.
Mackwell, S.J., Zimmerman, M.E., Kohlstedt, D.L., 1998. High-temperature deformation of dry diabase with application to tectonics on Venus. Journal of Geophysical Research 103, 975–984.
Maierová, P., Čadek, O., Lexa, O., Schulmann, K., 2012. A numerical model of exhumation of the orogenic lower crust in the Bohemian Massif during the Variscan orogeny. Studia Geophysica et Geodaetica 56, 595–619.
Mazur, S., Szczepański, J., Turniak, K., McNaughton, N.J., 2012. Location of the Rheic suture in the eastern Bohemian Massif: evidence from detrital zircon data. Terra Nova 24, 199–206.
Nahodilová, R., Štípská, P., Powell, R., Košler, J., Racek, M., 2012. High-Ti muscovite as a prograde relict in high pressure granulites with metamorphic Devonian zircon ages (Běstvina granulite body, Bohemian Massif): Consequences for the relamination model of subducted crust. Gondwana Research http://dx.doi.org/10.1016/j.gr.2012.08.021.
O'Brien, P.J., Rötzler, J., 2003. High-pressure granulites: formation, recovery of peak conditions and implications for tectonics. Journal of Metamorphic Geology 21, 3–20.
Petrakakis, K., 1997. Evolution of Moldanubian rocks in Austria: review and synthesis. Journal of Metamorphic Geology 15, 203–222.
Pin, C., Vielzeuf, D., 1983. Granulites and related rocks in Variscan median Europe: a dualistic interpretation. Tectonophysics 93, 47–74.
Prince, C.I., Košler, J., Vance, D., Günther, D., 2000. Comparison of laser ablation ICP-MS and isotope dilution REE analyses – implications for Sm-Nd garnet geochronology. Chemical Geology 168, 255–274.
Racek, M., Štípská, P., Pitra, P., Schulmann, K., Lexa, O., 2006. Metamorphic record of burial and exhumation of orogenic lower and middle crust: a new tectonothermal model for the Drosendorf window (Bohemian Massif, Austria). Mineralogy and Petrology 86, 221–251.
Racek, M., Štípská, P., Powell, R., 2008. Garnet-clinopyroxene intermediate granulites in the St. Leonhard massif of the Bohemian Massif: ultrahigh-temperature metamorphism at high pressure or not? Journal of Metamorphic Geology 26, 253–271.
Ranalli, G., 1995. Rheology of the Earth, 2nd Edition. Chapman and Hall, London, United Kingdom. Schulmann, K., Konopásek, J., Janoušek, V., Lexa, O., Lardeaux, J., Edel, J., Štípská, P., Ulrich, S., 2009. An Andean type Palaeozoic convergence in the Bohemian Massif. Comptes Rendus-Géoscience 341, 266–286.
Schulmann, K., Kröner, A., Hegner, E., Wendt, I., Konopásek, J., Lexa, O., Štípská, P., 2005. Chronological constraints on the pre-orogenic history, burial and exhumation of deep-seated rocks along the eastern margin of the Variscan orogen, Bohemian Massif, Czech Republic. American Journal of Science 305, 407–448.
Schulmann, K., Lexa, O., Štípská, P., Racek, M., Tajčmanová, L., Konopásek, J., Edel, J.B., Peschler, A., Lehmann, J., 2008. Vertical extrusion and horizontal channel flow of orogenic lower crust: key exhumation mechanisms in large hot orogens? Journal of

Metamorphic Geology 26, 273–297.
Skrzypek, E., Štípská, P., Schulmann, K., Lexa, O., Lexová, M., 2011. Prograde and retrograde metamorphic fabrics–a key for understanding burial and exhumation in orogens (Bohemian Massif). Journal of Metamorphic Geology 29, 451–472.
Štípská, P., Chopin, F., Skrzypek, E., Schulmann, K., Pitra, P., Lexa, O., Martelat, J.E., Bollinger, C., Žáčková, E., 2012. The juxtaposition of eclogite and mid-crustal rocks in the Orlica–Śnieżnik Dome, Bohemian Massif. Journal of Metamorphic Geology 30, 213–234.
Štípská, P., Powell, R., 2005a. Constraining the PT path of a MORB-type eclogite using pseudosections, garnet zoning and garnet-clinopyroxene thermometry: an example from the Bohemian Massif. Journal of Metamorphic Geology 23, 725–743.
Štípská, P., Powell, R., 2005b. Does ternary feldspar constrain the metamorphic conditions of high-grade meta-igneous rocks? Evidence from orthopyroxene granulites, Bohemian Massif. Journal of Metamorphic Geology 23, 627–647.
Štípská, P., Schulmann, K., Kröner, A., 2004. Vertical extrusion and middle crustal spreading of omphacite granulite: a model of syn-convergent exhumation (Bohemian Massif, Czech Republic). Journal of Metamorphic Geology 22, 179–198.
Štípská, P., Schulmann, K., Powell, R., 2008. Contrasting metamorphic histories of lenses of high-pressure rocks and host migmatites with a flat orogenic fabric (Bohemian Massif, Czech Republic): a result of tectonic mixing within horizontal crustal flow? Journal of Metamorphic Geology 26, 623–646.
Svojtka, M., Košler, J., Venera, Z., 2002. Dating granulite-facies structures and the exhumation of lower crust in the Moldanubian Zone of the Bohemian Massif. International Journal of Earth Sciences 91, 373–385.
Tajčmanová, L., Konopásek, J., Schulmann, K., 2006. Thermal evolution of the orogenic lower crust during exhumation within a thickened Moldanubian root of the Variscan belt of Central Europe. Journal of Metamorphic Geology 24, 119–134.
Tajčmanová, L., Soejono, I., Konopásek, J., Košler, J., Klötzli, U., 2010. Structural position of high-pressure felsic to intermediate granulites from NE Moldanubian domain (Bohemian Massif). Journal of the Geological Society 167, 329–345.
van Breemen, O., Aftalion, M., Bowes, D., Dudek, A., Mísař, Z., Povondra, P., Vrána, S., 1982. Geochronological studies of the Bohemian Massif, Czechoslovakia, and their significance in the evolution of Central Europe. Transactions of the Royal Society of Edinburgh, Earth Sciences 73, 89–108.
Verner, K., Žák, J., Nahodilová, R., Holub, F., 2008. Magmatic fabrics and emplacement of the cone-sheet-bearing Knížecí Stolec durbachitic pluton (Moldanubian Unit, Bohemian Massif): implications for mid-crustal reworking of granulitic lower crust in the Central European Variscides. International Journal of Earth Sciences 97, 19–33.
Vrána, S., 1989. Perpotassic granulites from southern Bohemia. Contributions to Mineralogy and Petrology 103, 510–522.
Wegmann, C., 1935. Zur Deutung der Migmatite. Geologische Rundschau 26, 305–350.
Zeng, L., Gao, L.E., Dong, C., Tang, C., 2012. High-pressure melting of metapelite and the formation of Ca-rich granitic melts in the Namche Barwa Massif, southern Tibet. Gondwana Research 21, 138–151.

Conclusions and perspectives

The Bohemian Massif consists of micro-plates assembled during a large mountain-building process called the Variscan orogeny (∼400–300 Ma). The formation of the Bohemian Massif was rather complicated and involved oceanic and continental subductions followed by continental collision. The oceanic subduction is documented by relics of the oceanic crust and by rocks that reveal metamorphism along a cold geotherm. Besides that, there is a remarkable volume of relatively light (felsic) rocks metamorphosed under high-pressure and high-temperature conditions now exposed at the surface. Based on observations of the structure and metamorphism of these rocks some authors (Schulmann et al., 2009; Lexa et al., 2011) proposed that during the continental collision the rocks were vertically displaced from ∼60 km to the middle crust and later subjected to (sub)horizontal flow. Lexa et al. (2011) further suggested, that the felsic material could have been emplaced to the lower crustal depth during the preceding continental subduction. The main goal of the presented study was to establish a numerical model of exhumation of these rocks.

We developed a computational tool suitable for modeling of crustal deformation during continental collision (Chapter 2). As a starting point, we used the multi-physical finite-element software Elmer (http://www.csc.fi/english/pages/elmer), in which we implemented main features of crustal deformation. This extended version of the Elmer software can treat the flow of materials with different properties (density, heat productivity, rheological parameters), visco-plastic rheology simulating the brittle-ductile character of crustal deformation, and surface processes (erosion and sedimentation of material). Testing of the software on several simple setups gives results comparable to those calculated by other numerical methods and published in scientific literature.

Using the software, we modeled convergence of two crustal blocks, one of which contains a layer of an anomalous felsic (light, rheologically weak and rich in radiogenic elements) material in the lower crust (Chapter 3). The lateral shortening of the domain leads to folding of the felsic layer and undulation of its upper boundary. As the felsic material is buoyant with respect to the overlying (partly mafic) layers, the folds are amplified by gravity forcing and gradually develop into diapiric upwellings. Subsequently, the rheologically weak felsic material forms a flat zone of deformation which is underthrusted by a tip of the second continental block. The numerical model shows that the scenario proposed by Schulmann et al. (2009) and Lexa et al. (2011) is dynamically feasible. Characteristics of the numerical model (topography evolution and related sedimentation, timing of the process, pressure-temperature paths) are in general agreement with those inferred from the geological record. The radiogenic heat sources within the crust in combination with tectonic stresses provide enough energy for deformation and metamorphism of rocks observed in the

Bohemian Massif. This means that delamination of the lithosphere is not required in order to reach high temperatures of ∼850 °C at pressures of ∼1.8 GPa.

The model with the stages of the vertical and horizontal flow is applicable only to the central — Moldanubian — part of the Bohemian Massif. The northern Lugian (also called Sudetic) part is similar to the Moldanubian domain, but it is significantly smaller and lacks structures related to the horizontal flow. Besides that, a belt of mafic rocks is associated with the highly metamorphosed core in the Lugian domain. In Chapter 4, we varied model parameters (velocity of convergence of the two crustal blocks, heat productivity of the felsic lower crust, rate of surface erosion) and obtained a family of models with distinct characteristics. According to the deformational style and pressure–temperature evolution calculated in individual models, two end-member types can be distinguished. The gravity-dominated type of models was already described in Chapter 3. Its multi-stage evolution is comparable to that of the Moldanubian domain, and it requires high radiogenic heating and/or a slow velocity of convergence. When low heating and/or rapid convergence is applied, the folding of the felsic material and the overlying layers is more persistent. These fold-dominated models show a gradual evolution without a distinct phase of horizontal flow. The exhumed material records lower peak temperatures and shorter time of residence at high pressure and temperature. Importantly, a continuous layer of mafic material surrounding the felsic upwellings is preserved, in line with the observations from the Lugian domain. The parametric study supports the hypothesis of a similar origin of the Moldanubian and Lugian domains and provides an interpretation of the differences between these two regions. The difference in the rate of deformation and amount of heat sources between the Moldanubian and Lugian domains can be related to their size and position within the orogen. In the Lugian domain, a smaller volume of the heat-productive material would lower the total heat budget and favor the fold-dominated behavior. In addition, its smaller lateral extent would lead to a higher deformational rate.

We investigated the role of three selected parameters only, while many others may be important. The most challenging task is an appropriate rheological description of the crustal material. Not only that the values of rheological parameters of different rock types are largely unknown (Burov, 2011), but even the rock types change due to melting or recrystallization. In the Bohemian Massif, there is an evidence that the flow of the felsic highly-metamorphosed rocks was governed by diffusion creep accommodated by grain-boundary sliding (Franěk et al., 2011). Involvement of this deformational mechanism would cause strain weakening, and may significantly influence strain partitioning within the crust. Diffusion creep of crustal material is currently neglected in numerical models, although it may have important consequences on crustal deformation.

It should be noted that we explored only one stage of one possible evolutionary scenario. In a future study, more attention shall be paid to the previous stage of continental subduction, when the felsic material was emplaced into the lower crust. The model of continental subduction can be rather complicated, because several small plates were probably accreted during the orogeny. Moreover, a large-scale (e.g. upper-mantle scale) model is required for treatment of lithospheric and sublithospheric mantle flow. The large-scale model could be used also for investigation the processes that caused detachment and exhumation of pieces of mantle material during the orogeny. With a reasonable approximation of melt generation and migra-

tion, the melting of the mantle, recorded in several plutons in the Bohemian Massif, could be studied.

Most of the issues outlined above require significant modifications of the modeling approach and the applied software. At the same time, the current version of the software is easily applicable to a number of problems related to crustal and lithospheric deformation. A big advantage is the relatively user-friendly design of the Elmer software, which allows easy implementation of different kinds of model setups (e.g. oceanic subduction with variable thermal properties, Maierová et al., 2012). In the research of the tectonics of the Bohemian Massif, as well as in the other topics mentioned above, the more we know the more questions arise. Nevertheless, we believe that this study contributed to the understanding of the crustal deformation during continental collision.

Bibliography[1]

Arnold J., Jacoby W.R., Schmeling H. and Schott B., 2001. Continental collision and the dynamic and thermal evolution of the Variscan orogenic crustal root — numerical models. *J. Geodyn.,* **31**, 273–291.

Babuška V. and Plomerová J., 2001. Subcrustal lithosphere around the Saxothuringian–Moldanubian Suture Zone — a model derived from anisotropy of seismic wave velocities. *Tectonophysics,* **332**, 185–199.

Babuška V., Plomerová J. and Vecsey L., 2008. Mantle fabric of western Bohemian Massif (central Europe) constrained by 3D seismic P and S anisotropy. *Tectonophysics,* **462**, 149–163.

Babuška V. and Plomerová J., 2012. Boundaries of mantle–lithosphere domains in the Bohemian Massif as extinct exhumation channels for high-pressure rocks. *Gondwana Res.*, doi: http://dx.doi.org/10.1016/j.gr.2012.07.005.

Beaumont C., Jamieson R.A., Nguyen M.H. and Lee B., 2001. Himalayan tectonics explained by extrusion of a low-viscosity crustal channel coupled to focused surface denudation. *Nature,* **414**, 738–742.

Beaumont C., Jamieson R.A., Butler J.P. and Warren C.J., 2009. Crustal structure: A key constraint on the mechanism of ultra-high-pressure rock exhumation. *Earth Planet. Sci. Lett.,* **287**, 116–129.

Bentley C., 2010. [online] url: http://mountainbeltway.wordpress.com.

Běhounková, 2007. *Global and regional scale modeling of dynamic processes in the Earth's mantle.* Ph.D. thesis, Charles University in Prague, Prague, Czech Republic.

Bielik M., Kloska K., Meurers B., Švancara J., Wybraniec S., Fancsik T., Grad M., Grand T., Guterch A., Katona M., Krolikowski C., Mikuška J., Pašteka R., Petecki Z., Polechońska O., Ruess D., Szalaiová V., Šefara J. and Vozár J., 2006. Gravity anomaly map of the CELEBRATION 2000 region. *Geol. Carpath.*, **57**, 145–156.

Blecha V., Štemprok M. and Fischer T., 2009. Geological interpretation of gravity profiles through the Karlovy Vary granite massif (Czech Republic). *Stud. Geophys. Geod.,* **53**, 295–314.

Bos B. and Spiers C.J., 2001. Experimental investigation into the microstructural and mechanical evolution of phyllosilicate-bearing fault rock under conditions favouring pressure solution. *Journal of Structural Geology,* **23**, 1187–1202, doi: 10.1016/S0191-8141(00)00184-X.

Bousquet R., Oberhänsli R., Goffé B., Wiederkehr M., Koller F., Schmid S.M., Schuster R., Engi M., Berger A. and Martinotti G., 2008. Metamorphism of metasediments in the scale of an orogen: A key to the Tertiary geodynamic evo-

[1]The references for Chapters 3 and 4 are listed in Sections 3.7 and 4.8, respectively.

lution of the Alps. In: Siegesmund S., Fügenschuh B. and Froitzheim N. (Eds.), *Tectonic Aspects of the Alpine-Dinaride-Carpathian System.* Geol. Soc. London, Spec., **298**, 393–412.

Braun J. and Yamato P., 2010. Structural evolution of a three-dimensional, finite-width crustal wedge. *Tectonophysics,* **484**, 181–192.

Buiter S.J.H., Babeyko A.Y., Ellis S., Gerya T.V., Kaus B.J.P., Kellner A., Schreurs G. and Yamada Y., 2006. The numerical sandbox: Comparison of model results for a shortening and an extension experiment. In: Buiter S.J.H. and Schreurs G. (Eds.), *Analogue and Numerical Modelling of Crustal–Scale Processes.* Geol. Soc. London, Spec., **253**, 29–64.

Burov E.B., 2011. Rheology and strength of the lithosphere. *Marine and Petroleum Geology,* **28**, 1402–1443.

Burša M. and Pěč K., 1988. *Tíhové pole a dynamika Země.* Academia, Praha, Czech Republic, pp. 328. In Czech.

Byerlee J.D., 1978. Friction of rocks. *Pure Appl. Geophys.* **116**, 615–626.

Chlupáč I., 1993. *Geology of the Barrandian—A field trip guide.* Senckenberg-Buch 69, W. Kramer, Frankfurt, Germany, pp. 163.

Chlupáč I. and Štorch P. (Eds.), 1992. Regionálně geologické dělení Českého masívu na území České republiky. *Čas. Mineral. Geol.*, **37**, 258–275. In Czech.

Cloetingh S., van Wees J.D., Ziegler P.A., Lenkey L., Beekman F., Tesauro M., Förster A., Norden B., Kaban M., Hardebol N., Bonté D., Genter A., Guillou-Frottier L., Ter Voorde M., Sokoutis D., Willingshofer E., Cornu T. and Worum G., 2010. Lithosphere tectonics and thermo-mechanical properties: An integrated modelling approach for Enhanced Geothermal Systems exploration in Europe. *Earth-Science Reviews,* **102**, 159–206.

Čermák V., 1994. Results of heat flow studies in Czechoslovakia. In: Bucha V. and Blížkovský M. (Eds.), *Crustal Structure of the Bohemian Massif and West Carpathians.* Academia, Praha, Czech Republic, pp. 85–120.

Čížková H., van Hunen J., van den Berg A.P. and Vlaar N.J., 2002. The influence of rheological weakening and yield stress on the interaction of slabs with the 670 km discontinuity. *Earth Planet. Sci. Lett.,* **199**, 447–457.

Davis T.A., 2004. Algorithm 832: UMFPACK v4.3–An unsymmetric-pattern multifrontal method. *ACM Trans. Math. Softw.,* **30**, 196–199.

Deubelbeiss Y. and Kaus B.J.P., 2008. Comparison of Eulerian and Lagrangian numerical techniques for the Stokes equations in the presence of strongly varying viscosity. *Phys. Earth Planet. Inter.,* **171**, 92–111.

Dèzes P., Schmid S.M. and Ziegler P.A., 2004. Evolution of the European Cenozoic Rift System: interaction of the Alpine and Pyrenean orogens with their foreland lithosphere. *Tectonophysics,* **389**, 1–33.

Dieterich J., 1979. Modeling of rock friction 1. Experimental results and constitutive equations, *J. Geophys. Res.,* **84**, 2161–2168.

Donea J. and Huerta A., 2003. *Finite element methods for flow problems.* John Wiley and Sons Ltd., Chichester, United Kingdom, pp. 350.

Donea J., Huerta A., Ponthot J.-Ph. and Rodríguez-Ferran A., 2004. Arbitrary Lagrangian–Eulerian Methods. In: Stein E., de Borst R. and Hughes T.J.R (Eds.), *Encyclopedia of Computational Mechanics. Volume 1: Fundamentals.* John Wiley and Sons Ltd., New York, 1–25.

Dörr W. and Zulauf G., 2010. Elevator tectonics and orogenic collapse of a Tibetan-

style plateau in the European Variscides: the role of the Bohemian shear zone. *Int. J. Earth Sci. (Geol. Rundsch.),* **99**, 299–325.

Drost K., Linnemann U., McNaughton N., Fatka O., Kraft P., Gehmlich M., Tonk C. and Marek J., 2004. New data on the Neoproterozoic — Cambrian geotectonic setting of the Teplá–Barrandian volcano-sedimentary successions: geochemistry, U-Pb zircon ages, and provenance (Bohemian Massif, Czech Republic). *Int. J. Earth Sci. (Geol. Rundsch.),* **93**, 742–757.

Dudek A., 1980. The crystalline basement block of the Outer Carpathians in Moravia. *Rozpravy Československé Akademie Věd*, **90**, 1–85.

Duran A.F., 2000. *A numerical formulation to solve the ALE Navier-Stokes equations applied to the withdrawal of magma chambers.* Ph.D. thesis, Universitat Politècnica de Catalunya, Barcelona, España.

Duretz T.M., Kaus B.J.P., Schulmann K., Gapais D. and Kermarrec J.-J., 2011. Indentation as an extrusion mechanism of lower crustal rocks in the Eastern Bohemian Massif: Insight from analogue and numerical modelling. *Lithos*, **124**, 158–168.

Faccenda M., Gerya T.V. and Chakraborty S., 2008. Styles of post-subduction collisional orogeny: Influence of convergence velocity, crustal rheology and radiogenic heat production. *Lithos*, **103**, 257–287.

Finger F., Gerdes A., René M. and Riegler G., 2009. The Saxo-Danubian Granite Belt: magmatic response to postcollisional delamination of mantle lithosphere below the southwestern sector of the Bohemian Massif (Variscan orogen). *Geol. Carpath.*, **60**, 205–212.

Fischer T. and Horálek J., 2003. Space-time distribution of earthquake swarms in the principal focal zone of the NW Bohemia/Vogtland seismoactive region: period 1985–2001. *J. Geodyn.,* **35**, 125–144.

Fischer T., Horálek J., Michálek J. and Boušková A., 2010. The 2008 West Bohemia earthquake swarm in the light of the WEBNET network. *J. Seismol.,* **14**, 665–682.

Franca L.P. and Frey S.L., 1992. Stabilized Finite Element Methods: II. The Incompressible Navier-Stokes Equations. *Comput. Methods Appl. Mech. Engrg.*, **99**, 209–233.

Franěk J., Schulmann K., Lexa O., Ulrich S., Štípská P., Haloda J. and Týcová P., 2011. Origin of felsic granulite microstructure by heterogeneous decomposition of alkali feldspar and extreme weakening of orogenic lower crust during the Variscan orogeny. *J. Metamorphic Geol.,* **29**, 103–130.

Franke W., 2000. The mid-European segment of the Variscides: tectonostratigraphic units, terrane boundaries and plate tectonic extension. In: Franke W., Altherr R., Haak V., Oncken O. and Tanner D. (Eds.), *Orogenic Processes: Quantification and Modelling in the Variscan Belt*. Geol. Soc. London, Spec., **179**, 35–61.

Fullsack P., 1995. An arbitrary Lagrangian-Eulerian formulation for creeping flows and its application in tectonic models. *Geophys. J. Int.,* **120**, 1–23.

Gerdes A., Wörner G. and Henk A., 2000. Post-collisional granite generation and LT-HP metamorphism by radiogenic heating: The Variscan South Bohemian Batholith. *J. Geol. Soc. London,* **157**, 577–587.

Gerya T.V. and Yuen D.A., 2003. Characteristics-based marker-in-cell method with conservative finite-differences schemes for modeling geological flows with strongly variable transport properties. *Phys. Earth Planet. Inter.,* **140**, 293–318.

Gerya T.V., Perchuk L.L., Maresch W.V. and Willner A.P., 2004. Inherent gravita-

tional instability of hot continental crust: Implications for doming and diapirism in granulite facies terrains. In: Whitney D.L, Teyssier C. and Siddoway C.S. (Eds.), *Gneiss domes in orogeny: Boulder, Colorado. Geological Society of America Special Paper,* **380,** 97–115.

Gerya T.V., Connolly J.A.D. and Yuen D.A., 2008. Why is terrestrial subduction one-sided? *Geology,* **36**, 43–46, doi: 10.1130/G24060A.1.

Gerya T., 2010. Dynamical instability produces transform faults at mid-ocean ridges. *Science*, **329**, 1047–1050.

Guy A., Edel J.-B., Schulmann K., Tomek Č. and Lexa O., 2011. A geophysical model of the Variscan orogenic root (Bohemian Massif): Implications for modern collisional orogens. *Lithos*, **124**, 144–157.

Hacker B.R., Kelemen P.B. and Behn M.D., 2011. Differentiation of the continental crust by relamination. *Earth Planet. Sci. Lett.,* **307**, 501–516.

Hartley A.J. and Otava J., 2001. Sediment provenance and dispersal in a deep marine foreland basin: the Lower Carboniferous Culm Basin, Czech Republic. *J. Geol. Soc. London,* **158**, 137–150.

Henk A., 1997. Gravitational orogenic collapse vs plate-boundary stresses: a numerical modelling approach to the Permo-Carboniferous evolution of Central Europe. *Int. J. Earth Sci. (Geol. Rundsch.),* **86**, 39–55.

Heuer B., Geissler W.H., Kind R. and Kämpf H., 2006. Seismic evidence for asthenospheric updoming beneath the western Bohemian Massif, central Europe. *Geophys. Res. Lett.,* **33**, L05311, doi:10.1029/2005GL025158.

Holyoke C.W. and Tullis J., 2006. Formation and maintenance of shear zones. *Geology,* **34**, 105–108, doi: 10.1130/G22116.1.

Hrubcová P., Środa P., Špičák A., Guterch A., Grad M., Keller G.R., Brueckl E. and Thybo H., 2005. Crustal and uppermost mantle structure of the Bohemian Massif based on CELEBRATION 2000 data. *J. Geophys. Res.,* **110**, B11305.

Hrubcová P., Środa P. and CELEBRATION 2000 Working Group, 2008. Crustal structure at the easternmost termination of the Variscan belt based on CELEBRATION 2000 and ALP 2002 data. *Tectonophysics,* **460**, 55–75, doi: 10.1016-/j.tecto.2008.07.009.

Hrubcová P. and Geissler W.H., 2009. The crust-mantle transition and the Moho beneath the Vogtland/West Bohemian region in the light of different seismic methods. *Stud. Geophys. Geod.,* **53**, 275–294, doi: 10.1007/s11200-009-0018-6.

Huismans R.S. and Beaumont C., 2003. Symmetric and asymmetric lithospheric extension: Relative effects of frictional-plastic and viscous strain softening. *J. Geophys. Res.,* **108**, 2496, doi:10.1029/2002JB002026.

Jamieson R.A., Beaumont C., Nguyen M.H. and Culshaw N.G., 2007. Synconvergent ductile flow in variable-strength continental crust: Numerical models with application to the western Grenville orogen. *Tectonics,* **26**, TC5005, doi:10.1029/2006TC002036.

Janoušek V., Bowes D.R., Rogers G., Farrow C.M. and Jelínek E., 2000. Modelling diverse processes in the petrogenesis of a composite batholith: the Central Bohemian Pluton, Central European Hercynides. *J. Petrol.,* **41**, 511–543.

Janoušek V. and Holub F.V., 2007. The causal link between HP-HT metamorphism and ultrapotassic magmatism in collisional orogens: case study from the Moldanubian Zone of the Bohemian Massif. *Proceedings of the Geologists Association,* **118**, 75–86.

Jiménez-Munt I. and Platt J.P., 2006. Influence of mantle dynamics on the topographic evolution of the Tibetan Plateau: Results from numerical modeling. *Tectonophysics,* **25**, TC6002, doi:10.1029/2006TC001963.

Kalvoda J., Babek O., Fatka O., Leichmann J., Melichar R., Nehyba S. and Spacek P., 2008. Brunovistulian terrane (Bohemian Massif, Central Europe) from late Proterozoic to late Paleozoic: a review. *Int. J. Earth Sci. (Geol. Rundsch.),* **97**, 497–518, doi:10.1007/s00531-007-0183-1.

Karousová H., Plomerová J. and Babuška V., 2012. Three-dimensional velocity model of the crust of the Bohemian Massif and its effects on seismic tomography of the upper mantle. *Stud. Geophys. Geod.,* **56**, 249–267.

Katz R.F., Spiegelman M. and Holtzman B., 2006. The dynamics of melt and shear localization in partially molten aggregates. *Nature*, **442**, 676–679.

Katz R.F., 2008. Magma Dynamics with the Enthalpy Method: Benchmark Solutions and Magmatic Focusing at Mid-ocean Ridges. *J. Petrol.,* **49**, 2099–2121.

Kaus B., 2009. Factors that control the angle of shear bands in geodynamic numerical models of brittle deformation. *Tectonophysics,* **484**, 36–47.

Kolínský P., Málek J. and Brokešová J., 2011. Shear wave crustal velocity model of the Western Bohemian Massif from Love wave phase velocity dispersion. *J. Seismol.,* **15**, 81–104, doi: 10.1007/s10950-010-9209-4.

Konopásek J. and Schulmann K., 2005. Contrasting Early Carboniferous field geotherms: evidence for accretion of a thickened orogenic root and subducted Saxothuringian crust (Central European Variscides). *J. Geol. Soc. London,* **162**, 463–470.

Kopecký L., 1978. Neoidic taphrogenic evolution and young magmatism of the Bohemian Massif. *Sbor. Geol. Věd,* **26**, 91–107.

Kossmat F., 1927. Gliederung des variszischen Gebirgbaues. *Sächs. Geol. Landesamt Abh.,* **1**, 1–39. In German.

Kotková J., O'Brien P.J. and Ziemann M.A., 2011. Diamond and coesite discovered in Saxony-type granulite: Solution to the Variscan garnet peridotite enigma. *Geology,* **39**, 667–670.

Lemiale V., Mühlhaus H.-B., Moresi L. and Stafford J., 2008. Shear banding analysis of plastic models formulated for incompressible viscous flows. *Phys. Earth Planet. Inter.,* **171**, 177–186.

Lexa O., Schulmann K., Janoušek V., Štípská P., Guy A. and Racek M., 2011. Heat sources and trigger mechanisms of exhumation of HP granulites in Variscan orogenic root. *J. Metamorphic Geol.,* **29**, 79–102.

Linnemann U., McNaughton N.J., Romer R.L., Gehmlich M., Drost K. and Tonk C., 2004. West African provenance for Saxo-Thuringia (Bohemian Massif): Did Armorica ever leave pre-Pangean Gondwana? — U/Pb-SHRIMP zircon evidence and the Nd-isotopic record. *Int. J. Earth Sci. (Geol. Rundsch.),* **93**, 683–705.

Lorinczi P. and Houseman G., 2010. Geodynamical models of lithospheric deformation, rotation and extension of the Pannonian Basin of Central Europe. *Tectonophysics,* **492**, 73–87.

Maierová P., Chust T., Steinle-Neumann G., Čadek O. and Čížková H., 2012. The effect of variable thermal diffusivity on kinematic models of subduction. *J. Geophys. Res.,* **117**, B07202, doi:10.1029/2011JB009119.

Málek J., Janský J., Novotný O. and Rössler D., 2004. Vertically inhomogeneous models of the upper crustal structure in the West-Bohemian seismoactive region

inferred from the celebration 2000 refraction data. *Stud. Geophys. Geod.,* **48**, 709–730.

Matte P., 2001. The Variscan collage and orogeny (480–290 Ma) and the tectonic definition of the Armorica microplate: a review. *Terra Nova*, **13**, 122–128.

Martin Y. and Church M., 1997. Diffusion in landscape development models: On the nature of basic transport relations. *Earth Surf. Process. Landf.*, **22**, 273–279.

Mazur S., Aleksandrowski P., Kryza R. and Oberc-Dziedzic T., 2006. The Variscan Orogen in Poland. *Geological Quarterly,* **50**, 89–118.

McKerrow W.S., MacNiocail C., Ahlberg P.E., Clayton G., Cleal C.J. and Eagar M.C., 2000. The Late Palaeozoic relations between Gondwana and Laurussia. In: Franke W., Altherr R., Haak V., Oncken O. and Tanner D. (Eds.), *Orogenic Processes: Quantification and Modelling in the Variscan Belt.* Geol. Soc. London, Spec., **179**, 9–20.

Mlčoch B. and Konopásek J., 2010. Pre-Late Carboniferous geology along the contact of the Saxothuringian and Teplá-Barrandian zones in the area covered by younger sediments and volcanics (western Bohemian Massif, Czech Republic). *J. Geosci.,* **55**, 81–94.

Montgomery D.R. and Brandon M.T., 2002. Topographic controls on erosion rates in tectonically active mountain ranges. *Earth Planet. Sci. Lett.,* **201**, 481–489.

Novotný M., Skácelová Z., Mrlina J., Mlčoch B. and Růžek B., 2009. Depth-Recursive Tomography Along the Eger Rift Using the S01 Profile Refraction Data: Tested at the KTB Super Drilling Hole, Structural Interpretation Supported by Magnetic, Gravity and Petrophysical Data. *Surv. Geophys.*, **30**, 561–600.

Novotný M., 2011. Depth-Recursive Tomography of the Bohemian Massif at the CEL09 Transect—Part A: Resolution Estimates and Deblurring Aspects. *Surv. Geophys.*, **32**, 827–855.

Novotný O., 1996. A preliminary seismic model for the region of the west-Bohemian earthquake swarms. *Stud. Geophys. Geod.,* **40**, 353–366.

O'Brien P.J. and Rötzler J., 2003. High-pressure granulites: formation, recovery of peak conditions and implications for tectonics. *J. Metamorphic Geol.,* **21**, 3–20.

Odin G.S., 1994. Geological Time Scale. *C. R. Acad. Sci.,* **318**, 59–71.

Petrakakis K., 1997. Evolution of Moldanubian rocks in Austria: review and synthesis. *J. Metamorphic Geol.,* **15**, 203–222.

Pharaoh T.C., 1999. Palaeozoic terranes and their lithospheric boundaries within the Trans-European Suture Zone (TESZ): a review. *Tectonophysics,* **314**, 17–41.

Plomerová J., Achauer U., Babuška V., Vecsey L. and BOHEMA working group, 2007. Upper mantle beneath the Eger Rift (Central Europe): plume or asthenosphere upwelling? *Geophys. J. Int.,* **169**, 675–682.

Plomerová J., Vecsey L. and Babuška V., 2012. Mapping seismic anisotropy of the lithospheric mantle beneath the northern and eastern Bohemian Massif (central Europe). *Tectonophysics,* **564–565**, 38–53, doi:10.1016/j.tecto.2011.08.011.

Pokorný L. and Beneš L., 1997. Magnetic Field. In: Vrána S. and Štědrá V. (Eds.), *Geological Model of Western Bohemia Related to the KTB Borehole in Germany. J. Geol. Sci.,* **47**, 38–42.

Racek M., Štípská P., Pitra P., Schulmann K. and Lexa O., 2006. Metamorphic record of burial and exhumation of orogenic lower and middle crust: a new tectonothermal model for the Drosendorf window (Bohemian Massif, Austria). *Mineral. and Petrol.*, **86**, 221–251.

Ramberg H., 1981. *Gravity, deformation and the Earth's crust, 2nd Edn.* Academic Press, London, United Kingdom, pp. 452.

Ranalli G., 1995. *Rheology of the Earth, 2nd Edn.* Chapman and Hall, London, United Kingdom, pp. 413.

Rötzler J. and Romer R.L., 2001. P-T-t evolution of ultrahightemperature granulites from the Saxon Granulite Massif, Germany. Part I: Petrology. *J. Petrol.,* **42**, 1995–2013.

Ruh J.B., Kaus B.J.P and Burg J.-P., 2012. Numerical investigation of deformation mechanics in fold-and-thrust belts: Influence of rheology of single and multiple décollements. *Tectonics,* **31**, TC3005, doi:10.1029/2011TC003047.

Ruina A., 1883. Slip instability and state variable friction laws. *J. Geophys. Res.,* **88**, 10359–10370.

Russo A., 1996. Bubble stabilization of finite element methods for the linearized incompressible Navier-Stokes equations. *Comput. Methods Appl. Mech. Engrg.*, **132**, 335–343.

Růžek B., Hrubcová P., Novotný M., Špičák A. and Karousová H., 2007. Inversion of travel times obtained during active seismic refraction experiments CELEBRATION 2000, ALP 2002 and SUDETES 2003. *Stud. Geophys. Geod.,* **51**, 141–164.

Růžek B., Plomerová J. and Babuška V., 2012. Joint inversion of teleseismic P waveforms and surface-wave group velocities from ambient seismic noise in the Bohemian Massif. *Stud. Geophys. Geod.,* **56**, 107–140.

Sedlák J., Gnojek I., Scheibe R. and Zabadal S., 2009. Gravity response of igneous rocks in the northwestern part of the Bohemian Massif. *J. Geosci.,* **54**, 325–342.

Schmädicke E., Gose J. and Will M., 2010. The P–T evolution of ultra high temperature garnet-bearing ultramafic rocks from the Saxonian Granulitgebirge Core Complex, Bohemian Massif. *J. Metamorphic Geol.,* **28**, 489–508.

Schmeling H., Babeyko A.Y., Enns A., Faccenna C., Funiciello F., Gerya T., Golabek G.J., Grigull S., Kaus B.J.P., Morra G., Schmalholz S.M. and van Hunen J., 2008. A benchmark comparison of spontaneous subduction models—Towards a free surface. *Phys. Earth Planet. Inter.,* **171**, 198–223.

Schmid D.W. and Podladchikov Y.Y., 2003. Analytical solutions for deformable elliptical inclusions in general shear. *Geophys. J. Int.,* **155**, 269–288.

Schulmann K., Lexa O., Štípská P., Racek M., Tajčmanová L., Konopásek J., Edel J.-B., Peschler A. and Lehmann J., 2008. Vertical extrusion and horizontal channel flow of orogenic lower crust: key exhumation mechanisms in large hot orogens? *J. Metamorphic Geol.,* **26**, 273–297.

Schulmann K., Konopásek J., Janoušek V., Lexa O., Lardeaux J.-M., Edel J.-B., Štípská P. and Ulrich S., 2009. An Andean type Palaezoic convergence in the Bohemian Massif. *C. R. Geoscience*, **341**, 266–286.

Scovazzi G. and Hughes T.J.R., 2007. *Lecture notes on continuum mechanics on arbitrary moving domains.* [online] url: http://www.cs.sandia.gov/∼gscovaz-/publications/CMAMD_SANDarticle.pdf.

Suess F.E., 1912. Die moravischen Fenster und ihre Beziehung zum Grundgebirge des Hohen Gesenke. *Denkschrichte des Koeniglischen Akademie der Wissenschaft, Mathematik. Naturwissenschaft*, **12**, 541–631. In German.

Šalanský, 1994. Geologic interpretation of main geomagnetic structures in the Bohemian Massif. In: Bucha V. and Blížkovský M. (Eds.), *Crustal Structure of the Bohemian Massif and West Carpathians.* Academia, Praha, Czech Republic,

pp. 200–207.
Štěpančíková P., Hók J., Nývlt D., Dohnal J., Sýkorová I. and Stemberk J., 2010. Active tectonics research using trenching technique on the south-eastern section of the Sudetic Marginal Fault (NE Bohemian Massif, central Europe). *Tectonophysics,* **485**, 269–282.
Štípská P. and Powell R., 2005. Does ternary feldspar constrain the metamorphic conditions of high-grade meta-igneous rocks? Evidence from orthopyroxene granulites, Bohemian Massif. *J. Metamorphic Geol.,* **23**, 627–647.
Štípská P., Chopin F., Skrzypek E., Schulmann K., Pitra P., Lexa O., Martelat E., Bollinger C. and Žáčková E., 2012. The juxtaposition of eclogite and mid-crustal rocks in the Orlica–Snieznik Dome, Bohemian Massif. *J. Metamorphic Geol.,* **30**, 213–234.
Švancara J. and Chlupáčová M., 1997. Density model of geological structure along the profile 9HR. In: Vrána S. and Štědrá V. (Eds.), *Geological Model of Western Bohemia Related to the KTB Borehole in Germany. J. Geol. Sci.,* **47**, 32–35.
Tait J.A., Bachtadse V., Franke W. and Soffel H.C., 1997. Geodynamic evolution of the European Variscan fold belt: palaeomagnetic and geological constraints. *Int. J. Earth Sci. (Geol. Rundsch.),* **86**, 585–598.
Tomek Č., Dvořáková V. and Vrána S., 1997. Geological interpretation of the 9HR and 503 M seismic profiles in western Bohemia. In: Vrána S. and Štědrá V. (Eds.), *Geological Model of Western Bohemia Related to the KTB Borehole in Germany. J. Geol. Sci.,* **47**, 43–51.
Torsvik T.H., 1998. Palaeozoic palaeogeography: A North Atlantic viewpoint, *Geol. Foreh. Förh.,* **120**, 109–118.
Travis B.J., Anderson C., Baumgardner J., Gable C.W., Hager B.H., O'Connell R.J., Olson P., Raefsky A. and Schubert G., 1990. A benchmark comparison of numerical methods for infinite Prandtl number thermal convection in two-dimensional Cartesian geometry. *Geophys. Astrophys. Fluid Dynamics*, **55**, 137–160.
Turcotte D.L. and Schubert G., 2002. *Geodynamics, 2nd Edn.* Cambridge University Press. Cambridge, United Kingdom, pp. 456.
Ulrych J., Pivec E., Lang M., Balogh K. and Kropáček V., 1999. Cenozoic intraplate volcanic rock series of the Bohemian Massif: a review. *Geolines*, **9**, 123–129.
Ulrych J., Pešek J., Štěpánková–Svobodová J., Bosák P., Lloyd F.E., von Seckendorff V., Lang M. and Novák J.K., 2006. Permo-Carboniferous volcanism in late Variscan continental basins of the Bohemian Massif (Czech Republic): geochemical characteristics. *Chemie der Erde,* **66**, 37–56.
van Keken P.E., King S.D., Schmeling H., Christensen U.R., Neumeister D. and Doin M.-P., 1997. A comparison of methods for the modeling of thermomechanical convection. *J. Geophys. Res.,* **102**, 22477–22495.
Vanderhaeghe O., Medvedev S., Fullsack P., Beaumont C. and Jamieson R.A., 2003. Evolution of orogenic wedges and continental plateaux: insights from crustal thermal-mechanical models overlying subducting mantle lithosphere. *Geophys. J. Int.,* **153**, 27–51.
Venera Z., Schulmann K. and Kröner A., 2000. Intrusion within a transtensional tectonic domain: the Čistá granodiorite (Bohemian Massif)—structure and rheological modelling. *Journal of Structural Geology,* **22**, 1437–1454.
Watts A.B., 2001. *Isostasy and Flexure of the Lithosphere.* Cambridge University

Press. Cambridge, United Kingdom, pp. 480.

Wessel P. and Smith W.H.F., 1998. New, improved version of Generic Mapping Tools released. *EOS Trans. Amer. Geophys. U.,* **79**, 579, doi:10.1029/98EO00426.

Wilde-Piórko M., Saul J. and Grad M., 2005. Differences in the crustal and uppermost mantle structure of the Bohemian Massif from teleseismic receiver functions. *Stud. Geophys. Geod.,* **49**, 85–107.

Willet S.D., Slingerland R. and Hovius N., 2001. Uplift, shortening, and steady state topography in active mountain belts. *Am. J. Sci.*, **301**, 455–485.

Willner A.P., Sebazungu E., Gerya T.V., Maresch W.V. and Krohe A., 2002. Numerical modelling of PT-paths related to rapid exhumation of high-pressure rocks from the crustal root in the Variscan Erzgebirge Dome (Saxony, Germany). *J. Geodyn.,* **33**, 281–314.

Winchester J.A. and PACE TMR Network Team, 2002. Palaeozoic amalgamation of Central Europe: new results from recent geological and geophysical investigations. *Tectonophysics,* **360**, 5–21.

Ziegler P.A. and Dèzes P., 2007. Cenozoic uplift of Variscan Massifs in the Alpine foreland: Timing and controlling mechanisms. *Global Planet. Change,* **58**, 237–269.

Žák J., Kratinová Z., Trubač J., Janoušek V., Sláma J. and Mrlina J., 2011. Structure, emplacement, and tectonic setting of Late Devonian granitoid plutons in the Teplá-Barrandian unit, Bohemian Massif. *Int. J. Earth Sci. (Geol. Rundsch.),* **100**, 1477–1495.

List of tables

List of abbreviations

2D	two dimensions, two-dimensional
3D	three dimensions, three-dimensional
ALE	Arbitrary Lagrangian–Eulerian
AV	Avalonia
AR	Armorica
B, BM	Bohemian Massif
CBPC	Central Bohemian Plutonic Complex
CMPC	Central Moldanubian Plutonic Complex
CS	České středohoří
DH	Doupovské hory
FLC	felsic lower crust
HP	high-pressure
HT	high-temperature
ISTZ	infrastructure–superstructure transition zone
KVP	Karlovy Vary Pluton
MLC	Mariánské Lázně Complex
P–T	pressure–temperature
P–T–t	pressure–temperature–time
P–t	pressure–time
SG	Saxon Granulite Massif
T–t	temperature–time
TBU	Teplá-Barrandian Unit (domain)
UHT	ultra-high-temperature

Notation

$A,\ \tilde{A}$	pre-exponential parameters in stress–strain relation
α	slope of the topography
B	buoyancy of the crust
β	angle between the principal stress axis and vector $\mathbf{n}$
c_p	specific heat capacity at constant pressure
$\mathbf{c}$	convective velocity
$\{c_i\}$	composition of the i-th material
C	cohesion
C_0	initial cohesion
C_∞	final cohesion
d	measure of local relief of topography
D	flexural rigidity
$\{\mathbf{e}_x, \mathbf{e}_z\}$	two-dimensional Cartesian basis
E	erosion parameter
E_d	local diffusive-erosion parameter
E_A	activation energy in viscosity determination
$\dot{\boldsymbol{\epsilon}}$	strain-rate tensor
$\dot{\epsilon}$	effective strain rate
$\dot{\epsilon}_{\mathrm{II}} = \sqrt{1/2\ \dot{\boldsymbol{\epsilon}} : \dot{\boldsymbol{\epsilon}}}$	second invariant of the strain-rate tensor
ϵ_{II}	second invariant of the plastic-strain tensor
$\epsilon_0,\ \epsilon_\infty$	reference values of plastic strain
$F,\ \mathbf{F}$	arbitrary property (scalar, tensorial)
g	gravity acceleration
G	gravitational constant $\approx 6.674\times10^{-11}\ \mathrm{m^3 kg^{-1} s^{-2}}$
h	topography
Δh	correction of the topography due to surface processes
η	viscosity
η_{eff}	effective viscosity
η_0	pre-exponential parameter of viscosity
j	degree of Legendre polynomials
k	thermal conductivity
$l, \tilde{l}$	coefficients in Fourier series
L	crustal load
L_{ref}	reference crustal load
n	viscosity stress exponent
$\mathbf{n}$	normal vector to a plane
p	pressure
π	Ludolph number 3.14159265358979...
$\mathbf{q_n}$	heat flux in the direction of vector $\mathbf{n}$
$\mathbf{q}_{\mathrm{BC}}$	normal heat flux prescribed at a boundary
Q	internal heat sources

r, θ, δ	spherical coordinates
r_E	radius of the Earth
R	gas constant
ρ	density
ρ_m	density of the mantle lithosphere
S	sedimentation parameter
$\boldsymbol{\sigma} = \begin{pmatrix} \sigma_{xx} & \sigma_{xz} \\ \sigma_{zx} & \sigma_{zz} \end{pmatrix} \mathbf{e}_x \otimes \mathbf{e}_z$	deviatoric stress tensor
σ	effective stress
$\sigma_{\mathrm{II}} = \sqrt{1/2\ \boldsymbol{\sigma} : \boldsymbol{\sigma}}$	second invariant of the deviatoric stress tensor
$\bar{\sigma}$	mean stress
$\Delta\sigma$	differential stress
σ_1, σ_3	principal stresses
$\sigma_{\min}$	minimum yield stress
σ_{yield}	yield stress (strength)
t	time
Δt	time-step length
$\mathbf{t}$	tangent vector to a plane
T	temperature
$\mathbf{T} = \{T_x, T_z\}$	traction
$T_{\mathbf{t}}$	shear stress
$T_{\mathbf{n}}$	normal stress
$\boldsymbol{\tau} = \begin{pmatrix} \tau_{xx} & \tau_{xz} \\ \tau_{zx} & \tau_{zz} \end{pmatrix} \mathbf{e}_x \otimes \mathbf{e}_z$	stress tensor
u	elastic flexure
u_0	initial position of the bottom of the crust
u_{prev}	position of the bottom of the crust in the previous time step
v	magnitude of velocity
v_{BC}	magnitude of velocity prescribed at a boundary
v_d	rate of local diffusive erosion
v_e	rate of slope-dependent erosion
v_s	rate of sedimentation
$\mathbf{v} = \{v_x, v_z\}$	velocity of material with respect to spatial frame
$\hat{\mathbf{v}}$	velocity of mesh with respect to spatial frame
w_i	weights for evaluation of composition-dependent parameters
$\mathbf{w}$	velocity of material with respect to referential frame
W	width of the model domain
ϕ	angle of internal friction
ϕ_0	initial angle of internal friction
ϕ_∞	final angle of internal friction
φ	mapping from material to spatial configuration
ψ	mapping from referential to spatial configuration
$\mathbf{x} = \{x, z\}$	spatial Cartesian coordinates
$x_{\min}$	position of the left boundary of the model domain
$x_{\max}$	position of the right boundary of the model domain
x_{ref}	reference point for reference-load evaluation
$\mathbf{X}$	material coordinates
$\boldsymbol{\chi}$	referential coordinates
Ω	model domain